D 2022

U.PORTO
FEUP FACULDADE DE ENGENHARIA
UNIVERSIDADE DO PORTO

MODELLING AND DESIGN OPTIMIZATION OF ALL-VANADIUM REDOX FLOW BATTERIES

NUNO MIGUEL AZEVEDO DIAS LIMA DELGADO
TESE DE DOUTORAMENTO APRESENTADA
À FACULDADE DE ENGENHARIA DA UNIVERSIDADE DO PORTO EM
ENGENHARIA QUÍMICA E BIOLÓGICA

MODELLING AND DESIGN OPTIMIZATION OF ALL-VANADIUM REDOX FLOW BATTERIES

Nuno Miguel Azevedo Dias Lima Delgado

This thesis has been submitted in partial fulfilment of the requirements to obtain degree of

Doctor of Philosophy in Chemical and Biological Engineering

at

University of Porto

Supervisor:

Professor Adélio Miguel Magalhães Mendes, Full Professor

Co-supervisor:

Doctor Ricardo André Ribeiro Monteiro, R&D Engineer (VisBlue Portugal)

Universidade do Porto, Porto 2022

Acknowledgments

This doctoral program presented me with many exciting challenges. I had the pleasure to have several people and institutions providing me support to face these challenges.

Firstly, I would like to express my sincere gratitude to my supervisors, Professor Adélio Mendes and Dr. Ricardo Monteiro, for their guidance, inspiration and shared knowledge about technical and personal matters. We had plenty of fruitful discussions that motivated me to perform my best during this thesis and thrive to be a better person and teammate. I am very grateful for their support and for the opportunity that they provided me with.

I want to thank Søren Bødker and Professor Anders Bentien, for their valuable insights about business, relations, research, batteries, and friendship. Relationships that last for more than 4 years and that can hardly be forgotten. I was also fortunate to work with Jorge Cruz, who helped me overcome many challenges, and Marta Boaventura, who was always available to support me.

To LEPABE team, Paulo Ribeirinha, Carlos Almeida, Frederico Relvas, Tânia Lopes, João Azevedo, Paula Dias and many others, thank you for your support, especially during the starting stage of this doctoral program.

I would not be able to overcome many challenges without the unconditional support from my family, Maria Helena Dias (mother), Pedro Delgado (father) and Pedro Delgado (brother), and my girlfriend, Diana Gomes. Their emotional support was fundamental to help me keep pushing through the tough challenges and keep me focused.

I would like to acknowledge VisBlue A/S and LEPABE for providing me the opportunity for enrolling in this doctoral program. Furthermore, I would like to acknowledge Faculty of Engineering of the University of Porto and VisBlue A/S for the research fellowship and support through the Research Collaboration Agreement “GoFlow”. The research leading to these results also received funding from: i) Projects SunStorage – POCI-01-0145-FEDER-016387 and SunFlow – PTDC/EQU-EQU/30510/2017, both funded by the European Regional Development Fund (FEDER), through COMPETE2020 - Operational Programme for Competitiveness and Internationalisation (POCI) and by national funds, through FCT; ii)

Projects Polysol – POCI-01-0247-FEDER-046109, Baterias2030 – POCI-01-0247-FEDER-046109, and BluEnergy – POCI-01-0247-FEDER-046846, co-funded by Operational Programme for Competitiveness and Internationalisation (COMPETE 2020), under the Portugal 2020 Partnership Agreement, through the European Regional Development Fund (ERDF); and iii) Base – UIDB/00511/2020 and Programmatic – UIDP/00511/2020 Funding of the Laboratory for Process Engineering, Environment, Biotechnology, and Energy – LEPABE - funded by national funds through the FCT/MCTES (PIDDAC).

Abstract

Vanadium redox flow batteries (VRFB) are a promising energy storage technology for stationary applications, but their commercial competitiveness must be increased.

This thesis focuses on optimizing the design of VRFBs with no flow field, using mathematical models, to improve their performance and cycle life. Firstly, the relevance of including distribution channels in the flow frames of VRFBs is assessed through CFD simulations and experiments. Secondly, the impact of the position (through-plane direction) of the distribution channels in the performance is evaluated using a 2D dynamic phenomenological model (DPM). The model was also used to provide more insights about energy losses related to the electrolyte regeneration rate at the electrode. Finally, the DPM, an equivalent circuit model, and an empirical model were used to perform a thorough sensitivity analysis to the parameters affecting shunt currents and optimize the design of the stack.

The results demonstrate that the energy efficiency of the system is maximized when the distribution channels are included in the flow frames and the battery is operated at low flow rates, particularly if the distribution channels are positioned near the membrane. It is also shown that the energy efficiency in larger VRFBs can be improved, and material damage can be minimized by using wider and thinner distribution channels, to improve the electrolyte distribution, and using narrower electrodes, to increase flow velocity. Regarding the stack design, the sensitivity analysis shows that the manifold geometric dimensions affect shunt current losses the most, followed by the geometric dimensions of the distribution channels. Thus, a novel stack design comprising dumping cells is proposed. The new stack design significantly improves the performance of VRFBs when compared to a conventional stack design. For a 343 cm^2 VRFB, the shunt current losses decreased by 23.6 %, the pump power consumption decreased by 33 % and the nominal power increased by 19 % at 80 mA cm^{-2}.

The findings of this work can be used to develop more performant and durable redox flow batteries comprising any liquid electrolyte. This work also proves that mathematical models can be used to accelerate the development of any technology. As such, the DPM developed for VRFBs was adapted to create the first 2D dynamic phenomenological model for solar

redox flow cells (SRFC) reported in the literature. The SRFC model is validated against experimental data and the response of the model under different bias potentials is also assessed. Furthermore, the impact of the recombination mechanisms in the response of the SRFC was studied. The development of this model represents a breakthrough in the research field of solar redox flow cells since it can be used as a reference to develop more complex models and for improving the performance of this technology.

Sumário

As baterias redox de escoamento de vanádio (*vanadium redox flow batteries*, VRFB) são uma tecnologia promissora para armazenamento estacionário de energia, mas o interesse comercial nesta tecnologia tem sido reduzido por causa do seu baixo desempenho.

O objetivo desta tese consiste em otimizar a configuração de VRFBs sem canais de escoamento (*flow fields*), de forma a melhorar o seu desempenho e a sua durabilidade. Este estudo é divido em três fases e realizado com diferentes modelos matemáticos. Na primeira fase é feito um levantamento sobre o impacto dos canais de distribuição no desempenho das VRFBs. Para tal, foram realizadas simulações de escoamento (CFD) e testes experimentais com duas células de 25 cm^2 de área ativa. Na segunda fase foi desenvolvido um modelo fenomenológico multidimensional para fazer um estudo teórico sobre as pernas de energias relacionadas com a regeneração do eletrólito no elétrodo e para avaliar o impacto da posição dos canais de distribuição nessas perdas energéticas. Por fim, foram desenvolvidos três modelos diferentes (multidimensional, circuitos equivalentes e empírico) para realizar uma análise de sensibilidade aprofundada aos parâmetros que afetam as correntes de derivação e para otimizar a configuração da pilha de uma VRFB.

Os resultados obtidos nesta tese comprovam que a introdução de canais de distribuição nas molduras da pilha permite aumentar a eficiência energética do sistema, mas apenas quando a VRFB é operada a caudais baixos. Para melhorar ainda mais o desempenho de uma VRFB e prolongar a sua vida útil, os canais de distribuição deverão ser posicionados perto da membrana e deve ser dada preferência a canais mais largos e finos. Desta forma, é garantida uma boa regeneração do eletrólito perto da membrana e uma boa distribuição do eletrólito no elétrodo. A utilização de elétrodos mais estreitos também irá melhorar a regeneração do eletrólito no elétrodo uma vez que a velocidade de escoamento do eletrólito aumenta. Com base na análise de sensibilidade realizada à configuração da VRFB, conclui-se que as dimensões geométricas do tubo de distribuição têm um impacto nas correntes de derivação bastante mais notável do que os restantes parâmetros. Com base nestes resultados, é proposta uma nova configuração para VRFB que pressupõe a introdução de um novo componente, a *dumping cell*. Esta nova configuração permite reduzir as perdas por correntes

de derivação em 23.6 % e a energia consumida pelas bombas em 33 %, e aumentar a potência nominal em 19 %, quando comparada com a configuração anterior e assumindo uma área ativa de 343 cm^3 e uma densidade de corrente de 80 mA cm^{-2}.

Esta tese providencia informações relevantes para o desenvolvimento de baterias redox de escoamento com elevado desempenho e mais duradouras. Também é demonstrado que os modelos matemáticos são uma ferramenta bastante útil para o desenvolvimento tecnológico de qualquer tecnologia. Por este motivo, o modelo multidimensional desenvolvido para as VRFBs foi utilizado como ponto de partida para o desenvolvimento do primeiro modelo fenomenológico multidimensional para células solar redox de escoamento (*solar redox flow cell*, SRFC). Este modelo foi validado com dados experimentais e foram utilizados diferentes potenciais para simular e avaliar as bandas de energia do fotoelétrodo. Também foi feito um estudo sobre o impacto dos mecanismos de recombinação no desempenho das SRFC. O modelo desenvolvido para SRFCs representa um avanço importante na investigação de SRFCs uma vez que pode ser utilizado como referência para o desenvolvimento de modelos mais complexos e para otimizar o desempenho desta tecnologia.

Table of contents

Acknowledgments i
Abstract v
Sumário ix
Table of contents xiii
List of Figures xix
List of Tables xxvii
Notation and glossary xxxi
1. Introduction 3
1.1. Global warming 3
1.1.1. Greenhouse gas emissions 3
1.1.2. Reducing greenhouse gas emissions 5
1.2. Energy storage systems 6
1.3. Redox flow batteries 8
1.4. Solar redox flow batteries 11
1.5. Motivation and outline 13
1.6. References 16
2. Vanadium redox flow batteries 25
2.1. Introduction 25
2.2. Working principle 25
2.3. In-situ characterization techniques 28
2.3.1. Charge-discharge cycling 29
2.3.2. Polarization curve 32
2.3.3. Electrochemical impedance spectroscopy 33
2.4. Components and materials 35
2.5. Performance losses 39
2.5.1. Activation losses 39
2.5.2. Ohmic losses 40
2.5.3. Concentration polarization 41
2.5.4. Shunt currents 42
2.5.5. Self-discharge reactions 42
2.5.6. Gas evolution 43
2.6. Mathematical models 44
2.6.1. Molecular and micro-scale models 45
2.6.2. Macro-scale models 46

2.7. Conclusions 49
2.8. References 50
3. Impact of the distribution channels in the performance 65
3.1. Abstract 65
3.2. Introduction 66
3.3. Experimental methods 67
3.3.1. Material 67
3.3.2. VRFB setup and performance 67
3.3.3. Pressure drop measurements 69
3.4. Mathematical methods 70
3.4.1. Governing equations 70
3.4.2. Boundary conditions 71
3.4.3. Numerical procedure 71
3.5. Results and discussion 72
3.5.1. Hydraulic performance 72
3.5.2. Electrochemical performance 77
3.6. Conclusions 84
3.7. References 86
4. Modelling and study of the concentration overpotential 93
4.1. Abstract 93
4.2. Introduction 94
4.3. Experimental setup 95
4.4. Mathematical model 96
4.4.1. Governing Equations 97
4.4.2. Boundary and initial conditions 103
4.4.3. Numerical procedure 106
4.5. Results and discussion 106
4.5.1. Model validation 106
4.5.2. Concentration overpotential during cycling 108
4.5.3. Influence of the current density 110
4.5.4. Influence of the flow rate 114
4.5.5. Distribution channel position 117
4.6. Conclusion 121
4.7. References 123
5. A parametric study for shunt current mitigation and stack design optimization 129
5.1. Abstract 129
5.2. Introduction 130

5.3. Redox flow cell stacks 131
5.3.1. 6 cells-stack 131
5.3.2. *N* cells-stack 132
5.3.3. 40 cells-stack equipped with dumping cells 133
5.4. Numerical methods 135
5.4.1. Dynamic phenomenological model 135
5.4.2. Equivalent circuit model 140
5.4.3. Mathematical correlation and sensitivity analysis 143
5.4.4. Pressure drop 145
5.5. Results and discussion 147
5.5.1. Model comparison 147
5.5.2. Effect of the internal resistances in the shunt currents 150
5.5.3. Effect of R_m, R_c, N, and I in the shunt currents 152
5.5.4. Novel stack equipped with M dumping cells 157
5.6. Conclusion 162
5.7. References 164
6. Modelling of a solar redox flow cell 171
6.1. Abstract 171
6.2. Introduction 172
6.3. Mathematical model 173
6.3.1. Governing Equations 175
6.3.2. Boundary and initial conditions 186
6.3.3. Numerical procedure 188
6.4. Results and discussion 189
6.4.1. Model validation 189
6.4.2. Energy band diagram 191
6.4.3. The effect of recombination 194
6.5. Conclusion 197
6.6. References 199
7. Conclusions and future work 205
7.1. Final remarks 205
7.2. Future work 208
Appendix A. Supplementary information for Chapter 4 213
A.1. Figures 213
A.2. Parameters for simulation 217
A.3. Determination of initial ion concentrations 219
A.4. Determination of the concentration overpotential 220
A.5. References 222

Appendix B. Supplementary information for Chapter 5 223
B.1. Parameters used in the simulations 223
B.2. Model comparison data 225
B.3. Mesh quality analysis 226
B.4. Effect of the internal resistances in the shunt currents 227
B.5. Effect of R_m, R_c, I and N in the shunt currents 229
B.6. References 232
Appendix C. Supplementary information for Chapter 6 233
C.1. Simulation parameters 233
C.2. References 237

List of Figures

Figure 1.1 – Contribution of human activities to the global greenhouse gas emissions in 2016. Figure from [8]. 4

Figure 1.2 – World electricity generation from 1990 to 2020 using nuclear, hydro, solar, wind and geothermal, biomass and other renewable sources as energy source. Data from [17]. ... 6

Figure 1.3 – Classification of energy storage technologies according to the form of stored energy. 7

Figure 1.4 – Electrolyte chemistries used in redox flow batteries based on the electrolyte phase (hybrid, liquid, and semi-solid). 10

Figure 2.1 – Schematic representation of the charge and discharge processes in a vanadium redox flow battery equipped with a cation exchange membrane (CEM) and an anion exchange membrane (AEM). 26

Figure 2.2 – Theoretical open circuit potential (V) of a vanadium redox flow battery equipped with a cation exchange membrane as function of the state of charge at a temperature of 298.15 K. A vanadium concentration of 1.6 M and a sulfuric acid concentration 2.0 M were used for calculations. 28

Figure 2.3 – Charge-discharge cycles of a 16 cm^2 VRFB (single cell) at a current density of 80 mA cm^{-2} and a flow rate of 150 ml min^{-1}. The electrolyte consisted in 1.6 M vanadium diluted in 2 M sulfuric acid. This VRFB displays 98 % coulombic efficiency, 84 % potential efficiency and 82 % energy efficiency. 29

Figure 2.4 – Polarization curve of a 16 cm^2 VRFB (single cell) at an open circuit potential of 1.60 V and a flow rate of 150 ml min^{-1}. The dotted line is used to limit the region where each overpotential is dominant. 32

Figure 2.5 – Schematic representation of the sinusoidal potential perturbation and the resulting current with a phase shift. Adapted from [15]. 33

Figure 2.6 – Schematic representation of an equivalent circuit model and EIS curve of a 16 cm^2 VRFB (single cell) at an E_{OCP} of 1.30 V, a flow rate of 150 ml min^{-1}, and a potential perturbation amplitude of 5 mV. The frequency ranged from 100 mHz to 50 kHz. Only a single circle is shown since one of the half-cells displays a resistance much greater than the other. 34

Figure 2.7 – 3D model of a vanadium redox flow battery system. Figure gently provided by VisBlue A/S. 36

Figure 2.8 – 3D model of a redox flow stack with 4 electrochemical cells. 37

Figure 2.9 – Schematic representation of (a) a single VRFB electrochemical cell comprising (b) no flow field, (c) the serpentine flow field, (d) the interdigitated flow field, and (e) the parallel flow field. Figure from [11]. 38

Figure 2.10 – Classification of mathematical models used in the literature to simulate vanadium redox flow batteries according to their approach and application. Figure from [69]. 45

Figure 3.1 – Half-cell designs based on conventional flow-through configurations used in this work: a) Multiple Distribution Path (MDP); b) Oriented Distribution Path (ODP). 1 – graphite felt electrode; 2 – EPDM gasket; 3 – graphite bipolar plate. 68

Figure 3.2 – Pressure drop of ODP (circle) and MDP (triangle) cells with (solid) and without (hollow) graphite felt (GF). 72

Figure 3.3 – Simulated (lines) and experimental (symbols) pressure drop of ODP (circle) and MDP (triangle) cells. 74

Figure 3.4 – Simulated average (line) and relative (square) flow velocity in the electrode using the ODP (dashed line) and the MDP (solid line) cells. The MDP cell is used as a reference to determine the relative flow velocity; positive values indicate that the ODP cell has a higher average flow velocity. 74

Figure 3.5 – Simulated uniformity index of the flow velocity in the electrode using the ODP (dashed line) and the MDP (solid line) cells and respective relative difference (square). The MDP cell is used as a reference to determine the relative uniformity index; negative values mean that the ODP cell has a lower average uniformity index. 75

Figure 3.6 – Contours of 1) flow velocity and 2) uniformity index of the flow velocity in the electrode using the a) MDP and the b) ODP cells at a flow rate of 300 ml min^{-1}. 76

Figure 3.7 – Discharge polarization curves at different flow rates of a) MDP and b) ODP cells. 78

Figure 3.8 – Species conversion in a single electrolyte pass when using the a) MDP and the b) ODP cells at different flow rates, 0 V and 50 % state of charge. 80

Figure 3.9 – ODP and MDP cell and system efficiencies at 80 mA cm^{-2} current density averaged over 20 cycles for a flow rate of a) 10 ml min^{-1}, b) 150 ml min^{-1} and c) 300 ml min^{-1}. The standard deviation of the efficiencies is displayed as error bars. 82

Figure 4.1 – Simulation and experimental charge-discharge curves for a VRFB with 16 cm^2 active area. 107

Figure 4.2 – Average concentration overpotential and SoC of the VRFB during charge-discharge cycling at 80 mA cm^{-2} and 160 ml min^{-1}..... 108

Figure 4.3 – Average concentration overpotential of the VRFB during cycling at current densities of 80 mA cm^{-2} (solid line), 120 mA cm^{-2} (dash line), and 160 mA cm^{-2} (dash dot line)..... 111

Figure 4.4 – Distribution profile of (a) local concentration overpotential, (b) net reaction rate and (c) V^{2+} concentration at the electrode fibers in the through-plane direction (*X* direction) of the negative electrode at 80 mA cm^{-2} (solid line), 120 mA cm^{-2} (dash line), and 160 mA cm^{-2} (dash dot dot line) and 80 % SoC. The bipolar plate | electrode interface is located at $X = 0.0$ mm and the electrode | membrane interface is located at $X = 3.5$ mm.. 113

Figure 4.5 – Average concentration overpotential of the VRFB during cycling at flow rates of 40 ml min^{-1} (dash dot line), 80 ml min^{-1} (dash line) and 160 ml min^{-1} (solid line)..... 115

Figure 4.6 – Distribution profile of the (a) local concentration overpotential and (b) reactant mass transfer coefficient in the through-plane direction (X direction) of the negative electrode at 40 ml min^{-1} (dash dot line), 80 ml min^{-1} (dash line) and 160 ml min^{-1} (solid line) and 80 % SoC. The bipolar plate | electrode interface is located at $X = 0.0$ mm, the electrode | membrane interface is located at $X = 3.5$ mm and the inlet/outlet channel is located at 0.0 mm < X < 1.0 mm..... 116

Figure 4.7 – Relative concentration overpotential for geometries M, C and E at a current density of 160 mA cm^{-2} and flow rates of 40 ml min^{-1}, 80 ml min^{-1} and 160 ml min^{-1}. 118

Figure 4.8 – Concentration overpotential contour in the through-plane direction of the negative electrode at 80 % SoC for cells (a) BP, (b) M, (c) C, and (d) E. The bipolar plate | electrode interface is located at $X = 0.0$ mm and the electrode | membrane interface is located at $X = 3.5$ mm. The inlet is located at $Y = 0$ mm and the outlet is located at $Y = 40$ mm. 120

Figure 5.1 – Schematic representation of the vanadium redox flow stack while charging with six cells, and dimensions of the distribution channels and manifold (in mm). 132

Figure 5.2 – 3D representation of a dumping cell. The electrolyte flow direction at the front (solid line) and back (dashed lined) of the dumping cell is represented by the arrows. 133

Figure 5.3 – Flow frame with (a) two short distribution channels (short frame channel, SFC) and (b) two long distribution channels (long frame channel, LFC). 134

Figure 5.4 – Schematic representation of the equivalent circuit model used to simulate shunt currents in the (a) positive side of a six cell VRFB stack, (b) VRFB stack with *N* cells and (c) VRFB stack with 40 cells (2 × 20 cells-stack) and one dumping cell. $R_{cell,i}$ is the cell internal resistance of cell *i*, R_{cc} is the resistance of the current collector and R_{dc} is the

resistance of the dumping cell. The c and m refer to the distribution channels and manifold, respectively, and the superscripts + and – refer to the positive and negative side, respectively. 142

Figure 5.5 – Shunt currents in the (a) manifold and (b) distribution channels and (c) cumulative cell potential of a VRFB six cells-stack simulated using the dynamic phenomenological model (DPM, black squares) and the equivalent circuit model (ECM, red circles) for charging step, and the relative difference between models (blue triangles). ... 148

Figure 5.6 – Average shunt current in the manifold and potential drop, $\Delta\phi_e$, in a VRFB six cells-stack simulated using the dynamic phenomenological model (DPM) and reference parameters (baseline simulation - BL), tenfold higher surface area, *a*, reaction rate constant, *k*, membrane, σ_{mem}, and electrode, σ_s, conductivities, and mass transfer coefficient, k_m, fivefold higher electrolyte conductivity, σ_e, tenfold lower flow rate, *Q*, and a lower electrode thickness (2.0 mm), δ_{elec}. 150

Figure 5.7 – Number of simulations that resulted in shunt current losses (SCL) within a specific range, e.g., above 1 % and less or equal than 2 % (> 1 - 2), and respective cumulative percentage. The simulations were carried out using the equivalent circuit model with different combinations of values of R_m, R_c, *I*, and *N*. 152

Figure 5.8 – Sensitivity index (SI) and average rate of change m ($\partial SCL = m \cdot \partial x$) of the manifold resistance, R_m, distribution channels resistance, R_c, operating current, *I*, and number of cells in a stack, *N*. 155

Figure 5.9 – Pressure drop caused by the dumping cells ($\Delta p_{dumping\ cells}$) and shunt current loss (SCL) of the 40 cells stack using one, three and seven dumping cells (dc). 158

Figure 5.10 – 2D drawing of the optimized dumping cell and geometric constrains used to optimize the dumping cell design. 159

Figure 6.1 – Schematic representation of the all-vanadium solar redox flow cell setup simulated in this work and labeling of boundary conditions. 174

Figure 6.2 – Schematic representation of the energy band diagram of a solar redox flow cell when (a) the photoelectrode (*n*-type) and the electrolyte are not in contact, (b) the photoelectrode and the electrolyte are in contact and in equilibrium, (c) a potential (E_{bias}) is applied to the cell and (d) a potential is applied to the cell and the cell is under solar illumination. Illustration not to scale. 183

Figure 6.3 – (a) Simulated and experimental current density (*i*) response (*i*-*V* curve) of the photoelectrode in a solar vanadium redox flow cell with 4 cm^2 active area and (b) comparison between the simulated current density response at the photoelectrode and at the negative electrode 190

Figure 6.4 – Potential of the conduction band (black dotted line), valence band (green dash-dotted line), *quasi*-Fermi energy level of the electrons (red dashed line), and *quasi*-Fermi energy level of the holes (blue solid line) when there is (a) accumulation of electrons ($\Delta E_{BB} < 0$ V, $E_{bias} = -1.00$ V), (b) no accumulation/depletion of charges ($\Delta E_{BB} = 0$ V, $E_{bias} = -0.73$ V) and (c) depletion of electrons ($\Delta E_{BB} > 0$ V, $E_{bias} = -0.50$ V). X is the distance from the photoelectrode | electrolyte interface ($X = 0$ nm, x_4, Figure 6.1) to the outer surface of the photoelectrode ($X = 200$ nm, x_5, Figure 6.1). 192

Figure 6.5 – Concentration of holes at the photoelectrode | electrolyte interface under illumination (c_p, black solid line) and dark ($c_{p,dark}$ red dashed line) conditions at different bias potentials..... 193

Figure 6.6 – Simulated (a) current density response (*i*-*V* curve) and (b) normalized *i*-*V* curve of the photoelectrode for baseline parameters (black solid line) and for higher band-to-band recombination (green dotted line, $10 \times k_{BTB,h}$), SRH recombination (yellow small dashed line, $10 \times k_{SRH}$), Auger recombination (red dashed line, $10 \times C_{Aug}$) and surface recombination (blue long dashed line, $10 \times k_{sr}$) rates. 195

Figure 6.7 – Concentration of holes at the photoelectrode | electrolyte interface (c_p) for baseline parameters (black solid line) and for higher band-to-band recombination (green dotted line, $10 \times k_{BTB,h}$), SRH recombination (yellow small dashed line, $10 \times k_{SRH}$), Auger recombination (red dashed line, $10 \times C_{Aug}$) and surface recombination (blue long dashed line, $10 \times k_{sr}$) rates. 196

Figure A.1 – Graphite plate of a VRFB with 16 cm^2 active area used in the experimental test and with milled distribution channels before and after the reactional area. 213

Figure A.2 – Schematic representation of the mass transfer mechanism between the electrode fibers and bulk electrolyte. 213

Figure A.3 – 2D schematic representation of the computational domain with labelled boundaries from 1 to 20. 214

Figure A.4 – Schematic representation of the computational domain and variables solved in each domain. 214

Figure A.5 – Simulated polarization curve (the current density is based on the projected area – solid line) and limiting current based on the polarization curve (dashed line, Eq. (4.43)) for feed flow rates of 10 ml min^{-1} and 160 ml min^{-1} and at a constant SoC of 50 %..... 215

Figure A.6 – Schematic representation of (a) cell BP, with inlet/outlet channel close to the bipolar plate, (b) cell M, with inlet/outlet channel close to the membrane, (c) cell C, with inlet/outlet channel at the center of the electrode and (d) cell E with inlet/outlet channel with the same length as the thickness of the electrode. 216

Figure A.7 – Concentration overpotential during charge-discharge cycling at 80 mA cm^{-2} and 160 ml min^{-1} considering the current density based on the surface area and a lower mass transfer coefficient (solid line) and the current density based on the projected area and a higher mass transfer coefficient (dashed line). 220

Figure B.1 – Average shunt current in the positive manifold of the six cells-stack using a mesh with 15 000, 45 000, 80 000 and 100 000 elements..... 226

List of Tables

Table 4.1 – Reaction rate source terms of species transport equations. 98

Table 5.1 – Design (manifold resistance, R_m and distribution channel resistance, R_c) and operating parameters (electric current, I) used in the equivalent circuit model to simulate shunt currents. The number of cells (N) used in the simulations is 5, 10, 20, 30, and 40. . 144

Table 5.2 – Shunt current loss (SCL) determined using the equivalent circuit model (ECM) and Eq. (5.40) with different combinations of values of manifold resistance, R_m, distribution channels resistance, R_c, internal cell resistance, R_{cell}, active area, A, operating current, I, and number of cells in a stack, N. 154

Table 5.3 – Pressure drop (Δp) and shunt current loss (SCL) in a conventional stack with 40 cells and long (long frame channel, LFC) and short (short frame channel, SFC) distribution channels at 80 mA cm^{-2}. 157

Table 5.4 – Minimum and maximum depth, width, and vertical length of the channels of the dumping cell. Values used in the Solver add-in to optimize the dumping cell flow channel design. 160

Table 6.1 – Comparison between the values used in the simulation and values found in the literature for the fitting parameters. 189

Table A.1 – Parameters used as electrolyte properties. 217

Table A.2 – Parameters used as electrode, bipolar plate and membrane properties. 218

Table A.3 – Electro-kinetic parameters used in the simulation. 218

Table A.4 – Equations used to determine the initial concentration of ion species at a specific SoC. 219

Table B.1 – Parameters used as electrode, bipolar plate and membrane properties. 223

Table B.2 – Dimensions of the channels and manifold of the six cells-stack. 224

Table B.3 – Parameters used as electrolyte properties. 224

Table B.4 – Electro-kinetic and mass transfer parameters used in the simulation. 225

Table B.5 – Shunt current in each channel and each manifold and potential of each cell of the positive side of the VRFB six cells-stack obtained using the dynamic phenomenological model (DPM) and the equivalent circuit model (ECM). The relative difference between

models is calculated using the DPM as reference. The shunt currents were simulated at 50 % state of charge, for the charging step, and with a current density of 80 mA cm^{-2}. 225

Table B.6 – Shunt current in each channel of positive side of the VRFB with six cells obtained for the simulation using the baseline parameters and for the simulations using tenfold higher reaction rate constant, k, mass transfer coefficient, k_m, electrode surface area, a and electrode, σ_s, and membrane, σ_{mem}, conductivities, using fivefold higher electrolyte conductivity, σ_e, tenfold lower flow rate, Q, and a lower electrode thickness (δ_{elec} = 2.0 mm). 227

Table B.7 – Shunt current in each manifold of positive side of the VRFB with six cells obtained for the simulation using the baseline parameters and for the simulations using tenfold higher reaction rate constant, k, mass transfer coefficient, k_m, electrode surface area, a and electrode, σ_s, and membrane, σ_{mem}, conductivities, using fivefold higher electrolyte conductivity, σ_e, tenfold lower flow rate, Q, and a lower electrode thickness (δ_{elec} = 2.0 mm). 228

Table B.8 – Total number of simulations that resulted in shunt current losses (SCL) lower or equal to 1 % and greater than 1 % for each value of manifold resistance, R_m, and channel resistance, R_c. 229

Table B.9 – Total number of simulations that resulted in shunt current losses (SCL) lower or equal to 1% and greater than 1% for each value of electric current, I, and number of cells in the stack, N. 230

Table B.10 – Mean absolute error between the shunt current losses (SCL) determined using the Simulink model and the correlation (Eq. (41)) for each value of manifold resistance, R_m, and channel resistance, R_c. 230

Table B.11 – Mean absolute error between the shunt current losses (SCL) determined using the Simulink model and the correlation (Eq. (41)) for each value of electric current, I, and number of cells in the stack, N. 231

Table C.1 – Properties of the negative electrode, bipolar plate, positive design chamber, photoelectrode, and membrane. 233

Table C.2 – Characteristics of the electrolytes. 235

Table C.3 – Electro-kinetic parameters used in the simulation. 235

Table C.4 – Parameters used to simulate electrons and holes dynamic behavior in the photoelectrode. 236

Notation and glossary

Latin letters

a	Electrode surface area, $m^2\ m^{-3}$
A	Area, m^2
c	Molar concentration, $mol\ m^{-3}$
C_{Aug}	Auger recombination constant, $m^6\ s^{-1}$
c_0	Speed of light in vacuum, $m\ s^{-1}$
D	Diffusion coefficient, $m^2\ s^{-1}$
D_{eq}	Equivalent diameter, m
d_f	Fiber diameter, m
E	Cell reaction potential, V
E_D	Donnan's exclusion potential, V
E_g	Bandgap potential, V
E^0	Standard cell reaction potential, V
F	Faraday constant, $C\ mol^{-1}$
f	Frequency, Hz
f_D	Friction factor, dimensionless
g	Gravitational acceleration, $m\ s^{-2}$
G_i	Charge generation rate, $mol\ m^{-3}\ s^{-1}$
h	Planck constant, J s
i	Current density, $A\ m^{-2}$
i_0	Amplitude of current signal, A
i_L	Limiting current density, $A\ m^{-2}$
I	Electric current, A
I_0	Incident Photon Flux, $m^{-2}\ s^{-1}$
j	Volumetric current density, $A\ m^{-3}$
K_P	Electrode permeability, m^2
k_{KC}	Kozeny-Carman constant, dimensionless
k_m	Mass transfer coefficient, $m\ s^{-1}$
k	Reaction rate constant, $m\ s^{-1}$
k_r	Surface roughness, m
l	length, m
m	Rate of change
$\dot{m}$	Mass flow rate, $kg\ s^{-1}$
N	Number of cells in a stack

N_i	Charge density i, m^{-3}
n	Number of electrons
$\vec{N}$	Superficial molar flux, mol m^{-2} s^{-1}
p	Pressure, Pa
P	Power, W
Q	Volumetric flow rate, m^3 s^{-1}
R_i	Resistance i, Ω
$R_{rec,i}$	Recombination rate i, mol m^{-3} s^{-1}
Re	Reynolds number, dimensionless
R	Universal gas constant, J mol^{-1} K^{-1}
SI	Sensitivity index, dimensionless
SCL	Shunt current loss, %
S	Source term
s	Standard deviation
SoC	State of charge, dimensionless
t	Time, s
T	Temperature, K
UI	Uniformity index, dimensionless
V	Volume, m^3
V_0	Amplitude of potential signal, V
V_{tank}	Electrolyte tank volume, m^3
$\vec{v}$	Velocity of the electrolyte, m s^{-1}
W	Width, m
x	Distance into the photoelectrode, m
z	Valence of ionic species, dimensionless
Z	Impedance, Ω

Greek letters

α	Charge transfer coefficient, dimensionless
$\alpha(\lambda)$	Absorption coefficient, m^{-1}
δ	Thickness, m
$\delta\downarrow$	Depth, m
ε	Electrode porosity, dimensionless
ε_{SC}	Photoelectrode permittivity, dimensionless
ε_0	Vacuum permittivity, $F\ m^{-1}$
η	Overpotential, V
η_C	Coulombic efficiency, %
η_{EE}	Cell or stack energy efficiency, %
η_p	Potential efficiency, %
η_{pump}	Pump efficiency, %
η_{SEE}	System energy efficiency, %
λ	Wavelength, m
μ	Dynamic viscosity, $kg\ m^{-1}\ s^{-1}$
ν_i	Stoichiometric number of species i, dimensionless
ρ	Electrolyte density, $kg\ m^{-3}$
σ	Conductivity, $S\ m^{-1}$
σ_i	Warburg coefficient, $\Omega\ s^{-1/2}$
τ	Charge lifetime, s^{-1}
υ_{th}	Thermal velocity, $m\ s^{-1}$
ϕ	Potential, V
φ	Phase shift amount, s
ω	Radial frequency, $rad\ s^{-1}$

Subscripts

1	Negative electrode | membrane interface
2	Positive electrode | membrane interface
act	Activation
advec	Advective
atm	Atmospheric
Aug	Auger
BB	Band bending
BP	Bipolar plate
BTB	Band-to-band
c	Charge step
cc	Current collector
conc	Concentration
ct	Charge transfer
CB	Conduction Band
d	Discharge step
dc	Dumping cell
dl	Double-layer
diff	Diffusion
e	Liquid property
elec	Electrode property
eq	Equilibrium
F	Fermi
in	Inlet
ini	Initial
inj	Injection
int	Intrinsic
i	Species
m	manifold
mem	Membrane
mig	Migration
mom	Momentum
n	Electrons
OCP	Open circuit potential
ohm	Ohmic
out	Outlet
ox	Oxidation/oxidized

p	Holes
PA	Projected area
red	Reduction/reduced
rel	Relative
s	Solid property
sr	Surface recombination
SC	Semiconductor/photoelectrode
SCL	Space charge layer
V	Vanadium
VB	Valence Band

Superscripts

+	Positive half-cell property
-	Negative half-cell property
eff	Effective
i	Positive or negative half-cell property
s	Surface of the fibers of the electrode

List of Acronyms

AEM	Anion exchange membrane
CEM	Cation exchange membrane
CFD	Computational fluid dynamics
DFT	Density functional theory
DPM	Dynamic phenomenological model
ECM	Equivalent circuit model
EIS	Electrochemical impedance spectroscopy
ESS	Energy storage systems
GF	Graphite felt
GHG	Greenhouse gas
LBM	Lattice Boltzmann Method
MC	Monte Carlo
MD	Molecular dynamics
MDP	Multi distribution path
NASA	National Aeronautics and Space Administration
ODP	Oriented distribution path
PEC	Photoelectrochemical cell

RFB	Redox flow battery
SHE	Standard hydrogen electrode
SRFC	Solar redox flow cell
SRFB	Solar redox flow battery
TEMPO	2,2,6,6-Tetramethylpiperidine-1-oxyl
VRFB	Vanadium redox flow battery

Chapter 1

Introduction

1. Introduction

Equation Chapter (Next) Section 1

1.1. Global warming

1.1.1. Greenhouse gas emissions

Greenhouse gases (GHG), such as methane (CH_4), nitrous oxide (N_2O), and carbon dioxide (CO_2), are responsible for regulating the temperature of the earth [1]. These gases prevent part of the heat radiated by the earth from being released to space (greenhouse effect). The average temperature on earth would be 33 ºC lower in the absence of greenhouse gases [2]. In the past 40 years, the CO_2 concentration in the atmosphere increased by nearly 22 % [3]. The concentration of CH_4 and N_2O in the atmosphere has also been increasing at an average rate of 0.3 % $year^{-1}$ since 2001 [4, 5]. Consequently, the average temperature on earth increased by 1.1 ºC since the 19^{th} century [6]. Increasing the average temperature on earth leads to more frequent extreme weather events, such as floods, cold and heat waves, wildfires, droughts and storms [7]. Ultimately, the impact of GHG on the environment and eco system of the earth can be devastating and irreversible.

Although the concentration of GHG is affected by natural sources, human activity contributed the most to the GHG emissions increase. As shown in Figure 1.1, most of the GHG emitted from human activity in 2016 resulted from energy generation.

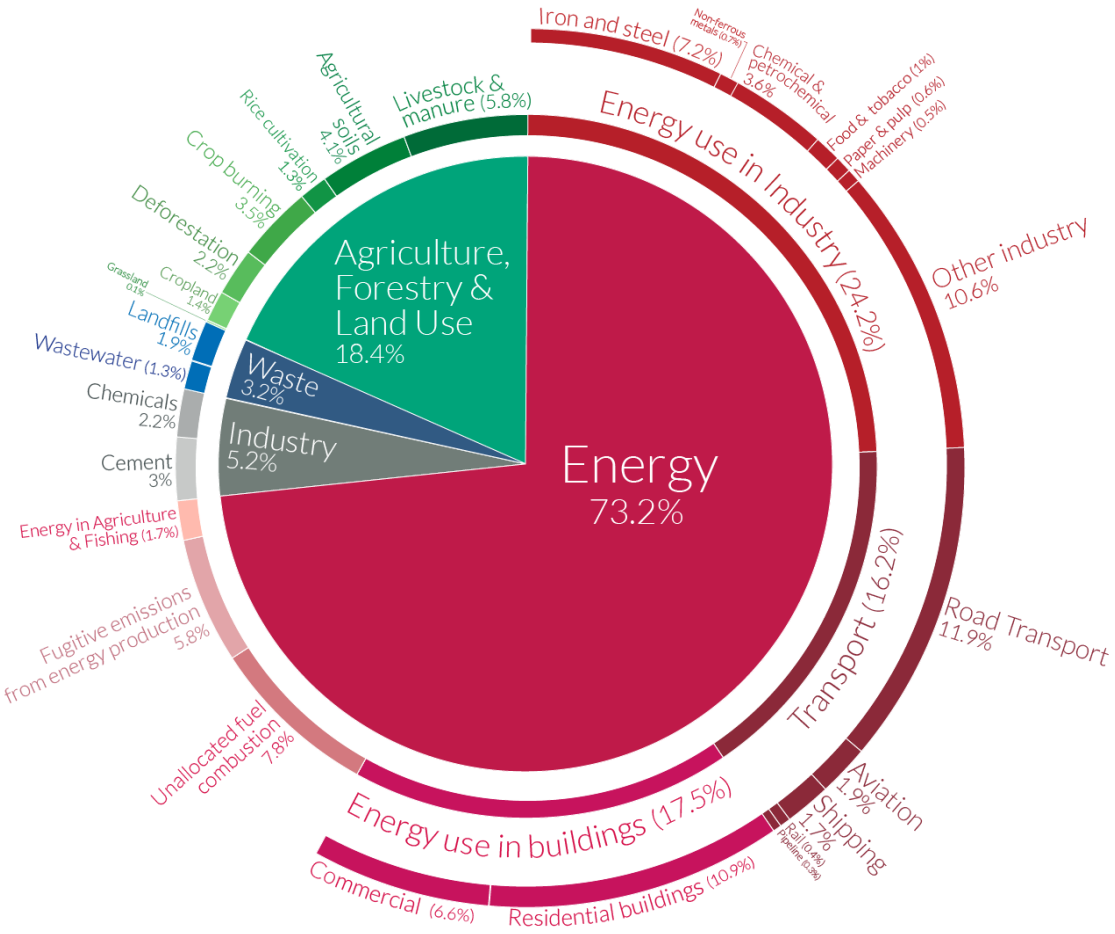

Figure 1.1 – Contribution of human activities to the global greenhouse gas emissions in 2016. Figure from [8].

Fossil fuels have been widely used as an energy source for industry, buildings, and transportation. They are burned to produce electricity, heat, and power. However, the combustion of fossil fuels produces CO_2, contributing to global warming and extreme weather events. Thus, more eco-friendly energy sources, such as wind, solar, biomass, hydrogen, biofuels and nuclear energy, have been a subject of great interest [9]. Other examples of CO_2 sources are the production of some chemicals and cement, deforestation and crop burning. Agriculture also has a significant impact on global warming, despite having a much smaller contribution to the emission of GHG than fossil fuels. Raising livestock and using manure as fertilizer contribute to the emission of N_2O and CH_4, which have a stronger greenhouse effect than CO_2. Wastewaters and landfills are other examples that also have a significant emission of N_2O and CH_4 [10].

1.1.2. Reducing greenhouse gas emissions

Reducing the emission of GHG to net zero by 2050 is a goal set by the European Union through the European Green Deal [11]. The latter is an effort to limit the average temperature on the earth to 1.5 ºC above pre-industrial levels, which is a global goal set through the Paris Agreement [12]. The purpose of these agreements is to reduce the impact of GHG on the ecosystem and biodiversity, and to restore the damages already caused by them. However, the goals set by the agreements will not be met if no further efforts are made [11]. Since 2010, yearly Conference of the Parties have been conducted to evaluate the measures applied by the participating countries towards mitigating climate change [13]; it is urgent to find more solutions to mitigate the emission of GHG and to act as soon as possible.

To further reduce GHG emissions, the life cycle of materials must be improved by increasing materials recirculation and production efficiency. The consumption of meat must be lowered to reduce livestock and food waste must be reduced to decrease the emission of GHG in the landfills and from food production. Agriculture practices need to be improved to increase harvest yields and decrease soil degradation [14]. For example, biochar can be used to improve the fertility of the soils and to capture CO_2 [15]. Natural carbon sink must also be increased through, for example, reforestation and forest, seagrass, peatland, and wetland management [14]. More environmentally friendly technologies must also be developed and implemented to replace fossil fuels. For example, novel nuclear reactors are being developed to make energy production from nuclear energy more affordable, more efficient, and safer [16]. Yet, technologies that produce electricity from renewable sources have been implemented at a much faster rate than technologies that require nuclear energy (Figure 1.2).

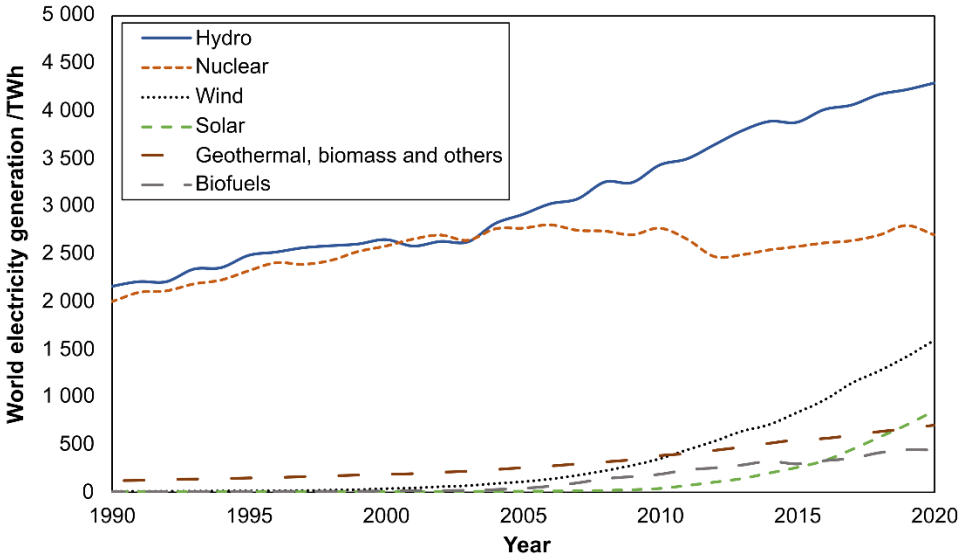

Figure 1.2 – World electricity generation from 1990 to 2020 using nuclear, hydro, solar, wind and geothermal, biomass and other renewable sources as energy source. Data from [17].

Renewables are expected to be responsible for producing 85 % of the world's energy requirements in 2050. Geothermal, biomass, and other renewables should provide 23 % of the total energy, while solar and wind energy should produce nearly 22 % and 20 % of the total energy, respectively [18]. Thus, the latter are crucial to reach net zero emissions.

1.2. Energy storage systems

The major disadvantage of using solar and wind power as energy sources is the unpredictability of weather conditions and limited daylight hours; the electricity generated from solar and wind power is intermittent which affects the grid stability. Such bottlenecks can be mitigated using energy storage systems (ESS) since they can provide support for maintaining grid frequency and stability (power quality) [19, 20]. ESS can also provide support for energy management through black start services, load leveling, and peak shaving [19, 20].

Different types of ESS have been developed over the years and they can be classified according to the form of stored energy [20, 21]:

- Thermal: Energy is stored in the form of latent heat, sensible heat, or thermochemical heat.
- Chemical: Energy is stored in chemicals through chemical reactions.
- Electrochemical: Energy is stored in the form of chemical energy through electrochemical reactions.
- Electrical: Energy is stored in the form of electric or magnetic fields.
- Mechanical: Energy is stored in the form of potential or kinetic energy through pressurized systems or body motion.

Figure 1.3 shows the different energy storage technologies classified according to the form of stored energy.

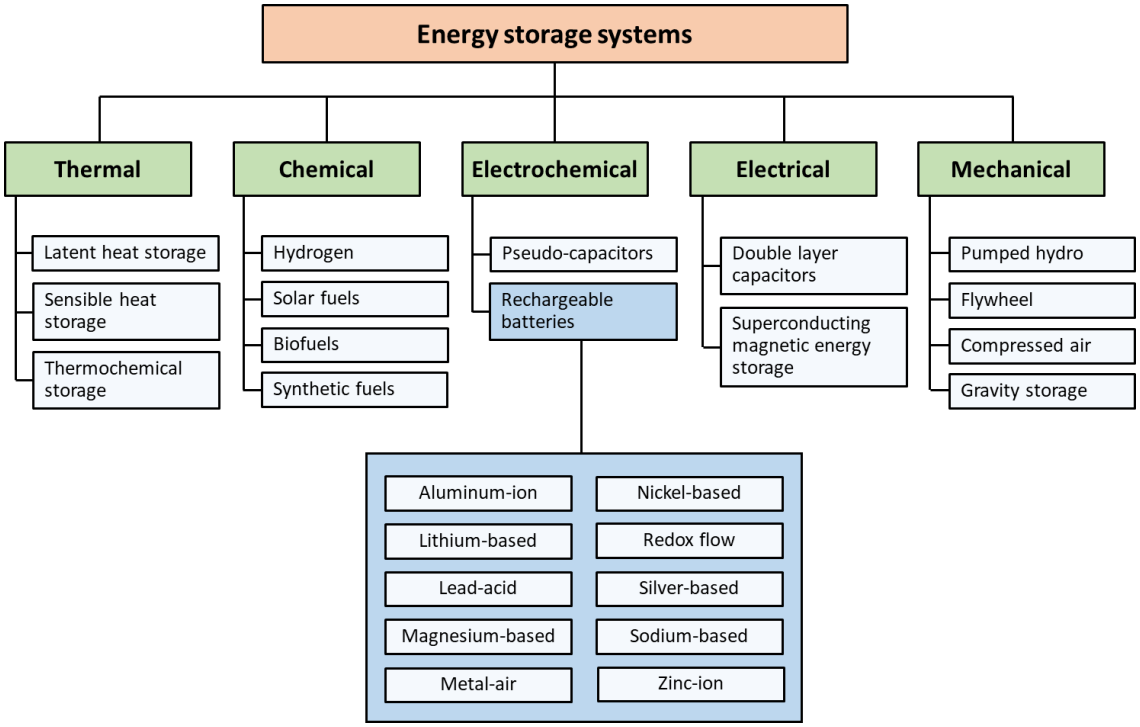

Figure 1.3 – Classification of energy storage technologies according to the form of stored energy.

In 2020, pumped hydro storage accounted for 96 % of the world's installed power capacity (159 GW) [22]. In this technology, water is pumped to an upper reservoir to store electricity and released to a lower reservoir to discharge electricity. Although it has a very low energy

density (0.5-3.0 Wh l^{-1}), it can be scaled up to have an extremely high power (GW) and energy (GWh) capacity. Additionally, its lifetime is remarkably high [23]. These characteristics make it very appealing to store energy, despite requiring large geographical areas to be installed. Thermal storage technologies account for 38 % of the remaining 6.4 GW world power capacity and batteries are the third most popular ESS with an installed power capacity of 2.3 GW (36 %) [22]. The latter are easy to install and have a low self-discharge rate, a high energy efficiency and a fast response time. Thus, they can be used for energy and power quality management [24]. Several battery technologies with different technical specifications have been created since they rely on electrochemical reactions to convert electricity to chemical energy and *vice-versa*. For example, lithium-ion batteries display a high power (500 - 2000 W l^{-1}) and energy (170 - 700 Wh l^{-1}) density [25, 26] and require low maintenance. Due to such attractive features, it is the battery with the most installed power capacity (1.6 GW) [22]. Lead-acid batteries have worse performance than lithium-ion batteries, but they have a lower capital cost (€254 kWh^{-1}) [25] which also makes them a very appealing technology for energy storage. Recently, Šimić et al. [27] carried out an extensive technical comparison between lead-acid, lithium-ion, nickel-cadmium, nickel-metal hydride, sodium-sulfur, and vanadium redox flow batteries (VRFB). The authors concluded lithium-ion batteries can be used for many applications, but other technologies may perform better for specific applications. For example, VRFBs are more suitable for long-term stationary storage applications than lithium-ion batteries since their lifetime is higher. Lastly, flywheel and compressed air storage technologies account for 15 % and 11 %, respectively, of 6.4 GW installed power capacity [22]. An in-depth comparison of the technical specifications, applications, cost, and environmental impact of the different ESS can be found elsewhere [28, 29]. There are many ESS technologies suitable for stationary applications. However, not all will be able to fulfill the Strategic Energy Technology Plan target for 2030 of €0.05 kWh^{-1} $cycle^{-1}$, 10 000 cycles of life cycle and 20 years of lifetime [30]; developing new ESS and optimizing the existing technologies is required.

1.3. Redox flow batteries

Redox flow batteries (RFB) are rechargeable batteries that require low maintenance and display a fast response time, a high energy efficiency (up to 85 %), and a long lifetime (up to

20 000 [30]). Also, they have the unique feature of decoupling power and energy capacity. The power is set by the battery stack size (e.g., number of electrochemical cells and active area size), and the energy is set by the electrolyte (e.g., total volume and concentration of redox species). The latter is stored in external tanks and pumped from the tanks to the stack and *vice-versa*. Thus, RFBs can be easily scaled to each application's requirements [30]. However, the energy density of RFBs is low [31] when compared to, for example, lithium-ion batteries, and a large area is required for installation [32]. RFBs are only suitable for large-scale stationary applications.

The concept of RFB was invented in 1954 by Kangro [33]. Two electrolytes – a positive electrolyte, displaying a higher redox potential, and a negative electrolyte, displaying a lower redox potential – are used as energy carriers. The electrolytes are separated by an ion-exchange membrane which, under charging and discharging conditions, allows selected ions to pass and complete redox reactions. However, no experimental demonstration of the RFB concept was carried out until the 1970s, when NASA developed the first RFB [34]. It employed the iron and chromium redox couples in diluted hydrochloric acid [35]. Later in the 1980s, Skyllas-Kazacos and colleagues developed the all-vanadium redox flow battery (or simply, vanadium redox flow battery – VRFB) [36]. RFBs started being widely researched in 2011 [37], after the Copenhagen Accord was established. Among other goals, the Copenhagen Accord aimed at providing financial support to developing countries for developing new technologies that could help reduce GHG emissions [38]. Significant improvements have been made to RFBs since 2011, leveraging them as the most promising battery technology for large-scale stationary applications. In fact, RFBs are already commercialized, and they currently represent about 4 % of the world's installed power capacity, excluding pumped hydro [22]. Along with performance improvements, many electrolyte chemistries (Figure 1.4) have been researched to find the RFB with the ideal characteristics: safe, recyclable, eco-friendly, cheap, and should display a good reversibility, a good electrolyte stability, a negligible capacity loss, a long cycle life, a high efficiency, and a high power and energy densities.

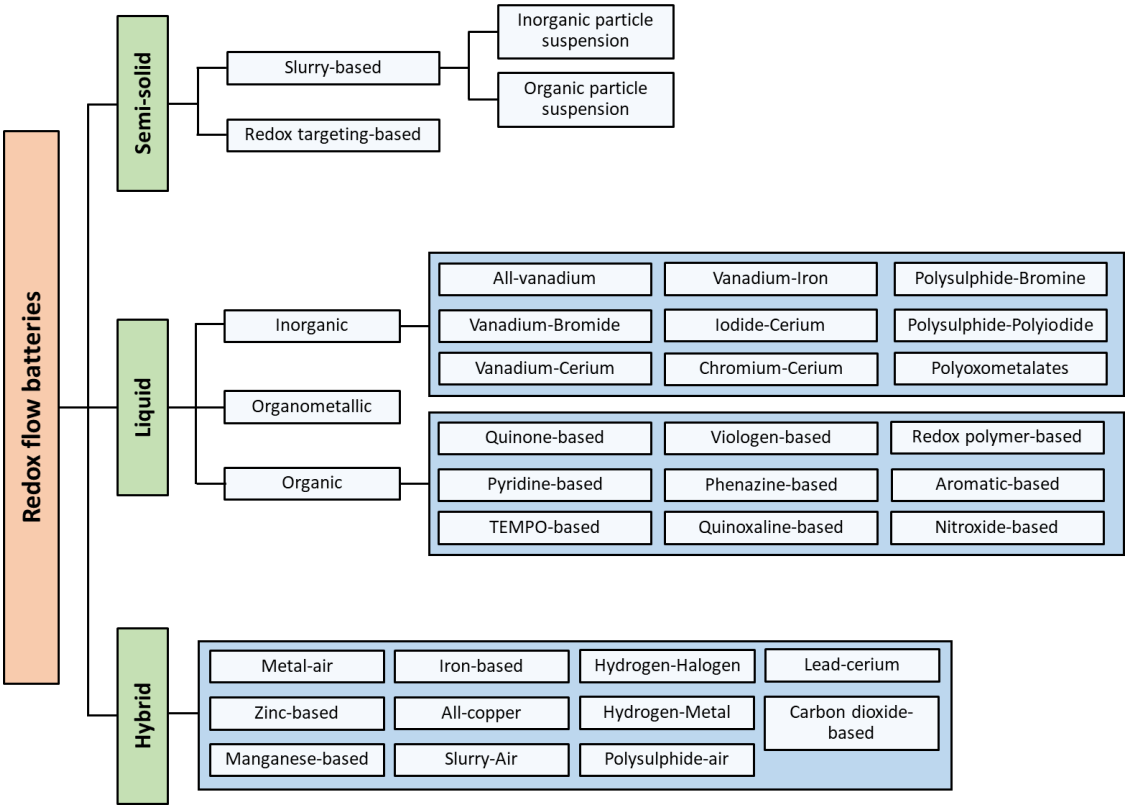

Figure 1.4 – Electrolyte chemistries used in redox flow batteries based on the electrolyte phase (hybrid, liquid, and semi-solid).

The VRFB is the most researched RFB technology since it fulfills several of the previous requirements: it is non-flammable and recyclable, it has a low environmental impact and it displays good reversibility, a long cycle life (>15 000 [30]), high efficiency and negligible capacity loss. Also, no precipitation of vanadium salts is observed up to a temperature of 40 ºC and the electrolyte cross-contamination can be easily recovered since both storage tanks have the same electrolyte solution [39]. This technology has been implemented in projects from kW up to MW scale [40] and is commercialized by several companies such as VisBlue, Dalian Rongke Power, Invinity Energy Systems, and Enerox. The all-iron RFB has also reached the commercialization stage. It is more eco-friendly and cheaper than the VRFB. However, the electrolyte has poor chemical stability due to pH variations during operation [41]. Other electrolyte chemistries have been receiving great research attention since the VRFB and the all-iron RFB display low power and energy densities. For example, the hydrogen-bromine RFB can be used for applications that require an ESS with a high-power

density [42] and the zinc-air RFB is suitable for applications that demand a high energy density [43]. Though, bromine is extremely toxic, hydrogen is flammable [42] and the zinc-air RFB has a low cycle life (<2000) and a low efficiency [43, 44]. Other RFB technologies such as, iron-salt (VoltStorage) [45], zinc-iron (ViZn Energy), zinc-bromine (RedFlow) [30] and hydrogen-manganese (RFC Power), are also being commercialized. Typically, zinc-based RFBs are cheap and have a high cell potential [46] but display low energy efficiency, and dendrite formation may lead to short-circuit and battery failure [47]. The manganese-hydrogen RFB is also a promising technology that employs cheap and abundant elements. It delivers high power [48] and energy (up to 263 $Wh\ l^{-1}$ [49]) densities and high energy efficiency at a fraction of the cost of VRFBs [48]. Organic RFBs have also been receiving a great deal of attention since they are more eco-friendly than inorganic RFBs. Currently, Kemiwatt commercializes a quinone-based RFB and JenaBetteries has installed a kW scale pyridine-based RFB [30]. A novel RFB technology employing CO_2 and bromide as redox couples was invented by Gyenge [50] and it is commercialized by Agora Energy. The CO_2 RFB is a recent technology and, thus, displays a very low power density [51]. Though, it holds great promise since it can contribute to lower the concentration of CO_2 in the atmosphere. Recently, a novel microbial RFB was also reported in the literature [52]. Despite the low power and energy (25 – 35 $Wh\ l^{-1}$) densities of VRFBs [30], their advantages overcome the benefits of other RFB technologies. Currently, VRFBs are the most viable RFB technology for large scale stationary applications.

1.4. Solar redox flow batteries

A solar redox flow battery (SRFB) consists of an RFB coupled to one or more photoelectrochemical cells (PEC). This technology stores energy from sunlight in the electrolyte. The PEC converts sunlight energy to chemical energy through photoelectrochemical reactions (charge step). The discharge step consists in converting chemical energy to electricity through electrochemical reactions, similar to RFBs. This process is typically carried out using carbon-based electrodes to minimize energy losses [53]. SRFBs have the same advantages as RFBs concerning scalability, safety, and environmental impact. Moreover, they are a very attractive technology due to their unique features: i) the capability to convert solar energy to chemical energy in a single device eliminates the need

for intermediate electronic components when compared to a solution with independent devices, reducing the overall cost; ii) it is more compact and, thus, more appealing than conventional configurations (e.g., using a photovoltaic panel and battery as independent devices, or a PEC for water splitting and a fuel cell) for production and storage of electricity in remote areas; iii) solar heat absorbed by the PEC is transferred to the electrolyte and can be used to heat water and buildings [54].

SRFBs were invented in 1976 by Hodes et al. [55], a few years after the first RFB was created. The authors developed a cell comprising a Cd-Se semiconductor as photoelectrode, a carbon-based electrode as the counter electrode, and an electrolyte containing S/S^{2-} as redox pair and 1 M OH^- as supporting electrolyte. Later, Fan et al. [56] introduced the first SRFB comprising two photoelectrodes (*n*-WSe_2 and *p*-WSe_2). This configuration does not require an external power source to store energy since photooxidation and photoreduction of the active species occur in the *n*-WSe_2 and *p*-WSe_2 photoelectrodes, respectively. Several SRFBs comprising different photoelectrode-electrolyte pairs have been studied since 1976 [57]. However, these devices were not able to function as a battery since they could only operate in the charge mode. Therefore, they should be denoted as solar redox storage cells, when there is no electrolyte flow, or solar redox flow cells (SRFC), when there is electrolyte flow. These studies demonstrated the feasibility of solar charging an RFB but the first unbiased SRFC capable of charging the electrolyte up to 90 % state of charge (SoC) was only reported in 2016 [58].

SRFBs only started receiving more research attention in 2011 due to the Copenhagen Accord, similar to RFBs. In fact, rechargeable SRFBs were only invented in 2013; Liu et al. [59] used a dye-sensitized solar cell with electrolyte flow, connected to an RFB through external electric and hydraulic circuits, to charge and discharge the electrolytes. More notably, Yan, Li and Gao [60] developed a device with a 3-electrode configuration (one photoelectrode and two electrodes) that can charge and discharge. Recent studies focus on finding new photoelectrode-electrolyte pairs that can provide long battery life and a high solar-to-output electricity efficiency [61]. The energy density of SRFBs is often neglected, despite being much lower than the energy density of RFBs; a low concentration of active species is used in SRFBs to minimize parasitic light absorption and increase the solar-to-

chemical energy conversion efficiency [57, 62]. RFBs and SRFBs comprising similar electrolyte chemistries (liquid phase, Figure 1.4) have been reported in the literature since their working principle is very similar [57]. Though, organic redox species are more promising than inorganic redox species for SRFBs. The redox potential of organic redox species can be tuned, through molecular modifications, to match the requirements (e.g., energy levels) of the photoelectrode and maximize the power output [63].

Despite the great interest in SRFBs, this technology has not reached the commercialization stage. It is far from being economically feasible since it displays a low energy efficiency and a low energy and power density [63] and poor stability [57]. Thus, further research is required to improve the performance of this technology.

1.5. Motivation and outline

Despite the great potential of vanadium redox flow batteries (VRFBs), this technology does not yet fulfill all the requirements of the Strategic Energy Technology Plan [30]. The round-trip efficiency and cycle life must be greatly improved to decrease the levelized cost of storage (€ kWh^{-1}); it is expected VRFBs to have a higher levelized cost of storage than lithium-ion batteries by 2050 [64]. The commercial models of VRFBs still underperform with current densities of 150 mA cm^{-2} @ 80 % round-trip efficiency, while current densities up to 600 mA cm^{-2} were already reported in the literature for lab-size cells @ 80 % of round-trip efficiency [65]. There are several key factors to be addressed that can improve the commercial competitiveness of this technology such as: i) optimize the manufacturing process and reduce the cost of the flow battery components to decrease the production costs; ii) improve or develop new active materials (e.g., electrodes, membranes, and electrolyte additives) to increase the round-trip; iii) optimize the design (e.g., flow fields, distribution channel and manifold design and arrangement of the electrochemical cells) of the VRFBs to increase the round-trip efficiency and the lifetime.

The main objective of this thesis is to provide insights for design optimization of VRFBs, aiming towards more efficient and durable batteries. To accomplish this objective, several mathematical models were developed. The models are used to perform fundamental research about energy losses related to the design of the VRFB (e.g., concentration polarization and shunt currents) and propose mitigation strategies. Additionally, the knowledge obtained

during the development of the VRFB models was used to develop the first phenomenological model for solar vanadium redox flow cells reported in the literature. This work was carried out at VisBlue Portugal under the research collaboration agreement "GoFlow" made by and between Visblue A/S and the Faculty of Engineering of the University of Porto.

This thesis is divided into seven chapters:

- **Chapter 1** introduces the problem of global warming and the role of energy storage systems as a solution to reduce greenhouse gas emissions. An overview of the existing energy storage systems is provided. Different redox flow battery (RFB) technologies are presented, and their main advantages and disadvantages are discussed. Solar redox flow batteries are also briefly introduced.
- A more in-depth introduction to VRFBs is carried out in **Chapter 2**. The most important fundamentals of VRFBs are also presented in this chapter, including the working principle, characterization techniques, components, performance loss mechanisms, and mathematical models.
- In **Chapter 3**, the influence of the distribution channels in the system energy efficiency of a VRFB is studied. Experiments and simulations are carried out to compare two 25 cm^2 VRFBs with and without distribution channels. Based on the results, insights for designing larger VRFBs with higher system energy efficiency are provided.
- **Chapter 4** reports a dynamic multi-dimensional model for a VRFB equipped with an anion exchange membrane. This model is used to study energy losses related to mass transfer during charge-discharge cycles under different operating conditions. The model is also used to provide guidelines for optimizing the design of VRFBs; the energy losses of VRFBs using distribution channels in different positions in the through-plane direction are compared.
- A systematic study about shunt currents in VRFBs is carried out in **Chapter 5** to optimize the design of the stack of a VRFB. The multi-dimensional model developed in **Chapter 4** and an equivalent circuit model are used to assess the impact of physicochemical properties of internal components and the design of the

stack in the shunt currents. An empirical model is also developed to determine the energy losses in RFBs due to shunt currents. Finally, a novel stack design is proposed to reduce shunt currents, pump energy consumption, and increase the nominal power.

- **Chapter 6** presents the first dynamic multi-dimensional model for solar redox flow cells (SRFC). The model is compared to experimental data and verified by analyzing the energy band diagrams for different bias potentials. The impact of the recombination mechanism in the performance of the SRFC is also analyzed using the model, providing relevant information for the development of more efficient SRFCs.
- **Chapter 7** is dedicated to the conclusions and suggestions for future work.

1.6. References

1. United States Environmental Protection Agency.*Greenhouse gases*. [accessed October, 2021]; Available from: https://www.epa.gov/report-environment/greenhouse-gases.
2. World Meteorological Organization.*Greenhouse gases*. [accessed October, 2021]; Available from: https://public.wmo.int/en/our-mandate/focus-areas/environment/greenhouse%20gases.
3. Global Monitoring Laboratory.*Trends in atmospheric carbon dioxide*. 2021 [accessed October, 2021]; Available from: https://gml.noaa.gov/ccgg/trends/global.html.
4. Global Monitoring Laboratory.*Trends in atmospheric nitrous oxide*. 2021 [accessed October, 2021]; Available from: https://gml.noaa.gov/ccgg/trends_n2o/.
5. Global Monitoring Laboratory.*Trends in atmospheric methane*. 2021 [accessed October, 2021]; Available from: https://gml.noaa.gov/ccgg/trends_ch4/.
6. World Meteorological Organization, *WMO statement on the state of the global climate in 2019*. 2020, World Meteorological Organization. p. 44.
7. National Aeronautics and Space Administration.*The effects of climate change*. [accessed October, 2021]; Available from: https://climate.nasa.gov/effects/.
8. H. Ritchie.*Sector by sector: where do global greenhouse gas emissions come from?* 2020 [accessed October, 2021]; Available from: https://ourworldindata.org/ghg-emissions-by-sector.
9. World Energy Council, *World energy scenarios: exploring innovation pathways to 2040*. 2019: World Energy Council.
10. World Resources Institute.*World Greenhouse Gas Emissions: 2016*. 2020 [accessed October, 2021]; Available from: https://www.wri.org/data/world-greenhouse-gas-emissions-2016.
11. European Commission, *The European Green Deal*. 2019: EUR-Lex.
12. European Commission.*Paris Agreement*. 2015 [accessed December, 2021]; Available from: https://ec.europa.eu/clima/eu-action/international-action-climate-change/climate-negotiations/paris-agreement_en.
13. Iberdrola.*Climate negotiations: 25 years of searching for consensus on the fight against climate change*. [accessed January, 2022]; Available from: https://www.iberdrola.com/sustainability/international-agreements-on-climate-change.

14. J. Falk; and O. Gaffney, *Scaling 36 solutionms to halve emissions by 2030*. 2020: Exponential roadmap.
15. A. Kumar, E. Singh, R. Mishra, and S. Kumar, *Biochar as environmental armour and its diverse role towards protecting soil, water and air.* Science of The Total Environment, 2022. **806**: p. 150444.
16. TerraPower.*Our work.* [accessed October, 2021]; Available from: https://www.terrapower.com/our-work/.
17. bp p.l.c.*Statistical Review of World Energy - all data, 1965-2020*. 2021 [accessed November, 2021]; Available from: https://www.bp.com/en/global/corporate/energy-economics/statistical-review-of-world-energy.html.
18. D. Gielen, F. Boshell, D. Saygin, M.D. Bazilian, N. Wagner, and R. Gorini, *The role of renewable energy in the global energy transformation.* Energy Strategy Reviews, 2019. **24**: p. 38-50.
19. National Renewable Energy Laboratory, *Energy storage possibilities for expanding electric grid flexibility*. 2016.
20. E. Hossain, H.M.R. Faruque, M.S.H. Sunny, N. Mohammad, and N. Nawar, *A Comprehensive Review on Energy Storage Systems: Types, Comparison, Current Scenario, Applications, Barriers, and Potential Solutions, Policies, and Future Prospects.* Energies, 2020. **13**(14): p. 3651.
21. H.H.L.L.S. Petersen, *DTU international energy report 2013*. 2013.
22. OnLocation, *Electricity storage technology review*. 2020: U.S. Department of Energy.
23. European Association for Storage Energy.*Energy storage technologies*. [accessed November, 2021]; Available from: https://ease-storage.eu/energy-storage/technologies/.
24. Q. Abbas, M. Mirzaeian, M.R.C. Hunt, P. Hall, and R. Raza, *Current State and Future Prospects for Electrochemical Energy Storage and Conversion Systems.* Energies, 2020. **13**(21).
25. A.A. Kebede et al., *Techno-economic analysis of lithium-ion and lead-acid batteries in stationary energy storage application.* Journal of Energy Storage, 2021. **40**: p. 102748.
26. K.A. Vishnumurthy and K.H. Girish, *A comprehensive review of battery technology for E-mobility*. Journal of the Indian Chemical Society, 2021. **98**(10): p. 100173.

27. Z. Šimić, G. Knežević, D. Topić, and D. Pelin, *Battery energy storage technologies overview.* International Journal of Electrical and Computer Engineering Systems, 2021. **12**(1): p. 53-65.
28. H.A. Behabtu et al., *A Review of Energy Storage Technologies' Application Potentials in Renewable Energy Sources Grid Integration.* Sustainability, 2020. **12**(24).
29. P. Alotto, M. Guarnieri, and F. Moro, *Redox flow batteries for the storage of renewable energy: A review.* Renewable and Sustainable Energy Reviews, 2014. **29**: p. 325-335.
30. E. Sánchez-Díez et al., *Redox flow batteries: Status and perspective towards sustainable stationary energy storage.* Journal of Power Sources, 2021. **481**: p. 228804.
31. I. Iradi, U. Fernandez-Gamiz, A. Martinez-San-Vicente, E. Zulueta, and J. Lopez-Guede, *Vanadium Redox Flow Batteries: A Review Oriented to Fluid-Dynamic Optimization.* Energies, 2020. **14**: p. 176.
32. L. da Silva Lima et al., *Life cycle assessment of lithium-ion batteries and vanadium redox flow batteries-based renewable energy storage systems.* Sustainable Energy Technologies and Assessments, 2021. **46**: p. 101286.
33. W. Kangro, *Process for storing electrical energy in liquids*. 1954, Walther Kangro: Germany.
34. M.K. Ravikumar, S. Rathod, N. Jaiswal, S. Patil, and A. Shukla, *The renaissance in redox flow batteries.* Journal of Solid State Electrochemistry, 2017. **21**(9): p. 2467-2488.
35. N.H. Hagedorn, *NASA redox storage system development project*. 1984.
36. M. Rychcik and M. Skyllas-Kazacos, *Characteristics of a new all-vanadium redox flow battery.* Journal of Power Sources, 1988. **22**(1): p. 59-67.
37. I. Iwakiri, T. Antunes, H. Almeida, J.P. Sousa, R.B. Figueira, and A. Mendes, *Redox Flow Batteries: Materials, Design and Prospects.* Energies, 2021. **14**(18): p. 5643.
38. United Nations, *Report of the Conference of the Parties on its fifteenth session*. 2010.
39. Y. Yang, Y. Zhang, L. Tang, T. Liu, S. Peng, and X. Yang, *Improved energy density and temperature range of vanadium redox flow battery by controlling the state of charge of positive electrolyte.* Journal of Power Sources, 2020. **450**: p. 227675.
40. J.H. Vinco, A.E.E.d.C. Domingos, D.C.R. Espinosa, J.A.S. Tenório, and M.P.G. Baltazar, *Unfolding the Vanadium Redox Flow Batteries: An indeep perspective on its*

components and current operation challenges. Journal of Energy Storage, 2021. **43**: p. 103180.

41. S. Yu et al., *A low-cost sulfate-based all iron redox flow battery.* Journal of Power Sources, 2021. **513**: p. 230457.
42. G.L. Soloveichik, *Flow Batteries: Current Status and Trends.* Chemical Reviews, 2015. **115**(20): p. 11533-11558.
43. A.R. Mainar et al., *An overview of progress in electrolytes for secondary zinc-air batteries and other storage systems based on zinc.* Journal of Energy Storage, 2018. **15**: p. 304-328.
44. B. Amunátegui, A. Ibáñez, M. Sierra, and M. Pérez, *Electrochemical energy storage for renewable energy integration: zinc-air flow batteries.* Journal of Applied Electrochemistry, 2018. **48**(6): p. 627-637.
45. M. Peither, *ECO21 Berlin: Michael Peither pitches VoltStorage*. 2021, ecosummitTV: www.youtube.com.
46. L.F. Arenas, A. Loh, D.P. Trudgeon, X. Li, C. Ponce de León, and F.C. Walsh, *The characteristics and performance of hybrid redox flow batteries with zinc negative electrodes for energy storage.* Renewable and Sustainable Energy Reviews, 2018. **90**: p. 992-1016.
47. L. Guo, H. Guo, H. Huang, S. Tao, and Y. Cheng, *Inhibition of Zinc Dendrites in Zinc-Based Flow Batteries.* Frontiers in Chemistry, 2020. **8**(557).
48. J. Rubio-Garcia et al., *Hydrogen/manganese hybrid redox flow battery.* Journal of Physics: Energy, 2018. **1**(1): p. 015006.
49. W. Chen et al., *A manganese–hydrogen battery with potential for grid-scale energy storage.* Nature Energy, 2018. **3**(5): p. 428-435.
50. E.L. Gyenge, *Redox flow battery with carbon dioxide based redox couple*. 2020, Agora Energy Technologies Ltd.
51. P. Hosseini-Benhangi, C.C. Gyenge, and E.L. Gyenge, *The carbon dioxide redox flow battery: Bifunctional CO2 reduction/formate oxidation electrocatalysis on binary and ternary catalysts.* Journal of Power Sources, 2021. **495**: p. 229752.
52. M.S.S. Santos et al., *Microbially-charged electrochemical fuel for energy storage in a redox flow cell.* Journal of Power Sources, 2020. **445**: p. 227307.

53. W. Li et al., *A Long Lifetime Aqueous Organic Solar Flow Battery.* Advanced Energy Materials, 2019. **9**(31): p. 1900918.
54. W. Li and S. Jin, *Design Principles and Developments of Integrated Solar Flow Batteries.* Accounts of Chemical Research, 2020. **53**(11): p. 2611-2621.
55. J. Manassen, G. Hodes, and D. Cahen, *Photoelectrochemical Energy Conversion and Storage: The Polycrystalline Cell with Different Storage Modes.* Journal of The Electrochemical Society, 1977. **124**(4): p. 532-534.
56. F.-R.F. Fan, H.S. White, B.L. Wheeler, and A.J. Bard, *Semiconductor electrodes. 31. Photoelectrochemistry and photovoltaic systems with n- and p-type tungsten selenide (WSe2) in aqueous solution.* Journal of the American Chemical Society, 1980. **102**(16): p. 5142-5148.
57. K. Wedege, D. Bae, W.A. Smith, A. Mendes, and A. Bentien, *Solar Redox Flow Batteries with Organic Redox Couples in Aqueous Electrolytes: A Minireview.* The Journal of Physical Chemistry C, 2018. **122**(45): p. 25729-25740.
58. J. Azevedo et al., *Unbiased solar energy storage: Photoelectrochemical redox flow battery.* Nano Energy, 2016. **22**.
59. P. Liu, Y.-l. Cao, G.-R. Li, X.-P. Gao, X.-P. Ai, and H.-X. Yang, *A Solar Rechargeable Flow Battery Based on Photoregeneration of Two Soluble Redox Couples.* ChemSusChem, 2013. **6**(5): p. 802-806.
60. N.F. Yan, G.R. Li, and X.P. Gao, *Solar rechargeable redox flow battery based on Li2WO4/LiI couples in dual-phase electrolytes.* Journal of Materials Chemistry A, 2013. **1**(24): p. 7012-7015.
61. W. Li et al., *High-performance solar flow battery powered by a perovskite/silicon tandem solar cell.* Nature Materials, 2020. **19**(12): p. 1326-1331.
62. S. Morawiec et al., *Experimental quantification of useful and parasitic absorption of light in plasmon-enhanced thin silicon films for solar cells application.* Scientific reports, 2016. **6**: p. 22481-22481.
63. L. Cao, M. Skyllas-Kazacos, and D.-W. Wang, *Solar Redox Flow Batteries: Mechanism, Design, and Measurement.* Advanced Sustainable Systems, 2018. **2**(8-9): p. 1800031.
64. O. Schmidt, S. Melchior, A. Hawkes, and I. Staffell, *Projecting the Future Levelized Cost of Electricity Storage Technologies.* Joule, 2019. **3**(1): p. 81-100.

65. H.R. Jiang, J. Sun, L. Wei, M.C. Wu, W. Shyy, and T.S. Zhao, *A high power density and long cycle life vanadium redox flow battery.* Energy Storage Materials, 2020. **24**: p. 529-540.

Chapter 2

Vanadium redox flow batteries

2. Vanadium redox flow batteries

Equation Chapter (Next) Section 1

2.1. Introduction

The objective of this chapter is to introduce the fundamentals of VRFBs. Firstly, the process of charging and discharging a VRFB, and the concept of state of charge are explained. Secondly, the most used techniques to assess the performance of a VRFB are briefly introduced. Then, the components of a VRFB, a stack, and a cell are presented. A discussion about their purpose and materials typically used is carried out. Mechanisms that lead to performance losses and methodologies to mitigate them are also briefly addressed. Finally, an introduction to the mathematical models reported in the literature of VRFBs is also carried out. The advantages and disadvantages of each mathematical mode, and their approach and applications are discussed.

2.2. Working principle

The VRFB employs vanadium salts dissolved in diluted sulfuric acid as positive and negative electrolytes. Therefore, this technology takes advantage of the four oxidation states of vanadium (V^{2+}, V^{3+}, V^{4+}, and V^{5+}) to store (charge) and release (discharge) energy. As Figure 2.1 shows, the process of charging a VRFB consists in reducing V^{3+} (green solution) to V^{2+} (purple solution) at the negative electrolyte and oxidizing VO^{2+} (blue solution) to VO_2^{+} (yellow solution) at the positive electrolyte. The electrons from the oxidation reaction migrate from the positive side to the negative side through an external circuit. To maintain charge balance, protons (H^{+}) cross through the cation exchange membrane (CEM) in the same direction. When an anion exchange membrane (AEM) is used, anions move from the negative electrolyte to the positive electrolyte; this type of membrane contains functional groups that are positively charged [1]. The discharge process is the opposite of the charge process since the electrochemical reactions are reversible.

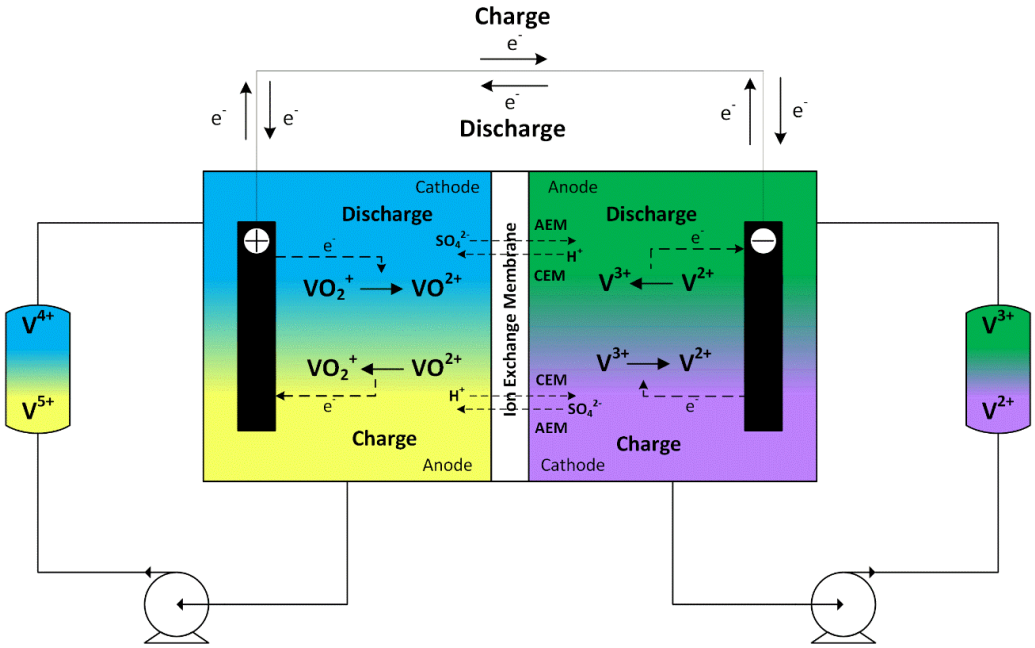

Figure 2.1 – Schematic representation of the charge and discharge processes in a vanadium redox flow battery equipped with a cation exchange membrane (CEM) and an anion exchange membrane (AEM).

The battery is fully charged (SoC = 100 %) when all V^{3+} ions are reduced to V^{2+} and all VO^{2+} ions are oxidized to VO_2^+ and fully discharge (SoC = 0 %) when the opposite is observed. The SoC of a VRFB is determined by the SoC of the half-cell with lowest SoC, which can be determined using the following equations:

$$\mathrm{SoC}_{-} = \frac{c_{\mathrm{V}^{2+}}}{c_{\mathrm{V}^{2+}} + c_{\mathrm{V}^{3+}}} \tag{2.1}$$

$$\mathrm{SoC}_{+} = \frac{c_{\mathrm{VO}_2^+}}{c_{\mathrm{VO}^{2+}} + c_{\mathrm{VO}_2^+}} \tag{2.2}$$

and c_i is the molar concentration (mol m^{-3}) of vanadium ions.

The electrochemical reactions that take place at the positive (Eq. (2.3)) and negative sides (Eq. (2.4)) are as follows:

$$\mathrm{VO_2^+ + 2H^+ + e^- \underset{\text{charge}}{\overset{\text{discharge}}{\rightleftharpoons}} VO^{2+} + H_2O} \tag{2.3}$$

$$V^{3+} + e^- \underset{\text{discharge}}{\overset{\text{charge}}{\rightleftharpoons}} V^{2+} \tag{2.4}$$

and the overall reaction becomes:

$$V^{3+} + VO^{2+} + H_2O \underset{\text{discharge}}{\overset{\text{charge}}{\rightleftharpoons}} V^{2+} + VO_2^+ + 2H^+ \tag{2.5}$$

Under standard conditions (298.15 K and 1 atm) and assuming the vanadium electrolyte is an ideal dilute solution (activity coefficients are equal to unity), the redox potential of Eq. (2.3) ($E^{0,+}$) is 1.00 V *vs*. SHE, while the redox potential of Eq. (2.4) ($E^{0,-}$) is -0.26 V *vs*. SHE [2]. Thus, the standard reduction potential of the overall reaction (E^0, Eq. (2.6)) is 1.26 V.

$$E^0 = E^{0,+} - E^{0,-} \tag{2.6}$$

However, the potential of a VRFB, in the absence of current (open circuit potential, E_{OCP}), is not equal to the standard reduction potential. The process of charging and discharging the VRFB affects the temperature of the electrolyte [3] and the concentration of vanadium ions. Assuming the activity coefficients are equal to unity, the theoretical E_{OCP} of a VRFB can be determined using the following equation [4, 5]:

$$E_{OCP} = E^0 + \frac{\partial E}{\partial T} \cdot (T - 298.15) + \frac{RT}{nF} \ln \left(\frac{c_{V^{2+}} c_{VO_2^+} \left(c_{H^+} \right)^2}{c_{V^{3+}} c_{VO^{2+}}} \right) \tag{2.7}$$

where T is the electrolyte temperature (K), R is the gas constant (8.314 J K^{-1} mol^{-1}), F is the faraday constant (96 485 A s mol^{-1}), n is the number of electrons exchanged in the electrochemical reactions and $\partial E/\partial T$ is the experimental variation of the standard reduction potential of the cell with the temperature (-2.4×10^{-3} V K^{-1})

As Figure 2.2 shows, the theoretical E_{OCP} of a VRFB ranges from 0.84 V to 1.80 V, depending on the state of charge.

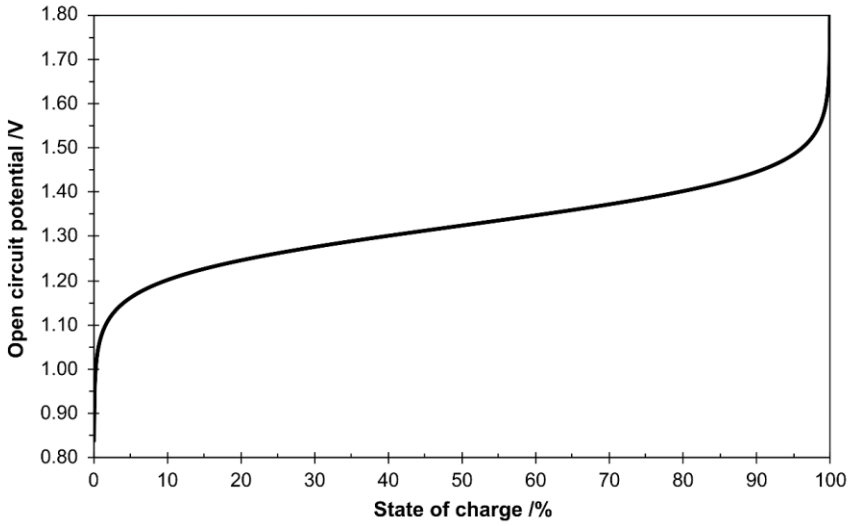

Figure 2.2 – Theoretical open circuit potential (V) of a vanadium redox flow battery equipped with a cation exchange membrane as function of the state of charge at a temperature of 298.15 K. A vanadium concentration of 1.6 M and a sulfuric acid concentration 2.0 M were used for calculations.

Despite the Nernst equation (Eq. (2.7)) being widely used to determine the theoretical E_{OCP}, it does not provide a precise estimation of the experimental E_{OCP}. Alternatives have been proposed to account for the potential generated due to the repulsion of ions at the membrane (Donnan potential) [5] or the permselectivity of the membrane [6]. These studies assumed that the electrolyte behaves as an ideal-dilute solution which also contributes to the discrepancy between the theoretical and the experimental E_{OCP} [7]; using the formal potential instead of the standard reduction potential may lead to more accurate results. Regardless, Eq. (2.7) is sufficient to provide insights about the relationship between the E_{OCP} and the state of charge.

2.3. In-situ characterization techniques

Several in-situ techniques can be used to evaluate the performance of a VRFB. Charge-discharge cycling is the most used since it provides information about the amount of energy stored, self-discharge rate, nominal power output, and energy efficiency. A polarization curve is a characterization technique that requires less time than charge-discharge cycles to perform. It provides important information about the energy losses under different operating

conditions (e.g., different flow rates and current densities) and the maximum power output. Despite not providing any performance indicator, electrochemical impedance spectroscopy (EIS) is useful to measure internal resistances. These characterization techniques are briefly discussed below.

2.3.1. Charge-discharge cycling

The charge-discharge cycling (Figure 2.3) is a characterization technique where a constant current I (galvanostatic mode) is applied to the VRFB, and the cell potential E is measured. The state of charge increases during the charge step and decreases during the discharge step. Thus, the cell potential follows a similar pattern to the E_{OCP}.

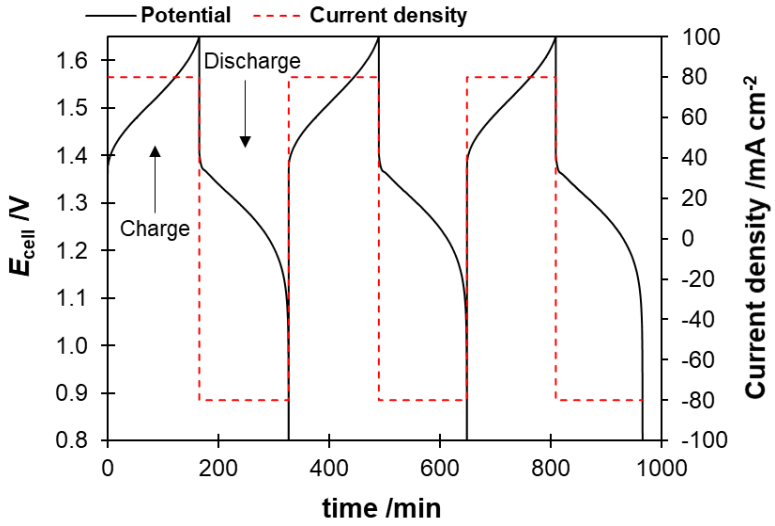

Figure 2.3 – Charge-discharge cycles of a 16 cm^2 VRFB (single cell) at a current density of 80 mA cm^{-2} and a flow rate of 150 ml min^{-1}. An electrolyte volume of 80 ml was used for each tank. The electrolyte consisted in 1.6 M vanadium diluted in 2 M sulfuric acid. This VRFB displays 98 % coulombic efficiency, 84 % potential efficiency and 82 % energy efficiency.

The data obtained with this technique is used to evaluate the performance of the VRFB through the determination of the following parameters:

- **Potential efficiency**

When the cell is operated in galvanostatic mode (constant applied current), the cell potential (E_{cell}) is not equal to the E_{OCP} owing to intrinsic energy losses related to activation (η_{act}), ohmic (η_{ohm}), and concentration (η_{conc}) overpotentials (Eq. (2.8)) [8]:

$$E_{cell} = E_{OCP} \pm (\eta_{act} + \eta_{ohm} + \eta_{conc}) \tag{2.8}$$

where the positive sign refers to the charge step and the negative sign refers to the discharge step. The potential efficiency (η_P) can be determined using Eq. (2.9) to evaluate the impact of these overpotentials during charge-discharge cycling.

$$\eta_P(\%) = \frac{\text{Average discharge potential (V)}}{\text{Average charge potential (V)}} = \frac{\int E_d \mathrm{d}t_d}{\int E_c \mathrm{d}t_c} \times 100 \tag{2.9}$$

where t_d and t_c are the discharge and charge time, respectively, and E_c and E_d are the cell, or stack, potential during the charge and discharge step, respectively.

- **Coulombic efficiency**

The coulombic efficiency (η_C, Eq. (2.10)) is used to quantify the impact of electric current losses, due to gas evolution and capacity loss mechanisms (e.g., shunt currents, side reactions, vanadium crossover, and vanadium precipitation), in the performance of a VRFB [9].

$$\eta_C(\%) = \frac{\text{Discharge capacity (Ah)}}{\text{Charge capacity (Ah)}} = \frac{\int I_d \mathrm{d}t_d}{\int I_c \mathrm{d}t_c} \times 100 \tag{2.10}$$

where I_c and I_d are the current during the charge and discharge steps, respectively.

- **Energy efficiency**

The energy efficiency (η_{EE}, Eq. (2.11)) is used to evaluate all the energy losses inherent to a VRFB that cause the amount of energy discharged to be lower than the amount of energy stored.

$$\eta_{EE}(\%) = \frac{\text{Discharged energy (Wh)}}{\text{Stored energy (Wh)}} = \eta_P \times \eta_C = \frac{\int E_d I_d \mathrm{d}t_d}{\int E_c I_c \mathrm{d}t_c} \times 100 \tag{2.11}$$

- **System energy efficiency**

Other energy losses, such as the energy consumed by the pumps (P_{pump}), must also be considered to have an accurate estimation of the overall energy efficiency of a VRFB (η_{SEE}, Eq. (2.12)).

$$\eta_{SEE}(\%) = \frac{\int \left(E_{\text{d}} I_{\text{d}} - P_{\text{pump}} \right) \text{d}t_{\text{d}}}{\int \left(E_{\text{c}} I_{\text{c}} - P_{\text{pump}} \right) \text{d}t_{\text{c}}} \times 100 \tag{2.12}$$

The system energy efficiency is often neglected since most studies found in the literature are dedicated to improving or developing new materials for VRFBs. However, the latter must be determined when comparing VRFBs with different geometric (flow field and distribution channels) and physical (electrode) properties since the pump energy consumption can have a significant impact on the results [10].

- **Energy storage capacity**

Charge-discharge cycling is also a useful technique to determine the amount of energy that the VRFB can store (capacity) (Eq. (2.13)).

$$\text{Experimental capacity (Ah)} = \int I_{\text{d}} \, \text{d}t_{\text{d}} \tag{2.13}$$

Due to capacity loss mechanisms, the experimental capacity is always lower than the thermodynamic capacity (Eq. (2.14)) [11, 12].

$$\text{Thermodynamic capacity (Ah)} = 2.78 \times 10^{-4} \times nFc_{\text{V}}V \tag{2.14}$$

where F is the Faraday constant (96 485 A s mol^{-1}), c_{V} is the total vanadium concentration and V is the electrolyte volume in a single tank.

The electrolyte utilization can be determined by dividing the experimental capacity (Eq. (2.13)) by the thermodynamic capacity (Eq. (2.14)). The latter quantifies the percentage of electrolyte that is being effectively used to store energy. Additionally, the capacity loss can be quantified by comparing the energy discharged in each cycle with the energy discharged in the first cycle. The determination of the capacity loss allows an evaluation of the longevity and stability of the system [13]. The nominal power output can also be calculated by multiplying the average cell potential by the current.

2.3.2. Polarization curve

The discharge polarization curve (*i-E*, Figure 2.4) is performed by applying a potential to the cell (potentiostatic mode) that changes according to a specified scan rate (mV s^{-1}) and measuring the current. The correlation between current and potential changes according to the dominant resistance (kinetic, ohmic, or mass transfer). Thus, it is a useful tool to identify the predominant loss mechanism

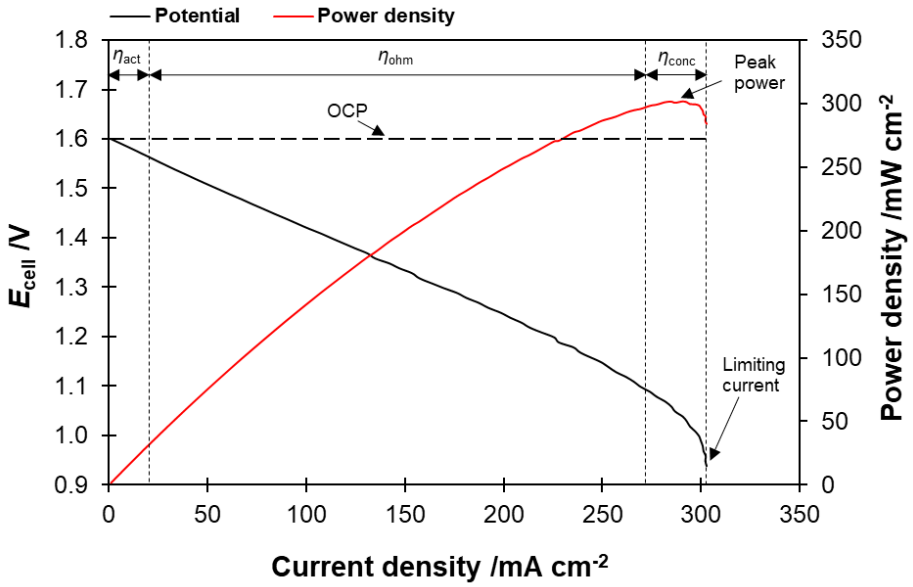

Figure 2.4 – Polarization curve of a 16 cm^2 VRFB (single cell) at an open circuit potential of 1.60 V and a flow rate of 150 ml min^{-1}. The dotted line is used to limit the region where each overpotential is dominant.

Contrarily to charge-discharge cycling, polarization curves do not provide information about losses related to capacity loss mechanisms. The potential is applied during a short period, sufficient to slightly reduce the state of charge of the electrolyte at the electrode fibers but not in the storage tanks. The data obtained with this technique provides a quantitative evaluation of the activation (dominant at low current densities), ohmic (dominant at the linear region of the *i-E* curve), and concentration (dominant in the exponential region of the *i-E* curve, or low potentials) overpotentials [14].

A rough estimation of the potential efficiency can be obtained through polarization curves; for a specific current density, the discharge potential efficiency can be determined by

dividing the measured potential by the E_{OCP}. The potential efficiency can then be calculated by raising the result by a power of two, assuming the potential efficiency of the charge and discharge steps is equal. For more accurate results, the polarization curves should be started at 50 % state of charge. Additionally, the data obtained with the polarization curve can be used to determine the maximum power and current delivered by the VRFB (Figure 2.4).

2.3.3. Electrochemical impedance spectroscopy

Electrochemical impedance spectroscopy (EIS) is a characterization technique that is used to determine resistances associated with ohmic and activation losses and concentration polarization. Contrarily to a polarization curve, it provides direct quantification of such resistances.

This method is performed by applying a very small potential perturbation with a sinusoidal behavior and measuring a current. The resulting current has the same frequency as the potential perturbation, but phase shifted by an amount φ (Figure 2.5).

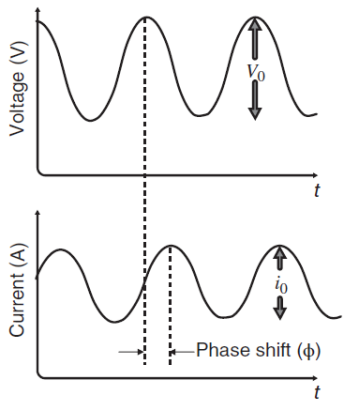

Figure 2.5 – Schematic representation of the sinusoidal potential perturbation and the resulting current with a phase shift. Adapted from [15].

The impedance Z (Eq. (2.15)), similarly to electrical resistance, is used to measure the ability of a system to impede electrical current but it can deal with time- or frequency-dependent phenomena [15]. It can be written in terms of a real Z_r (ohmic resistances) and an imaginary Z_i (dynamic resistances) components:

$$Z = Z_0 \frac{e^{j\omega t}}{e^{j\omega t - j\phi}} = Z_0 e^{j\phi} = Z_0 \cos\phi + Z_0 j \sin\phi = Z_r + Z_i \qquad (2.15)$$

where j is the imaginary number ($\sqrt{-1}$), t is the time and ω is the radial frequency in rad s^{-1} ($\omega = 2\pi f$, where f is the frequency in Hz). The impedance data can be plotted on a Nyquist plot (Figure 2.6).

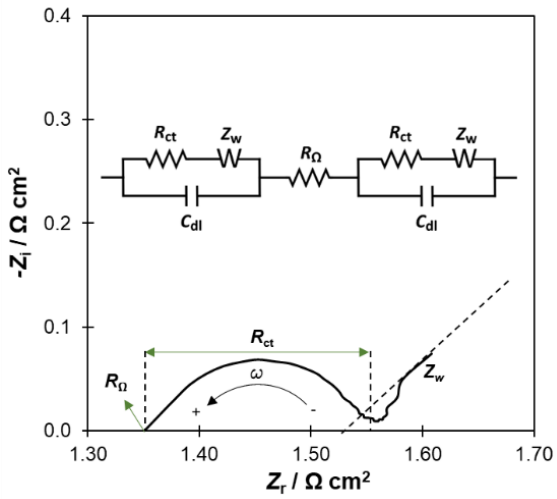

Figure 2.6 – Schematic representation of an equivalent circuit model and EIS curve of a 16 cm^2 VRFB (single cell) at an E_{OCP} of 1.30 V, a flow rate of 150 ml min^{-1}, and a potential perturbation amplitude of 5 mV. The frequency ranged from 100 mHz to 50 kHz. Only a single circle is shown since one of the half-cells displays a resistance much greater than the other.

Since ohmic resistances are described by a simple resistor, they can be determined when the imaginary (dynamic) component is zero (Figure 2.6). The charge transfer resistance, however, considers the contribution of the Faradaic (kinetic) resistance and double-layer capacitance; the impedance behavior is modeled as a parallel combination of a resistor, R_{ct}, and a capacitor, C_{dl} (Eq. (2.16)) [16].

$$\frac{1}{Z} = \frac{1}{Z_{ct}} + \frac{1}{Z_{dl}} = \frac{1}{R_{ct}} + j\omega C_{dl} \quad \longrightarrow \quad Z = \frac{1}{\frac{1}{R_{ct}} + j\omega C_{dl}} \tag{2.16}$$

The mass transfer can be modelled by a porous bounded Warburg circuit element [16], which relates the impedance with the radial frequency as follows [15]:

$$Z = \frac{\sigma_i}{\sqrt{\omega}}(1-j)\tanh\left(\delta\sqrt{\frac{j\omega}{D_i}}\right) \tag{2.17}$$

where D_i is the diffusion coefficient of species i, δ is the diffusion layer thickness and σ_i is the Warburg coefficient of species i (Eq. (2.18)), which describes the effectiveness of diffusion transport.

$$\sigma_i = \frac{RT}{(nF)^2 a\sqrt{2}}\left(\frac{1}{c_{\mathrm{eq},i}\sqrt{D_i}}\right) \tag{2.18}$$

where c_{eq} is the concentration of species i in the electrolyte solution and a is the electrode surface area.

The impedance response in a VRFB tends to an infinite value; the diffusion layer is infinitely thick (infinite Warburg). Thus, Eq. (2.19) can be simplified as follows:

$$Z = \frac{\sigma_i}{\sqrt{\omega}}(1-j) \tag{2.19}$$

and the Warburg coefficient can be determined when the imaginary impedance is 0. The equivalent circuit model of a VRFB is shown in Figure 2.6.

2.4. Components and materials

Similar to most RFBs that employ liquid electrolytes, a VRFB comprises three essential components: stack, piping system and external storage tanks (Figure 2.7). Other relevant components are also shown in Figure 2.7.

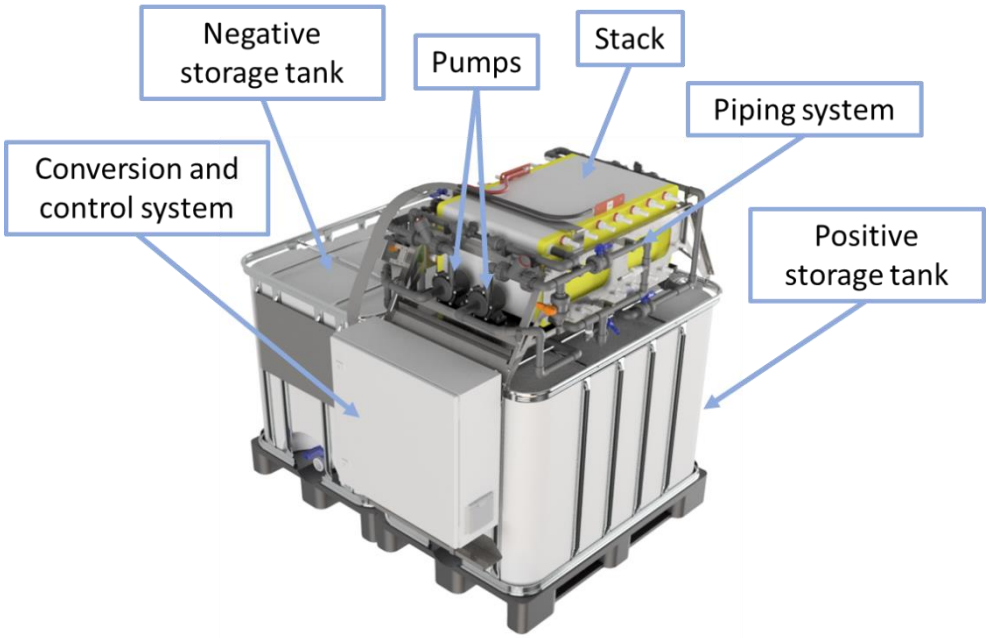

Figure 2.7 – 3D model of a vanadium redox flow battery system. Figure gently provided by VisBlue A/S.

The storage tanks are used to store the electrolyte solutions, which are pumped through the piping system into the stack, and *vice-versa*. The stack (Figure 2.8) consists of several electrochemical cells electrically connected in series and hydraulically connected in parallel. It is responsible for converting electricity into chemical energy and chemical energy into electricity and, thus, the performance of a VRFB is established by this component. However, developing a high-performance and leak-free stack is a challenge faced by several commercial companies. A good stack design ensures that both requirements are fulfilled. Additionally, choosing the appropriate internal components (membrane, electrode, gaskets, bipolar plate) and having a rigorous stack assembly procedure can have a significant impact on the performance and lifetime of the stack.

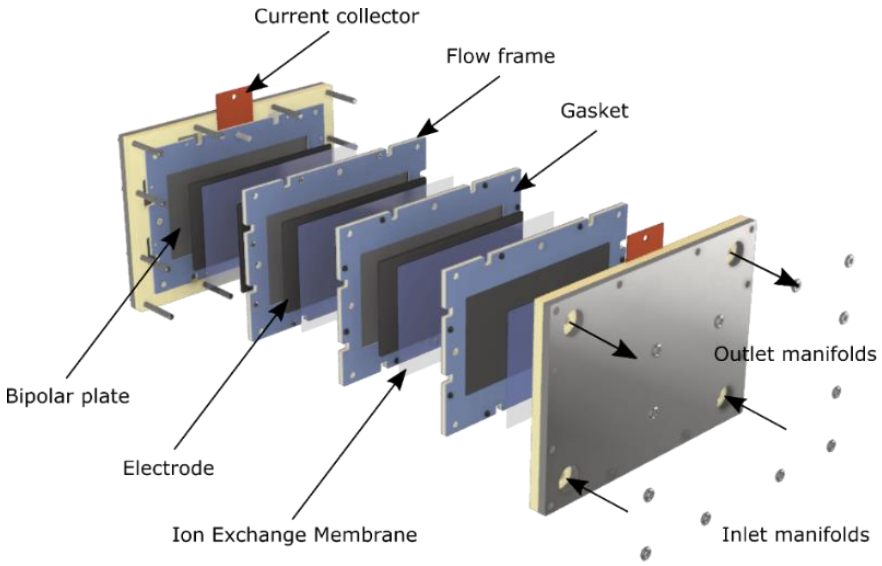

Figure 2.8 – 3D model of a redox flow stack with 4 electrochemical cells.

An electrochemical cell (Figure 2.9 (a)) comprehends two half-cells (positive and negative half-cells), divided by an ion exchange membrane. Both half-cells contain a bipolar plate, a flow frame, an electrode, an electrolyte, and gaskets. The difference lies in the redox species present in the electrolyte. The positive half-cell contains the electrolyte with the redox species that display the highest redox potential (VO^{2+}/VO_2^{+}), and the negative half-cell comprises the electrolyte with the redox species that provide the lowest redox potential (V^{2+}/V^{3+}).

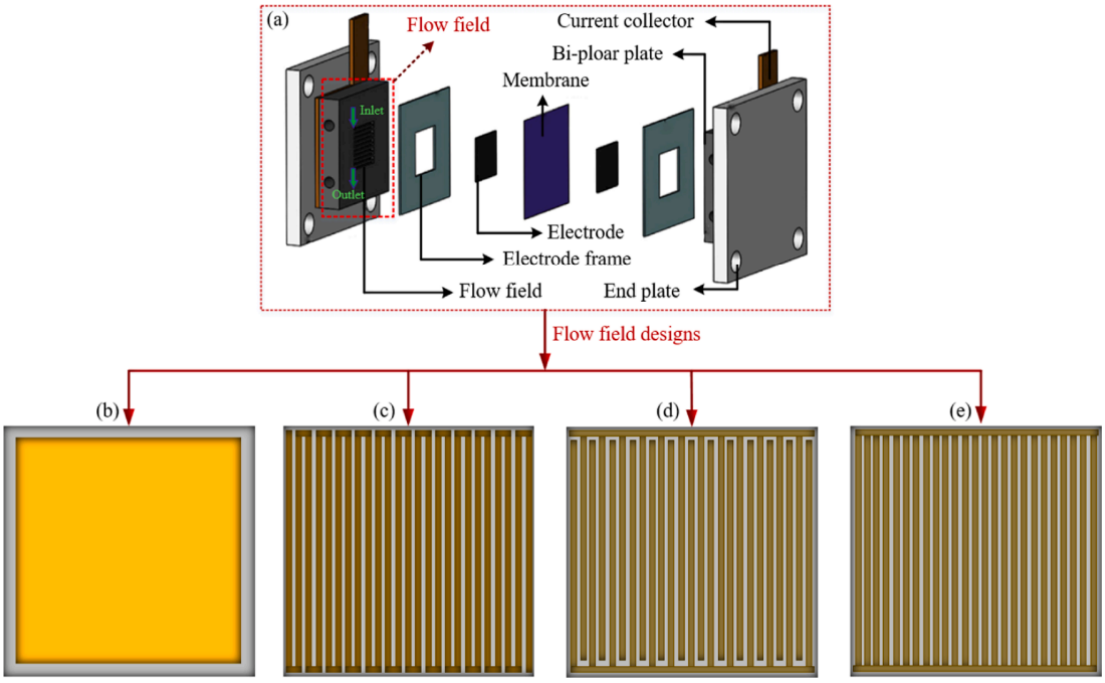

Figure 2.9 – Schematic representation of (a) a single VRFB electrochemical cell comprising (b) no flow field, (c) the serpentine flow field, (d) the interdigitated flow field, and (e) the parallel flow field. Figure from [11].

The bipolar plates are used to separate two different electrochemical cells and to allow electrons to transfer between them. Additionally, flow fields may be engraved in the bipolar plates to enhance the electrolyte distribution in the electrodes. A significant amount of flow fields for VRFBs may be found in the literature. RFBs with no flow field (Figure 2.9 (b)) are widely reported in the literature. The serpentine (Figure 2.9 (c)), the interdigitated (Figure 2.9 (d)) and the parallel (Figure 2.9 (e)) flow fields have also been extensively researched [11]. However, the information found in the literature is contradictory and unable to clarify which flow field is best to improve the electrolyte distribution and the performance of VRFBs. On a commercial scale, most VRFBs employ the no flow field configuration since it is cheaper and easier to produce. Graphite-based composites are typically used as materials for bipolar plates since they have a high resistance to acidic solutions and corrosion and good chemical stability, and they are cheap and easy to produce [17, 18]. Copper plates are placed on top of the first and last bipolar plates of the stack to act as current collectors. Flow frames are placed on top of the bipolar plates of each electrochemical cell to provide structural

support to the cells. Typically, distribution channels are engraved in the frames to promote a uniform electrolyte distribution in the electrodes and minimize energy losses due to shunt currents. Internal and external electrolyte leakages can be prevented by using gaskets in-between flow frames and in-between flow frames and bipolar plates. The electrodes are used to provide more active sites for electrochemical reactions. They consist of a carbon-based material with high porosity. More specifically, four different materials have been widely used in the literature: graphite felt, carbon felt, carbon paper, and carbon cloth [19]. Polyacrylonitrile carbon felts are the most suitable electrodes for VRFBs since they have a high surface area, a high electronic conductivity, and good mechanical stability [20]. Though, they require an activation treatment to improve their wettability and electrochemical activity [19]. The ion exchange membrane is placed in-between the electrodes to avoid electrolyte mixing and to allow selected ions to pass and complete the redox reactions. Several types of membranes have been tested in VRFBs [21]. Cation exchange membranes (e.g., Nafion®) are currently the most used type of membrane in commercial VRFBs since they display high conductivity and good chemical stability, promoting a better performance and a longer lifetime [22]. Anion exchange membranes have also been receiving great research attention. They are cheaper and display a better ion selectivity than CEMs but lead to a worse performance, especially when the VRFB is operated at high current densities [23].

2.5. Performance losses

Despite VRFBs being a very attractive technology, their market penetration has been hindered by their poor performance. Inherent losses limit the power density and greatly reduce the energy efficiency. These losses, and approaches to minimize them, are briefly addressed below.

2.5.1. Activation losses

The activation losses refer to the energy required to overcome the activation barrier of the electrochemical reactions. they provide information about the reaction kinetics and charge transfer at the electrode | electrolyte interface. These losses generate an overpotential (activation overpotential, η_{act}) and they display a significant impact on the performance of a VRFB when it is operated using a low to medium current density [24].

The introduction of functional groups on the surface of the electrodes (e.g., by oxygen [23], nitrogen [25], phosphor [26] or boron [27] doping, or deposition of metals [28]) can reduce the activation losses [24] since they act as active sites and catalyze the electrochemical reactions [1]. Using additives in the electrolyte (e.g., nanoparticles [29-31], nanotubes [32] and organic additives [33]) can also provide a catalytic effect and enhance the reaction kinetics [34].

2.5.2. Ohmic losses

The ohmic losses are associated with the resistance to transport of electrons through, for example, the electrode and the bipolar plate, and ions through the ion exchange membrane and the electrolyte (ohmic resistances). These losses also generate an overpotential (ohmic overpotential, η_{ohm}). The ionic transport contributes significantly to the low performance of VRFBs [35] since the ionic conductivity of the membrane and electrolyte are lower than the electronic conductivity of the electrodes and bipolar plates. A bad contact between conductive materials [36, 37] and electrodes with low surface area [35] can also significantly increase the ohmic losses and decrease the potential efficiency. Although the surface area does not affect kinetic losses, it affects the reaction extension by providing more active sites for the electrochemical reaction. Naturally, the flux of electrons increases at the electrode | electrolyte interface with the increasing surface area; electrodes with surface defects, such as corroded active sites, enhance the ohmic losses since the surface area is lower [29].

The ohmic losses can be reduced by increasing the compression [38] and the surface area of the electrodes or using thinner materials. Improving the ionic conductivity of the electrolyte, by using additives (e.g., tungsten [39] and molybdenum trioxide [40]) or increasing the concentration of the supporting electrolyte [41], and membrane, by modifying its functional groups [42], are also viable pathways for reducing the ohmic losses. These losses are also affected by the SoC since the electrolyte conductivity increases with the increasing SoC [43].

2.5.3. Concentration polarization

The energy losses caused by concentration polarization are related to the flux of mass transferred between the surface of the fibers of the electrode and the electrolyte solution. Near the electrode fibers, the species concentrations are different from their value in the bulk electrolyte (concentration polarization) due to a slow mass transfer and fast reaction kinetics. Thus, the E_{OCP} (Eq. (2.7)) at the electrode fiber is different from the E_{OCP} at the bulk electrolyte, leading to an overpotential (concentration overpotential, η_{conc}) [44]. These losses are negligible at low current densities because the flux of transferred mass is sufficient to regenerate the electrolyte at the electrode fiber. However, they scale exponentially with the increasing current density and decreasing reactant concentration; the concentration overpotential is greater at low (during discharge step) and high (during charge step) SoC [45]. A high concentration overpotential greatly reduces the potential efficiency of the battery and may lead to corrosion of carbon-based materials, promote side-reactions and increase the electrolyte temperature, causing precipitation of the positive electrolyte [46]. As such, the maximum depth of charge and discharge of a VRFB must be restricted, reducing the storage capacity. Minimizing concentration polarization is of great concern since it can rapidly become the limiting performance factor, increase the cost, and reduce the lifetime of redox flow batteries. Battery failure may also occur under severe concentration polarization conditions.

Strategies to reduce losses related to concentration polarization include increasing the electrolyte flow velocity and improving the electrolyte distribution in the electrode. Increasing the electrolyte regeneration rate at the electrode | electrolyte interface reduces reactant depletion rate at the electrode fibers. The regeneration rate can also be increased by increasing the flow rate, improving the permeability of the electrode, and optimizing the design of the flow field or distribution channels [11]. A good flow field or distribution channels design promotes a uniform electrolyte distribution, eliminating local reactant depletion at the electrode. Regardless, the previous approaches should be addressed carefully since they can lead to an excessive pressure drop and, consequently, an increased pump energy consumption; although the potential efficiency of the stack may increase, the efficiency of the battery may decrease. Increasing the surface area of the electrode also decreases the concentration overpotential since the number of active sites increases [47].

2.5.4. Shunt currents

The presence of vanadium ions and sulfuric acid in the vanadium electrolyte results in an electrolyte with high ionic conductivity (> 20 S m^{-1}). Consequently, the distribution channels and the manifolds of a stack become pathways for charged ions to migrate from high potential to low potential cells, forming shunt currents [48]. The latter makes the current in each cell of the stack decrease during charging and increase during discharging steps [49]. This is observed as self-discharge, lowering the coulombic efficiency and the overall energy efficiency [50]. Since the shunt currents are different at each cell, the cell potential also becomes different [50]. As such, corrosion of conductive material (e.g., sensors and electrodes [51]), gas evolution, and electrolyte temperature increase, leading to electrolyte precipitation, can occur at cells with higher potential [52]. Corrosion of the edges of the electrode may also occur since shunt currents lead to an overpotential increase at the electrode | distribution channel interface [53]. Finding strategies to reduce the shunt currents is, thus, of utmost importance to increase the energy performance and lifetime of RFBs.

A stack carefully designed can greatly reduce losses from shunt currents; the geometric dimensions of the distribution channels and manifold can be modified to increase the transport resistance of ions and decrease the shunt currents [54]. The size of the active area [54] and the number of cells [49] also affect the shunt currents. Additionally, an external piping system can be used to reduce the shunt currents. Though, it increases the complexity of the battery and the chances of failure [55].

2.5.5. Self-discharge reactions

Self-discharge reactions are reactions that discharge the battery through interaction with active species (vanadium ions). For example, the transport of vanadium ions through the ion exchange membrane from positive-to-negative half-cells, or *vice-versa* (crossover), leads to self-discharge since the vanadium ions react with each other (Eq. (2.20) - (2.23)) [56]. Thus, vanadium crossover is also a form of shunt current that reduces the coulombic efficiency [48]. However, the term “shunt currents” is often used in the literature of VRFBs to reference the transport of ions through the distribution channels and manifold but not through the ion exchange membrane.

$$2VO_2^+ + V^{2+} + 2H^+ \longrightarrow 3VO^{2+} + H_2O \quad (2.20)$$

$$VO_2^+ + V^{3+} \longrightarrow 2VO^{2+} \quad (2.21)$$

$$VO_2^+ + 2V^{2+} + 4H^+ \longrightarrow 3V^{3+} + 2H_2O \quad (2.22)$$

$$VO^{2+} + V^{2+} + 2H^+ \longrightarrow 2V^{3+} + H_2O \quad (2.23)$$

In addition to self-discharge, the crossover of vanadium ions also leads to charge imbalance in the electrolyte. The latter reduces the storage capacity of the VRFB since one tank will have fewer redox species than the other; the storage capacity is settled by the tank with the least number of redox species. The crossover of vanadium ions can be minimized by improving the ion selectivity of the membrane [57]. Also, the capacity lost can be recovered by discharging the battery to 0 % SoC and remixing the electrolytes of both storage tanks, or by adding a reducing agent after remixing [58], without observing an extensive electrolyte degradation.

The presence of oxygen in the negative electrolyte also discharges the battery. Oxygen promotes the oxidation of V^{2+} (Eq. (2.24)), leading to an imbalance between V^{2+} and VO_2^+ ions at the negative and positive electrolytes, respectively, and limiting the discharge capacity [59].

$$O_2 + 4H^+ + 4V^{2+} \rightleftharpoons 4V^{3+} + 2H_2O \quad (2.24)$$

Inert air can be used to avoid excessive oxygen concentration in the negative storage tank. Alternatively, reducing the electrolyte area in contact with air in the storage tanks reduces the reaction extension. Regardless, this self-discharge reaction becomes less noticeable as the electrolyte volume increases [59].

2.5.6. Gas evolution

Gas evolution is a harmful phenomenon that reduces the energy efficiency and the storage capacity of VRFBs. The formation of bubbles reduces the surface area of the electrode, promoting higher ohmic and concentration overpotentials. Additionally, side reactions that

produce gas compete with the vanadium reactions and reduce the current that is used to charge the battery and, consequently, the amount of energy stored [1].

During operation, hydrogen is formed in the negative half-cell (Eq. (2.25)) since the potential of the negative half-cell is lower than 0 V. In addition to the previous problems, hydrogen can also oxidize the electrode fibers, affecting the longevity of this component [60]. The effects of hydrogen evolution are stronger at the end of the charge step since the potential at the negative half-cell is lower [61].

$$2H^+ + 2e^- \rightleftarrows H_2 \qquad E^0 = 0.000\ \text{V}\ vs.\ \text{SHE} \tag{2.25}$$

Oxygen evolution (Eq. (2.26)) occurs in the positive half-cell and, similarly to hydrogen evolution, it occurs to a greater extent at the end of the charge step, when the positive half-cell displays a higher potential [62].

$$O_2 + 4H^+ + 4e^- \rightleftarrows 2H_2O \qquad E^0 = 1.229\ \text{V}\ vs.\ \text{SHE} \tag{2.26}$$

The formation of CO_2 bubbles at the positive half-cell is also reported in the literature [63, 64] due to the oxidation of carbon-based materials. Though, it is required a potential above 1.94 V_{SHE} for the performance of a VRFB to be significantly affected by such phenomenon [65].

$$C + O_2 \longrightarrow CO_2 \tag{2.27}$$

Gas evolution is very difficult to eliminate since it occurs under normal operating conditions. However, it can be minimized by avoiding overcharging (e.g., avoiding a high SoC) or avoiding operating the battery with a current density that leads to high overpotentials. Also, the electrolyte imbalance caused by gas evolution can be restored using a regeneration cell [66].

2.6. Mathematical models

Mathematical models are a time and cost-saving tool that can be used to study performance loss mechanisms, optimize operating conditions, design and material properties (e.g., through parametric studies), control the battery in real time [67], or perform market

analysis. Several mathematical models can be found in the literature for different electrochemical reactors, such as fuel cells, RFBs, and electrowinning of metals [68]. The mathematical models used to simulate VRFBs are summarized in Figure 2.10 according to their approach and application and are briefly discussed in this chapter.

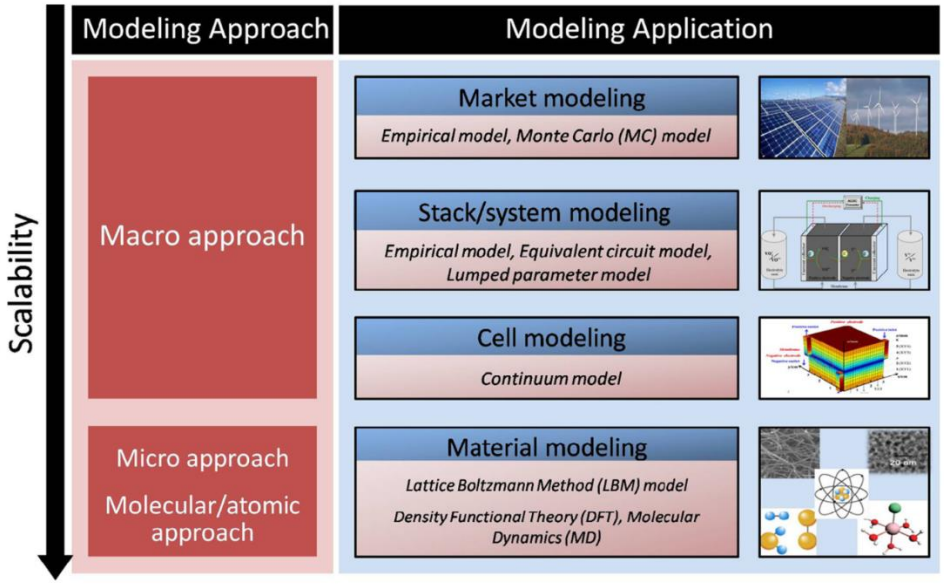

Figure 2.10 – Classification of mathematical models used in the literature to simulate vanadium redox flow batteries according to their approach and application. Figure from [69].

2.6.1. Molecular and micro-scale models

Molecular scale models, such as density functional theory, molecular dynamics, and metadynamics, are useful to research methodologies to improve the stability of the electrolyte [70], solubility of vanadium ions [71], ion selectivity of membranes [72], and catalytic activity of electrodes [73]. They provide information about the structure and interaction between materials at a molecular and atomic scale. On the other hand, micro scale models can be used to study the impact of the electrode microstructure on the performance of a VRFB and provide insights for optimization. For example, the lattice Boltzmann method can be used to study the impact of the flow rate and electrode porosity in the performance of a VRFB [74] and the impact of oxygen evolution on the surface area of the electrodes [75]; it simulates the electrolyte flow in the electrode at the pore scale [76]. However, micro-scale models must be coupled to a macro scale model to simulate local concentrations of species and

electrochemical behavior of VRFBs [77]. Molecular and micro-scale models provide important information for the development of new materials, but they are computationally expensive; they are not suitable for simulating electrochemical cells, stacks, or battery systems.

2.6.2. Macro-scale models

Simulations carried out using macro-scale models are considerably faster than simulations using micro and molecular models [76]. Some macro-scale models simulate the microstructure of the components or molecular interactions using algebraic equations which reduces the simulation time. Other macro-scale models assume that the impact of these properties is negligible, which can decrease the accuracy of the model. However, macro-scale models can be used to simulate characterization techniques for electrochemical cells, stacks, and battery systems. Additionally, they are a very useful tool to optimize the design of the flow fields, distribution channels, stack, and piping system. The most relevant macro scale models used in the literature and their applications for VRFBs are discussed below. The Monte Carlo model is a stochastic method that, for VRFBs, is used mostly to perform market analysis [78, 79] which is not within the scope of this work; this model is not addressed in the sections below. Interestingly, kinetic Monte Carlo simulations (molecular scale) were used to predict parameters for macro-scale models of Li-ion batteries [77] but not for VRFBs.

Continuum model

For the continuum model (e.g., multi-dimensional phenomenological models), it is assumed that all materials are homogenous, and that the microscopic, molecular, and atomic structures are negligible. It can simulate the electrolyte flow through the electrode and any flow conveyances (e.g., distribution channels, flow fields, and manifolds) at macro scale; the electrolyte flow pattern is assumed uniform at the pore scale. This model can also simulate the electrochemical reactions, transport of electrons and redox species, and charge conservation [80]. Thus, at cell-scale, multi-dimensional models can provide relevant information about the distribution of the electrolyte, redox species, and current in the electrodes [2]; a performance comparison between cells with different flow fields, distribution channels, and electrode designs can be carried out using this tool. The temperature distribution within the cell can also be simulated to assess the presence of

hotspots and avoid material damage during operation [4]. Furthermore, multi-dimensional models can be used to study the impact of each transport mechanism (diffusion, convection and migration) and compare the crossover when using different types of ion exchange membranes [81] to provide insights for the development of membranes with higher ion selectivity. The oxygen [62] and hydrogen [61] evolution can also be simulated using this model. At stack-scale, the continuum model can be used to evaluate the impact of shunt currents in the performance of a VRFB [50]. Regardless, a multi-dimensional computational domain (mesh) is required to perform the simulations since the finite volume method is used to solve the partial differential equations. Depending on the size of the computational domain and on the complexity of the model, the simulations can last from seconds to several weeks.

Reduced-order model

The continuum and reduced-order models can simulate the same physicochemical phenomena, but the latter are less complex and require less computational power. Thus, they have similar applications. Reduced-order models may [82] or may not [83] require a mesh to solve the equations which also affects the required computational power. For example, Vynnycky and Assunção [67] used an asymptotic method to reduce the complexity of a 2D phenomenological model from eleven to four equations. As result, the simulation time was reduced by 300 times. Cheng et al. [82] simplified a 3D model of a VRFB equipped with a serpentine flow field to a 2D model by using empirical equations for the inlet and outlet boundary conditions. Such model simplification allowed the authors to carry out 7350 simulations to study the impact of different electrode property combinations on the pressure drop and electrochemical performance of a VRFB. The reduced-order models are, thus, suitable to simulate the electrochemical performance of electrochemical cells and stacks. However, variations of physical quantities in one or more directions are typically neglected which can lead to simulation results with lower accuracy than the continuum model.

Lumped parameter model

The lumped parameter model is a 0D dynamic model that uses equations with far less complexity (ordinary differential equations) than the previous macro-scale models (partial differential equations) [84]. This model can be used to determine the concentration of the redox species under transient conditions and simulate charge-discharge cycling; a mass

balance of the redox species, in the electrodes and storage tanks, is used to determine the concentration of the redox species, and algebraic equations are used to calculate the potential of the VRFB [85]. However, the distribution of the electrolyte, redox species, and current in the components is assumed uniform. The effect of using a flow field can be simulated by coupling the lumped parameter model with an equivalent circuit model [86]. This model also needs to be coupled with an equivalent circuit model to simulate shunt currents since it does not consider charge conservation and species transport equations [87]. The thermal behavior of a VRFB [88] and self-discharge due to crossover [89] can also be simulated using the lumped parameter model.

Compared to the continuum model, the duration of the simulations carried out using the lumped parameter model is much lower. Thus, this model is typically favored over the continuum model to simulate stacks and battery systems. The latter can be used, for example, to compare all the inherent losses (e.g., shunt currents, crossover, overpotentials, inverter and pumping) of a VRFB system [90] or to optimize the stack layout and flow rate in a battery system comprising several stacks [91].

Equivalent circuit model

Equivalent circuit models have been widely used to simulate batteries since they are simple to create, and the simulations are very fast (seconds). This model uses electrical components to simulate physicochemical phenomena [92]. For example, each electrochemical cell is simulated as a potential source connected in series to an equivalent circuit model that simulates the overpotentials generated by activation, ohmic, and concentration polarization losses. Shunt currents in flow conveyances are simulated as simple resistors. However, this model assumes that the distribution of the electrolyte, species and current in each cell and electrode is uniform, similarly to the lumped parameter model. Regardless, it is a powerful tool that can be used to simulate charge-discharge cycles [93, 94], polarization curves [95] and EIS [16]. The equivalent circuit model can also be used to simulate the hydraulic losses, crossover [96], and thermal behavior [97] of electrochemical cells, stacks, and battery systems. Other applications, such as using the model as a tool to estimate the state of charge [98] and capacity [95] in real time, to develop cooling strategies

[99], or to complement other models [100], are also reported in the literature. For VRFBs, this model has been mostly used to study shunt currents in stacks [101].

Empirical models

Empirical models are developed based on experimental data. The experimental data is used to create correlations that can be used to estimate the parameters of VRFBs. Thus, physicochemical phenomena are not considered in these models. Empirical models to estimate the open circuit potential [6], diffusivity of the ions [102], electrolyte conductivity [103], and viscosity [104] are reported in the literature. These models are used in combination with other mathematical models since they are very simple. Other authors [105] used empirical models to estimate the optimal number of battery systems to maximize the overall energy efficiency in a megawatt-scale battery. The previous model was also used by the same authors to simulate the VRFB when combined with a wind farm and to perform a market analysis [106]. Empirical models have also been used to characterize and optimize a microgrid system comprising a VRFB and a photovoltaic panel [107].

2.7. Conclusions

Vanadium redox flow batteries display a simple working principle but the mechanisms that cause performance losses present many challenges. A careful selection of materials (electrodes, membrane, and bipolar plates) is required to ensure that a battery displays a good energy and stability performance. However, it was concluded that the most critical bottleneck for the development of high performant and durable stacks are the design of the distribution channels and manifold, and the arrangement of the electrochemical cells. A poor stack design leads to a low energy efficiency and may lead to battery failure. Furthermore, it was concluded that macro scale models can be used to research and accelerate the development of stacks; the continuum models are useful for optimizing the design of the distribution channels since they can simulate losses from concentration polarization, and equivalent circuit models can be used to optimize the design of the stack since they required less time to simulate shunt currents in stacks. Ultimately, it can be concluded that this chapter provides relevant information about the challenges that need to be addressed to develop VRFBs that display a high performance and a long cycle life.

2.8. References

1. J.H. Vinco, A.E.E.d.C. Domingos, D.C.R. Espinosa, J.A.S. Tenório, and M.P.G. Baltazar, *Unfolding the Vanadium Redox Flow Batteries: An indeep perspective on its components and current operation challenges.* Journal of Energy Storage, 2021. **43**: p. 103180.
2. D. You, H. Zhang, and J. Chen, *A simple model for the vanadium redox battery.* Electrochimica Acta, 2009. **54**(27): p. 6827-6836.
3. T. Zou, X. Shi, and L. Yu, *Study on energy loss of 35 kW all vanadium redox flow battery energy storage system under closed-loop flow strategy.* Journal of Power Sources, 2021. **490**: p. 229514.
4. H. Al-Fetlawi, A.A. Shah, and F.C. Walsh, *Non-isothermal modelling of the all-vanadium redox flow battery.* Electrochimica Acta, 2009. **55**(1): p. 78-89.
5. K.W. Knehr and E.C. Kumbur, *Open circuit voltage of vanadium redox flow batteries: Discrepancy between models and experiments.* Electrochemistry Communications, 2011. **13**(4): p. 342-345.
6. B. Kleinsteinberg, S. Klick, and D.U. Sauer, *Empirical approach to determine open-circuit voltage of a vanadium-redox-flow battery for models, based on published data for anion-exchange and cation-exchange membranes and temperature dependency.* Journal of Energy Storage, 2020. **28**: p. 101109.
7. M. Pavelka, F. Wandschneider, and P. Mazur, *Thermodynamic derivation of open circuit voltage in vanadium redox flow batteries.* Journal of Power Sources, 2015. **293**: p. 400-408.
8. M. Pugach, V. Vyshinsky, and A. Bischi, *Energy efficiency analysis for a kilo-watt class vanadium redox flow battery system.* Applied Energy, 2019. **253**: p. 113533.
9. R.K. Sankaralingam, S. Seshadri, J. Sunarso, A.I. Bhatt, and A. Kapoor, *Overview of the factors affecting the performance of vanadium redox flow batteries.* Journal of Energy Storage, 2021. **41**: p. 102857.
10. T. Zou, L. Luo, Y. Liao, P. Wang, J. Zhang, and L. Yu, *Study on operating conditions of household vanadium redox flow battery energy storage system.* Journal of Energy Storage, 2022. **46**: p. 103859.

11. Z. Huang, A. Mu, L. Wu, and H. Wang, *Vanadium redox flow batteries: Flow field design and flow rate optimization.* Journal of Energy Storage, 2021: p. 103526.
12. A. Di Blasi, N. Briguglio, O. Di Blasi, and V. Antonucci, *Charge–discharge performance of carbon fiber-based electrodes in single cell and short stack for vanadium redox flow battery.* Applied Energy, 2014. **125**: p. 114-122.
13. Z. Wei, A. Bhattarai, C. Zou, S. Meng, T.M. Lim, and M. Skyllas-Kazacos, *Real-time monitoring of capacity loss for vanadium redox flow battery.* Journal of Power Sources, 2018. **390**: p. 261-269.
14. D. Aaron, Z. Tang, A.B. Papandrew, and T.A. Zawodzinski, *Polarization curve analysis of all-vanadium redox flow batteries.* Journal of Applied Electrochemistry, 2011. **41**(10): p. 1175.
15. R. O'Hayre, S.-W. Cha, W. G. Colella, and F. B. Prinz, *Fuel Cell Fundamentals*. third ed. 2016: John Wiley & Sons.
16. Y. Li, J. Bao, M. Skyllas-Kazacos, M.P. Akter, X. Zhang, and J. Fletcher, *Studies on dynamic responses and impedance of the vanadium redox flow battery.* Applied Energy, 2019. **237**: p. 91-102.
17. B. Satola, *Review—Bipolar Plates for the Vanadium Redox Flow Battery.* Journal of The Electrochemical Society, 2021. **168**(6): p. 060503.
18. R.K. Gautam and A. Kumar, *A review of bipolar plate materials and flow field designs in the all-vanadium redox flow battery.* Journal of Energy Storage, 2022. **48**: p. 104003.
19. R. Li and Y. Sato, *Recent Development of Carbon-based Electrode for Vanadium Redox Flow Battery.* Electrochemistry, 2020. **88**(5): p. 344-346.
20. S. Mehboob, G. Ali, S. Abbas, K.Y. Chung, and H.Y. Ha, *Elucidating the performance-limiting electrode for all-vanadium redox flow batteries through in-depth physical and electrochemical analyses.* Journal of Industrial and Engineering Chemistry, 2019. **80**: p. 450-460.
21. D. Düerkop, H. Widdecke, C. Schilde, U. Kunz, and A. Schmiemann, *Polymer Membranes for All-Vanadium Redox Flow Batteries: A Review.* Membranes, 2021. **11**(3): p. 214.

22. J. Balaji, M.G. Sethuraman, S.-H. Roh, and H.-Y. Jung, *Recent developments in sol-gel based polymer electrolyte membranes for vanadium redox flow batteries – A review.* Polymer Testing, 2020. **89**: p. 106567.
23. H.R. Jiang, J. Sun, L. Wei, M.C. Wu, W. Shyy, and T.S. Zhao, *A high power density and long cycle life vanadium redox flow battery.* Energy Storage Materials, 2020. **24**: p. 529-540.
24. A. Hassan and T. Tzedakis, *Facile chemical activation of graphite felt by KMnO4 acidic solution for vanadium redox flow batteries.* Applied Surface Science, 2020. **528**: p. 146808.
25. Y. Li et al., *Deciphering the exceptional kinetics of hierarchical nitrogen-doped carbon electrodes for high-performance vanadium redox flow batteries.* Journal of Materials Chemistry A, 2022.
26. R. Wang, Y. Li, Y. Wang, and Z. Fang, *Phosphorus-doped graphite felt allowing stabilized electrochemical interface and hierarchical pore structure for redox flow battery.* Applied Energy, 2020. **261**: p. 114369.
27. H.R. Jiang, W. Shyy, L. Zeng, R.H. Zhang, and T.S. Zhao, *Highly efficient and ultra-stable boron-doped graphite felt electrodes for vanadium redox flow batteries.* Journal of Materials Chemistry A, 2018. **6**(27): p. 13244-13253.
28. D.J. Suárez, Z. González, C. Blanco, M. Granda, R. Menéndez, and R. Santamaría, *Graphite Felt Modified with Bismuth Nanoparticles as Negative Electrode in a Vanadium Redox Flow Battery.* ChemSusChem, 2014. **7**(3): p. 914-918.
29. J. Lobato, J. Oviedo, P. Cañizares, M.A. Rodrigo, and M. Millán, *Impact of carbonaceous particles concentration in a nanofluidic electrolyte for vanadium redox flow batteries.* Carbon, 2020. **156**: p. 287-298.
30. S. Aberoumand et al., *Reduced graphene oxide nanofluidic electrolyte with improved electrochemical properties for vanadium flow batteries.* Journal of Energy Storage, 2022. **49**: p. 104133.
31. B. Li et al., *Bismuth Nanoparticle Decorating Graphite Felt as a High-Performance Electrode for an All-Vanadium Redox Flow Battery.* Nano Letters, 2013. **13**(3): p. 1330-1335.

32. J. Kim and H. Park, *Impact of nanofluidic electrolyte on the energy storage capacity in vanadium redox flow battery.* Energy, 2018. **160**: p. 192-199.
33. J. Liu, S. Liu, Z. He, H. Han, and Y. Chen, *Effects of organic additives with oxygen- and nitrogen-containing functional groups on the negative electrolyte of vanadium redox flow battery.* Electrochimica Acta, 2014. **130**: p. 314-321.
34. Z.H. Zhang, L. Wei, M.C. Wu, B.F. Bai, and T.S. Zhao, *Chloride ions as an electrolyte additive for high performance vanadium redox flow batteries.* Applied Energy, 2021. **289**: p. 116690.
35. R. Monteiro, J. Leirós, M. Boaventura, and A. Mendes, *Insights into all-vanadium redox flow battery: A case study on components and operational conditions.* Electrochimica Acta, 2018. **267**: p. 80-93.
36. M.-Y. Lu, W.-W. Yang, X.-Y. Tang, Y.-H. Jiao, M. Ye, and Q. Xu, *Asymmetric structure design of a vanadium redox flow battery for improved battery performance.* Journal of Energy Storage, 2021. **44**: p. 103337.
37. S. Jung, B. Choi, S. Park, D.-W. Lee, Y.-B. Kim, and S. Kim, *Computational study of effects of contact resistance on a large-scale vanadium redox flow battery stack.* International Journal of Energy Research, 2019. **43**(6): p. 2343-2360.
38. J. Charvát et al., *Performance enhancement of vanadium redox flow battery by optimized electrode compression and operational conditions.* Journal of Energy Storage, 2020. **30**: p. 101468.
39. M. Kim, H. Yoo, G. Lee, and J. Choi, *Enhanced VRB electrochemical performance using tungsten as an electrolyte additive.* Electrochimica Acta, 2017. **246**: p. 190-196.
40. L. Cao, M. Skyllas-Kazacos, and D.-W. Wang, *Modification Based on MoO3 as Electrocatalysts for High Power Density Vanadium Redox Flow Batteries.* ChemElectroChem, 2017. **4**(8): p. 1836-1839.
41. M.R. Mohamed, P.K. Leung, and M.H. Sulaiman, *Performance characterization of a vanadium redox flow battery at different operating parameters under a standardized test-bed system.* Applied Energy, 2015. **137**: p. 402-412.
42. X. Li, H. Zhang, Z. Mai, H. Zhang, and I. Vankelecom, *Ion exchange membranes for vanadium redox flow battery (VRB) applications.* Energy & Environmental Science, 2011. **4**(4): p. 1147-1160.

43. M. Skyllas-Kazacos and M. Kazacos, *State of charge monitoring methods for vanadium redox flow battery control.* Journal of Power Sources, 2011. **196**(20): p. 8822-8827.
44. E.L. Cussler, *Diffusion: Mass Transfer in Fluid Systems*. third ed. 2009, Cambridge: Cambridge University Press.
45. Q. Zheng, F. Xing, X. Li, G. Ning, and H. Zhang, *Flow field design and optimization based on the mass transport polarization regulation in a flow-through type vanadium flow battery.* Journal of Power Sources, 2016. **324**: p. 402-411.
46. A. Trovò and M. Guarnieri, *Standby thermal management system for a kW-class vanadium redox flow battery.* Energy Conversion and Management, 2020. **226**: p. 113510.
47. A. Tang, J. Bao, and M. Skyllas-Kazacos, *Studies on pressure losses and flow rate optimization in vanadium redox flow battery.* Journal of Power Sources, 2014. **248**: p. 154-162.
48. M. Skyllas-Kazacos, J. McCann, Y. Li, J. Bao, and A. Tang, *The Mechanism and Modelling of Shunt Current in the Vanadium Redox Flow Battery.* ChemistrySelect, 2016. **1**(10): p. 2249-2256.
49. Y.-S. Chen, S.-Y. Ho, H.-W. Chou, and H.-J. Wei, *Modeling the effect of shunt current on the charge transfer efficiency of an all-vanadium redox flow battery.* Journal of Power Sources, 2018. **390**: p. 168-175.
50. C. Yin, S. Guo, H. Fang, J. Liu, Y. Li, and H. Tang, *Numerical and experimental studies of stack shunt current for vanadium redox flow battery.* Applied Energy, 2015. **151**: p. 237-248.
51. D. Pletcher and F.C. Walsh, *Industrial Electrochemistry*. 2 ed. 1993: Blackie Academic & Professional. 672.
52. L.F. Arenas, C. Ponce de León, and F.C. Walsh, *Engineering aspects of the design, construction and performance of modular redox flow batteries for energy storage.* Journal of Energy Storage, 2017. **11**: p. 119-153.
53. R.M. Darling, H.-S. Shiau, A.Z. Weber, and M.L. Perry, *The Relationship between Shunt Currents and Edge Corrosion in Flow Batteries.* Journal of The Electrochemical Society, 2017. **164**(11): p. E3081-E3091.

54. F. Xing, H. Zhang, and X. Ma, *Shunt current loss of the vanadium redox flow battery.* Journal of Power Sources, 2011. **196**(24): p. 10753-10757.
55. Q. Ye, J. Hu, P. Cheng, and Z. Ma, *Design trade-offs among shunt current, pumping loss and compactness in the piping system of a multi-stack vanadium flow battery.* Journal of Power Sources, 2015. **296**: p. 352-364.
56. J. Shin, B. Jeong, M.F. Chinannai, and H. Ju, *Mitigation of water and electrolyte imbalance in all-vanadium redox flow batteries.* Electrochimica Acta, 2021. **390**: p. 138858.
57. J. Ye, C. Zheng, J. Liu, T. Sun, S. Yu, and H. Li, *In Situ Grown Tungsten Trioxide Nanoparticles on Graphene Oxide Nanosheet to Regulate Ion Selectivity of Membrane for High Performance Vanadium Redox Flow Battery.* Advanced Functional Materials, 2021. **n/a**(n/a): p. 2109427.
58. L. Wei, X.Z. Fan, H.R. Jiang, K. Liu, M.C. Wu, and T.S. Zhao, *Enhanced cycle life of vanadium redox flow battery via a capacity and energy efficiency recovery method.* Journal of Power Sources, 2020. **478**: p. 228725.
59. T. Jirabovornwisut and A. Arpornwichanop, *A review on the electrolyte imbalance in vanadium redox flow batteries.* International Journal of Hydrogen Energy, 2019. **44**(45): p. 24485-24509.
60. A. Fetyan, G.A. El-Nagar, I. Lauermann, M. Schnucklake, J. Schneider, and C. Roth, *Detrimental role of hydrogen evolution and its temperature-dependent impact on the performance of vanadium redox flow batteries.* Journal of Energy Chemistry, 2019. **32**: p. 57-62.
61. A.A. Shah, H. Al-Fetlawi, and F.C. Walsh, *Dynamic modelling of hydrogen evolution effects in the all-vanadium redox flow battery.* Electrochimica Acta, 2010. **55**(3): p. 1125-1139.
62. H. Al-Fetlawi, A.A. Shah, and F.C. Walsh, *Modelling the effects of oxygen evolution in the all-vanadium redox flow battery.* Electrochimica Acta, 2010. **55**(9): p. 3192-3205.
63. S. Rudolph, U. Schröder, I.M. Bayanov, and G. Pfeiffer, *Corrosion prevention of graphite collector in vanadium redox flow battery.* Journal of Electroanalytical Chemistry, 2013. **709**: p. 93-98.

64. S. Möller et al., *Online Monitoring of Electrochemical Carbon Corrosion in Alkaline Electrolytes by Differential Electrochemical Mass Spectrometry.* Angewandte Chemie International Edition, 2020. **59**(4): p. 1585-1589.
65. H. Liu, Q. Xu, C. Yan, and Y. Qiao, *Corrosion behavior of a positive graphite electrode in vanadium redox flow battery.* Electrochimica Acta, 2011. **56**(24): p. 8783-8790.
66. N. Poli, M. Schäffer, A. Trovò, J. Noack, M. Guarnieri, and P. Fischer, *Novel electrolyte rebalancing method for vanadium redox flow batteries.* Chemical Engineering Journal, 2021. **405**: p. 126583.
67. M. Vynnycky and M. Assunção, *The Vanadium Redox Flow Battery: an Asymptotic Perspective.* SIAM Journal on Applied Mathematics, 2019. **79**(4): p. 1147-1172.
68. F.F. Rivera, T. Pérez, L.F. Castañeda, and J.L. Nava, *Mathematical modeling and simulation of electrochemical reactors: A critical review.* Chemical Engineering Science, 2021. **239**: p. 116622.
69. Q. Zheng, X. Li, Y. Cheng, G. Ning, F. Xing, and H. Zhang, *Development and perspective in vanadium flow battery modeling.* Applied Energy, 2014. **132**: p. 254-266.
70. V. Murugesan et al., *Accelerated design of vanadium redox flow battery electrolytes through tunable solvation chemistry.* Cell Reports Physical Science, 2021. **2**(2): p. 100323.
71. S. Gupta, T.M. Lim, and S.H. Mushrif, *Insights into the solvation of vanadium ions in the vanadium redox flow battery electrolyte using molecular dynamics and metadynamics.* Electrochimica Acta, 2018. **270**: p. 471-479.
72. D. Zhang et al., *Oriented Proton-Conductive Nanochannels Boosting a Highly Conductive Proton-Exchange Membrane for a Vanadium Redox Flow Battery.* ACS Applied Materials & Interfaces, 2021. **13**(3): p. 4051-4061.
73. H.R. Jiang, Y.K. Zeng, M.C. Wu, W. Shyy, and T.S. Zhao, *A uniformly distributed bismuth nanoparticle-modified carbon cloth electrode for vanadium redox flow batteries.* Applied Energy, 2019. **240**: p. 226-235.
74. G. Qiu, C.R. Dennison, K.W. Knehr, E.C. Kumbur, and Y. Sun, *Pore-scale analysis of effects of electrode morphology and electrolyte flow conditions on performance of vanadium redox flow batteries.* Journal of Power Sources, 2012. **219**: p. 223-234.

75. L. Chen, Y. He, W.-Q. Tao, P. Zelenay, R. Mukundan, and Q. Kang, *Pore-scale study of multiphase reactive transport in fibrous electrodes of vanadium redox flow batteries.* Electrochimica Acta, 2017. **248**: p. 425-439.
76. G. Qiu, A.S. Joshi, C.R. Dennison, K.W. Knehr, E.C. Kumbur, and Y. Sun, *3-D pore-scale resolved model for coupled species/charge/fluid transport in a vanadium redox flow battery.* Electrochimica Acta, 2012. **64**: p. 46-64.
77. M.T. Castro, J.A.D. Del Rosario, M.N. Chong, P.-Y.A. Chuang, J. Lee, and J.D. Ocon, *Multiphysics modeling of lithium-ion, lead-acid, and vanadium redox flow batteries.* Journal of Energy Storage, 2021. **42**: p. 102982.
78. B. Battke, T.S. Schmidt, D. Grosspietsch, and V.H. Hoffmann, *A review and probabilistic model of lifecycle costs of stationary batteries in multiple applications.* Renewable and Sustainable Energy Reviews, 2013. **25**: p. 240-250.
79. J.M. Lujano-Rojas, G. Zubi, R. Dufo-López, J.L. Bernal-Agustín, and J.P.S. Catalão, *Novel probabilistic optimization model for lead-acid and vanadium redox flow batteries under real-time pricing programs.* International Journal of Electrical Power & Energy Systems, 2018. **97**: p. 72-84.
80. A.A. Shah, M.J. Watt-Smith, and F.C. Walsh, *A dynamic performance model for redox-flow batteries involving soluble species.* Electrochimica Acta, 2008. **53**(27): p. 8087-8100.
81. L. Hao, Y. Wang, and Y. He, *Modeling of Ion Crossover in an All-Vanadium Redox Flow Battery with the Interfacial Effect at Membrane/Electrode Interfaces.* Journal of The Electrochemical Society, 2019. **166**: p. A1310-A1322.
82. Z. Cheng et al., *Data-driven electrode parameter identification for vanadium redox flow batteries through experimental and numerical methods.* Applied Energy, 2020. **279**: p. 115530.
83. A.K. Sharma, C.Y. Ling, E. Birgersson, M. Vynnycky, and M. Han, *Verified reduction of dimensionality for an all-vanadium redox flow battery model.* Journal of Power Sources, 2015. **279**: p. 345-350.
84. S.B. Lee et al., *Open Data, Models, and Codes for Vanadium Redox Batch Cell Systems: A Systems Approach Using Zero-Dimensional Models.* Journal of Electrochemical Energy Conversion and Storage, 2019. **17**(1).

85. A.A. Shah, R. Tangirala, R. Singh, R.G.A. Wills, and F.C. Walsh, *A Dynamic Unit Cell Model for the All-Vanadium Flow Battery.* Journal of The Electrochemical Society, 2011. **158**(6): p. A671.
86. Z. Wei, J. Zhao, M. Skyllas-Kazacos, and B. Xiong, *Dynamic thermal-hydraulic modeling and stack flow pattern analysis for all-vanadium redox flow battery.* Journal of Power Sources, 2014. **260**: p. 89-99.
87. A. Trovò et al., *Standby thermal model of a vanadium redox flow battery stack with crossover and shunt-current effects.* Applied Energy, 2019. **240**: p. 893-906.
88. Y. Yan, Y. Li, M. Skyllas-Kazacos, and J. Bao, *Modelling and simulation of thermal behaviour of vanadium redox flow battery.* Journal of Power Sources, 2016. **322**: p. 116-128.
89. A. Tang, J. Bao, and M. Skyllas-Kazacos, *Dynamic modelling of the effects of ion diffusion and side reactions on the capacity loss for vanadium redox flow battery.* Journal of Power Sources, 2011. **196**(24): p. 10737-10747.
90. A. Trovò, F. Picano, and M. Guarnieri, *Comparison of energy losses in a 9 kW vanadium redox flow battery.* Journal of Power Sources, 2019. **440**: p. 227144.
91. H. Chen, M. Cheng, X. Feng, Y. Chen, F. Chen, and J. Xu, *Analysis and optimization for multi-stack vanadium flow battery module incorporating electrode permeability.* Journal of Power Sources, 2021. **515**: p. 230606.
92. N. Ra and A. Bhattacharjee, *An Extensive Study and Analysis of System Modeling and Interfacing of Vanadium Redox Flow Battery.* Energy Technology, 2021. **9**: p. 2000708.
93. A. Bhattacharjee, A. Roy, N. Banerjee, S. Patra, and H. Saha, *Precision dynamic equivalent circuit model of a Vanadium Redox Flow Battery and determination of circuit parameters for its optimal performance in renewable energy applications.* Journal of Power Sources, 2018. **396**: p. 506-518.
94. M.R. Mohamed, H. Ahmad, M.N.A. Seman, S. Razali, and M.S. Najib, *Electrical circuit model of a vanadium redox flow battery using extended Kalman filter.* Journal of Power Sources, 2013. **239**: p. 284-293.
95. B. Khaki and P. Das, *An equivalent circuit model for Vanadium Redox Batteries via hybrid extended Kalman filter and Particle filter methods.* Journal of Energy Storage, 2021. **39**: p. 102587.

96. Y. Zhang, J. Zhao, P. Wang, M. Skyllas-Kazacos, B. Xiong, and R. Badrinarayanan, *A comprehensive equivalent circuit model of all-vanadium redox flow battery for power system analysis.* Journal of Power Sources, 2015. **290**: p. 14-24.
97. B. Xiong et al., *An Enhanced Equivalent Circuit Model of Vanadium Redox Flow Battery Energy Storage Systems Considering Thermal Effects.* IEEE Access, 2019. **7**: p. 162297-162308.
98. S. Dong, J. Feng, Y. Zhang, S. Tong, J. Tang, and B. Xiong. *State of Charge Estimation of Vanadium Redox Flow Battery Based on Online Equivalent Circuit Model*. in *2021 31st Australasian Universities Power Engineering Conference (AUPEC)*. 2021.
99. Z. Wei, J. Zhao, and B. Xiong, *Dynamic electro-thermal modeling of all-vanadium redox flow battery with forced cooling strategies.* Applied Energy, 2014. **135**: p. 1-10.
100. Y.-H. Jiao, M.-Y. Lu, W.-W. Yang, X.-Y. Tang, M. Ye, and Q. Xu, *A 3D macro-segment network model for vanadium redox flow battery with serpentine flow field.* Electrochimica Acta, 2022. **403**: p. 139657.
101. O.C. Esan, X. Shi, Z. Pan, X. Huo, L. An, and T.S. Zhao, *Modeling and Simulation of Flow Batteries.* Advanced Energy Materials, 2020. **10**(31): p. 2000758.
102. Q. Xu and T.S. Zhao, *Determination of the mass-transport properties of vanadium ions through the porous electrodes of vanadium redox flow batteries.* Physical Chemistry Chemical Physics, 2013. **15**(26): p. 10841-10848.
103. R. Badrinarayanan, K.J. Tseng, B.H. Soong, and Z. Wei, *Modelling and control of vanadium redox flow battery for profile based charging applications.* Energy, 2017. **141**: p. 1479-1488.
104. F.T. Wandschneider et al., *Model of a vanadium redox flow battery with an anion exchange membrane and a Larminie-correction.* Journal of Power Sources, 2014. **272**: p. 436-447.
105. B. Turker, S. Arroyo Klein, E.-M. Hammer, B. Lenz, and L. Komsiyska, *Modeling a vanadium redox flow battery system for large scale applications.* Energy Conversion and Management, 2013. **66**: p. 26-32.
106. B. Turker et al., *Utilizing a vanadium redox flow battery to avoid wind power deviation penalties in an electricity market.* Energy Conversion and Management, 2013. **76**: p. 1150-1157.

107. T.A. Nguyen, X. Qiu, I. J. D. Guggenberger, M.L. Crow, and A.C. Elmore, *Performance Characterization for Photovoltaic-Vanadium Redox Battery Microgrid Systems*. IEEE Transactions on Sustainable Energy, 2014. **5**(4): p. 1379-1388.

Chapter 3

Impact of the distribution channels in the performance

The content of this chapter is adapted from: N. M. Delgado, C. M. Almeida, R. Monteiro, and A. Mendes., *Flow-through design for enhanced redox flow battery performance*. Journal of the Electrochemical Society, 2022. **169**(2): p. 020532

3. Impact of the distribution channels in the performance

Equation Chapter (Next) Section 1

3.1. Abstract

The high capital cost, driven by the poor performance, still hinders the widespread application of vanadium redox flow batteries. This work compares two different cell designs to demonstrate that the electrolyte flow velocity and pattern are of critical importance to increase the overall battery performance. The Oriented-Distribution-Path (ODP) cell design includes inlet and outlet distribution channels, while the Multi-Distribution-Path (MDP) design does not. The introduction of the distribution channels in the ODP caused the electrolyte flow pattern through the electrode to be less uniform. However, the latter reduced the concentration polarization under high current density and low flow rate conditions. In a charge-discharge cycle comparison, the MDP displayed the highest cell energy efficiency at 80 mA cm^{-2} and at a flow rate of 300 ml min^{-1}. However, the best overall performance was obtained using the ODP at 80 mA cm^{-2} and a flow rate of 10 ml min^{-1}. This work demonstrates that the highest system energy efficiency is achieved when using low flow rates together with a cell design that promotes a high pressure drop. The insights of this study apply to other chemistries making it useful to define guidelines for designing energy-efficient redox flow batteries.

3.2. Introduction

A myriad of flow field designs has been considered in the proton-exchange membrane fuel cell research field, and many of those configurations have been adopted in vanadium redox flow batteries (VRFB). The most used flow field designs are the conventional (i.e., without flow field) and the interdigitated. In the conventional design, the electrolyte is pumped through porous carbon felt electrodes, flowing parallel to the membrane and bipolar plate, while in the interdigitated configuration, the channels are blocked alternately at the inlet and outlet; the electrolyte is forced to flow through the electrode perpendicular and parallel to the membrane. Since the electrolyte is forced to flow through the electrode, these flow fields display a flow-through configuration. Flow-by configurations, namely, serpentine, parallel, and spiral, have also been investigated [1-4]; the electrolyte may flow through the electrode and flow field channels

It is still unclear which flow field configuration provides the best performance; in an experimental study conducted by Xu et al. [1], the conventional flow-through design was compared with the serpentine flow field; the latter exhibited a 5 % higher energy efficiency. Other authors [5-7] also demonstrated that the serpentine flow field outperforms the conventional design. The study carried out by Maurya et al. [8] consisted in comparing the performance of a VRFB using the conventional design with the interdigitated and serpentine flow fields designs. The results showed that the conventional design outperforms the other two; this contradicts the conclusion of previous authors [5-7]. Yin et al. [9] compared the conventional design with the interdigitated and concluded that, at cell scale, the conventional design outperforms the interdigitated. At system scale (e.g., including pump energy consumption), the opposite was observed since the conventional design displays a higher pressure drop. Reed et al. [10] also demonstrated that a VRFB stack with a conventional design achieves higher energy efficiencies than a stack with an interdigitated flow field at the expense of having a higher pressure drop.

Although it seems generally accepted that using flow fields may be useful to increase the performance of a given VRFB, a critical disadvantage arises: the need for thicker bipolar plates, which leads to an increase in stack weight, dimensions, material use and manufacturing costs [10], and higher bipolar plate electrical resistance. Thus, the

conventional flow-through design seems to be the most desirable and suitable for the widespread commercialization of VRFB systems [11].

In this work, two conventional flow-through designs are presented and assessed: a) the Multiple Distribution Path (MDP), where no distribution channels are used for the inlet and the outlet; b) the Oriented Distribution Path (ODP), where the electrolyte is routed through an inlet distribution channel to the electrode and collected by an outlet distribution channel. Very few studies are found in the literature analyzing cells using inlet and outlet distribution channels [5, 12], but none of them address the impact of such feature. Comparative computational fluid dynamics (CFD) simulations were carried out to assess the effect of the cell design on the electrolyte distribution and flow velocity. Additionally, the ODP and the MDP cells were experimentally characterized and compared concerning charge-discharge cycling, polarization curves performance, and pump energy consumption.

3.3. Experimental methods

3.3.1. Material

A cation exchange membrane (CEM) Nafion® 212 was purchased from Ion Power. Polyacrylonitrile-based graphite felts (GF, GFD 4.6 EA, SGL Group, Germany) with 4.6 mm of uncompressed thickness were used as electrodes. All GF electrode samples were boiled in 1.0 M H2SO4 solution to remove non-carbon residues from the manufacturing process and thoroughly rinsed with deionized water. Afterwards, the electrode samples were dried overnight at 80 ºC and stored until further use. Based on our previous work [13], GF electrode samples were thermally treated under an air atmosphere at 400 ºC for 12 h using a furnace muffle. A commercially available vanadium solution (1.6 M V3+/V4+ 50:50 molar ratio, GfE Metalle und Materialien GmbH, Germany) was used as electrolyte, without further treatment or purification.

3.3.2. VRFB setup and performance

Each cell included two stainless steel endplates and two copper plates, working as current collectors, directly connected to two bipolar plates. The electrical insulation of the endplates was ensured by using 2 mm thick LDPE (low-density polyethylene) separators. To ensure the desired compression and to prevent leakage of electrolyte, EPDM (ethylene propylene

diene monomer) rubber gaskets were placed between parts. Further details may be found elsewhere [13]. Figure 3.1 illustrates the two flow-through designs used in this study. Both cell configurations use two 0.60 mm thick graphite foils as bipolar plates (PV15, SGL Group, USA) with an active area of 50 mm × 50 mm. The distribution channels included in the ODP design are 2 mm wide and 2 mm deep. GF electrodes were compressed by 25 % of their initial thickness.

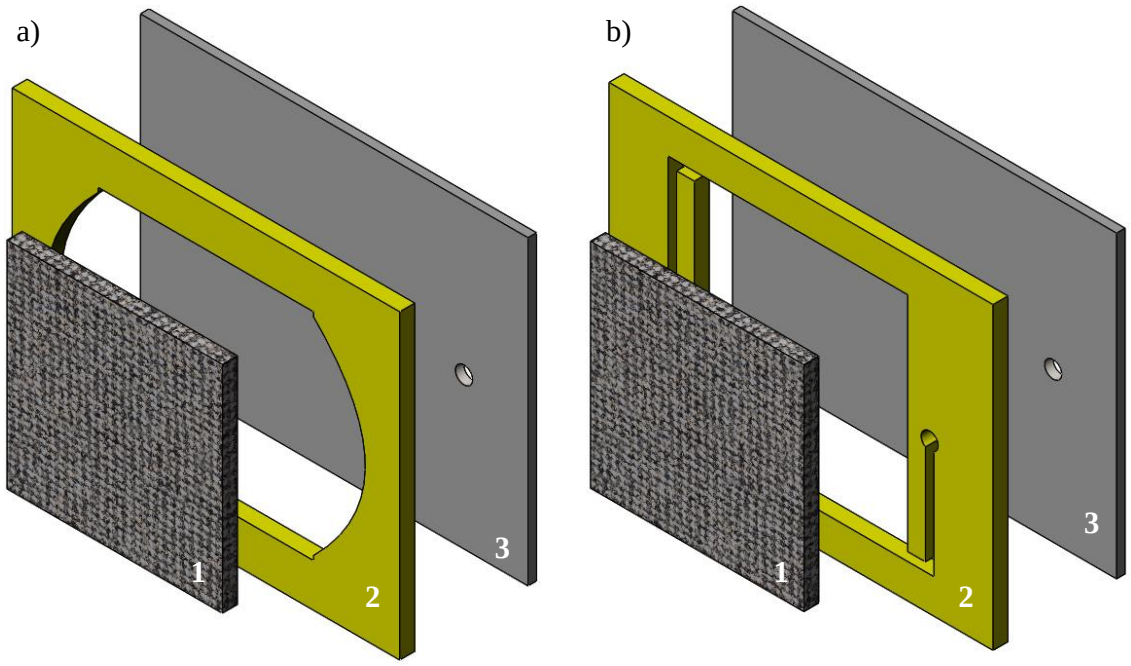

Figure 3.1 – Half-cell designs based on conventional flow-through configurations used in this work: a) Multiple Distribution Path (MDP); b) Oriented Distribution Path (ODP). 1 – graphite felt electrode; 2 – EPDM gasket; 3 – graphite bipolar plate.

The electrolyte was pumped from the reservoirs to the cell using two QDOS 120 Watson-Marlow (91 % nominal efficiency – given by supplier). 150 ml of electrolyte was used in each tank and the system was purged with nitrogen throughout the experiments to prevent oxidation of vanadium redox species.

The electrochemical measurements were carried out at room temperature using an electrochemical workstation (Zahner Zennium) coupled to a potentiostat (PP240, Zahner Elektrik). The discharge polarization curves were obtained using a scan rate of 10 mV s^{-1} from *ca*. 1.40 V, corresponding to 50 % SoC, down to 0 V. The cell was considered 50 %

charged whenever the electric current was < 20 mA at 1.40 V. Neither hydrogen nor oxygen evolution were observed during the experiments. Also, post-experiment inspections of the components of the cell did not exhibit any deposition or agglomeration of corrosion-resulting materials. To ensure identical initial conditions, fresh electrolyte, newly prepared electrodes, and clean membranes were used for each new test.

Coulombic (η_C), potential (η_P), cell energy (η_{EE}), and system energy (η_{SEE}) efficiencies were calculated from the following equations:

$$\eta_C = \frac{\int I_d dt_d}{\int I_c dt_c} \tag{3.1}$$

$$\eta_P = \frac{\int E_d dt_d}{\int E_c dt_c} \tag{3.2}$$

$$\eta_{EE} = \eta_C \times \eta_P \tag{3.3}$$

$$\eta_{SEE} = \frac{\int \left(I_d E_d - P_{pump} \right) dt_d}{\int \left(I_c E_c + P_{pump} \right) dt_c} \tag{3.4}$$

where I is the operating current (A), E is the cell potential (V), and subscripts c and d denote charging and discharging stages, respectively. The power consumption of both pumps (P_{pumps}) was determined using the following equation [14]:

$$P_{pumps} = 2\frac{Q\Delta p}{\eta_{pump}} \tag{3.5}$$

where η_{pump} is the pump efficiency, Q is the volumetric flow rate ($m^3\ s^{-1}$), and Δp is the total pressure drop (Pa).

3.3.3. Pressure drop measurements

The pressure drop measurements in both configurations were carried out using pressure gauges (Wika, 100 kPa maximum pressure) placed at the inlet and outlet of the cell. Fresh electrolyte was fed to both sides of the cell. Each pressure reading was obtained after flow rate stabilization to obtain accurate readings. Inlet and outlet pressures were recorded

between 10 ml min^{-1} and 300 ml min^{-1} in 10 ml min^{-1} increments. The pressure drop of the cell was calculated by subtracting the outlet pressure from the inlet pressure for each flow rate. The pressure drop was determined for both cell configurations with and without electrodes. No limitations were observed in the experiments when using tanks with 150 ml of electrolyte and high flow rates (e.g., 300 ml min^{-1}) since the cell electrolyte intake is much lower (< 10 ml) than the available electrolyte volume.

3.4. Mathematical methods

3.4.1. Governing equations

The electrolyte flow in both cells was simulated assuming that the vanadium electrolyte is incompressible and isothermal. The porous electrodes were assumed isotropic. The mass (Eq. (3.6)) and momentum (Eq. (3.7)) conservation equations were used to simulate the electrolyte flow in the distribution channels and electrode:

$$\frac{\partial \varepsilon \rho}{\partial t} + \nabla \cdot \left(\varepsilon \rho \vec{v} \right) = 0 \tag{3.6}$$

$$\frac{\partial (\varepsilon \rho \vec{v})}{\partial t} + \nabla \cdot \left(\varepsilon \rho \vec{v} \vec{v} \right) = -\varepsilon \nabla p + \rho \vec{g} + \nabla \cdot \left(\varepsilon \mu \nabla \vec{v} \right) + S_{\text{mom}} \tag{3.7}$$

where ε is the porosity, ρ is the density (assumed 1350 kg m^{-3}), p is the pressure (kg m^{-1} s^{-2}), $\vec{g}$ is the gravity acceleration vector (9.8 m s^{-2}), $\vec{v}$ is the electrolyte velocity vector, expressed in m s^{-1} and S_{mom} is the source term of the momentum equation (kg m^{-2} s^{-2}).

Darcy's law (Eq. (3.8)) was used to simulate the pressure drop in the electrode:

$$S_{\text{mom}} = -\frac{\mu}{K_p} \vec{v} \tag{3.8}$$

where μ is the viscosity (assumed 4.928 × 10^{-3} kg m^{-1} s^{-1} [15]). The permeability of the electrode, K_p, was determined with the Kozeny-Carman equation:

$$K_p = \frac{d_f^2 \varepsilon^3}{16 k_{\text{KC}} \left(1 - \varepsilon\right)^2} \tag{3.9}$$

where d_f is the fiber diameter (17.6 μm [13]) and k_{KC} is the Kozeny-Carman constant; the Kozeny-Carman constant was obtained as a fitting parameter. An electrode porosity, ε, of 0.92 was obtained for 25 % compression, according to the following equation [16]:

$$\varepsilon = 1 - \frac{\delta_0}{\delta}\left(1 - \varepsilon_0\right) \tag{3.10}$$

where δ_0 and δ are the initial (4.60 mm) and the compressed (3.45 mm) electrode thickness, respectively, and ε_0 is the initial porosity (0.94, provided by the supplier).

At the distribution channels, the porosity and the momentum source term assumed values of 1 and 0, respectively.

3.4.2. Boundary conditions

The mass flow rate ($\dot{m}$), determined using Eq. (3.11), was used as a boundary condition at both inlets.

$$\dot{m} = \frac{Q}{\rho} \tag{3.11}$$

The pressure at the outlet was assumed constant and equal to atmospheric pressure. The no-flux boundary condition was used for the remaining boundaries.

3.4.3. Numerical procedure

The simulations were carried out under steady-state conditions using Ansys Fluent. The computational domains are 3D domains divided into three different element zones (electrode, inlet, and outlet) with over 170 000 polyhedral elements. The mass and momentum conservation equations were solved with SIMPLE algorithms pre-installed within the software package. A PRESTO! and second order upwind spatial discretization schemes were used for pressure and flow velocity, respectively. A residual convergence criterion of $1x10^{-6}$ was used for all variables.

3.5. Results and discussion

3.5.1. Hydraulic performance

Pressure drop

A low pressure drop, in the VRFB, minimizes the pump energy consumption and the degradation of the electrodes [17]. Thus, the pressure drop of both cells was determined experimentally and compared. Figure 3.2 shows the pressure drop as a function of the electrolyte flow rate for both cells with and without electrodes. Two important observations can be drawn from Figure 3.2: (1) for a given flow rate, the ODP cell exhibits a higher pressure drop than that of MDP cell, regardless of the electrodes being inserted in the cell or not; (2) the pressure drop increase rate as a function of the flow rate in the ODP cell is greater than the increase rate in the MDP cell.

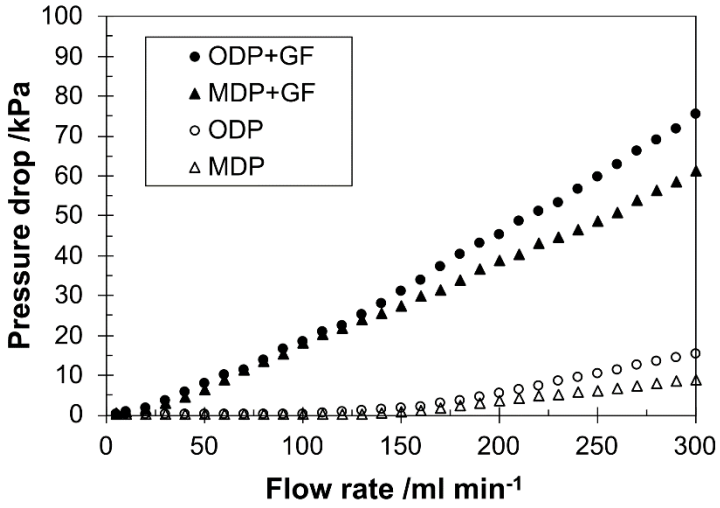

Figure 3.2 – Pressure drop of ODP (circle) and MDP (triangle) cells with (solid) and without (hollow) graphite felt (GF).

In the ODP cell, the cross-sectional area of the distribution channels is smaller than the cross-sectional area of the distribution channels of the MDP cell. Thus, the flow velocity in the ODP cell is higher than in the MDP cell. Also, the pressure drop is proportional to the square of velocity in a square cross-section channel [18]; the pressure drop increases at a higher rate in the ODP cell due to the lower channel cross-sectional area. Even at lower flow rates, the ODP cell exhibited a slightly higher pressure drop than the MDP cell. Furthermore,

for the same electrolyte flow rate, the ODP cell should display higher flow velocity than the MDP cell within the electrode zone since the cross-sectional area of the distribution channel | electrode interface in the ODP cell (2 mm × 2 mm) is lower than in the MDP cell (3.45 mm × 4 mm).

Electrolyte distribution

Three-dimensional flow simulations were carried out to analyze the electrolyte distribution in both cells. The Kozeny-Carman constant (k_{ck}) was used as a fitting parameter and a value of 13.5 was obtained; the permeability of the electrode is 1.75×10^{-10} m^2, which is similar to the value found in the literature (2.50×10^{-10} m^2) [19]. The Kozeny-Carman constant is related to the morphology (e.g., fiber geometry and tortuosity) of the graphite felt [20]. A carbon felt electrode with a high tortuosity displays lower permeability, leading to a higher pressure drop. In this work, the effect of the tortuosity was assumed negligible since it is close to unity at 25 % compression [21].

Figure 3.3 shows that the simulated pressure drop fits well with the experimental data for both cells. A larger difference between the simulated and the experimental data is observed at lower flow rates. This is expected since the reading error of the experimental data (± 2.5 kPa) is more significant at lower pressure drops. Regardless, the fitting quality is sufficient to perform a flow velocity and an electrolyte distribution comparison between the ODP and the MDP cells.

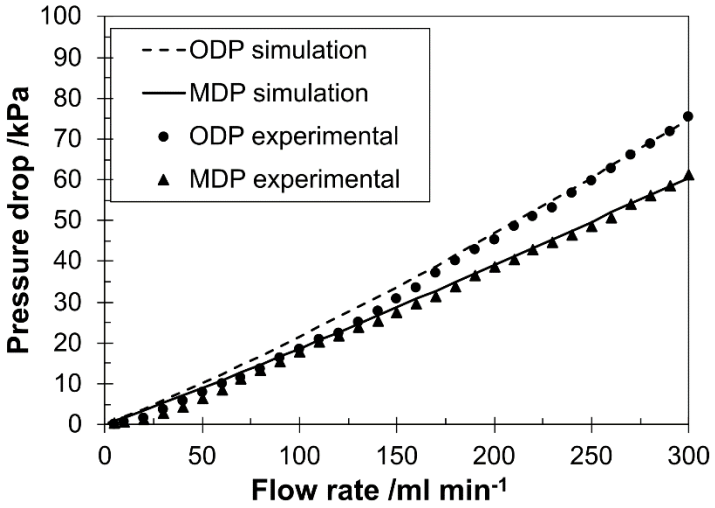

Figure 3.3 – Simulated (lines) and experimental (symbols) pressure drop of ODP (circle) and MDP (triangle) cells.

The flow velocity and electrolyte distribution in the electrode are more relevant for the performance of the cell since it is where the reaction occurs; the average electrolyte velocity in the electrode of the ODP and the MDP cells was also simulated (Figure 3.4). The flow velocity difference between the two cell designs was calculated using the MDP cell as reference (Eq. (3.12)):

$$x_{\mathrm{rel}} = \frac{x_{\mathrm{MDP}} - x_{\mathrm{ODP}}}{x_{\mathrm{MDP}}} \tag{3.12}$$

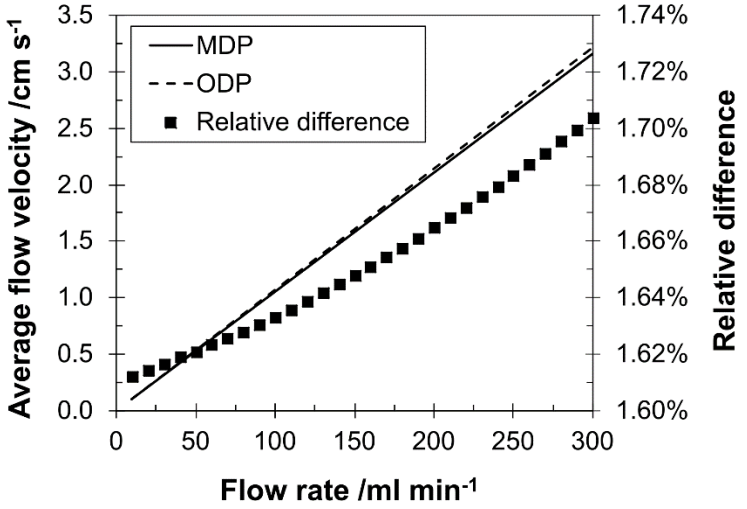

Figure 3.4 – Simulated average (line) and relative (square) flow velocity in the electrode using the ODP (dashed line) and the MDP (solid line) cells. The MDP cell is used as a reference to determine the relative flow velocity; positive values indicate that the ODP cell has a higher average flow velocity.

The average flow velocity in the electrode of the ODP cell is 1.65 % higher than in the electrode of the MDP cell since the area of the distribution channel | electrode interface in the ODP cell is lower (Figure 3.4). Such a slight difference led to an average pressure drop increase of 17.6 % (Figure 3.3). This means that a 1.65 % flow velocity increase can lead to a pump energy consumption increase higher than 17.6 % (Eq. (3.5)). Depending on the energy output of the VRFB, such a small variation of the flow velocity may have a substantial

impact on the performance of the redox flow cells. Moreover, the electrolyte refresh rate and distribution depend on the flow velocity; a lower concentration overpotential is expected and unfed areas at the electrode may arise in the presence of a high flow velocity.

Since the electrolyte flow is mainly controlled by advection, the electrolyte distribution can be assessed using the uniformity index (UI) of the flow velocity (Eq. (3.13)).

$$\mathrm{UI} = 1 - \frac{\int \left| |\vec{v}| - |\overline{\vec{v}}| \right| \mathrm{d}V}{2 \left| |\overline{\vec{v}}| \right| V} \tag{3.13}$$

where V is the electrode volume, $|\vec{v}|$ and $\overline{|\vec{v}|}$ are the local and the average electrolyte flow velocity. The uniformity index compares the local flow velocity with the average flow velocity in the electrode; a higher uniformity index indicates a more uniform flow velocity in the electrode and, thus, a more uniform electrolyte distribution. The relative uniformity index was determined using the MDP cell as a reference (Figure 3.5).

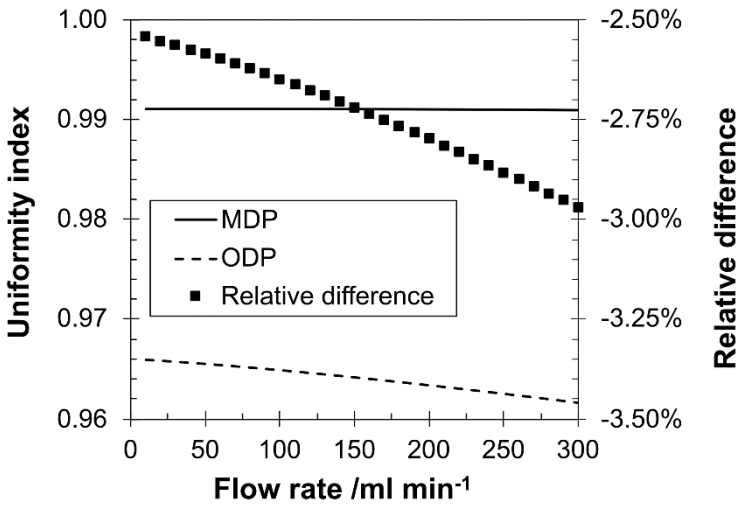

Figure 3.5 – Simulated uniformity index of the flow velocity in the electrode using the ODP (dashed line) and the MDP (solid line) cells and respective relative difference (square). The MDP cell is used as a reference to determine the relative uniformity index; negative values mean that the ODP cell has a lower average uniformity index.

Overall, the results show that the ODP cell has a more uneven electrolyte distribution than the MDP cell; the ODP cell has an average uniformity index 2.74 % lower than the MDP.

The more uneven electrolyte distribution displayed by the ODP cell can lead to a lower cell performance when compared with the MDP cell. Though, the impact of having a uniformity index of 0.96 (ODP) *vs*. 0.99 (MDP) in the performance of a VRFB is still unclear.

Figure 3.5 also shows that the electrolyte distribution in the ODP cell becomes more uneven as the flow rate increases. Such behavior is not observed in the MDP cell; the quality of the electrolyte distribution remains mostly similar for all flow rates. Thus, the electrolyte distribution in the ODP cell becomes more uneven with the flow rate increase than in the MDP cell. The opposite trend was observed for the average flow velocity (Figure 3.4); the average flow velocity in the ODP cell increased at a higher rate with the flow rate increase than the MDP cell.

The contours of flow velocity and uniformity index at the electrode of the MDP and ODP cells, for a flow rate of 300 ml min^{-1}, are shown in Figure 3.6.

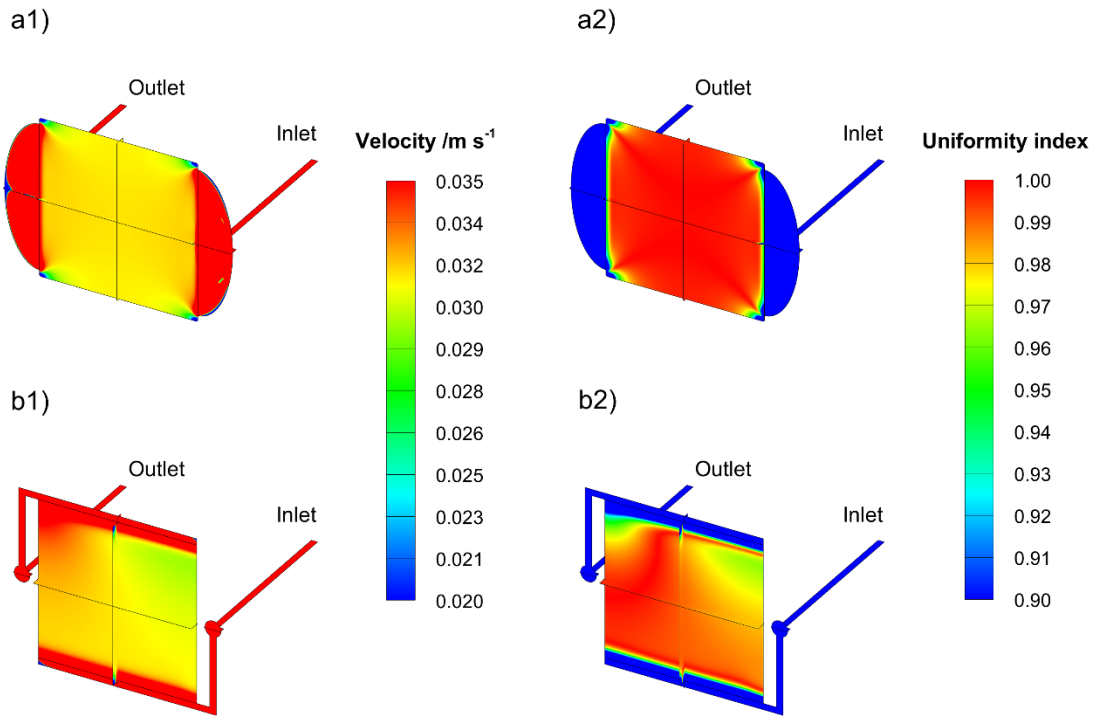

Figure 3.6 – Contours of 1) flow velocity and 2) uniformity index of the flow velocity in the electrode using the a) MDP and the b) ODP cells at a flow rate of 300 ml min^{-1}.

The MDP cell displays a symmetric electrolyte distribution; the uniformity index is lower in the entry and exit regions than in the middle region of the electrode. Also, the uniformity index is lower at the corners of the electrode since the flow velocity is lower. In this cell design, the area of the electrode | feeding zone surface can be increased to increase the flow velocity at the corners of the electrode and improve the uniformity index. Concerning the ODP cell, the uniformity index is higher at the entry region of the electrode, but it decreases significantly towards the exit. The narrow distribution channels force the electrolyte to flow in a diagonal path (from the right bottom corner to the top left corner of the electrode); the flow velocity is greater in the top left corner than in the top right corner. Such velocity gradient can be reduced, and the uniformity index can be increased, by creating an accumulation zone before and after the electrode (e.g., increasing the width of the distribution channels). Also, the average uniformity index of both cells can be increased by increasing the active area since the regions with a lower uniformity index are located at the corners of the electrodes. The ODP cell can benefit the most from the increase of active area, particularly by increasing the cell width, since the distance between the bottom right and top left corners of the electrode increases, and a flow pattern close to a plug flow is obtained in the middle region of the electrode.

Both cells offer different benefits that can improve the performance of a VRFB; the ODP displays a higher average flow velocity which can contribute to a faster electrolyte refresh rate at the electrode | electrolyte interface and the MDP offers a more uniform electrolyte distribution and a lower pressure drop, which can help at increasing the material stability and decreasing the pump energy consumption. The electrochemical characterization of both cells designs is then required to understand the impact of such differences in electrochemical performance.

3.5.2. Electrochemical performance

Discharge polarization

Discharge polarization curves at different flow rates (Figure 3.7) were carried out to further investigate the impact of the electrolyte distribution and flow velocity in the VRFB performance.

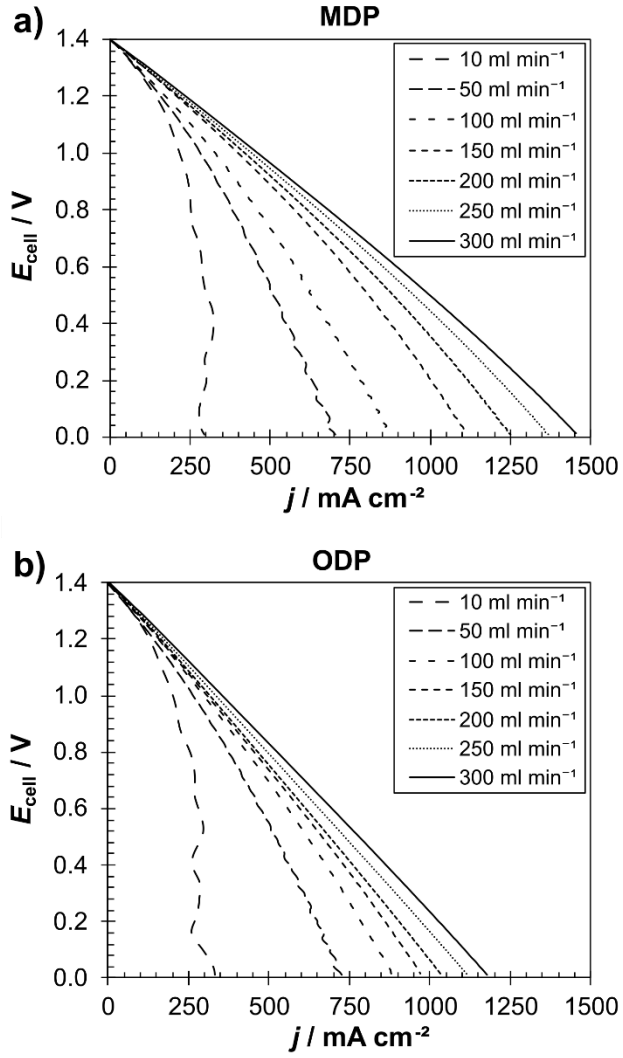

Figure 3.7 – Discharge polarization curves at different flow rates of a) MDP and b) ODP cells.

In vanadium redox flow cells, the overpotentials (energy losses) arise from (1) kinetics of the electrochemical reactions at the electrode | electrolyte interface, noticeable at low current densities; (2) ohmic losses, related to contact resistances between bipolar plate and electrode, electronic resistances and ionic transport resistances – the latter includes the transport of the redox species and charge balancing through the electrolyte and membrane and; (3) concentration polarization, related to the refresh rate of active species at the electrode | electrolyte interface [22].

A linear relationship between the cell potential and the current density is observed at low current densities in both cases, regardless of the flow rate (Figure 3.7). This is a result of small kinetic losses. Furthermore, it is expected the ohmic resistances to be identical between cells since they were operated at similar conditions and using similar components (bipolar plate, electrode, membrane, and electrolyte). Any performance difference should be assigned to the introduction of the distribution channels, which affects the electrolyte refresh rate and distribution.

The impact of the concentration polarization in the performance of the cell is observed at high overpotentials, which is equivalent to the low cell potential region in the discharge polarization curves. The current density measured at the lowest cell potential is limited by the concentration of reagents at the surface of the electrode. Among other parameters, the latter is affected by the flow velocity [23]. The results (Figure 3.7) show that as the flow rate increases from 10 ml min^{-1} to 300 ml min^{-1}, the limiting current density increases, as expected; the dominant effect of concentration polarization, caused by the low electrolyte refresh rate, becomes gradually smaller. For the MDP cell, the current increases from 294 mA cm^{-2} up to 1454 mA cm^{-2}. For the ODP cell, the current increases from 329 mA cm^{-2} up to 1178 mA cm^{-2}. Figure 3.7 also shows that the ODP cell outperformed the MDP cell up to a flow rate of 100 ml min^{-1}. This trend reverses for higher flow rates; in the ODP, the average flow velocity increases at the expense of decreasing the uniformity of the electrolyte distribution. Yet, the ODP cell outperforms the MDP at low flow rates. Clearly, the electrolyte refresh rate was the performance limiting mechanism of the cells. As the flow rate increases, the electrolyte refresh rate increases on both cells and the electrolyte distribution in the ODP cell becomes more uneven when compared to the MDP cell. The electrolyte flow velocity increase was not able to compensate for the performance loss caused by a more uneven electrolyte distribution.

Another important performance indicator that the electrolyte distribution and refresh rate can affect is the conversion of the redox species [24, 25]. The latter is determined as a ratio between the experimental and theoretical limiting current densities and can be used to evaluate the fraction of vanadium converted in a single pass. Thus, the theoretical limiting

current (i_L) was calculated assuming the active vanadium ions are completely converted in a single pass [26]:

$$i_L = \frac{nFQ}{A} c \cdot \mathrm{SoC} \tag{3.14}$$

where n is the number of electrons, F is the Faraday constant (96 485 mol A s^{-1}), and A is the active area of the cells (25 cm^2), c is the total vanadium concentration (1.6 M) and SoC is the state of charge (50 %).

As Figure 3.8 shows, the conversion of the redox species decreases as the flow rate increases, for both cell designs; high flow rates lead to lower concentration polarization but also lead to a lower residence time of the vanadium ions. Regardless, the ODP cell displays a higher conversion than the MDP cell at flow rates below 100 ml min^{-1} and the opposite is observed at higher flow rates. Such difference was assigned to a lower concentration polarization, which is observed at low flow rates for the ODP cell and at high flow rates for the MDP cell, similar to the results discussed above.

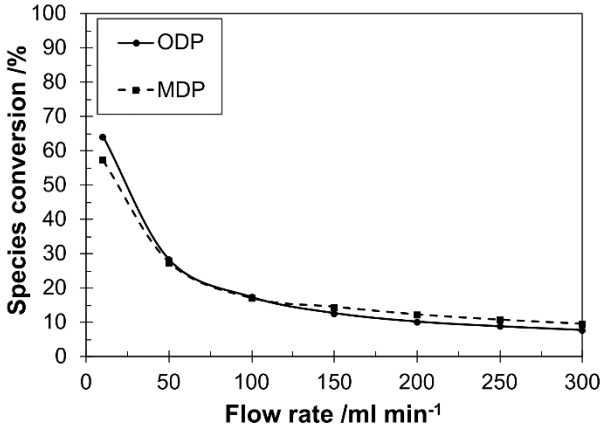

Figure 3.8 – Species conversion in a single electrolyte pass when using the a) MDP and the b) ODP cells at different flow rates, 0 V and 50 % state of charge.

These results show that cells with a poor electrolyte distribution (ODP) can outperform cells with better electrolyte distribution (MDP) if the flow velocity can compensate for the loss of electrolyte distribution quality. However, along with a higher average flow velocity comes a higher pump energy consumption. The increase in average flow velocity may

improve the performance at cell scale (cell energy efficiency), but not at system scale (system energy efficiency).

Charge-discharge cycles

Charge-discharge cycles were carried out at different flow rates for the ODP and for the MDP cells to evaluate the impact of the cell design on the cell and system efficiencies. For the cycling tests (Figure 3.9), both the MDP and the ODP cells were operated under similar experimental conditions. For each set of operating conditions, the cells underwent 20 cycles to have a representative amount of data. A constant current density of 80 mA cm^{-2} was applied. Electric potential cut-offs of 0.80 V and 1.65 V were defined as lower and upper limits, respectively. Electrolyte flow rates of 10 ml min^{-1}, 150 ml $min^{-1,}$ and 300 ml min^{-1} were used. The system efficiency was determined using the pressure drop data shown above and Eq. (3.4).

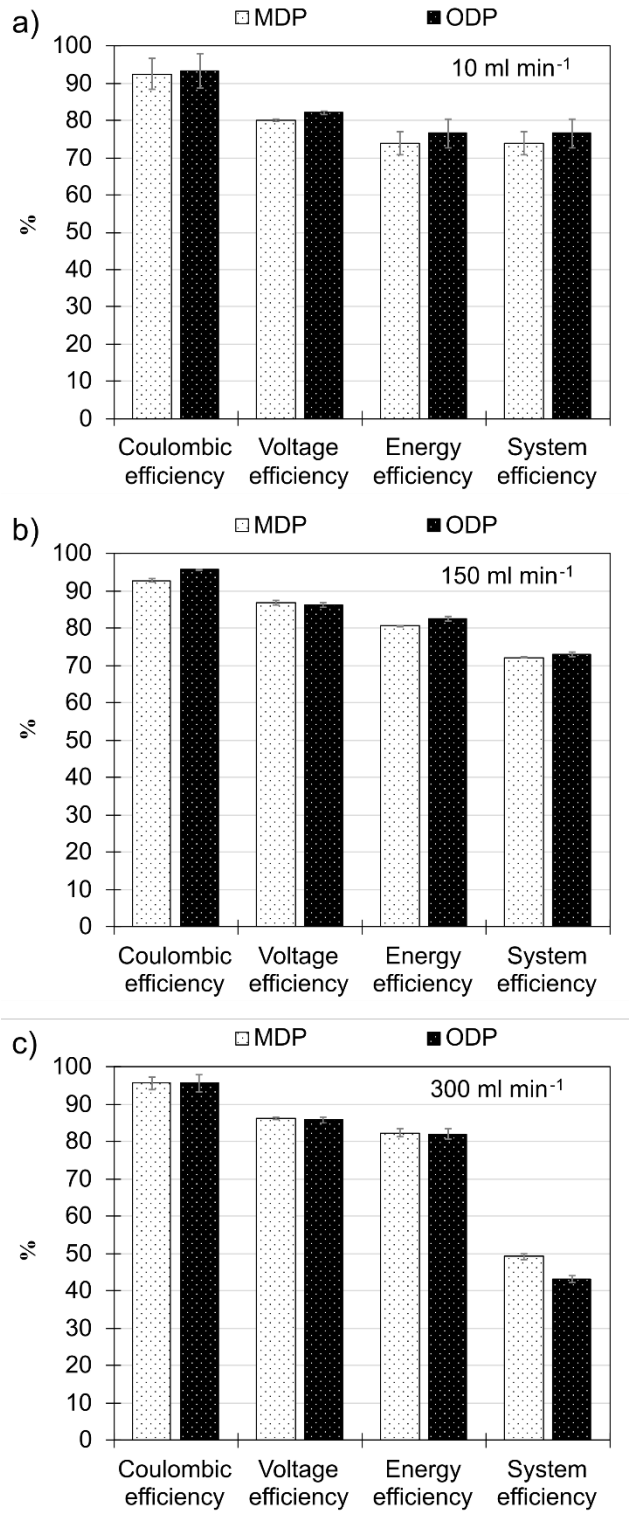

Figure 3.9 – ODP and MDP cell and system efficiencies at 80 mA cm^{-2} current density averaged over 20 cycles for a flow rate of a) 10 ml min^{-1}, b) 150 ml min^{-1} and c) 300 ml min^{-1}. The standard deviation of the efficiencies is displayed as error bars.

The coulombic, potential, and energy efficiencies of the two cell designs are relatively similar with a slight advantage for ODP at 10 ml min^{-1} and 150 ml min^{-1}. On average, the ODP cell outperforms the MDP cell in *ca.* 3 % energy efficiency. For the highest flow rate (300 ml min^{-1}), the MDP cell outperforms the ODP cell in 0.4 % energy efficiency. The standard deviation of the efficiencies for 20 cycles was obtained. As shown in Figure 3.9, the standard deviation of the energy efficiency is significant at a flow rate of 10 ml min^{-1} (± 3.0 % for the MDP and ± 3.8 % for the ODP) since the standard deviation of the coulombic efficiency is also significant (± 4.2 % for the MDP and ± 4.6 % for the ODP). The introduction of the distribution channels should increase the coulombic efficiency since the resistance to shunt currents increases [27]. However, shunt currents arise when several cells are electrically connected in series and hydraulically connected in parallel; in this work, the introduction of the distribution channels should only affect the potential efficiency, which displays a maximum standard deviation of ± 0.7 % (ODP using a flow rate of 150 ml min^{-1}). The data shown in Figure 3.9 can be used to assess the impact of the distribution channels on the performance of a VRFB regarding electrolyte distribution and refresh rate.

The potential efficiency provides information regarding the energy expended on the reaction (kinetic losses), electronic and ionic transport (ohmic losses), and concentration polarization. During charge-discharge cycling, the concentration polarization is only significant at the end of the charging and discharging steps [23]. The latter has a small contribution to the performance of the VRFB during charge-discharge cycles. The overall impact of the concentration polarization in the performance of the cells is then not so obvious when using the potential efficiency as comparison criteria. Regardless, the results shown in Figure 3.9 agree well with the information shown above: at a flow rate of 10 ml min^{-1} the ODP design displays a higher potential efficiency; the ODP has a higher electrolyte refresh rate than the MDP due to a higher average electrolyte flow velocity. At 150 ml min^{-1} and 300 ml min^{-1}, the MDP cell displays a higher potential efficiency than the ODP cell; the increased flow velocity in the ODP cell is not able to compensate for the poor electrolyte distribution.

The cell efficiencies were computed according to Eq. (3.1)-(3.3). The cell energy efficiency, however, only accounts for energy used by the cell, and pumping power is not

considered. Figure 3.9 shows that the highest system energy efficiency is obtained when using the ODP cell at the lowest flow rate (10 ml min^{-1}). The performance improvement obtained in the MDP cell by using high flow rates was not able to compensate for the energy consumed by the pumps. These results demonstrate that having a cell design that promotes a higher electrolyte refresh rate at the electrode | electrolyte interface is more advantageous at a commercial scale; low flow rates are preferred to minimize the pump energy consumption and unfed areas within the electrode, maximizing the overall efficiency.

3.6. Conclusions

This work compares the performance of two vanadium redox flow cells with distributions channels (named Oriented Distribution Path, ODP) and without distribution channels (named Multiple Distribution Path, MDP). This comparison is carried out to assess whether the presence of distribution channels in a vanadium redox flow cell with no flow field is relevant for electrochemical performance. The obtained results provided useful insights:

- It was shown experimentally and from the flow simulations that the introduction of the distribution channels (ODP) promoted a more uneven electrolyte distribution and higher pressure drop and, consequently, a higher electrolyte flow velocity in the electrode.
- The polarization curves, together with the simulation results, show that a good electrolyte distribution alone is not sufficient to obtain the best electrochemical performance of the cell; at low flow rates, the ODP outperformed the MDP due to increased electrolyte flow velocity, resulting in a lower concentration overpotential. The opposite was observed at high flow rates; the electrolyte flow velocity becomes sufficiently high for the electrolyte distribution to become the limiting factor in the performance.
- The charge-discharge cycles agreed well with the previous results; the potential efficiency of the ODP was higher than the MDP at low flow rates, but inferior at high flow rates. Furthermore, the best cell performance was obtained using the MDP at high flow rates (300 ml min^{-1}). Such a high flow rate, however, led to a

significant pump energy consumption; the ODP displayed the best overall performance at 10 ml min^{-1}.

The results obtained in this work suggest that to improve the overall electrochemical performance, vanadium redox flow batteries should be operated at low flow rates and have a cell design that promotes a high electrolyte flow velocity. The introduction of the distribution channels clearly enhances the overall performance of the vanadium redox flow battery. Regardless, further improvements can be made to the conventional cell design to outperform both the MDP and the ODP cells at all flow rates. The system energy efficiency of larger VRFBs can be improved by using wider and thinner distribution channels to improve the electrolyte distribution. Also, narrow electrodes should be used to increase flow velocity.

3.7. References

1. Q. Xu, T.S. Zhao, and C. Zhang, *Performance of a vanadium redox flow battery with and without flow fields.* Electrochimica Acta, 2014. **142**: p. 61-67.
2. R.M. Darling and M.L. Perry, *The Influence of Electrode and Channel Configurations on Flow Battery Performance.* Journal of The Electrochemical Society, 2014. **161**(9): p. A1381-A1387.
3. C.R. Dennison, E. Agar, B. Akuzum, and E.C. Kumbur, *Enhancing Mass Transport in Redox Flow Batteries by Tailoring Flow Field and Electrode Design.* Journal of The Electrochemical Society, 2016. **163**(1): p. A5163-A5169.
4. J. Houser, J. Clement, A. Pezeshki, and M.M. Mench, *Influence of architecture and material properties on vanadium redox flow battery performance.* Journal of Power Sources, 2016. **302**: p. 369-377.
5. S. Kumar and S. Jayanti, *Effect of flow field on the performance of an all-vanadium redox flow battery.* Journal of Power Sources, 2016. **307**: p. 782-787.
6. A.M. Pezeshki, R.L. Sacci, F.M. Delnick, D.S. Aaron, and M.M. Mench, *Elucidating effects of cell architecture, electrode material, and solution composition on overpotentials in redox flow batteries.* Electrochimica Acta, 2017. **229**: p. 261-270.
7. R.D. Pichugov et al., *Electrolyte Flow Field Variation: A Cell for Testing and Optimization of Membrane Electrode Assembly for Vanadium Redox Flow Batteries.* ChemPlusChem, 2020. **85**(8): p. 1919-1927.
8. S. Maurya, P.T. Nguyen, Y.S. Kim, Q. Kang, and R. Mukundan, *Effect of flow field geometry on operating current density, capacity and performance of vanadium redox flow battery.* Journal of Power Sources, 2018. **404**: p. 20-27.
9. C. Yin, Y. Gao, G. Xie, T. Li, and H. Tang, *Three dimensional multi-physical modeling study of interdigitated flow field in porous electrode for vanadium redox flow battery.* Journal of Power Sources, 2019. **438**: p. 227023.
10. D. Reed et al., *Performance of a low cost interdigitated flow design on a 1 kW class all vanadium mixed acid redox flow battery.* Journal of Power Sources, 2016. **306**: p. 24-31.
11. B. Satola, *Review—Bipolar Plates for the Vanadium Redox Flow Battery.* Journal of The Electrochemical Society, 2021. **168**(6): p. 060503.

12. J. Houser, A. Pezeshki, J.T. Clement, D. Aaron, and M.M. Mench, *Architecture for improved mass transport and system performance in redox flow batteries.* Journal of Power Sources, 2017. **351**: p. 96-105.
13. R. Monteiro, J. Leirós, M. Boaventura, and A. Mendes, *Insights into all-vanadium redox flow battery: A case study on components and operational conditions.* Electrochimica Acta, 2018. **267**: p. 80-93.
14. W. Xiao and L. Tan, *Control strategy optimization of electrolyte flow rate for all vanadium redox flow battery with consideration of pump.* Renewable Energy, 2019. **133**: p. 1445-1454.
15. D. You, H. Zhang, and J. Chen, *A simple model for the vanadium redox battery.* Electrochimica Acta, 2009. **54**(27): p. 6827-6836.
16. P.C. Ghimire, A. Bhattarai, R. Schweiss, G.G. Scherer, N. Wai, and Q. Yan, *A comprehensive study of electrode compression effects in all vanadium redox flow batteries including locally resolved measurements.* Applied Energy, 2018. **230**: p. 974-982.
17. I. Derr, M. Bruns, J. Langner, A. Fetyan, J. Melke, and C. Roth, *Degradation of all-vanadium redox flow batteries (VRFB) investigated by electrochemical impedance and X-ray photoelectron spectroscopy: Part 2 electrochemical degradation.* Journal of Power Sources, 2016. **325**: p. 351-359.
18. T.-C. Jen and T.Z. Yan, *Developing fluid flow and heat transfer in a channel partially filled with porous medium.* International Journal of Heat and Mass Transfer, 2005. **48**(19): p. 3995-4009.
19. S. Wan, X. Liang, H. Jiang, J. Sun, N. Djilali, and T. Zhao, *A coupled machine learning and genetic algorithm approach to the design of porous electrodes for redox flow batteries.* Applied Energy, 2021. **298**: p. 117177.
20. R. Schulz, N. Ray, S. Zech, A. Rupp, and P. Knabner, *Beyond Kozeny–Carman: Predicting the Permeability in Porous Media.* Transport in Porous Media, 2019. **130**(2): p. 487-512.
21. R. Jervis et al., *In situ compression and X-ray computed tomography of flow battery electrodes.* Journal of Energy Chemistry, 2018. **27**(5): p. 1353-1361.

22. R. O'Hayre, S.W. Cha, W. Colella, and F.B. Prinz, *Fuel Cell Fundamentals*. 3rd ed. 2016, New York: John Wiley & Sons.
23. N.M. Delgado, R. Monteiro, M. Abdollahzadeh, P. Ribeirinha, A. Bentien, and A. Mendes, *2D-dynamic phenomenological modelling of vanadium redox flow batteries – Analysis of the mass transport related overpotentials.* Journal of Power Sources, 2020. **480**: p. 229142.
24. H.R. Jiang, J. Sun, L. Wei, M.C. Wu, W. Shyy, and T.S. Zhao, *A high power density and long cycle life vanadium redox flow battery.* Energy Storage Materials, 2020. **24**: p. 529-540.
25. J. T. Clement, D. S. Aaron, and M.M. Mench, *In Situ Localized Current Distribution Measurements in All-Vanadium Redox Flow Batteries.* Journal of The Electrochemical Society, 2016. **163**: p. 5220-5228.
26. X. Ke, J.M. Prahl, J.I.D. Alexander, J.S. Wainright, T.A. Zawodzinski, and R.F. Savinell, *Rechargeable redox flow batteries: flow fields, stacks and design considerations.* Chemical Society Reviews, 2018. **47**(23): p. 8721-8743.
27. N.M. Delgado, R. Monteiro, J. Cruz, A. Bentien, and A. Mendes, *Shunt currents in vanadium redox flow batteries – a parametric and optimization study.* Electrochimica Acta, 2021. **403**: p. 139667.

Chapter 4

Modelling and study of the concentration overpotential

The content of this chapter is adapted from: N. M. Delgado, R. Monteiro, M. Abdollahzadeh, P. Ribeirinha, A. Bentien, and A. Mendes, *2D-dynamic phenomenological modelling of vanadium redox flow batteries – Analysis of the mass transport related overpotentials.* Journal of Power Sources, 2020. **480**: p. 229142.

4. Modelling and study of the concentration overpotential

Equation Chapter (Next) Section 1

4.1. Abstract

Flow batteries exhibit relatively low power density owing to ohmic and concentration overpotentials, which leads to higher system costs. In this work, a phenomenological model of a vanadium redox flow battery (VRFB) equipped with an anion exchange membrane (AEM) was developed and validated. The model is used to assess the concentration overpotential during charge-discharge cycling at different operating conditions and a method to determine the mass transfer coefficient is presented. Also, a strategy to reduce the concentration overpotential is proposed. The simulated charge-discharge curve displays the lowest relative error reported in the literature for VRFB equipped with an AEM; the results reveal that the mass transfer coefficient is overestimated in most models in the literature. It is demonstrated that the concentration overpotentials during charging and discharging steps are not equal owing to a mismatch between the state of charge and the state of discharge. Also, the current density has a greater impact on this overpotential than the flow rate. Higher overpotentials were found near the membrane since the electronic conductivity is higher than the ionic conductivity. The simulation results show that positioning the distribution channels close to the membrane allows a reduction of the concentration overpotential up to 3.9 %.

4.2. Introduction

Multi-dimensional models and simulations are time and cost-saving tools that can be used, for example, to study phenomena that hinder the performance of a vanadium electrochemical cell; Shah et al. [1] developed a transient model where mass and momentum conservation and species transport equations were combined with a kinetic model to study the effect of vanadium concentration, electrode porosity and flow rate in the performance of the VRFB. Later, the same authors included hydrogen and oxygen evolution [2, 3] and energy conservation [4] in their model to study the effect of gas evolution and temperature in the operation of a VRFB. Knehr et al. [5] studied the influence of operating conditions in the capacity loss by developing and using a transient model where vanadium crossover and side reactions are considered. The more recent work carried out involving multi-dimensional modelling consists in studying various effects in VRFBs, e.g., vanadium and water crossover on the capacity loss [6, 7], the influence of the flow field configurations on the performance [8-12] and electrolyte distribution and pressure loss optimization [12]. Nonetheless, most of these studies were performed for serpentine and interdigitated flow fields. Information about the influence of the electrolyte distribution in the through-plane direction of the electrode in the mass transfer resistances when using a conventional flow field design is scarcely found in the literature. Also, to the best knowledge of the authors, information regarding the effect of the operating parameters in such mass transfer resistance under transient conditions is scarce; Zheng et al. [13] used a steady-state three-dimensional model to study the influence of the current density in the mass transfer resistance. However, the simulations were only carried out for the charging step; the effect of mass transfer in the step transition and during the discharging step was not evaluated. Tang et al. [14] quantified the mass transfer resistance of a VRFB at a constant and a variable flow rate during the discharging step. Nonetheless, no further research regarding this topic was carried out by the authors.

There is a knowledge gap regarding the mass transfer resistance on a VRFB under charge-discharge cycling, which is of paramount importance for improving the energy efficiency and overall performance of the VRFB technology. Therefore, the main goal of this work is to systematically analyze the mass transfer resistance by determining the concentration overpotential under charge-discharge cycling at different operating conditions, and to

propose a strategy to reduce such overpotential. So far, concentration overpotential has been determined by comparing the limiting current density based on the surface area of the electrode with the current density based on the projected area [13-15] which may lead to overestimation of the overpotential. Therefore, this work clarifies the calculation of the concentration overpotential, and a more accurate method to determine such overpotential is proposed and compared to simulation results. This work analysis the mass transfer related overpotentials in a VRFB, which is critical for assisting in design and operation optimization. Also, it demonstrates that the mass transfer coefficient can be estimated from the polarization curves. The use of an experimental mass transfer coefficient allows the development of more accurate simulators. To the best of our knowledge, the influence of the distribution channel position, in a through-plane direction, in the mass transfer resistance has never been studied. In addition, the mass transfer resistances of four conventional VRFB with different distribution channel positions in a through-plane direction are also assessed.

This work is carried out using a 2D dynamic phenomenological model for a VRFB equipped with an anion exchange membrane (AEM). The mathematical model considers the electrochemical reactions, mass, and species transport in the porous medium, mass conservation for the tanks, and Donnan exclusion. The reported phenomenological models for VRFB equipped with an AEM consider only the transport of ions (mostly HSO_4^-) through the membrane [6, 16]; this is a simplified approach to model charge balancing when using an AEM. However, this model considers that only SO_4^{2-} is transported through the membrane. As such, in the presence of an applied driving force (e.g., electric field), the reversible ionic reaction $H^+ + SO_4^{2-} \rightleftharpoons HSO_4^-$ will occur at the electrode | membrane interface [17]. This allows capturing more accurately the potential change at the electrode | membrane interface due to the Donnan exclusion effect. To the best knowledge of the authors, the model presented in this work displays the lowest mean relative error for a VRFB equipped with an AEM.

4.3. Experimental setup

The redox flow cell uses two graphite plates with milled distribution channels before and after the reactional area to force the electrolyte to flow through the electrode (Figure **Error! Use the Home tab to apply Título 6;ND Appendix Header 1 to the text that you want to**

appear here..1). These channels have a cross-sectional area of 2 x 2 mm^2. In the reactional zones, polyacrylonitrile-based graphite felts (GF, GFD 4.6 EA, SGL Group, Germany) with an active area of 16 cm^2 and 4.6 mm uncompressed thickness (compressed to 25 %) were used as electrodes. The electrodes were boiled in 1 M H_2SO_4 and thermally treated in a furnace muffle under and air atmosphere at 400 ºC for 12 h. The AEM FAP 450 was purchased from Fumatech (BWT AG, Germany) and used without any treatment. A commercial vanadium solution with 1.6 M V^{3+}/V^{4+} 50:50 molar ratio and 2 M H_2SO_4 (GfE Metalle und Materialien GmbH, Germany) was used as electrolyte, without further treatment or purification. More details may be found elsewhere [18].

4.4. Mathematical model

The mass conservation and electrolyte flow were described using the continuity and momentum conservation equations. The charge transport was described using the Nernst-Planck equation and the charge conservation equations. The Butler-Volmer equation was used to describe the electrochemical reaction kinetics. Additionally, the following assumptions were made [19]:

- Incompressible fluid;
- Isotropic electrodes and membrane;
- Negligible gravity effect;
- Dilute solution approximation (activity coefficient is equal to unity);
- Negligible membrane crossover;
- Negligible hydrogen and oxygen evolution reactions;
- Isothermal behavior;
- Newtonian fluid;
- No precipitation of vanadium.

4.4.1. Governing Equations

Fluid flow conservation equations

The hydrodynamic flow was described using the momentum conservation equation (Eq. (4.1)), which is a balance of linear momentum (Newton's second law), together with the continuity equation (Eq. (4.2)), which describes the conservation of mass [20]. The total mass of the vanadium electrolyte was assumed constant and, to describe the hydrodynamic flow of the electrolyte, a low Reynolds number – laminar flow – was assumed:

$$\frac{\partial(\varepsilon\rho\vec{v})}{\partial t}+\nabla\cdot\left(\varepsilon\rho\vec{v}\vec{v}\right)=-\varepsilon\nabla p+\nabla\cdot\left(\varepsilon\mu\nabla\vec{v}\right)+S_{\text{mom}} \tag{4.1}$$

$$\frac{\partial\varepsilon\rho}{\partial t}+\nabla\cdot\left(\varepsilon\rho\vec{v}\right)=0 \tag{4.2}$$

where ε is the porosity of the electrode, ρ is the density of the electrolyte, $\vec{v}$ is the velocity of the electrolyte, p is the pressure, μ is the viscosity of the electrolyte and S_{mom} is the source term of the momentum equation. The source term of the momentum equation in the electrode region is given by the Darcy's law (Eq. (4.3)) .

$$S_{\text{mom}}=-\frac{\mu}{K_p}\vec{v} \tag{4.3}$$

where μ is the viscosity, and the permeability of the electrode (K_P) was determined with the Kozeny-Carman equation (Eq. (4.4)).

$$K_p=\frac{d_{\text{f}}^2\varepsilon^3}{16k_{\text{KC}}\left(1-\varepsilon\right)^2} \tag{4.4}$$

where d_{f} is the fiber diameter and k_{KC} is the Kozeny-Carman constant, used as fitting parameter to describe the morphology of the porous media.

Species transport equations

The transport of ions in the dilute solution was described by the Nernst-Planck, as follows:

$$\frac{\partial\varepsilon c_i}{\partial t}+\nabla\cdot\vec{N}_i=S_i \tag{4.5}$$

where c_i is the molar concentration of ion i and $\vec{N}_i$ is the total flux of ion i. S_i is the source term used to implement the concentration variations due to electrochemical reactions (Eq. (4.6) at the positive electrode and Eq. (4.7) at the negative electrode) - Table 4.1.

$$VO_2^+ + 2H^+ + e^- \underset{\text{charge}}{\overset{\text{discharge}}{\rightleftharpoons}} VO^{2+} + H_2O \tag{4.6}$$

$$V^{3+} + e^- \underset{\text{discharge}}{\overset{\text{charge}}{\rightleftharpoons}} V^{2+} \tag{4.7}$$

Table 4.1 – Reaction rate source terms of species transport equations.

Source term	Positive electrode	Negative electrode
$\boldsymbol{S}_{V^{2+}}$	-	$-\frac{j^-}{nF}$
$\boldsymbol{S}_{V^{3+}}$	-	$\frac{j^-}{nF}$
$\boldsymbol{S}_{VO^{2+}}$	$-\frac{j^+}{nF}$	-
$\boldsymbol{S}_{VO_2^+}$	$\frac{j^+}{nF}$	-
$\boldsymbol{S}_{H^+}$	$\frac{2j^+}{nF}$	0

The flux of each species, $\vec{N}_i$, was determined considering the additive contribution of three different transport mechanisms: diffusion, advection, and migration (Eq. (4.8)).

$$\vec{N}_i = \vec{N}_{\text{diff}} + \vec{N}_{\text{advec}} + \vec{N}_{\text{mig}} \tag{4.8}$$

The diffusion transport, due to concentration gradients of species i, was described using Fick's law (Eq. (4.9)).

$$\vec{N}_{\text{diff}} = -D_i^{\text{eff}} \nabla c_i \tag{4.9}$$

where $\vec{N}_{\text{diff}}$ is the ion flux due to diffusion, ∇c_i is the concentration gradient of ion i and D_i^{eff} is the effective ion diffusivity which was determined as follows:

$$D_i^{\text{eff}} = \varepsilon^{1.5} D_i \frac{\mu^0}{\mu} \tag{4.10}$$

where μ^0 is the solvent viscosity and D_i is the ion diffusivity (Table **Error! Use the Home tab to apply Título 6;ND Appendix Header 1 to the text that you want to appear here.**.1)

The advective flux ($\vec{N}_{\text{advec}}$) refers to the transport of ions due to pressure gradient as follows [21]:

$$\vec{N}_{\text{advec}} = c_i \vec{v} \tag{4.11}$$

The migration transport is caused by electric potential gradients within the system. The velocity at which the ions are transported is limited by their mobility [22]. Therefore, the migration flux ($\vec{N}_{\text{mig}}$) of species *i* can be determined as follows:

$$\vec{N}_{\text{mig}} = -\frac{z_i F D_i^{\text{eff}}}{RT} c_i \nabla \phi_{\text{e}} \tag{4.12}$$

where z_i is the valence state, R is the gas constant, F is the Faraday constant (96 485 C·mol^{-1}), T is the temperature (assumed to be 298.15 K), and $\nabla\phi_{\text{e}}$ is the electric potential gradient of the liquid phase.

The complete Nernst-Planck equation is:

$$\frac{\partial \varepsilon c_i}{\partial t} + \nabla \cdot \left(c_i \vec{v} \right) - \nabla \cdot \left(D_i^{\text{eff}} \nabla c_i \right) - \nabla \cdot \left(\frac{z_i F D_i^{\text{eff}}}{RT} c_i \nabla \phi_{\text{e}} \right) = S_i \tag{4.13}$$

The former equation was solved for V^{2+}, V^{3+}, VO^{2+}, VO_2^+, H^+, and HSO_4^- ions. The concentration of SO_4^{2-} was obtained according to the electroneutrality condition (Eq. (4.14)):

$$\sum_i z_i c_i = 0 \tag{4.14}$$

Charge conservation equations

The electric current, expressed as current density ($\vec{i}$), due to transport of ions was determined using the following equation [22]:

$$\vec{i} = F\sum_i z_i \vec{N}_i \tag{4.15}$$

The volumetric current density ($\nabla \cdot \vec{i}$) can be determined combining Eq. (4.8) with Eq. (4.15), as follows:

$$\nabla \cdot \vec{i} = \nabla \cdot \left(F\sum_i z_i c_i \vec{v} - F\sum_i z_i D_i^{\text{eff}} \nabla c_i - F^2 \sum_i \frac{z_i^2 D_i^{\text{eff}}}{RT} c_i \nabla \phi_{\text{e}} \right) \tag{4.16}$$

Thus, the electrolyte conductivity (σ_{e}) can be estimated using Eq. (4.17).

$$\sigma_{\text{e}} = F^2 \sum_i \frac{z_i^2 D_i^{\text{eff}}}{RT} c_i \tag{4.17}$$

In this work, the electrolyte conductivity is determined using a linear regression that relates experimental values of conductivity with the state of charge (Table **Error! Use the Home tab to apply Título 6;ND Appendix Header 1 to the text that you want to appear here.**.1). Thus, Eq. (4.16) was rewritten as function of the electrolyte conductivity as shown in Eq. (4.18). Also, in the event of an electrochemical reaction, charges between the electrolyte and electrode are exchanged. The volumetric current density is given by the flux of charges leaving or entering each phase [23]:

$$\nabla \cdot \left(F\sum_i z_i c_i \vec{v} \right) - \nabla \cdot \left(\frac{RT}{F\sum_i z_i} \nabla \sigma_{\text{e}} \right) - \nabla \cdot \left(\sigma_{\text{e}} \nabla \phi_{\text{e}} \right) = +j \tag{4.18}$$

Considering the charge conservation between phases, the flux of charges entering/leaving the solid phase ($\overrightarrow{i_{\text{s}}}$) must be the same leaving/entering the liquid phase ($\overrightarrow{i_{\text{e}}}$) (Eq. (4.19)).

$$\nabla \cdot \overrightarrow{i_{\text{s}}} = -\nabla \cdot \overrightarrow{i_{\text{e}}} = -j \tag{4.19}$$

The charge conservation equation of the solid phase was described using Ohm's law (Eq. (4.20)).

$$\overrightarrow{i_{\text{s}}} = -\sigma_{\text{s}}^{\text{eff}} \nabla \phi_{\text{s}} \tag{4.20}$$

where ϕ_{s} is the potential in the solid phase and $\sigma_{\text{s}}^{\text{eff}}$ is the effective conductivity of the electrodes and bipolar plates.

SO_4^{2-} was assumed to be transported through the membrane only by migration, where the current density in the membrane region ($\vec{i}_{e,mem}$) was determined with Eq. (4.21).

$$\vec{i}_{e,mem} = -\sigma_{mem} \nabla \phi_{e,mem} \tag{4.21}$$

The conductivity of the membrane was provided by the manufacturer (Table **Error! Use the Home tab to apply Título 6;ND Appendix Header 1 to the text that you want to appear here.**.2) and assumed constant.

Reaction kinetics

The relationship between the net reaction rate (j/nF) and the activation overpotential was described by the Butler-Volmer equation:

$$j = aFc_{red}^{\alpha_{red}^i} c_{ox}^{\alpha_{ox}^i} \left(k_{ox}^i \left(\frac{c_{red}^{s,i}}{c_{red}^i} \right) e^{\frac{\alpha_{ox}^i F \eta_{act}^i}{RT}} - k_{red}^i \left(\frac{c_{ox}^{s,i}}{c_{ox}^i} \right) e^{\frac{-\alpha_{red}^i F \eta_{act}^i}{RT}} \right) \tag{4.22}$$

where j is the volumetric current density, a is the surface area of the pore walls per total volume of the electrode, c^i_{red} and c^i_{ox} are molar concentrations of the vanadium ion with lowest and highest oxidation state, respectively, in the electrode i; superscript s refers to the electrode fibers, k^i is the reaction rate constant, α is the charge transfer coefficient and η^i_{act} is the activation overpotential (Eq. (4.23)). These parameters are summarized in Appendix A.2.

$$\eta_{act}^i = \phi_s^i - \phi_e^i - E^i \tag{4.23}$$

where E^i is the cell reaction potential in the absence of current (OCV) in the positive (Eq. (2.7)) and negative (Eq. (4.25)) electrodes, estimated from the Nernst equation.

$$E^+ = E^{0,+} + \frac{RT}{F} \ln \left(\frac{c_{VO_2^+} \left(c_{H^+} \right)^2}{c_{VO^{2+}}} \right) \tag{4.24}$$

$$E^- = E^{0,-} + \frac{RT}{F} \ln \left(\frac{c_{V^{3+}}}{c_{V^{2+}}} \right) \tag{4.25}$$

where $E^{0,i}$ is the standard cell reduction potential and the superscript i refers to the electrodes.

Mass transfer

In a non-equilibrium state, the concentration of reactants at the electrode fibers and in the bulk electrolyte is different. Therefore, the overpotential associated with reactant depletion on the electrode fibers, known as concentration overpotential, can be determined with Eq. (4.26) [21].

$$\eta_{\text{conc}}^{i} = E^{i} - E^{\text{s},i} = \frac{RT}{F}\ln\left(\frac{c_{\text{reactant}}^{i}}{c_{\text{reactant}}^{\text{s},i}}\right) \tag{4.26}$$

where $E^{\text{s},i}$ is the cell reaction potential at the electrode fibers (Eq. (4.24) and (4.25)). Thus, the cell concentration overpotential η_{conc} can be determined with Eq. (4.27).

$$\eta_{\text{conc}} = \frac{RT}{F}\ln\left(\frac{c_{\text{reactant}}^{-}}{c_{\text{reactant}}^{\text{s},-}}\right) + \frac{RT}{F}\ln\left(\frac{c_{\text{reactant}}^{+}}{c_{\text{reactant}}^{\text{s},+}}\right) \tag{4.27}$$

where c^{i}_{reactant} is the reactant concentration at the electrode i.

The mass transfer phenomenon is described by the flux of mass transferred between the electrode fibers and the bulk solution (Eq. (4.28)) [24].

$$N_i^{\text{s}} = k_m\left(c_i - c_i^{\text{s}}\right) \tag{4.28}$$

where the mass transfer coefficient (k_m) refers to the mass transfer rate of species i from/to the electrode fibers to/from the bulk electrolyte. The mass transfer mechanism considers three different steps (Figure **Error! Use the Home tab to apply Título 6;ND Appendix Header 1 to the text that you want to appear here.**.2). The first and third steps are controlled by advection and diffusion mechanisms, while the second step is controlled by the electrochemical reaction [24].

The mass transfer coefficient used was computed using a correlation described elsewhere [25], and where the first coefficient ($5.35\text{x}10^{-3}$) was used as a fitting parameter:

$$k_{m,i} = 5.35\times10^{-3}\left(\frac{\mu}{D_i^{\text{eff}}}\right)^{-0.615}\left(\frac{\rho d_{\text{f}}}{\mu}\right)^{0.409}\left|\vec{v}\right|^{0.409} \tag{4.29}$$

The electrochemical reactions occur only at the electrode fibers (second step); any change in the ion concentration between the electrode and the bulk electrolyte (first and third steps)

is the result of an exchange of charges between the liquid and the solid phases. Since charge is conserved, the flux of ions must be in equilibrium with the flux of electrons at the electrode surface (Eq. (4.30) and Eq. (4.31)).

$$k_{m,\mathrm{red}}\left(c_{\mathrm{red}}-c_{\mathrm{red}}^{\mathrm{s}}\right)=\frac{j}{aF} \tag{4.30}$$

$$k_{m,\mathrm{ox}}\left(c_{\mathrm{ox}}-c_{\mathrm{ox}}^{\mathrm{s}}\right)=-\frac{j}{aF} \tag{4.31}$$

The expressions used to determine the concentration of vanadium ions on the electrode fibers ($c^{\mathrm{s}}{}_i$) can be found elsewhere [19].

4.4.2. Boundary and initial conditions

The boundary conditions of the computational domain used in this simulation are identified and numbered in Figure **Error! Use the Home tab to apply Título 6;ND Appendix Header 1 to the text that you want to appear here.**.3.

At the inlet of both electrodes (boundaries 1 and 3 - Figure **Error! Use the Home tab to apply Título 6;ND Appendix Header 1 to the text that you want to appear here.**.3), the flow rate was given (Eq. (4.32)). Additionally, the concentration of each species at the inlet varied at every timestep (Eq. (4.33)).

$$-\vec{n}\cdot\vec{v}=\frac{Q_{\mathrm{in}}}{A_{\mathrm{in}}} \tag{4.32}$$

$$c_i=c_{\mathrm{in},i}(t) \tag{4.33}$$

where Q_{in} is the inlet volumetric flow rate, A_{in} is the inlet channel area, and $c_{\mathrm{in},i}(\mathrm{t})$ is the inlet concentration of species i at instant t.

The inlet concentration of species i at a given instant t was determined from a mass balance on the tanks (Eq. (4.34)).

$$\frac{\mathrm{d}c_{\mathrm{in},i}(t)}{\mathrm{d}t}=\frac{1}{V_{\mathrm{tank}}}\left(\int\vec{v}_{\mathrm{out}}c_{\mathrm{out},i}dA_{\mathrm{out}}-\int\vec{v}_{\mathrm{in}}c_{\mathrm{in},i}dA_{\mathrm{in}}\right) \tag{4.34}$$

where V_{tank} is the electrolyte volume in each tank and $c_{out,i}$ is the outlet concentration of species *i*.

The absolute pressure at the outlets (boundaries 4 and 2 - Figure **Error! Use the Home tab to apply Título 6;ND Appendix Header 1 to the text that you want to appear here.**.3) was assumed constant and equal to the atmospheric pressure (p_{atm}, Eq. (4.35)). The following boundary conditions were used for the remaining variables:

$$p = p_{atm} \mid \vec{n} \cdot \vec{N}_i = 0 \mid \vec{n} \cdot \left(-\sigma_s^{eff} \nabla \phi_s\right) = 0 \mid \vec{n} \cdot \left(-\sigma_e \nabla \phi_e\right) = 0 \tag{4.35}$$

The transport mechanism of sulfate and bisulfate ions through the AEM, for balancing the electronic current, suggested by Lorrain et al. [17] was adopted in this model; only sulfate ions permeate the membrane and the bisulfate ions may transfer the proton to the electrolyte before permeating as sulfate ion; on the other side of the membrane, the permeated sulfate ion may acquire a proton from the electrolyte becoming bisulfate ion. To ensure the electroneutrality of the system, the flux of sulfate ions across the AEM must be proportional to the reaction rate ($\vec{N}_{SO_4^{2-}} = i/nFz_{SO_4^{2-}}$). It is reasonable to assume that half of the permeated sulfate ions ($\vec{N}_{SO_4^{2-}}/2$) arise from the bisulfate dissociation reaction ($H^+ + SO_4^{2-} \rightleftharpoons HSO_4^-$), which occurs at the electrode | membrane interface [17], and that such reaction is instantaneous. Thus, at the electrode | membrane interface we have: $\vec{N}_{H^+} = -\vec{N}_{HSO_4^-} = \vec{N}_{SO_4^{2-}}/2$. At the negative electrode | membrane interface, protons react with sulfate ions to produce bisulfate and the reverse reaction occurs at the positive electrode | membrane interface. Therefore, the boundary conditions for H^+ and HSO_4^- at the electrode | membrane interface can be written as:

$$\vec{n} \cdot \vec{N}_{H^+} = \pm \frac{i}{2nFz_{SO_4^{2-}}} \tag{4.36}$$

$$\vec{n} \cdot \vec{N}_{HSO_4^-} = \pm \frac{i}{2nFz_{SO_4^{2-}}} \tag{4.37}$$

At the negative electrode | membrane interface (boundary 18 - Figure **Error! Use the Home tab to apply Título 6;ND Appendix Header 1 to the text that you want to appear**

here..3), the right-hand term of Eq. (4.36) is negative and the right-hand term of Eq. (4.37) is positive. At the positive electrode | membrane interface (boundary 19 - Figure **Error! Use the Home tab to apply Título 6;ND Appendix Header 1 to the text that you want to appear here.**.3), the signs are reversed. Since the concentration of SO_4^{2-} is determined with the electroneutrality condition (Eq. (4.14)), no boundary conditions were used for this species.

The charge-discharge cycling of a VRFB was carried out at constant current (galvanostatic mode). This operating mode was simulated using the following boundary condition at the bipolar plate in contact with the positive electrode:

$$-\vec{n}\cdot\left(\sigma_s^{\text{eff}}\nabla\phi_s\right)=i \quad \left(\text{boundary } 6\right) \tag{4.38}$$

where i is the operating current density, which is positive for charging and negative for discharging. At the bipolar plate in contact with the negative electrode, the potential of the solid phase was set to 0 to act as reference electrode. For the other external boundaries (boundaries 7 to 16), the following boundary conditions were adopted for all variables:

$$\vec{n}\cdot\vec{N}_i=0 \mid \vec{n}\cdot\left(-\sigma_{\text{s}}^{\text{eff}}\nabla\phi_{\text{s}}\right)=0 \mid \vec{n}\cdot\left(-\sigma_{\text{e}}\nabla\phi_{\text{e}}\right)=0 \tag{4.39}$$

A single-domain approach was implemented for the inner boundaries between the electrodes and the membrane (boundaries 18 and 19 - Figure **Error! Use the Home tab to apply Título 6;ND Appendix Header 1 to the text that you want to appear here.**.3) for the potential in the liquid phase [20]. A similar approach was adopted for the potential in the solid phase for the inner boundaries between the bipolar plates and the electrodes (boundaries 17 and 20 - Figure **Error! Use the Home tab to apply Título 6;ND Appendix Header 1 to the text that you want to appear here.**.3). Eq. (4.20) was also solved for the membrane and the single-domain approach was used at the interfaces between the electrodes and the membrane (boundaries 18 and 19 - Figure **Error! Use the Home tab to apply Título 6;ND Appendix Header 1 to the text that you want to appear here.**.3). This is possible by using an extremely low value of electronic conductivity (1×10^{-18} S m^{-1}) for the membrane since it acts as an insulator.

The Donnan potential (E_D, Eq. (4.40)) within the VRFB was calculated in this model to simulate the effect of the repulsion of protons at the interface between the negative electrode and the membrane (c_{1,H^+}) and between the positive electrode and the membrane (c_{2,H^+}) in the cell potential [26].

$$E_D = \frac{RT}{F} \ln\left(\frac{c_{2,H^+}}{c_{1,H^+}}\right) \tag{4.40}$$

The initial conditions (t = 0 s) used in the present model for positive and negative electrodes are:

$$c_i = c_i^0 \mid \phi_s^+ = E^+ \mid \phi_s^- = E^- \mid \phi_e = 0 \tag{4.41}$$

where the initial concentration of the species (c_i^0) was defined as function of the state of charge of the battery, which denotes the ratio between the amount of energy stored in the VRFB and the total energy storage capacity, or (SoC, Eq. (4.42)), and total vanadium (c_V) and sulfuric acid concentration.

$$\mathrm{SoC} = \frac{\overline{c_{V^{2+}}} + \overline{c_{VO_2^+}}}{2c_V} \tag{4.42}$$

where $\overline{c_{V^{2+}}}$ and $\overline{c_{VO_2^+}}$ are the molar concentration of V^{2+} and VO_2^+ ions averaged over the volume of a half-cell.

The equations used to determine the initial concentrations of the ionic species are summarized in Table **Error! Use the Home tab to apply Título 6;ND Appendix Header 1 to the text that you want to appear here.**.4. It was assumed that, after the charge separation step, at the positive electrode only VO^{2+} are present and at the negative electrode only V^{3+} are present.

4.4.3. Numerical procedure

The computational domain was divided into 5 zones with a total of 2100 elements. The model variables for each domain are shown in Figure **Error! Use the Home tab to apply Título 6;ND Appendix Header 1 to the text that you want to appear here.**.4. The governing equations were discretized using a finite volume method and solved using the

commercial software package Fluent 19.2. The SIMPLE algorithm, pre-installed within the software package, was used to solve the pressure-velocity coupling for unsteady state conditions. Species and charge transport equations were implemented using user-define scalars and solved with the Second Order Upwind discretization method. The remaining equations, including the boundary and initial conditions, were implemented using user-defined functions. Under-relaxation factor was used for species and charge transport equations to handle convergence problems. A residual value of 10^{-6} was used as stop condition for every time step for all governing equations. All the parameters used in the simulation are described in Appendix A.2.

4.5. Results and discussion

4.5.1. Model validation

The electrochemical model was validated against experimental data obtained for a lab-scale cell. The lab cell was run at 160 ml min^{-1} feed rate, for each electrolyte, and at 80 mA cm^{-2}; the volume of each electrolyte storage tank was 80 ml. Applied potential cut-offs of 1.65 V and 0.80 V were used for the charging and discharging steps, respectively. The SoC at the start of the charging step was assumed to be 7.5 %. Figure 4.1 shows the experimental and the simulated charge-discharge curves.

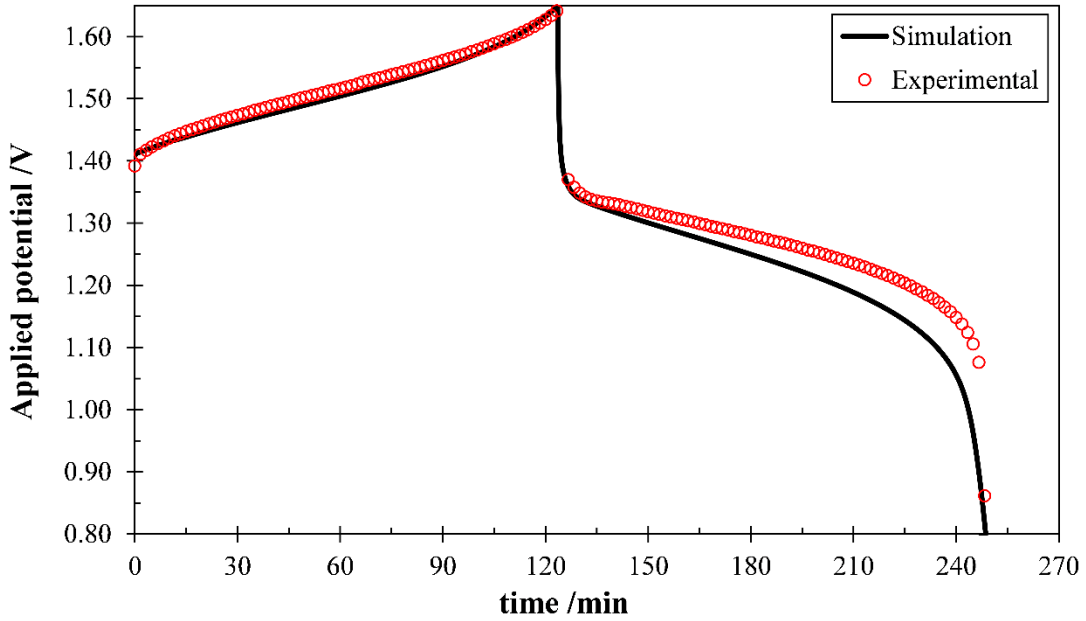

Figure 4.1 – Simulation and experimental charge-discharge curves for a VRFB with 16 cm^2 active area.

The simulation results agree with the experimental data with a mean relative error of 0.51 % for the charging step and a mean relative error of 3.65 % for the discharging step; the different behavior between both steps is known in the literature and may be attributed to the kinetic parameters (k and α) [27]. The kinetic parameters for the oxidation reaction may not be equal to the kinetic parameters for the reduction reaction at both electrodes. In this work, it was assumed that the kinetic parameters of the oxidation reaction are equal to the parameters of the reduction reaction due to the lack of experimental data for the GFD 4.6 EA electrode. Nonetheless, the simulated and the experimental data match at end of the discharging step, which is not observed in most models found in the literature. This is related to the mass transfer coefficient which was used as a fitting parameter. It is expected that the mass transfer resistance displays a significant contribution to the total overpotential in this region [14]; this means that most of the reported models are overestimating the mass transfer coefficient. Mass transfer coefficients close to the obtained are reported in the literature [28]. This evidence supports the accuracy of the developed model, which to the best knowledge of the authors displays the lowest mean relative error for a VRFB equipped with an AEM.

4.5.2. Concentration overpotential during cycling

The average concentration overpotential of the VRFB, which is independent of the axial (x) and coronal (y) positions in the electrode, was analyzed during charge-discharge cycling (Figure 4.2); the operating conditions were the same as for the previous section.

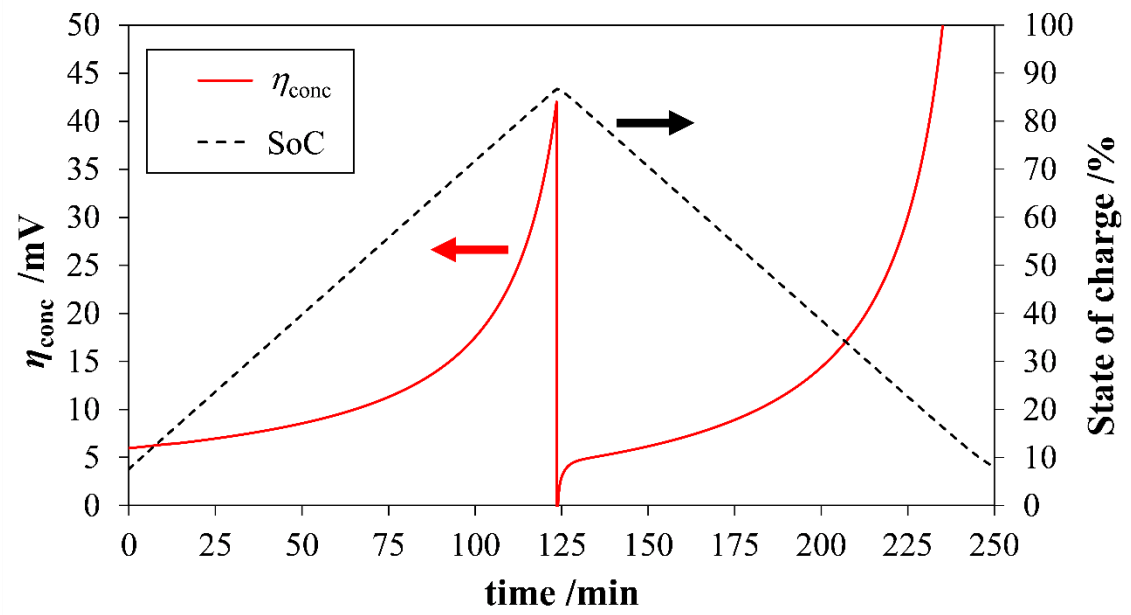

Figure 4.2 – Average concentration overpotential and SoC of the VRFB during charge-discharge cycling at 80 mA cm^{-2} and 160 ml min^{-1}.

Figure 4.2 shows that the concentration overpotential increases exponentially over the charging and the discharging steps, with the highest concentration overpotential values being observed at the end of each step. At the end of the charging and discharging steps, the concentration of reactants available at the electrode fibers and in the bulk electrolyte is very low; even a slight decrease of the concentration of the reactant at the electrode fibers leads to a sharp increase in the concentration overpotential. This behavior was confirmed by discharging the VRFB to an SoC of 8.6 %, corresponding to a state of discharge of 91.4 %, where the concentration overpotential increased from 10.9 mV (mean value for the charging step) to 23.9 mV (mean value for the discharging step). Also, a maximum concentration overpotential of 189 mV was obtained at 8.6 % SoC during the discharging step while during the charging step a maximum concentration overpotential of 42 mV was observed at 86.7 % SoC. It must be pointed out that operating a VRFB at low or high SoC should be avoided

since depletion of reactants at the electrode fibers may lead to side reactions, such as hydrogen [2, 29, 30] and oxygen [3] evolutions, and oxidation of carbon materials [31].

A sharp increase in the concentration overpotential was also observed at the beginning of the discharging step. This behavior was attributed to the ability of the VRFB to work as a capacitor; at the beginning of the discharging step, there is an accumulation of reactants on the electrode fibers, which are immediately available to react. Thus, the reactants concentration gradient between the electrode fibers and the bulk electrolyte is extremely low and the concentration overpotential is also low.

The mass transfer coefficient (Eq. (4.29)) used in this simulation is up to three orders of magnitude lower than the mass transfer coefficient used by other authors [13-15]. According to You et al. [19], a lower mass transfer coefficient should yield a higher overpotential. However, the values of concentration overpotential obtained in this work are within the range of values found in the literature [13-15]. This discrepancy may be ascribed to the mathematical terms used in the equation to determine the concentration overpotential, where some authors typically use current density based on the projected area instead of the surface area of the electrode as in this work (Figure **Error! Use the Home tab to apply Título 6;ND Appendix Header 1 to the text that you want to appear here.**.7). The approach used in this work is more accurate since the electrochemical reactions occur at the electrode fibers, and not only at the electrode | bipolar interface; the above mentioned reports use simulators developed based on the projected area but fail to compare with the corresponding simplified model, indicated by Eq. (4.43):

$$i_{L,PA} = a\frac{V_{\text{electrode}}}{A} nFk_m c_R \tag{4.43}$$

These authors compare with Eq. (4.44):

$$i_L = nFk_m c_R \tag{4.44}$$

which gives the current density based on the electrode surface area. The term $a \cdot V_{\text{electrode}}/A$ in Eq. (4.43) is the ratio between the electrode real surface area by the project area at the bipolar plate, and it is often in the order of thousands.

Figure **Error! Use the Home tab to apply Título 6;ND Appendix Header 1 to the text that you want to appear here.**.5 shows two simulated polarization curves (50 % SoC and a feed flow rate of 10 ml min^{-1} and 160 ml min^{-1}), where the limiting current density is compared with the one obtained with Eq. (4.43). When Eq. (4.43) is used, the limiting current density obtained are close to each other, with a maximum relative difference of *ca*. 3.70 %. Thus, the mass transfer coefficient can be estimated with reasonable accuracy using experimental polarization curves and Eq. (4.43).

The mass transfer resistances are the second highest source of overpotential of this VRFB, with an average overpotential of 16.4 mV @ 80 mA cm^{-2}, while the ohmic losses are the main source of overpotential with an average value of 117.0 mV and the activation overpotential is 14.5 mV. The negative electrode displays a higher concentration (11.9 mV) and activation overpotentials (9.5 mV) than the positive electrode (9.0 mV and 0.5 mV, respectively) due to the slower reaction rate and diffusion of V^{2+} and V^{3+} ions. This result agrees with the experimental results in the literature [32].

4.5.3. Influence of the current density

The concentration overpotential behavior was also studied at three different current densities: 80 mA cm^{-2}, 120 mA cm^{-2} and 160 mA cm^{-2} - Figure 4.3. The flow rate was set to 160 ml min^{-1}, which corresponds to stoichiometric ratios between flow and current (λ) of 160, 107, and 80 at 50 % SoC, respectively. The applied potential cut-off for the charging step was increased to 1.80 V and 1.95 V for current densities of 120 mA cm^{-2} and 160 mA cm^{-2}, respectively, to compensate for the total overpotential increase. For the discharging step, applied cut-offs of 0.65 V and 0.40 V were used for a current density of 120 mA cm^{-2} and 160 mA cm^{-2}, respectively. All the remaining variables used in the simulation were kept unchanged.

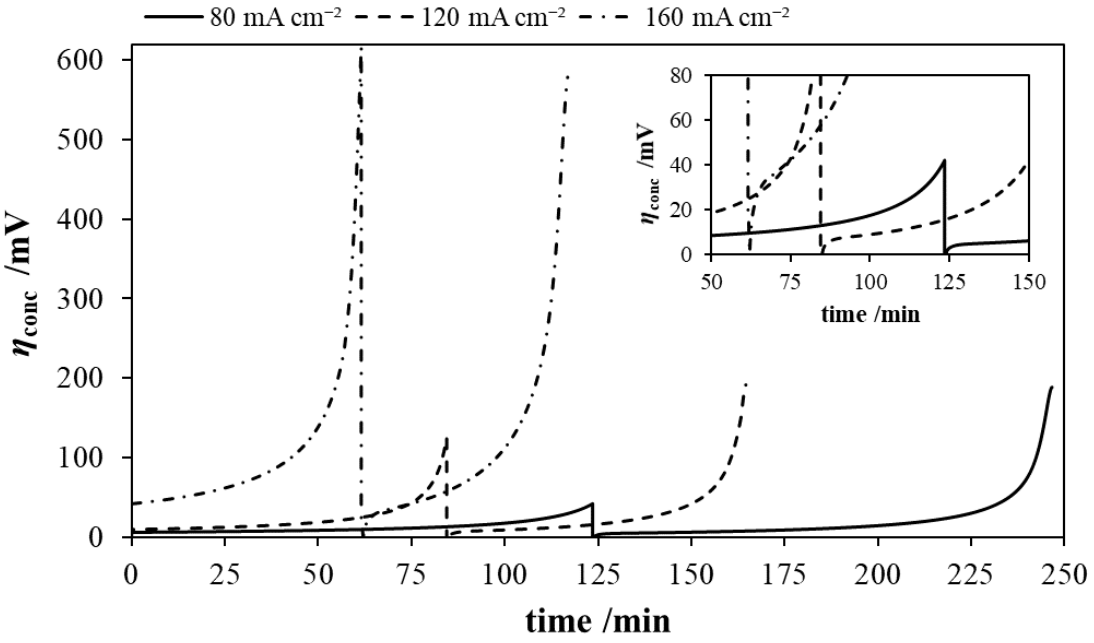

Figure 4.3 – Average concentration overpotential of the VRFB during cycling at current densities of 80 mA cm^{-2} (solid line), 120 mA cm^{-2} (dash line), and 160 mA cm^{-2} (dash dot line).

Figure 4.3 shows that the concentration overpotential increases with the current density. This trend is in agreement with the information found in the literature [13]. Within the range of the current densities used in this work, the relationship between the two variables is linear; at a current density of 120 mA cm^{-2}, the average concentration overpotential for the charging step was 26.4 mV while at 160 mA cm^{-2} a value of 118 mV was obtained. For the discharging step, average concentration overpotentials of 27.9 mV and 104 mV were obtained at current densities of 120 mA cm^{-2} and 160 mA cm^{-2}, respectively. The number of electrons available to participate in the electrochemical reaction increases with the current. Thus, increasing the current density will increase the reaction rate. When the reaction rate increases and the mass transfer rate is unchanged, the rate of reactants' depletion at the electrode fibers increases, leading to an increase in concentration overpotential.

The results obtained in this work also demonstrate that for high values of SoC the concentration overpotential increase is sharper than predicted by Zheng et al. [13]. For example, these authors obtained an average concentration overpotential as high as 0.8 mV

for 10 % SoC and slightly below 7.5 mV for 85 % SoC at a current density of 160 mA cm^{-2}, while in the present work values of 43 mV and 585 mV were obtained for the same SoC and current density, during charge step. The present work considers a much lower mass transfer rate, which explains such discrepancy; the reactant depletion at the electrode fibers is faster for lower mass transfer rates and, thus, the concentration overpotential increase rate is increased.

At higher current densities, the performance of a VRFB as a capacitor improves; a faster increase in the concentration overpotential at the start of the discharging step is observed. During the charging step, the product accumulation at the electrode fibers is higher when applying higher current densities. When changing to the discharging step, the combined effect of increased reaction rate and a higher accumulation of reactants lead to a sharper increase in the concentration overpotential.

Figure 4.4 (a), Figure 4.4 (b), and Figure 4.4 (c) show the influence of the current density in the local concentration overpotential, which is a function of the axial position in the electrode, and net reaction rate distribution profiles and the concentration profile of V^{2+} ion at the electrode fibers, respectively, in the through-plane direction of the negative electrode.

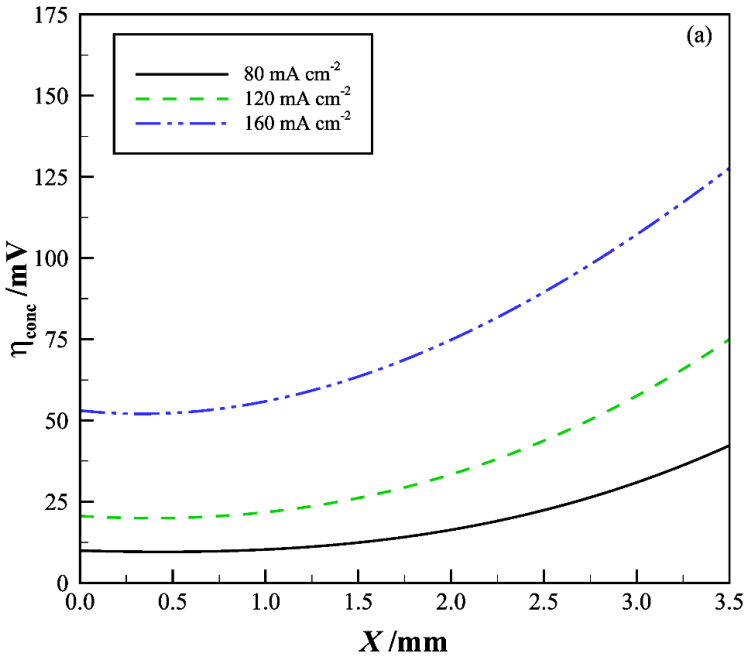

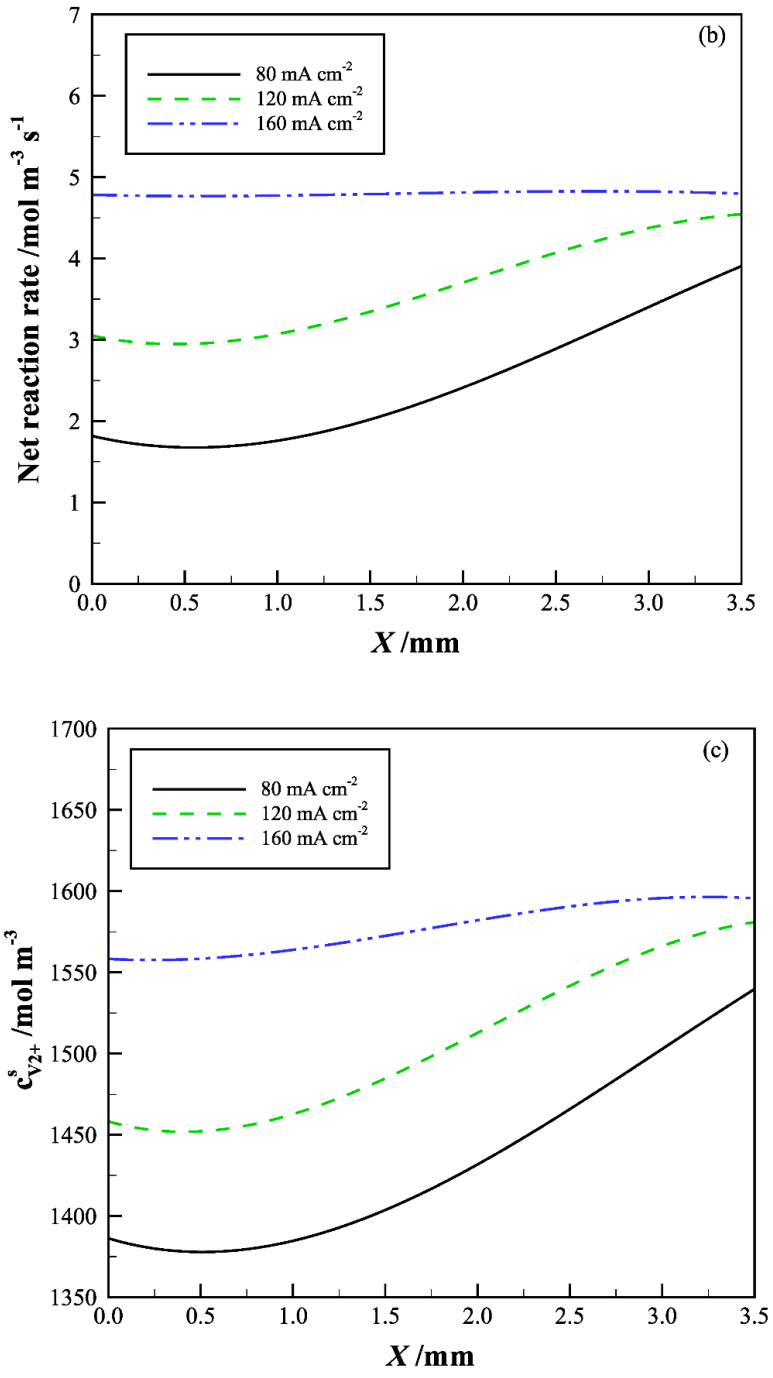

Figure 4.4 – Distribution profile of (a) local concentration overpotential, (b) net reaction rate and (c) V^{2+} concentration at the electrode fibers in the through-plane direction (*X* direction) of the negative electrode at 80 mA cm^{-2} (solid line), 120 mA cm^{-2} (dash line), and 160 mA cm^{-2} (dash dot dot line) and 80 % SoC. The bipolar plate | electrode interface is located at X = 0.0 mm and the electrode | membrane interface is located at X = 3.5 mm.

Increasing the current density leads to a more uniform distribution of the local concentration overpotential in the through-plane direction of the electrodes (Figure 4.4 (a)); the increasing overpotential in the middle of the electrode and near the electrode | bipolar plate interface (X = 0.0 mm) is slightly higher compared to the increasing overpotential near the membrane (X = 3.5 mm). The net reaction rate distribution also becomes more uniform with the current density increase (Figure 4.4 (b)); the mass transfer rate is much lower when compared to the increasing reaction rate and a more uniform distribution of the reactant at the electrode is observed (Figure 4.4 (c)). Thus, for higher current densities, the distribution of the local concentration overpotential is more uniform. These results show that the design of the distribution channels of a VRFB becomes more critical when operating the battery at high current density; a proper electrolyte distribution and high mass transfer rates must be guaranteed to ensure low concentration overpotentials, low overpotential gradients and, consequently, a long lifespan of the materials of the battery. Figure 4.4 (b) also shows that at 0.0 mm < X < 1.0 mm there is a lower contribution to the reaction extension and, thus, a thinner electrode could be more beneficial to the performance of the battery at lower current densities.

4.5.4. Influence of the flow rate

To study the influence of the advective flux (Eq. (4.11)) in the mass transfer resistance, the average concentration overpotential of the VRFB was determined during charge-discharge cycling at three different flow rates: 40 ml min^{-1}, 80 ml min^{-1} and 160 ml min^{-1} - Figure 4.5. All the remaining variables used in the simulation were kept unchanged, including the current density (80 mA cm^{-2}).

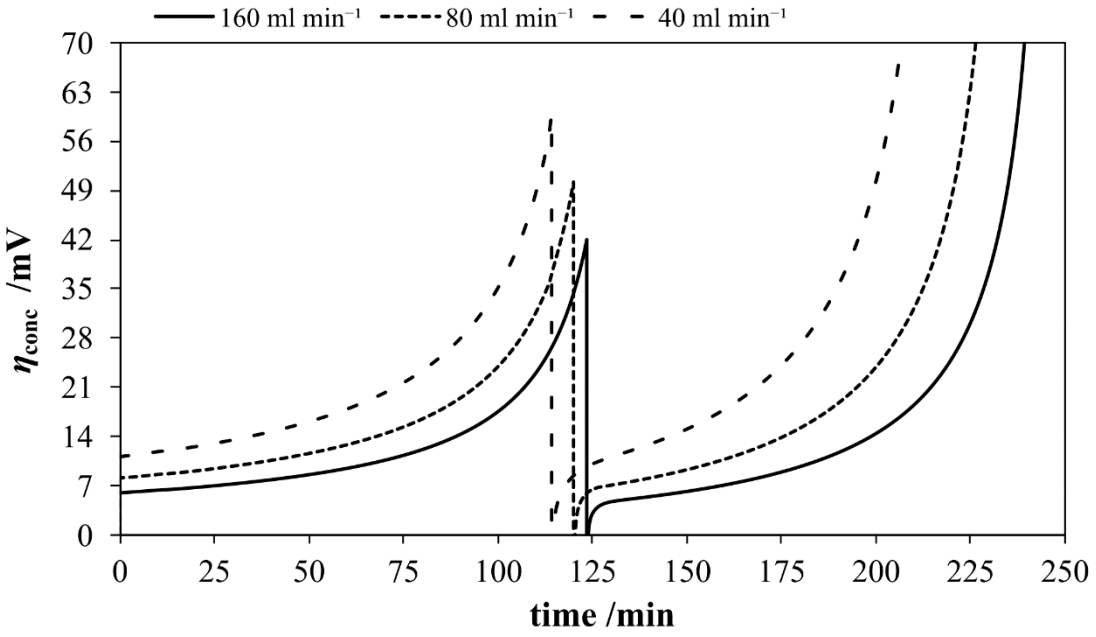

Figure 4.5 – Average concentration overpotential of the VRFB during cycling at flow rates of 40 ml min^{-1} (dash dot line), 80 ml min^{-1} (dash line) and 160 ml min^{-1} (solid line).

When the flow rate was decreased from 160 ml min^{-1} to 80 ml min^{-1}, the average concentration overpotential increased from 10.9 mV to 16.8 mV at the charging step and from 23.9 mV to 34.9 mV at the discharging step. Within the range of the flow rates studied, the highest overpotential was observed at a flow rate of 40 ml min^{-1}; an average concentration overpotential of 20.7 mV was obtained for the charging step and 41.8 mV for the discharging step. These results are related to the advective flux decrease in the electrodes, which reduces the reactant transfer rate within the pores of the electrode; for the same reaction rate, the reactant concentration gradient between the electrode fibers and bulk electrolyte increases and, consequently, the concentration overpotential also increases. A similar trend was observed by Monteiro et al. [18] who performed polarization curves and charge-discharge cycles under different flow rates; for a fixed current density, lower flow rates led to higher overpotentials. Nonetheless, the advective flux is highly dependent on the design of the distribution channels; low flow rates may be safely used if the cell design allows a high flow velocity in the electrode.

The flow rate also affects the distribution of the ions in the electrode. Figure 4.6 (a) and Figure 4.6 (b) show the distribution profiles of the local concentration overpotential and reactant mass transfer coefficient, respectively, in the negative electrode at 80 % SoC for flow rates between 40 ml min^{-1} and 160 ml min^{-1}.

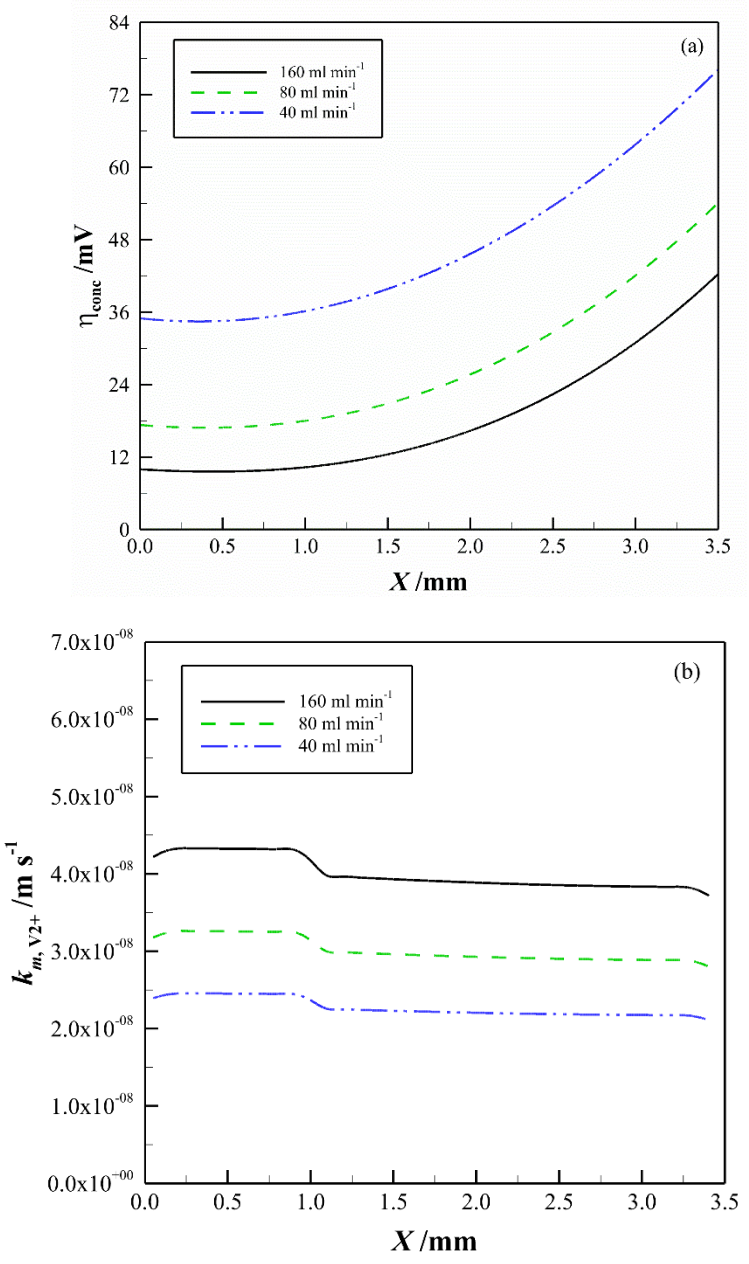

Figure 4.6 – Distribution profile of the (a) local concentration overpotential and (b) reactant mass transfer coefficient in the through-plane direction (X direction) of the negative electrode at 40 ml min^{-1} (dash dot line), 80 ml min^{-1} (dash line) and 160 ml min^{-1} (solid line) and 80 %

SoC. The bipolar plate | electrode interface is located at X = 0.0 mm, the electrode | membrane interface is located at X = 3.5 mm and the inlet/outlet channel is located at 0.0 mm < X < 1.0 mm.

The local concentration overpotential increase with the flow rate decrease was observed in all zones of the electrode (Figure 4.6 (a)). The vanadium ions are distributed through the electrode by advective and diffusive transport mechanisms. A lower advective flux leads to a higher residence time in the electrode. Consequently, the regeneration rate of the electrolyte in the electrode is slower, and the reactant concentration gradient in the pores of the electrode increases. Figure 4.6 (a) also shows that the distribution of the local concentration overpotential in the electrode is slightly improved when using lower flow rates; a steeper increase in the concentration overpotential is observed closer to the bipolar plate interface when compared to other regions of the electrode. Figure 4.6 (b) shows that the mass transfer coefficient profile in the through-plane direction is more uniform at lower feed flow rates due to a better electrolyte distribution over the electrodes. Additionally, the mass transfer coefficient decrease is more notorious closer to the bipolar plate interface, where the inlet/outlet channels are located, than closer to the membrane; as the feed flow rate decreases, the concentration overpotential (Figure 4.6 (a)) increase closer to the membrane is less notorious when compared to the region close to bipolar plate interface. Thus, the more uniform concentration overpotential profile may be attributed to the more uniform flow velocity when decreasing the flow rate.

4.5.5. Distribution channel position

The effect of the inlet and outlet channel position in the through-plane direction in the concentration overpotential was analyzed. Three new cells with different distribution channel positions were created (Figure **Error! Use the Home tab to apply Título 6;ND Appendix Header 1 to the text that you want to appear here.**.6): cell M featuring the inlet and outlet channels close to the membrane, cell C with the distribution channels positioned at the center of the electrode and cell E with the distribution channels with the same depth as the thickness of the electrode. Cell BP refers to the cell used to validate the model. The inlet/outlet channel depth of cells BP, M and C is 1 mm. .

The simulations were carried out at three different flow rates (40 ml min^{-1}, 80 ml min^{-1} and 160 ml min^{-1}) and at a constant current density of 160 $mA \cdot cm^{-2}$. The relative concentration overpotential ($\eta_{conc,rel}$, Eq. (4.45)) was calculated to compare the average concentration overpotential at the charging step of cells M, C, and E with the results obtained for the reference cell, BP, at the same operating conditions.

$$\eta_{conc,\,rel} = \frac{\eta_{conc,i} - \eta_{conc,BP}}{\eta_{conc,BP}} \times 100 \qquad (4.45)$$

The results (Figure 4.7) show that cells M, C, and E performed better at all flow rates when compared to cell BP.

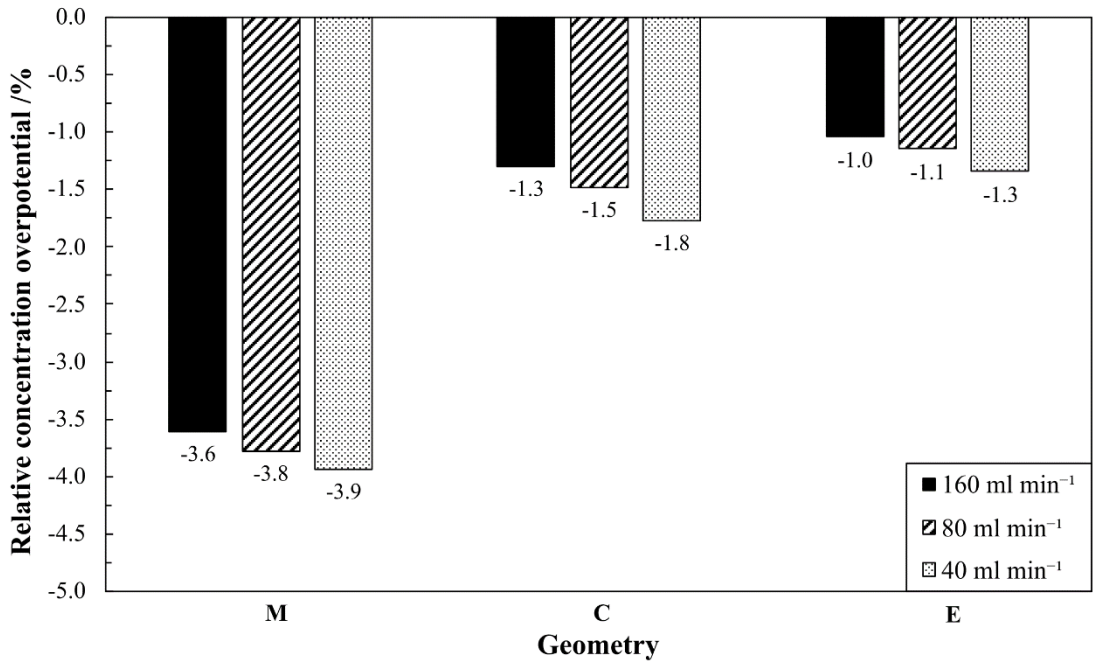

Figure 4.7 – Relative concentration overpotential for geometries M, C and E at a current density of 160 mA cm^{-2} and flow rates of 40 ml min^{-1}, 80 ml min^{-1} and 160 ml min^{-1}.

Cell M displayed the best result among the other geometries when a flow rate of 160 ml min^{-1} was used. Cells C and E exhibited a concentration overpotential improvement up to 1.8 % and 1.3 %, respectively, when compared to the cell BP. Figure 4.7 also shows that cell E displayed higher relative concentration overpotentials when compared to cells M and C; most likely owing to the higher inlet/outlet area which results in a lower advective

flux in the electrodes. These results also show that a uniform electrolyte flow in the through-plane direction does not provide the best performance results.

Figure 4.8 shows the concentration overpotential in the negative electrode for all cells at an SoC of 80 % during the charging step to further understand the previous results. A flow rate of 160 ml min^{-1} and a current density of 160 mA cm^{-2} were used in the simulation.

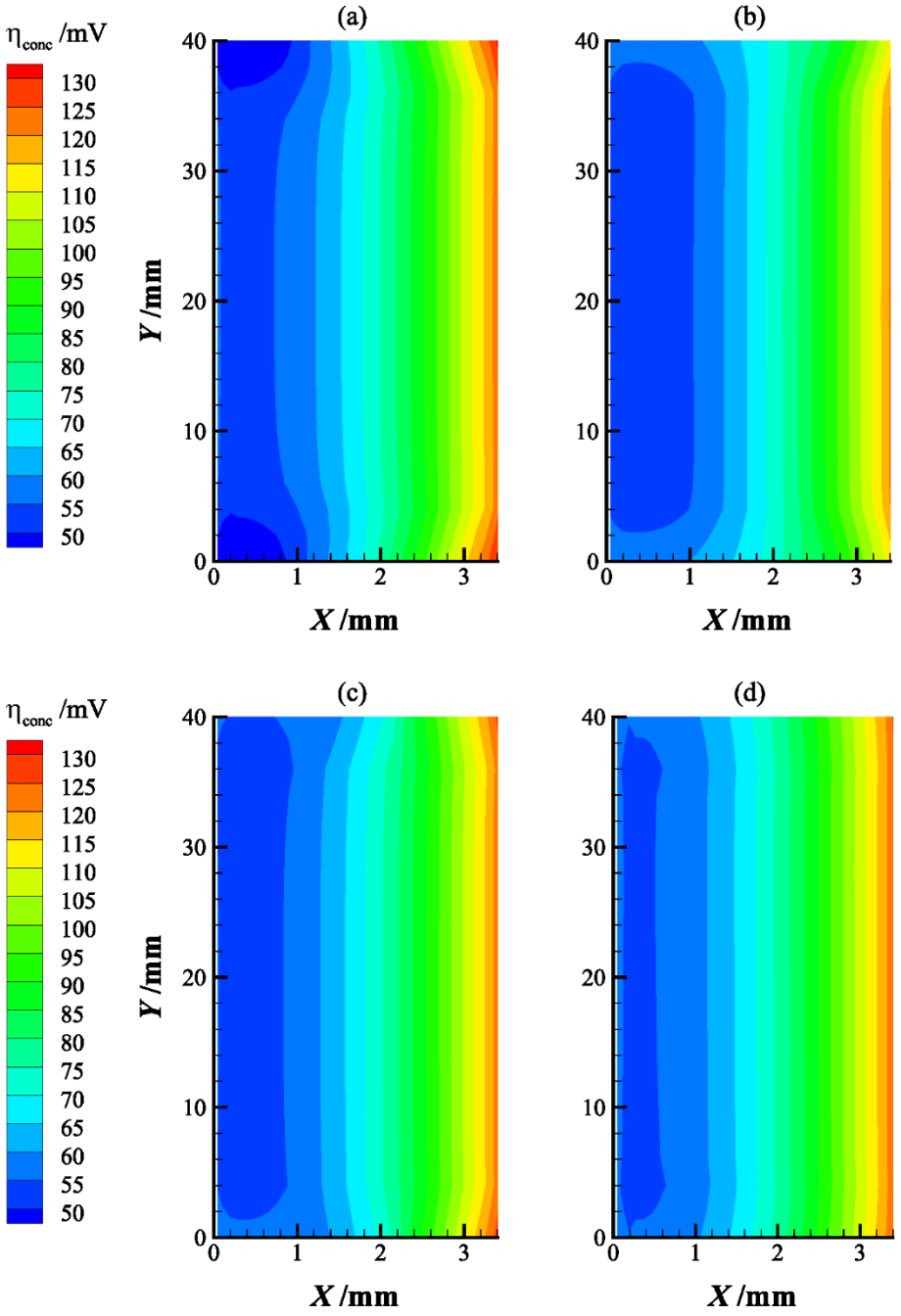

Figure 4.8 – Concentration overpotential contour in the through-plane direction of the negative electrode at 80 % SoC for cells (a) BP, (b) M, (c) C, and (d) E. The bipolar plate | electrode interface is located at $X = 0.0$ mm and the electrode | membrane interface is located at $X = 3.5$ mm. The inlet is located at $Y = 0$ mm and the outlet is located at $Y = 40$ mm.

It is possible to observe that the zone with the highest concentration overpotential is located closer to the membrane ($X = 3.5$ mm), regardless of the position of the distribution channels. The resistance to the transport of electrons through carbon felt is lower than to the transport of ions through the electrolyte; there is a higher accumulation of ions and higher reaction rates closer to the membrane. Increasing the advective flux closer to the membrane provides higher mass transfer rates in this zone and, thus, the highest overall reduction in the concentration overpotential is obtained. The results discrepancy between cells M and BP could be minimized by improving the conductivity of the electrolyte using, for example, chloride acid [33].

The zone with lowest concentration overpotential is located at $0.0 \text{ mm} < X < 1.4$ mm. Positioning the inlet and outlet distribution channels at $0.0 \text{ mm} < X < 1.0$ mm (cell BP) results in higher average concentration overpotentials since the overpotential and the advective flux are exponentially related; the concentration overpotential reduction near bipolar plate will be lower than at any other position (cell M, C, and E). Thus, improving mass transfer rates at the location with the lowest concentration overpotential leads to a worse cell performance. This effect becomes even more relevant when decreasing the flow rate due to the exponential relationship between the two parameters.

When designing a larger VRFB, the position of the inlet/outlet channels may become more important than for a lab-scale cell. Typically, the electrolyte velocity inside the electrode of a larger VRFB is lower than in lab-scale cells; a higher pressure drop would be observed in stacks for the same electrolyte velocity due to the increased electrode dimensions. Nonetheless, designing a cell with an inlet/outlet channel location near the membrane increases the difficulty of building a redox flow battery. Also, despite the positive results obtained for cell M, it should be noticed that the transport mechanisms of vanadium ions through the ion exchange membrane were not included in this model. Increasing the flow

velocity near the membrane may increase the vanadium crossover, leading to higher capacity loss rates [5].

4.6. Conclusion

A 2D, dynamic, isothermal model, incorporating the charge and species transport and the electrochemical reaction equations was successfully developed, implemented in a CFD platform (ANSYS Fluent 19.2) and validated against experimental results from a vanadium redox flow cell equipped with an AEM; a charge-discharge cycle was simulated with a mean relative error of 1.85 %, using only the mass transfer coefficient as a fitting parameter. Also, contrarily to most of the models found in the literature, a good match between the simulated and experimental data at the end of the discharge step is observed, where the mass transfer resistances are dominant; this may indicate that most of the reported models overestimate the mass transfer coefficient.

The developed simulator was used to compute the concentration overpotentials during charge-discharge cycling, at different flow rates and current densities. Although the mass transfer coefficient used in this work is lower than most of the mass transfer coefficients used in literature simulators, the overpotentials determined with the developed simulator are within the range found in experimental and theoretical studies; it is demonstrated that, for flow batteries, using the current density based on the projected area to determine the concentration overpotential leads to unrealistic values. Instead, the reactant concentration at the electrode fibers or the current density based on the surface area of the electrode should be used. It was found that the charging and discharging steps display different average concentration overpotentials, regardless of the operating conditions; a mismatch between the state of charge during the charging step and the state of discharge during the discharging step is then observed. To minimize the impact of the concentration overpotential in the performance and lifetime of a VRFB, the battery should be operated using a lower potential range. For example, VRFB equipped with AEM and CEM should be operating within 1.14 V – 1.60 V and 1.10 V – 1.55 V, respectively, which corresponds to a state of charge of 20 % – 80 %. The results also show that at the beginning of the discharging step, the VRFB acts as a capacitor due to the accumulation of charges at the electrode fibers at the end of the

charging step. This behavior was more prominent for lower flow rates, or higher current densities.

The concentration overpotential was also studied at different feed flow rates and current densities in the through-plane direction for a fixed SoC. The results show that increasing the current density, compared with lowering the feed flow rate, has a greater effect on the concentration overpotential gradient in the through-plane direction. Optimizing the electrolyte feed position in the through-plane direction is critical to minimize the concentration overpotential at high current densities.

Through simulations, it was found that the discrepancy between the electrode and the electrolyte conductivities leads to a significant concentration overpotential gradient at the electrodes; higher concentration overpotentials are observed at the surface between the electrode and the membrane. This is a consequence of the electronic conductivity of the bipolar plate and porous electrode being higher than the ionic conductivity of the electrolyte and the ion exchange membrane. Thus, the concentration overpotential is not only sensitive to the mass transfer mechanism. Also, the position of the inlet and outlet distribution channels should not be neglected when designing a vanadium redox flow cell with a conventional flow field. Simulations performed for geometries with different inlet/outlet channel positions suggest that the highest reduction in concentration overpotential is obtained when using higher advective fluxes near the membrane.

4.7. References

1. A.A. Shah, M.J. Watt-Smith, and F.C. Walsh, *A dynamic performance model for redox-flow batteries involving soluble species.* Electrochimica Acta, 2008. **53**(27): p. 8087-8100.
2. A.A. Shah, H. Al-Fetlawi, and F.C. Walsh, *Dynamic modelling of hydrogen evolution effects in the all-vanadium redox flow battery.* Electrochimica Acta, 2010. **55**(3): p. 1125-1139.
3. H. Al-Fetlawi, A.A. Shah, and F.C. Walsh, *Modelling the effects of oxygen evolution in the all-vanadium redox flow battery.* Electrochimica Acta, 2010. **55**(9): p. 3192-3205.
4. H. Al-Fetlawi, A.A. Shah, and F.C. Walsh, *Non-isothermal modelling of the all-vanadium redox flow battery.* Electrochimica Acta, 2009. **55**(1): p. 78-89.
5. K. Knehr, E. Agar, C. Dennison, A. Kalidindi, and E. C. Kumbur, *A Transient Vanadium Flow Battery Model Incorporating Vanadium Crossover and Water Transport through the Membrane.* Journal of The Electrochemical Society, 2012. **159**: p. A1446-A1459.
6. L. Hao, Y. Wang, and Y. He, *Modeling of Ion Crossover in an All-Vanadium Redox Flow Battery with the Interfacial Effect at Membrane/Electrode Interfaces.* Journal of The Electrochemical Society, 2019. **166**: p. A1310-A1322.
7. K. Oh, M. Moazzam, G. Gwak, and H. Ju, *Water crossover phenomena in all-vanadium redox flow batteries.* Electrochimica Acta, 2019. **297**: p. 101-111.
8. Q. Wang, Z.G. Qu, Z.Y. Jiang, and W.W. Yang, *Numerical study on vanadium redox flow battery performance with non-uniformly compressed electrode and serpentine flow field.* Applied Energy, 2018. **220**: p. 106-116.
9. B.W. Zhang, Y. Lei, B.F. Bai, and T.S. Zhao, *A two-dimensional model for the design of flow fields in vanadium redox flow batteries.* International Journal of Heat and Mass Transfer, 2019. **135**: p. 460-469.
10. M. Messaggi et al., *Analysis of flow field design on vanadium redox flow battery performance: Development of 3D computational fluid dynamic model and experimental validation.* Applied Energy, 2018. **228**: p. 1057-1070.
11. C. Yin, Y. Gao, G. Xie, T. Li, and H. Tang, *Three dimensional multi-physical modeling study of interdigitated flow field in porous electrode for vanadium redox flow battery.* Journal of Power Sources, 2019. **438**: p. 227023.

12. H. Ishitobi, J. Saito, S. Sugawara, K. Oba, and N. Nakagawa, *Visualized cell characteristics by a two-dimensional model of vanadium redox flow battery with interdigitated channel and thin active electrode.* Electrochimica Acta, 2019. **313**: p. 513-522.
13. Q. Zheng, F. Xing, X. Li, G. Ning, and H. Zhang, *Flow field design and optimization based on the mass transport polarization regulation in a flow-through type vanadium flow battery.* Journal of Power Sources, 2016. **324**: p. 402-411.
14. A. Tang, J. Bao, and M. Skyllas-Kazacos, *Studies on pressure losses and flow rate optimization in vanadium redox flow battery.* Journal of Power Sources, 2014. **248**: p. 154-162.
15. T. Wang, J. Fu, M. Zheng, and Z. Yu, *Dynamic control strategy for the electrolyte flow rate of vanadium redox flow batteries.* Applied Energy, 2018. **227**: p. 613-623.
16. F.T. Wandschneider et al., *Model of a vanadium redox flow battery with an anion exchange membrane and a Larminie-correction.* Journal of Power Sources, 2014. **272**: p. 436-447.
17. Y. Lorrain, G. Pourcelly, and C. Gavach, *Transport mechanism of sulfuric acid through an anion exchange membrane.* Desalination, 1997. **109**(3): p. 231-239.
18. R. Monteiro, J. Leirós, M. Boaventura, and A. Mendes, *Insights into all-vanadium redox flow battery: A case study on components and operational conditions.* Electrochimica Acta, 2018. **267**: p. 80-93.
19. D. You, H. Zhang, and J. Chen, *A simple model for the vanadium redox battery.* Electrochimica Acta, 2009. **54**(27): p. 6827-6836.
20. X. Yang, Q. Ye, P. Cheng, and T.S. Zhao, *Effects of the electric field on ion crossover in vanadium redox flow batteries.* Applied Energy, 2015. **145**: p. 306-319.
21. R. O'Hayre, S.-W. Cha, W. G. Colella, and F. B. Prinz, *Fuel Cell Fundamentals*. third ed. 2016: John Wiley & Sons.
22. R.F. Probstein, *Physicochemical Hydrodynamics*. second ed. 2005: Wiley-Interscience.
23. Y. Ashraf Gandomi, D. S. Aaron, T. A. Zawodzinski, and M.M. Mench, *In Situ Potential Distribution Measurement and Validated Model for All-Vanadium Redox Flow Battery.* Journal of The Electrochemical Society, 2016. **163**: p. 5188-5201.

24. E.L. Cussler, *Diffusion: Mass Transfer in Fluid Systems*. third ed. 2009, Cambridge: Cambridge University Press.
25. M.D.R. Kok et al., *Mass transfer in fibrous media with varying anisotropy for flow battery electrodes: Direct numerical simulations with 3D X-ray computed tomography.* Chemical Engineering Science, 2019. **196**: p. 104-115.
26. K.W. Knehr and E.C. Kumbur, *Open circuit voltage of vanadium redox flow batteries: Discrepancy between models and experiments.* Electrochemistry Communications, 2011. **13**(4): p. 342-345.
27. Y.Y. Choi, S. Kim, S. Kim, and J.-I. Choi, *Multiple parameter identification using genetic algorithm in vanadium redox flow batteries.* Journal of Power Sources, 2020. **450**: p. 227684.
28. J.L. Barton, J.D. Milshtein, J.J. Hinricher, and F.R. Brushett, *Quantifying the impact of viscosity on mass-transfer coefficients in redox flow batteries.* Journal of Power Sources, 2018. **399**: p. 133-143.
29. L. Wei, T.S. Zhao, Q. Xu, X.L. Zhou, and Z.H. Zhang, *In-situ investigation of hydrogen evolution behavior in vanadium redox flow batteries.* Applied Energy, 2017. **190**: p. 1112-1118.
30. C.-N. Sun, F.M. Delnick, L. Baggetto, G.M. Veith, and T.A. Zawodzinski, *Hydrogen evolution at the negative electrode of the all-vanadium redox flow batteries.* Journal of Power Sources, 2014. **248**: p. 560-564.
31. H. Liu, Q. Xu, C. Yan, and Y. Qiao, *Corrosion behavior of a positive graphite electrode in vanadium redox flow battery.* Electrochimica Acta, 2011. **56**(24): p. 8783-8790.
32. H. Lim, J.S. Yi, and D. Lee, *Operando studies on through-plane cell voltage losses in vanadium redox flow battery.* Journal of Power Sources, 2019. **422**: p. 65-72.
33. Y. Yang et al., *Investigations on physicochemical properties and electrochemical performance of sulfate-chloride mixed acid electrolyte for vanadium redox flow battery.* Journal of Power Sources, 2019. **434**: p. 226719.

Chapter 5

A parametric study for shunt current mitigation and stack design optimization

The content of this chapter is adapted from: N. M. Delgado, R. Monteiro, J. Cruz, A. Bentien, and A. Mendes, *Shunt currents in vanadium redox flow batteries – a parametric and optimization study.* Electrochimica Acta, 2021. **403**: p. 139667.

5. A parametric study for shunt current mitigation and stack design optimization

Equation Chapter (Next) Section 1

5.1. Abstract

Shunt currents can hinder the performance and reduce the lifespan of redox flow batteries. This work focuses on finding the best approach to mitigate the shunt currents in vanadium redox flow batteries. A 2D dynamic phenomenological model was used to compute the shunt currents as a function of the design and operating conditions of a stack with 6 cells and 16 cm^2 active area, operated at 80 mA cm^{-2}. In parallel, an equivalent circuit model was used to compute the same shunt currents but with a far smaller computing time. Finally, an artificial intelligence-based software was used to obtain a simple mathematical correlation that best fit the simulated shunt currents, as a function of the external resistances (manifold and distribution channels, from 0.08 Ω to 2621 Ω), operating current (from 4 A to 512 A) and the number of cells (from 5 to 40) in a stack. The correlation was then used to perform a sensitivity analysis to the previous parameters.

The results show that the shunt currents decrease with the internal resistances (activation, ohmic, and mass transfer). Nonetheless, the external resistances have the greatest impact on the shunt currents, particularly the manifold electrical resistance. Based on these findings, a novel redox flow battery stack design (343 cm^2 active area), with high manifold resistance and a low distribution channel resistance, is proposed to mitigate the shunt currents; cells with no electrochemical activity (dumping cells), evenly inserted into the stack, were considered to increase the manifold resistance. This new stack displays 23.6 % lower shunt current losses, 33 % lower pressure drop and 19 % higher nominal power output at 80 mA cm^{-2} when compared with a conventional stack.

5.2. Introduction

Shunt currents have been subject of study for many years. In 1976, Prokopius [1] suggested that shunt currents in flow batteries can be determined using an equivalent circuit model (ECM). This approach assumes that the shunt currents depend only on the cell potential, conductivity of the electrolyte, and geometry of the distribution channels and manifold. Later, other authors adopted the same approach and used an ECM to study the shunt currents in redox flow batteries [2] and fuel cells [3]. Few methodologies have been reported to measure shunt currents, such as using a magnetic amplifier to measure the magnetic field created by the shunt currents [4] and directly measure the potential drop [5] or the shunt current [6] in the manifolds. However, most studies found in the literature focus on the impact of the stack design and operating parameters in the shunt currents; Chen et al. [7] used an ECM to demonstrate that the shunt currents increase with the increasing state of charge (SoC) and with the increasing number of cells. Feng et al. [8] used a similar approach to show that the shunt current loss (SCL), relative to the cell current, decreases as the cell current increases. The influence of the shunt currents in the temperature of the stack during standby conditions has also been subject of study; Tang et al. [9] used a dynamic model to simulate shunt currents in a 40 cell-stack and found that 14% of the total heat generated in a stack is related to shunt currents. More recently, Trovò et al. [10] demonstrated that shunt currents may lead to temperature differences between cells of up to 10 ºC. Strategies to reduce shunt currents, such as optimizing the piping [11] and the electrical [12] system design, are reported in the literature. Other approaches include decreasing the electrolyte conductivity [13] or changing the geometry of the distribution channels [14] and manifold [8]; most stacks found in the literature [15-17] use long and narrow distribution channels and short distances between adjacent cells. However, there is a clear information gap in the literature regarding the impact of other factors, such as flow rate and physical and chemical properties of the internal components (electrolyte, electrode, and membrane), in the shunt currents. Also, these studies are carried out for specific stack designs which can lead to contradictory conclusions. For example, Yin et al. [13] concluded that the geometry of the manifold has a greater impact in the shunt currents than the flow channels. In opposition, Xing et al. [8] and Chen et al. [7] concluded that the flow channels are more relevant to minimize shunt currents.

This work aims at studying the impact of operating and design parameters, and physical and chemical properties of internal components, e.g., electronic conductivity and electrode surface area, in the shunt currents. Also, a novel strategy to reduce the shunt currents is presented. This study is based on the simulation of the shunt currents in VRFB stacks using a 2D dynamic phenomenological model (DPM) and an equivalent circuit model (ECM) for several stack configurations. The impact of the flow rate and physical and chemical properties of the internal components are studied using the DPM; shunt currents are simulated for different values of kinetic, ohmic and mass transfer related parameters. The ECM is used to simulate shunt currents for more than 20 000 combinations of values of external resistances (distribution channels and manifold geometry), operating current, and number of cells in a stack. A simple mathematical correlation relating the latter parameters with the relative shunt current losses was then obtained using an artificial intelligence (AI) based software (Eureqa, DataRobot, Inc.) in combination with the data from the ECM. The impact of the stack design and operating current in the shunt currents is studied by using the correlation to perform a sensitivity analysis. The sensitivity analysis includes a wide range of conditions to provide critical information regarding which parameters affect the SCL the most and how they scale with the SCL. Lastly, the ECM was used to benchmark several stack designs to reduce the shunt currents and the pressure drop and increase the stack nominal power output. A novel stack design including cells with no electrochemical activity – named dumping cells (dc) – is proposed. This work provides critical information to optimize the stack design by providing a pathway to minimize the SCL and the pressure drop and increase the stack nominal power output.

5.3. Redox flow cell stacks

5.3.1. 6 cells-stack

The six cells-stack (Figure 5.1) simulated in this work consists of a stack of six electrochemical cells. The design of each cell is described elsewhere [18]. Briefly, each redox flow cell comprises two graphite felts as electrodes (GFD 4.6 EA, SGL Group, Germany) with a compressed thickness of 3.5 mm (25 % compression) and an anion exchange membrane (FAP450, Fumatech, BWT AG, Germany). The latter has a lower cost and lower vanadium crossover rates than cation exchange membranes. The active area of the redox flow

cell is 4 cm × 4 cm. The vanadium electrolyte used consists of 1.6 M V^{3+}/V^{4+} 50:50 molar ratio in 2 M H_2SO_4 (GfE Metalle und Materialien GmbH, Germany). The stack design was adapted to a 2D geometry to reduce computational time; 1 mm thick bipolar plates and 3 mm thick current collectors were assumed. The shunt currents were only simulated for the positive half-cell. This is a conservative assumption since the positive electrolyte has a higher conductivity than the negative electrolyte (Table **Error! Use the Home tab to apply Título 6;ND Appendix Header 1 to the text that you want to appear here.**.3). The distribution channels and manifold dimensions (in mm) can be found in Figure 5.1.

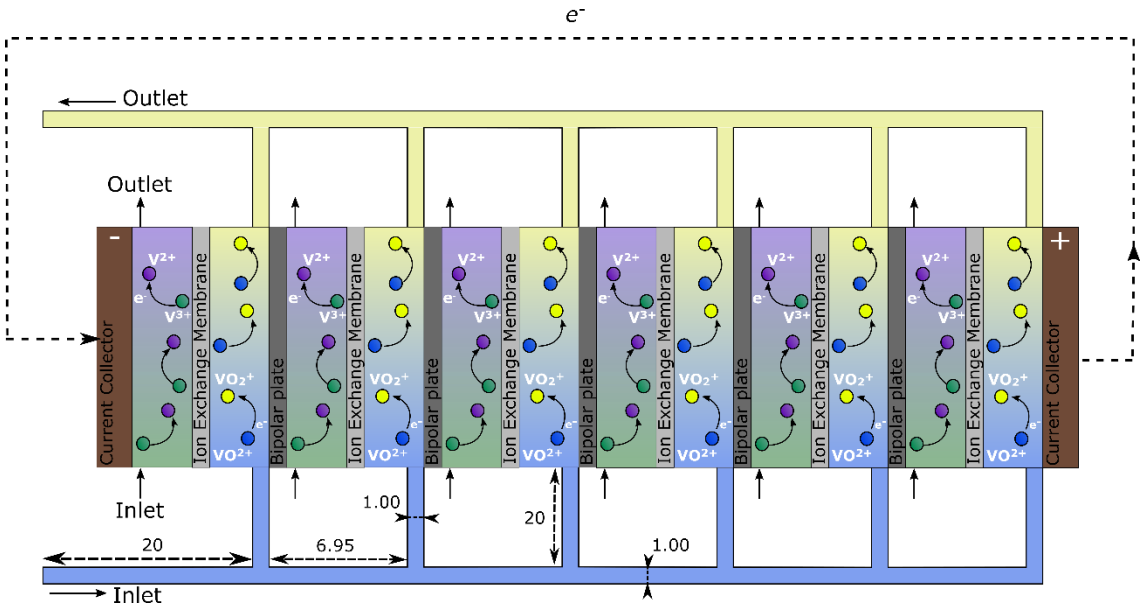

Figure 5.1 – Schematic representation of the vanadium redox flow stack while charging with six cells, and dimensions of the distribution channels and manifold (in mm).

5.3.2. *N* cells-stack

The *N* cells-stack comprises *N* cells electrically connected in series. The *N* cells-stack is used to study the influence of the distribution channels and manifold geometry, operating current, and number of cells on the shunt current intensity. Thus, different stack, distribution channels and manifold designs are considered and simulated.

5.3.3. 40 cells-stack equipped with dumping cells

A dumping cell (dc) consists of a cell that contains a flow channel, herein referred to as dumping cell channel, connecting feed and collecting streams from adjacent electrochemical cells – Figure 5.2.

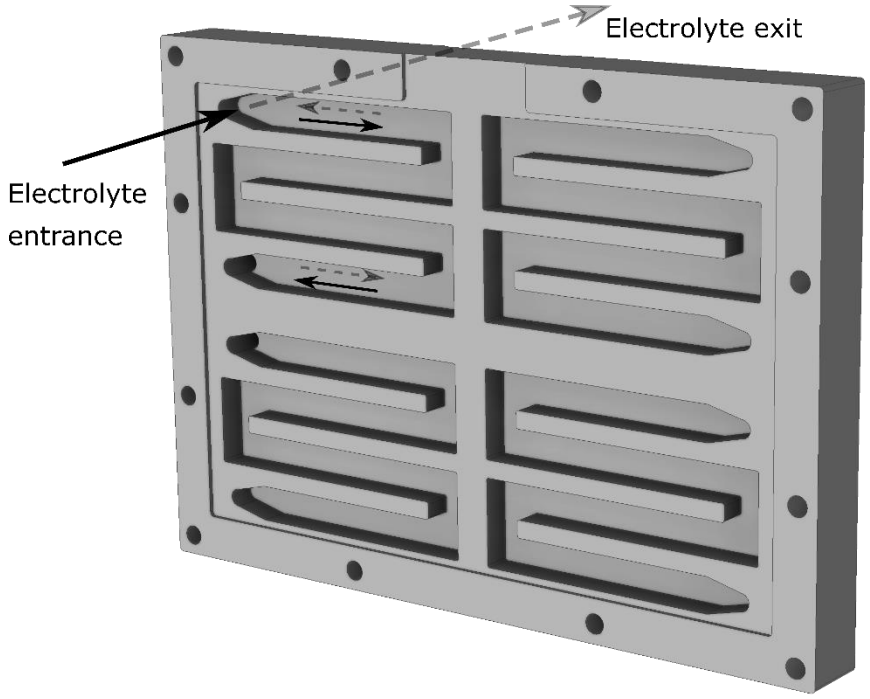

Figure 5.2 – 3D representation of a dumping cell. The electrolyte flow direction at the front (solid line) and back (dashed lined) of the dumping cell is represented by the arrows.

The dumping cell does not have any components that allow the electrochemical reactions to occur, nor does it have components to measure currents. Thus, it cannot be used to monitor shunt currents or the state of charge. The purpose of the dumping cell is to act as a manifold extension and, consequently, to dump shunt currents. The electrical connection between adjacent electrochemical cells can be established using electrically connected current collectors placed at the adjacent electrochemical cells. The 40 cells-stack equipped with M dumping cells can, thus, be described as follows: a stack of several N electrochemical cells-stacks with a dumping cell between two adjacent N cells-stacks. For example, a 40 cells-stack equipped with one dumping cell consists of two stacks comprising 20 electrochemical cells, and a dumping cell between these stacks.

Each electrochemical cell comprises similar internal components as the six cells stack. The flow frame has a height of 200 mm, a width of 300 mm and a thickness of 2 mm. Furthermore, each flow frame has two distribution channels (Figure 5.3), for feeding and collecting the electrolyte, with a width of 3 mm, a depth of 1.5 mm and a length of 27 mm (short frame channel, SFC, Figure 5.3 (a)) or 540 mm (long frame channel, LFC, Figure 5.3 (b)). Both distribution channel designs display low manufacturing complexity and a low pressure drop. Additionally, the LFC can reduce shunt currents. The distance from the manifold to the distribution channel | electrode interface, known as elevation, is 11.0 mm and 22.5 mm, respectively for the SFC and LFC. The distance between two adjacent electrochemical cells is 7.95 mm; the manifold has a total length of 318 mm (7.95 mm × 40 electrochemical cells) and a diameter of 8.00 mm.

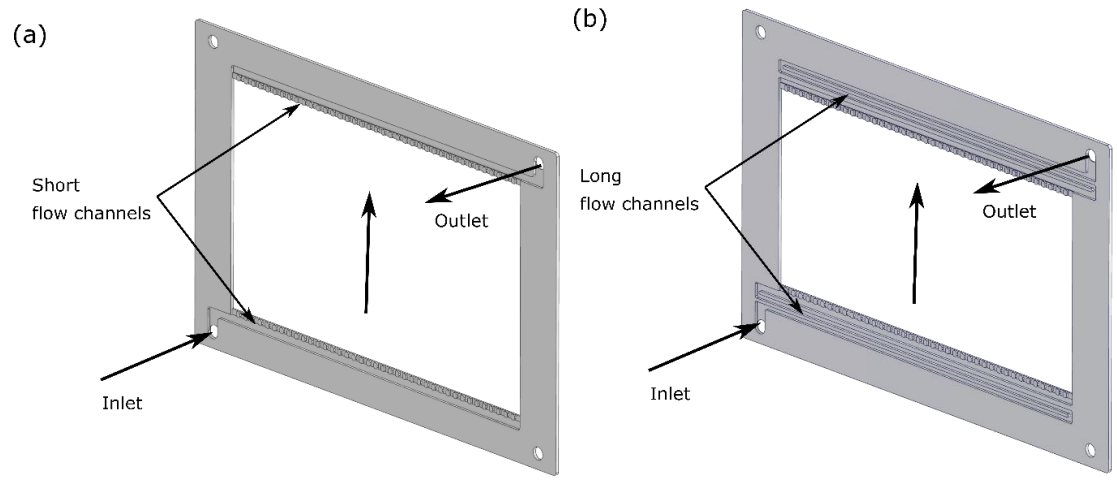

Figure 5.3 – Flow frame with (a) two short distribution channels (short frame channel, SFC) and (b) two long distribution channels (long frame channel, LFC).

The dumping cell has the same height and width as the flow frame. The area available to design the dumping cell channels is limited to less than half of the height (100 mm) and half of the width (150 mm) of the flow frames; the stack has four manifolds (two inlets and two outlets) and one dumping cell channel per manifold is required. Furthermore, the dumping cell should be designed such that the electrolyte flows on both sides of the dumping cell; the electrolyte is forced to flow through the dumping cell channels and a pass-through hole is used to ensure the electrolyte flows to the opposite side of the dumping cell (Figure 5.2). The

electrolyte entrance and exit are parallel to each other and at opposite sides of the dumping cell. Thus, it is not required to make modifications to the stack design. Different dimensions of the dumping cell channel are considered throughout this work.

The SCL and the pressure drop of the 40 cells-stack equipped with *M* dumping cells are compared to the results of a 40 cells-stack with no dumping cell. To minimize shunt currents, the latter has flow frames with long channels (Figure 5.3 (b)), contrarily to the stack equipped with *M* dumping cells which has flow frames with short channels (Figure 5.3 (a)). The remaining distribution channel and outer dimensions, as well as manifold dimensions, are the same as for the 40 cells-stack equipped with *M* dumping cells.

5.4. Numerical methods

5.4.1. Dynamic phenomenological model

The 2D dynamic phenomenological model (DPM) used to simulate shunt currents in a six cells-stack (Figure 5.1) is described and was validated with experimental data in our previous work (Chapter 4) [18]. The model considers the momentum (Eq. (5.1)) and mass (Eq. (5.2)) conservation equations and the Nernst-Planck equation (Eq. (5.3)) in the electrodes to describe the electrolyte flow and the transport of ions in the electrolyte, respectively.

$$\frac{\partial(\varepsilon\rho\vec{v})}{\partial t}+\nabla\cdot\left(\varepsilon\rho\vec{v}\vec{v}\right)=-\varepsilon\nabla p+\nabla\cdot\left(\varepsilon\mu\nabla\vec{v}\right)-\frac{\mu}{K_p}\vec{v} \tag{5.1}$$

$$\frac{\partial\varepsilon\rho}{\partial t}+\nabla\cdot\left(\varepsilon\rho\vec{v}\right)=0 \tag{5.2}$$

$$\frac{\partial\varepsilon c_i}{\partial t}+\nabla\cdot\left(c_i\vec{v}\right)-\nabla\cdot\left(D_i^{\text{eff}}\nabla c_i\right)-\nabla\cdot\left(\frac{z_i F D_i^{\text{eff}}}{RT}c_i\nabla\phi_{\text{e}}\right)=\pm\frac{\nu_i j}{nF} \tag{5.3}$$

where ε is the porosity of the electrode, ρ is the electrolyte density, $\vec{v}$ is the velocity of the electrolyte, p is the pressure, μ is the viscosity of the electrolyte, K_p is the permeability of the electrode [18], c_i, D_i^{eff}, z_i and ν_i are the molar concentration, the effective diffusion coefficient, the valence state and the stoichiometric number of species *i*, respectively, F is Faraday constant (96 485 C mol^{-1}), R is the ideal gas constant (8.314 J K^{-1} mol^{-1}), T is the

temperature (assumed 298.15 K), n is the number of electrons, ϕ_e is the potential in the liquid phase and j is the volumetric current density. The concentration of SO_4^{2-} was determined using the electroneutrality condition:

$$\sum_i z_i c_i = 0 \tag{5.4}$$

Charge conservation equations were used in the liquid (electrolyte and membrane) (Eq.(5.5)) and solid (electrodes, bipolar plates, and current collectors) (Eq. (5.6)) phases to simulate the electric current that arises due to the transport of electrons (solid phase) and ions (liquid phase).

$$-\nabla\cdot\left(\frac{RT}{F\sum_i z_i}\nabla\sigma_e\right)-\nabla\cdot\left(\sigma_e\nabla\phi_e\right)=+j \tag{5.5}$$

$$-\nabla\cdot\left(\sigma_s^{eff}\nabla\phi_s\right)=-j \tag{5.6}$$

where σ_e is the electrolyte/membrane conductivity, σ_s^{eff} is the effective conductivity of the electrode/bipolar plate/current collector and ϕ_s is the potential in the solid phase.

Shunt currents arise due to the transport of ions in the electrolyte, through the distribution channels and the manifold, which is promoted by a potential gradient. By implementing Eq. (5.3) and Eq. (5.5) in the distribution channels and manifolds, shunt currents can be simulated. The electric current flowing in the distribution channels and manifold can be determined by calculating the electric current in the y and x directions, respectively, as follows:

$$I_y=\left(-\sigma_e\frac{\partial\phi_e}{\partial y}-\frac{RT}{F\sum_i z_i}\frac{\partial\sigma_e}{\partial y}\right)\times A_{xz} \tag{5.7}$$

$$I_x=\left(-\sigma_e\frac{\partial\phi_e}{\partial x}-\frac{RT}{F\sum_i z_i}\frac{\partial\sigma_e}{\partial x}\right)\times A_{yz} \tag{5.8}$$

where $A_{xz/yz}$ is the area perpendicular to the electrolyte flow.

The electrochemical reaction that occurs at the electrodes was simulated using the Butler-Volmer equation (Eq. (5.9)).

$$j = aFc_{\text{red}}^{\alpha_{\text{red}}^i} c_{\text{ox}}^{\alpha_{\text{ox}}^i} \left(k_{\text{ox}}^i \left(\frac{c_{\text{red}}^{\text{s},i}}{c_{\text{red}}^i} \right) e^{\frac{\alpha_{\text{ox}}^i F \eta_{\text{act}}^i}{RT}} - k_{\text{red}}^i \left(\frac{c_{\text{ox}}^{\text{s},i}}{c_{\text{ox}}^i} \right) e^{\frac{-\alpha_{\text{red}}^i F \eta_{\text{act}}^i}{RT}} \right) \tag{5.9}$$

where a is the surface area of the electrode, α is the charge transfer coefficient and k is the reaction rate constant, ox and red subscripts refer to the vanadium species with highest (V^{5+} and V^{3+}) and lowest (V^{4+} and V^{2+}) oxidation state at electrode i and η_{act} is the activation overpotential [18].

The mass transfer mechanism was modelled assuming the transport of ions between the surface of the fibers of the electrodes and the bulk electrolyte described by a linear equation (Eq. (5.10) and Eq. (5.11)):

$$k_{m,\text{red}} \left(c_{\text{red}} - c_{\text{red}}^{\text{s}} \right) = \frac{j}{aF} \tag{5.10}$$

$$k_{m,\text{ox}} \left(c_{\text{ox}} - c_{\text{ox}}^{\text{s}} \right) = -\frac{j}{aF} \tag{5.11}$$

where k_m is the mass transfer coefficient [18] and the superscript s refers to the surface of the fibers of the electrode. Further details regarding the parameters used in this work can be found in Appendix B.1.

Boundary and initial conditions

The galvanostatic operating mode was simulated applying the Neumann type of boundary condition for the potential in the solid phase, and setting it equal to the operating current (Eq. (5.12)), at the positive current collector.

$$-\vec{n} \cdot \nabla \cdot \left(\sigma_{\text{s}}^{\text{eff}} \nabla \phi_{\text{s}} \right) = i \tag{5.12}$$

The negative current collector was assumed to be the reference electrode and the potential in the solid phase was set to 0. The species concentration at the inlet, under dynamic conditions, was determined from a mass balance on the tanks (Eq.(5.13)).

$$\frac{\mathrm{d}c_{\mathrm{in},i}(t)}{\mathrm{d}t} = \frac{1}{V_{\mathrm{tank}}}\left(\int \vec{v}_{\mathrm{out}} c_{\mathrm{out},i} dA_{\mathrm{c,out}} - \int \vec{v}_{\mathrm{in}} c_{\mathrm{in},i} dA_{\mathrm{c,in}}\right) \tag{5.13}$$

where the subscripts in and out refer to the inlet and outlet boundary conditions, V_{tank} is the electrolyte volume for each side of the RFB and t is the instant t.

At the inlets of the negative electrodes and positive manifold, the following boundary condition can be used to simulate the flow of the electrolyte at a given flow rate Q:

$$-\vec{n}\cdot\vec{v} = \frac{Q_{\mathrm{in}}}{A_{\mathrm{c,in}}} N \tag{5.14}$$

where N is the number of cells, which is equal to six for the inlet at the positive manifold and equal to one for the inlets at the negative electrodes; the negative side does not have a common manifold. At the outlets, the pressure was set equal to the atmospheric pressure.

Eq. (5.5) and Eq. (5.6) were solved for all zones using a single domain approach. Eq. (5.1) - (5.3) were solved only in the electrodes and the following boundary conditions were used at the bipolar plate | electrode and membrane | electrode interfaces:

$$\vec{n}\cdot\vec{N}_i = 0 \tag{5.15}$$

where $\vec{N}_i$ is the molar flux of species i. The equations used to determine the initial species concentrations can be found in [18]. To accelerate convergency, different initial guess values were provided to the potential in the solid and liquid phases of each negative (Eq. (5.16) and Eq. (5.17)) and positive (Eq. (5.18) and Eq. (5.19)) half-cells, manifold and distribution channels (Eq. (5.19)). The potential in the liquid phase at the ion exchange membrane is $(\phi_{\mathrm{e}}^{+}+\phi_{\mathrm{e}}^{-})/2$. The negative electrode is used as reference electrode in each cell and, thus, the potential in the solid phase is set equal to the potential of the positive electrode from the previous cell. At the positive electrode, the total potential at each cell is assumed for the

potential in the solid phase. The potential in the liquid phase is determined for the case where the activation overpotential is 0 at both electrodes.

$$\phi_s^- = \left(E^+ - E^- + \eta_{ini}\right)\cdot\left(N-1\right) \tag{5.16}$$

$$\phi_e^- = \phi_s^- - E^- \tag{5.17}$$

$$\phi_s^+ = \left(E^+ - E^- + \eta_{ini}\right)\cdot N \tag{5.18}$$

$$\phi_e^+ = \phi_s^+ - E^+ \tag{5.19}$$

where E^+ and E^- are the cell reaction potential, in the absence of current (OCV), of the positive (Eq. (5.20)) and negative (Eq. (5.21)) half-cells, respectively, and η_{ini} is the initial guess for the overpotential.

$$E^+ = E^{0,+} + \frac{RT}{F}\ln\left(\frac{c_{VO_2^+}\left(c_{H^+}\right)^2}{c_{VO^{2+}}}\right) \tag{5.20}$$

$$E^- = E^{0,-} + \frac{RT}{F}\ln\left(\frac{c_{V^{3+}}}{c_{V^{2+}}}\right) \tag{5.21}$$

where $E^{0,+}$ and $E^{0,-}$ are the standard cell reaction potential in the positive and negative half-cells.

Numerical procedure

The mathematical model was implemented in Ansys Fluent 19.2. The mass and momentum equations were solved using the built-in PISO algorithm. The remaining partial differential equations were implemented using user-defined scalars, through a custom script, and were solved with the second order upwind discretization method. The boundary conditions were implemented using pre-defined macros provided by Ansys, Inc. The remaining equations were also implemented in the custom script using user-defined memory macros. Convergency issues were solved using under-relaxations factors for species and

charge transport equations. The domain of the six cell-stack consisted of ten zones. The mesh had a total of 80 200 quadrilateral elements. The stop condition criteria consisted in having residual values, for all governing equations, lower than 10^{-6} and the value of Eq. (5.9) changing by no more than 10^{-1} A m^{-3}.

5.4.2. Equivalent circuit model

The equivalent circuit model (ECM) was developed following the assumptions below:

- Negligible membrane crossover;
- Negligible side reactions;
- Isothermal behavior;
- Negligible electrolyte flow effect in the shunt currents;
- Negligible kinetic and mass transfer resistances;
- Each cell is well described by an open circuit potential and a resistor.

The ECM uses Simscape blocks, included in the Simulink®/MATLAB® software, to create a circuit model with ohmic resistances in parallel and in series connected to potential sources (E_{OCP}) and to a current source (I) (Figure 5.4). The internal cell ohmic resistances, R_{cell}, are connected in series to each other and to the potential sources while most of the external resistances (channels, R_c, and manifold, R_m) are connected in parallel to each other and to the internal resistances. The resistance of the distribution channels was determined as follows:

$$R_c = \frac{1}{\sigma_e}\frac{\ell_c}{A_c} \tag{5.22}$$

where ℓ_c and A_c are the length and area of the distribution channel. The manifold resistance is determined using the distance between two adjacent cells, ℓ_m, and the area perpendicular to the flow of the electrolyte, A_m:

$$R_m = \frac{1}{\sigma_e}\frac{\ell_m}{A_m} \tag{5.23}$$

The internal ohmic resistance of each electrochemical cell can be determined taking into consideration the ohmic resistances of the membrane (mem), electrolytes (e), electrodes, and bipolar plate (BP):

$$R_{\text{cell},i} = \frac{1}{\sigma_{\text{mem}}}\frac{\delta_{\text{mem}}}{A} + \frac{1}{\sigma_{\text{e}}^{+}}\frac{\delta_{\text{electrode}}}{A} + \frac{1}{\sigma_{\text{e}}^{-}}\frac{\delta_{\text{electrode}}}{A} + 2\frac{1}{\sigma_{\text{s}}}\frac{\delta_{\text{electrode}}}{A} + \frac{1}{\sigma_{\text{BP}}}\frac{\delta_{\text{BP}}}{A} \tag{5.24}$$

where δ_i is the thickness of the component and A is the active area of the stack. The resistance of the current collector (cc) can be determined using the following equation:

$$R_{\text{cc}} = \frac{1}{\sigma_{\text{cc}}}\frac{\delta_{\text{cc}}}{A} \tag{5.25}$$

The open circuit potential (OCP) of each cell, E_{OCP}, was determined using Eq. (5.26).

$$E_{\text{OCP}} = E^{+} - E^{-} \tag{5.26}$$

Figure 5.4 (a) and (b) show the schematic representation of the ECM used for the six cells-stack and N cells-stack, respectively. Figure 5.4 (c) shows the schematic representation of the ECM used for the 40 cells-stack with one dumping cell.

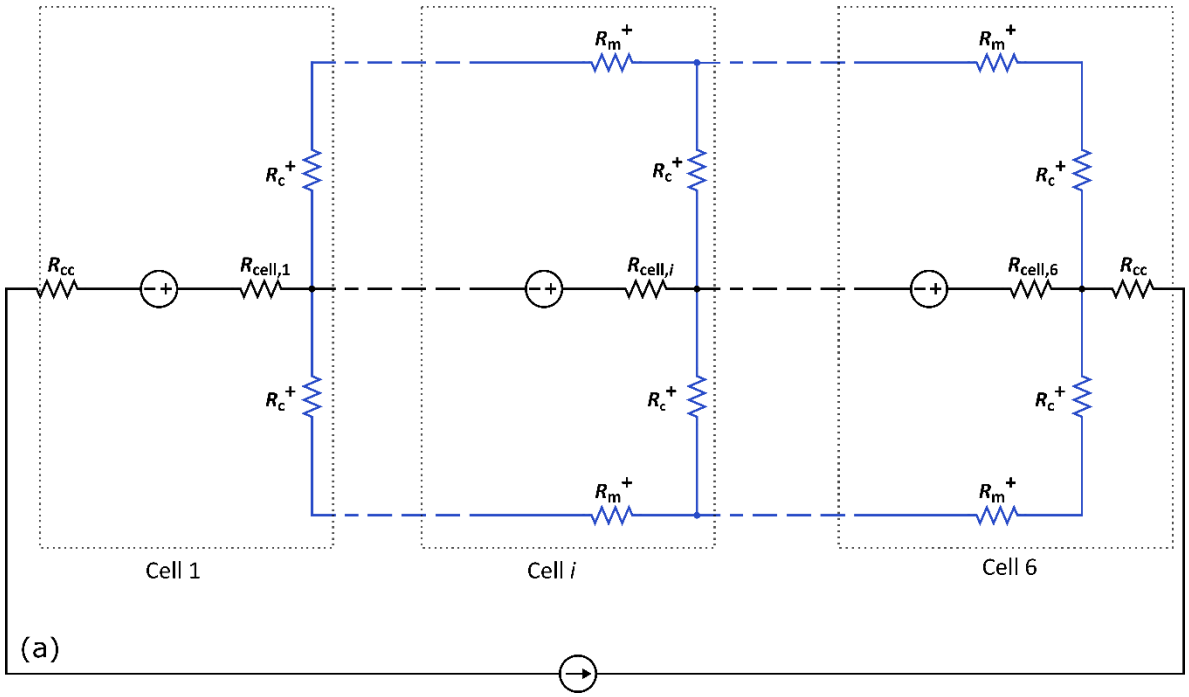

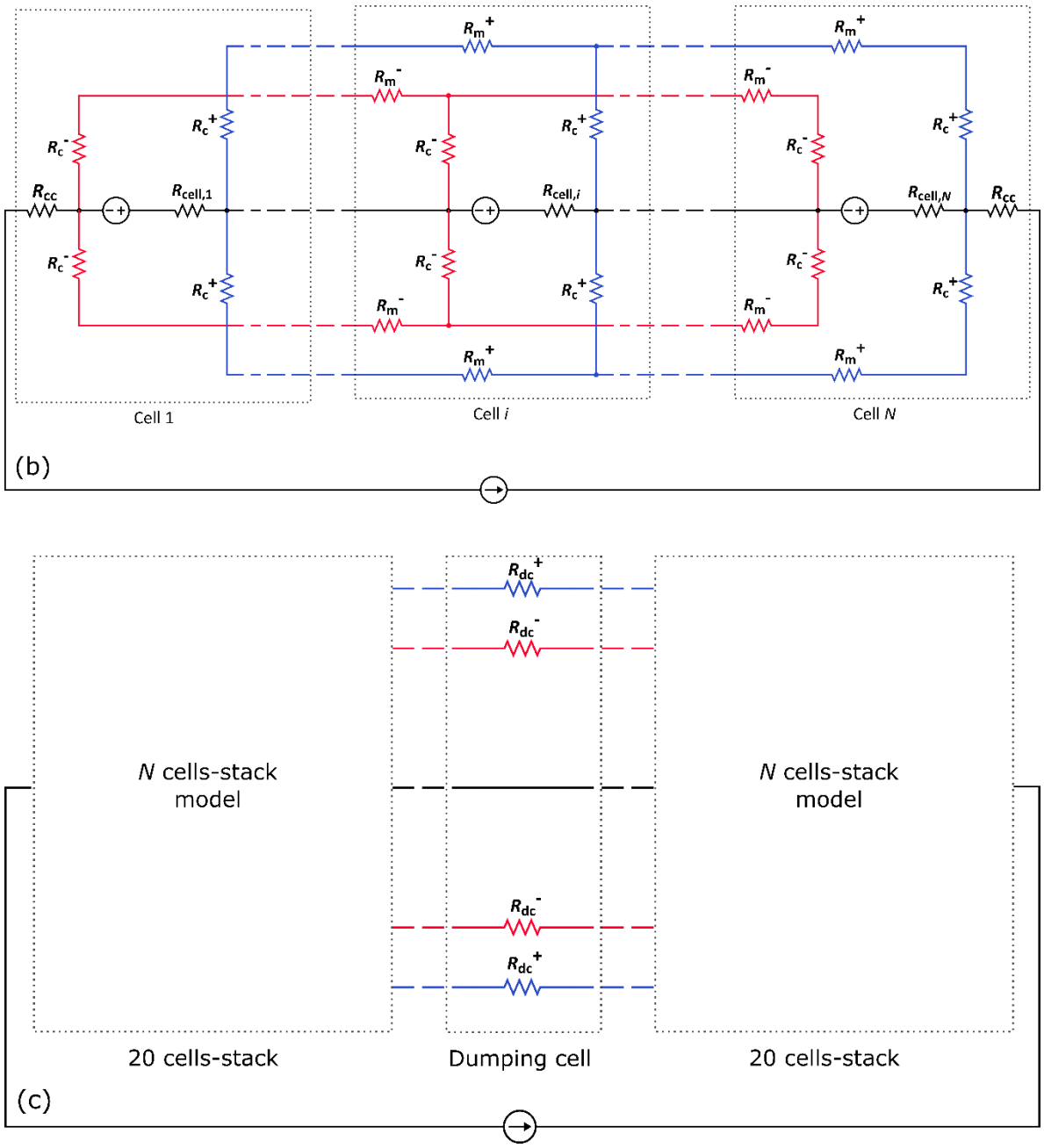

Figure 5.4 – Schematic representation of the equivalent circuit model used to simulate shunt currents in the (a) positive side of a six cell VRFB stack, (b) VRFB stack with N cells and (c) VRFB stack with 40 cells (2×20 cells-stack) and one dumping cell. $R_{\text{cell},i}$ is the cell internal resistance of cell i, R_{cc} is the resistance of the current collector and R_{dc} is the resistance of the dumping cell. The c and m refer to the distribution channels and manifold, respectively, and the superscripts + and – refer to the positive and negative side, respectively.

In the equivalent circuit of the six cells-stack (Figure 5.4 (a)), the electrical resistance of the distribution channels and manifold of the negative side was not simulated. The circuit model for the *N* cell-stack (Figure 5.4 (b)) considers the electrical resistances of the inlet and outlet manifold and distribution channels for both positive and negative sides, as typically described in the literature [10]. The models shown in Figure 5.4 (a) and Figure 5.4 (b) can be divided into three different sections: first cell, middle cell *i*, which is repeated *N*-2 times, and last cell *N*. The shunt currents in a 40 cell-stack equipped with *M* dumping cells (Figure 5.4 (c)) is simulated using the *N* cell-stack model. Additionally, a resistor is added after each *N* cell-stack in parallel with the manifold resistance to simulate the resistance of the dumping cell (dc) to shunt currents. The latter was calculated using the following equation:

$$R_{\mathrm{dc}} = \frac{1}{\sigma_{\mathrm{e}}} \frac{\ell_{\mathrm{dc}}}{A_{\mathrm{dc}}} \tag{5.27}$$

where ℓ_{dc} and A_{dc} are the length and area of the dumping cell channels.

5.4.3. Mathematical correlation and sensitivity analysis

The determination of the mathematical correlation and the sensitivity analysis were carried out using the Eureqa software (Nutonian, Inc.). This software uses symbolic regression to automatically generate sets of symbolic equations that relate the independent variables with the dependent variable while minimizing the error between the supplied and the simulated data. This is accomplished by simultaneously searching for parameters and mathematical equations and optimizing the fitting criteria of the mathematical equations with a given dataset. Further reading is suggested for more information regarding the software [19] and symbolic regression [20, 21]. Thus, the dataset obtained for the *N* cells-stack can be provided to this software to generate a correlation that relates the relative shunt current losses (SCL) with the external cell resistances, operating current, and number of cells in a stack (Eq. (5.28)).

$$\mathrm{SCL}(\%) = f(R_{\mathrm{m}}, R_{\mathrm{c}}, I, N) \tag{5.28}$$

The relative SCL defines the total current efficiency lost in the stack due to shunt currents. It is determined by comparing the electric current generated by the electrochemical reaction

at the charging and discharging steps (Eq. (5.29)). Charge loss due to crossover of vanadium ions is not simulated.

$$\mathrm{SCL}(\%) = \left(1 - \frac{\sum_{i=1}^{N} I_{\mathrm{charge},i}}{\sum_{i=1}^{N} I_{\mathrm{discharge},i}} \right) \times 100 \tag{5.29}$$

where I_i is the average current in the electrodes of the cell i. The dataset is generated running the ECM for a large number of design and operating conditions. The design parameters were changed as shown in Table 5.1, except for N which assumes values of 5, 10, 20, 30, and 40 cells.

Table 5.1 – Design (manifold resistance, R_m and distribution channel resistance, R_c) and operating parameters (electric current, I) used in the equivalent circuit model to simulate shunt currents. The number of cells (N) used in the simulations is 5, 10, 20, 30, and 40.

Value	**R_m (for each R_c)**	**R_c (for each I)**	**I (for each N)**
Minimum	0.08 Ω	0.08 Ω	4 A
Maximum	2621 Ω	2621 Ω	512 A
Increment	$x_{i+1} = 2\ x_i$		

The simulations were carried out for the charging (I) and discharging ($-I$) steps so that the SCL can be determined (Eq. (5.29)). Thus, a total of 10 240 data points were obtained from a total of 20 480 combinations of simulated conditions. Conversely to what is found in conventional stack designs, higher manifold resistances are considered in this study. The goal is to study the viability of using long manifolds to reduce SCL. The fitting criteria consisted in minimizing the logarithm squashed error since the dataset contained large outliers (e.g., when SCL > 20 %).

The sensitivity analysis was carried out using the correlation obtained in this work to determine the relative impact of each variable in the relative SCL through a first order derivative-based method:

$$\mathrm{SI} = \overline{\left|\frac{\partial \mathrm{SCL}}{\partial x}\right|} \frac{s_x}{s_{\mathrm{SCL}}} \tag{5.30}$$

where SI is the sensitivity index (SI), x is the input variable (R_m, R_c, I or N) and s_x is the standard deviation of x (Eq. (5.31)).

$$s_x = \sqrt{\frac{1}{n}\sum_{i=1}^{n}\left(x_i - \bar{x}\right)^2} \tag{5.31}$$

where $\bar{x}$ is the average value of x. The standard deviations of x and SCL were used in Eq. (5.30) to uniformize the scale and units. The mathematical meaning of the sensitivity index can be explained as follows: on average, if x is changed by a value of s_x, then the shunt current losses will change by a value of $\mathrm{SI}\cdot s_{\mathrm{SCL}}$. Thus, the greater the average rate of change $\bar{m}$ (Eq. (5.32)), the greater the impact that x has, on average, in the SCL:

$$\partial\bar{y} = \bar{m}\cdot\partial\bar{x} \longrightarrow \partial\overline{\mathrm{SCL}} = \frac{\mathrm{SI}\cdot s_{\mathrm{SCL}}}{s_x}\cdot\partial\bar{x} \xrightarrow{\partial\bar{x}=s_x} \partial\overline{\mathrm{SCL}} = \mathrm{SI}\cdot s_{\mathrm{SCL}} \tag{5.32}$$

5.4.4. Pressure drop

To minimize shunt currents, the geometric ratio between the length and the cross-sectional area (l/A) of the distribution channels and manifold must be maximized (Eq. (5.22) and Eq. (5.23)). However, the pressure drop in such conveyances increases with the increasing l/A ratio. High pressure drop values increase pump energy consumption, can produce early leaks, and accelerate stack degradation.

The pressure drop caused by the electrolyte flow through the porous carbon felt electrode ($\Delta p_{\mathrm{electrode}}$) was obtained using the Darcy's law and by considering the pressure drop gain/loss due to gravity (Eq. (5.33)):

$$\Delta p_{\mathrm{electrode}} = \frac{\mu v}{K_p} l + \rho g \Delta y \tag{5.33}$$

where l is the length of the electrode, g is the gravitational acceleration (9.81 $m^2\ s^{-1}$) and Δy is the elevation, which assumes a positive value when the ending point of flow (outlet) is above the starting point of flow (inlet) and a negative value when the opposite is observed.

The pressure drop (Δp) in the remaining flow conveyances (distribution channels, manifolds, and dumping cells) was determined using the Darcy-Weisbach equation where gravity was also taken into account (Eq. (5.34)).

$$\Delta p = f_D \frac{l}{D_{eq}} \frac{\rho v^2}{2} + \rho g \Delta y \tag{5.34}$$

where l is the length of the flow conveyance. The friction factor f_D and the equivalent diameter of a rectangular flow conveyance, D_{eq}, were determined using Eq. (5.35) [22] and Eq. (5.36) [23], respectively:

$$f_D = \left(\frac{64}{\mathrm{Re}}\right)^a \left[0.75 \ln\left(\frac{\mathrm{Re}}{5.37}\right)\right]^{2(a-1)b} \left[0.88 \ln\left(6.82 \frac{D_{eq}}{k_r}\right)\right]^{2(a-1)(1-b)} \tag{5.35}$$

$$D_{eq} = 1.3 \frac{\left(W \cdot \delta_{\downarrow}\right)^{0.625}}{\left(W + \delta_{\downarrow}\right)^{0.25}} \tag{5.36}$$

where k_r is the surface absolute roughness (assumed 2.5 x 10^{-6} m for plastic [24]) and W and $\delta\downarrow$ are the width and depth of the rectangular flow conveyance, respectively. The parameters a and b and the Reynolds number can be determined using the following equations [22]:

$$a = \frac{1}{1 + \left(\frac{\mathrm{Re}}{2712}\right)^{8.4}} \tag{5.37}$$

$$b = \frac{1}{1 + \left(\frac{\mathrm{Re}}{150 \frac{D_{eq}}{k_r}}\right)^{1.8}} \tag{5.38}$$

$$\mathrm{Re} = \frac{\rho D_{eq} v}{\mu} \tag{5.39}$$

5.5. Results and discussion

5.5.1. Model comparison

The dynamic phenomenological model (DPM) and the equivalent circuit model (ECM) employ different methodologies to simulate the shunt currents. The DPM uses several complex equations solved in multi-dimensional meshes while the ECM uses mostly Ohm's and Kirchhoff laws. A comparison between both models is required to understand the implications of using each model to study the shunt currents.

Figure 5.5 shows the simulated shunt currents in the manifold and distribution channels and the cumulative cell potential of the six cells-stack (Figure 5.1) using the DPM and the ECM, and the relative difference between models. The shunt currents were simulated at 50 % SoC, for the charging step, and with a current density of 80 mA cm^{-2}. The simulation data can be found in Appendix B.2.

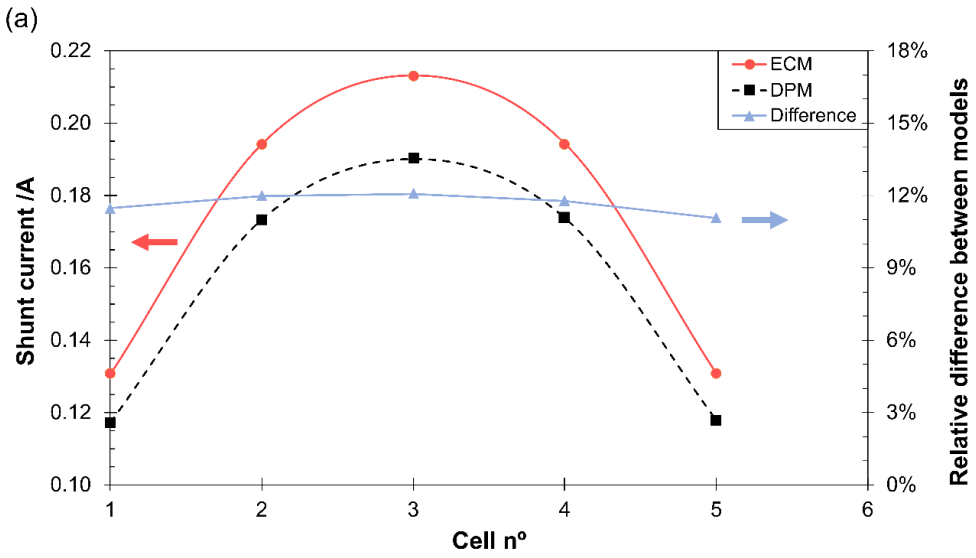

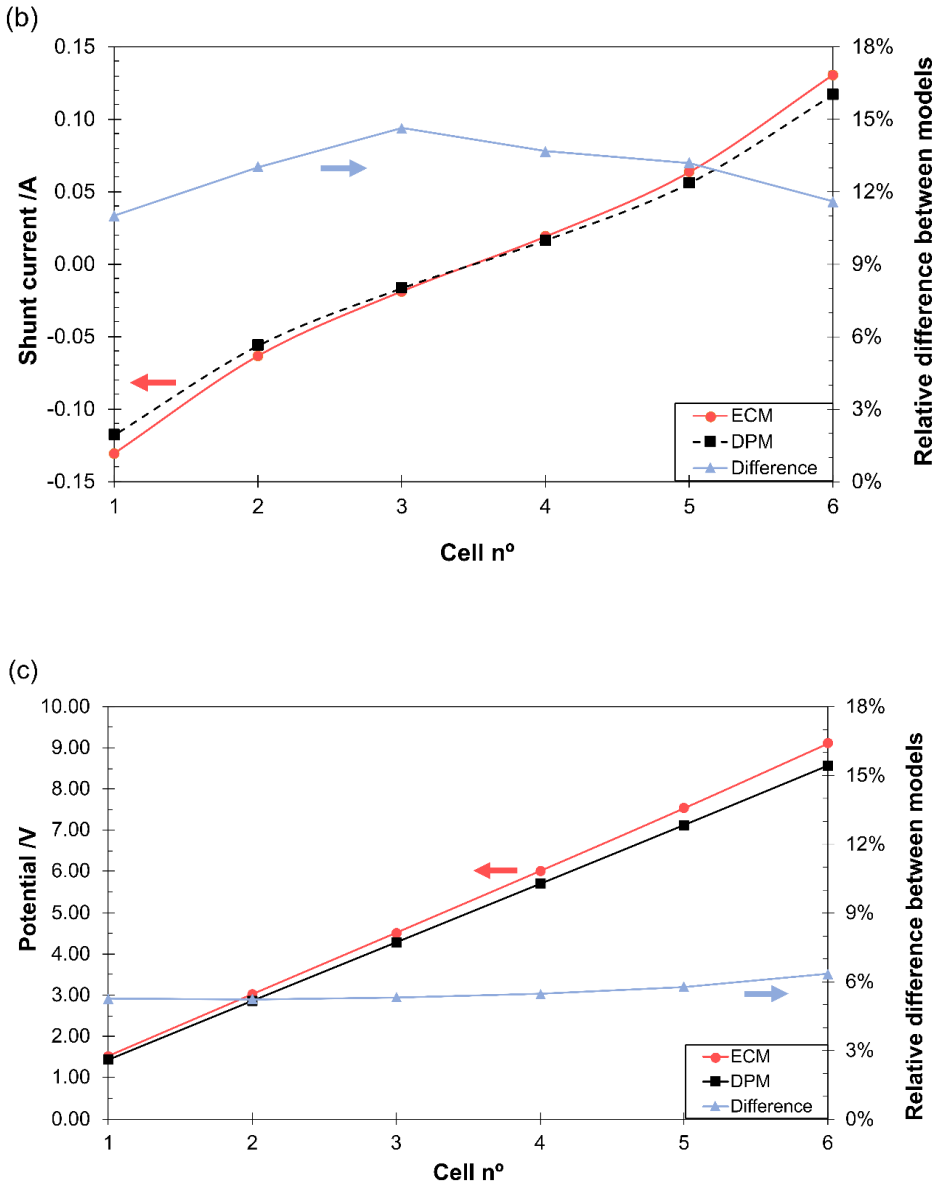

Figure 5.5 – Shunt currents in the (a) manifold and (b) distribution channels and (c) cumulative cell potential of a VRFB six cells-stack simulated using the dynamic phenomenological model (DPM, black squares) and the equivalent circuit model (ECM, red circles) for charging step, and the relative difference between models (blue triangles).

The results show that there is an average relative difference between the shunt currents determined using both models of 11.7 % and 12.8 % in the manifold (Figure 5.5 (a)) and distribution channels (Figure 5.5 (b)), respectively. Such difference was assigned to the

oversimplification of the ECM, which led to an overestimation of the cell potentials (Figure 5.5 (c)). The errors of the DPM model were minimized by using an optimized mesh (Figure **Error! Use the Home tab to apply Título 6;ND Appendix Header 1 to the text that you want to appear here.**.1), a timestep of 10^{-3} s, and strict convergency criteria. The ECM was solved using the Kirchhoff law which results in a set of linear algebraic equations [25]; the solution algorithm of the ECM does not introduce significant numerical errors. The ECM does not simulate the electrochemical reactions, which include the reaction kinetics and the charge separation at the electrolyte | electrode interface – double layer capacitance effect [26]; the ECM is a steady state model, and capacitances are dynamic resistances that can only be simulated at unsteady state. Thus, the ECM assumes that the cell overpotential is only generated by the ohmic resistances. The electrochemical reaction is typically modelled in ECMs using a capacitor (dynamic resistance) in parallel with a resistor (ohmic resistance) [27]. The overpotential generated by the kinetic resistance is much lower than the overpotential generated by the ohmic resistance [28]. Thus, a lower potential difference between the first and last cell of the stack - the driving force of shunt currents - is obtained when the electrochemical reaction simulation is included in the ECM. Consequently, the shunt currents simulated by the ECM become lower.

The DPM should produce more realistic shunt current values since it simulates the electrochemical reaction. The difference between the models results becomes larger with the increasing number of cells; the stacks are electrically connected in series and the source of this difference is caused by the assumptions of the equivalent circuit model that is used to simulate the internal resistances of each cell – the results difference is additive. However, the downside of the DPM is that it is extremely time-consuming compared to the ECM, particularly when it is required to simulate stacks with high number of cells and complex distribution channel designs. For example, the DPM required 60 hours to simulate the six cells stack (2D mesh with 80 000 elements), while the ECM required less than 30 seconds in a computer equipped with an i9-9900K processor and 32 GB RAM. The simulation time difference becomes even greater as the number of cells increases. Furthermore, the ECM overestimates the shunt currents; the real stacks will perform better than predicted by the model. The ECM can be considered an acceptable alternative when simulating shunt currents

in a stack with many cells or complex distribution channel designs because the simulation time is greatly reduced.

5.5.2. Effect of the internal resistances in the shunt currents

The shunt currents were studied as a function of the cell internal resistances, as indicated in Figure 5.6. Parameters related to a) reaction rate – reaction rate constant, k; b) charge transport – membrane, σ_{mem}, electrode, σ_s, and electrolyte, σ_e, conductivities; and c) mass transfer – surface area, a, and mass transfer coefficient, k_m were considered. The parameters a, k, σ_{mem}, σ_s and k_m were increased tenfold and σ_e was increased fivefold, compared with the simulation results using the reference parameter values (baseline simulation results, BL, Appendix B.1). The flow rate, Q, and the thickness of the electrode, δ_{elec}, were also studied since they affect the mass transfer and the ohmic resistances, respectively. The flow rate was decreased tenfold and the electrode thickness was decreased from 3.45 mm to 2.00 mm. An SoC of 50 % and a current density of 80 mA cm^{-2} were used in the simulations, which were carried out for the charging step.

In general, the shunt currents in the distribution channels (Table **Error! Use the Home tab to apply Título 6;ND Appendix Header 1 to the text that you want to appear here.**.6) and in the manifold (Table **Error! Use the Home tab to apply Título 6;ND Appendix Header 1 to the text that you want to appear here.**.7) are slightly affected by the internal resistances; when the internal resistances decrease, the shunt currents also decrease (Figure 5.6).

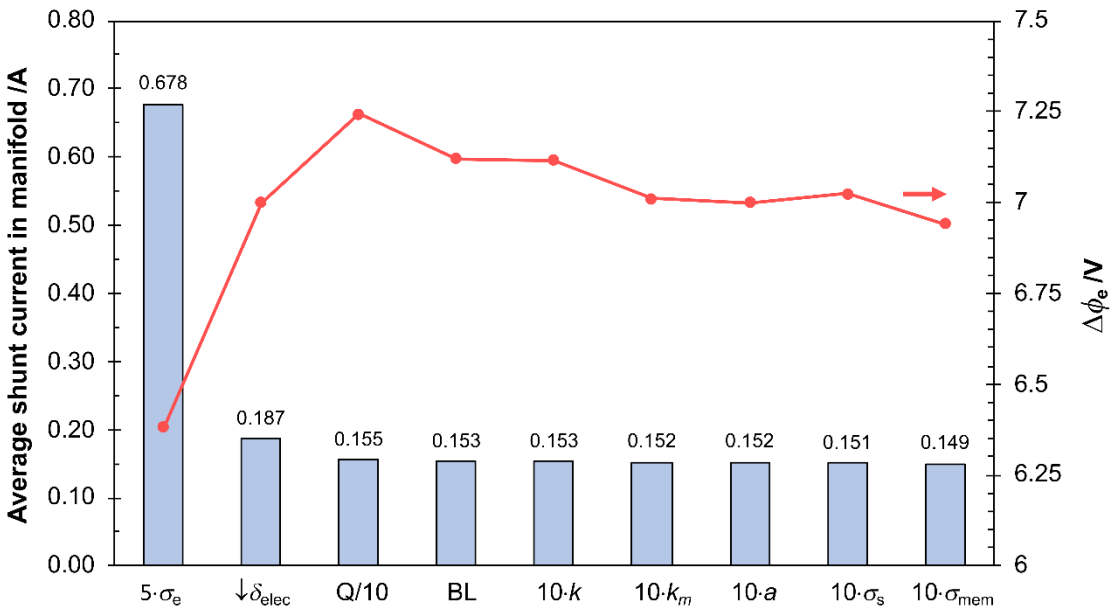

Figure 5.6 – Average shunt current in the manifold and potential drop, $\Delta\phi_e$, in a VRFB six cells-stack simulated using the dynamic phenomenological model (DPM) and reference parameters (baseline simulation - BL), tenfold higher surface area, a, reaction rate constant, k, membrane, σ_{mem}, and electrode, σ_s, conductivities, and mass transfer coefficient, k_m, fivefold higher electrolyte conductivity, σ_e, tenfold lower flow rate, Q, and a lower electrode thickness (2.0 mm), δ_{elec}.

As the results indicate, increasing σ_{mem} and σ_s leads to the highest reduction of the average shunt current in the manifolds (by 4 mA and 2 mA, respectively) followed by a and k_m increase which provided an average shunt current reduction of 1 mA relative to the baseline simulation. Increasing k had the lowest impact in the shunt currents, with an average shunt current reduction of 0.1 mA. This trend is consistent with the contribution of each internal resistance on the potential difference between the first and last cells of the stack (potential drop, $\Delta\phi_e$); the charge transport resistances display the highest effect on the shunt currents, followed by the mass transfer and reaction kinetic resistances [28]. Such potential drop is the driving force of the shunt currents. When the potential drop is decreased (e.g., by decreasing internal resistances), the shunt currents decrease (Figure 5.6). For example, the potential drop

was reduced from 7.1 V to 6.9 V when σ_{mem} was increased tenfold. As result, the average shunt current in the manifold was reduced by 2.5 %.

The internal resistances decrease when σ_e is increased or δ_{elec} is decreased; shunt currents should have also decreased since the charge transport resistance and, consequently, the potential drop decrease. Nonetheless, this was not observed (Figure 5.6). Shunt currents arise from the transport of ions through the distribution channels and manifold. Thus, shunt currents increase when such transport is facilitated. When σ_e is increased, the mobility of ions in the electrolyte is increased and the transport of ions is facilitated. The resistance to the transport of ions through the manifold was also decreased when δ_{elec} was decreased since the distance between two adjacent cells was shortened. Nevertheless, when δ_{elec} is decreased without modifying the manifold dimensions, shunt currents also decrease; the bipolar plate thickness can be increased to compensate for the δ_{elec} decrease. Seems clear that the shunt currents increase due to increased ionic flux in the distribution channels and manifold is greater than the shunt currents decrease due to the reduction of $\Delta\phi_e$; the external resistances have a greater impact in the shunt currents than the internal resistances.

5.5.3. Effect of R_m, R_c, N, and I in the shunt currents

The effect of the external resistances (R_c and R_m) in the shunt currents is addressed in this section aiming to optimize the stack design. The operating current, I, and number of cells in a stack, N, are also included in this section since both affect the shunt currents [8, 13]. This study is carried out using the ECM for a stack with N cells (Figure 5.4 (b)) at a fixed SoC (50 %) for both the charging and discharging steps. The internal resistance of each cell is assumed constant (0.0045 Ω, Eq. (5.24)) since it has a very low impact on the shunt currents. Data with no physical meaning, e.g., SCL > 100 %, were excluded.

The shunt current losses (SCL) determined using the different combinations of R_m, R_c, I and N ranged between 5.0 x 10^{-4} % and 99.9 % (Figure 5.7).

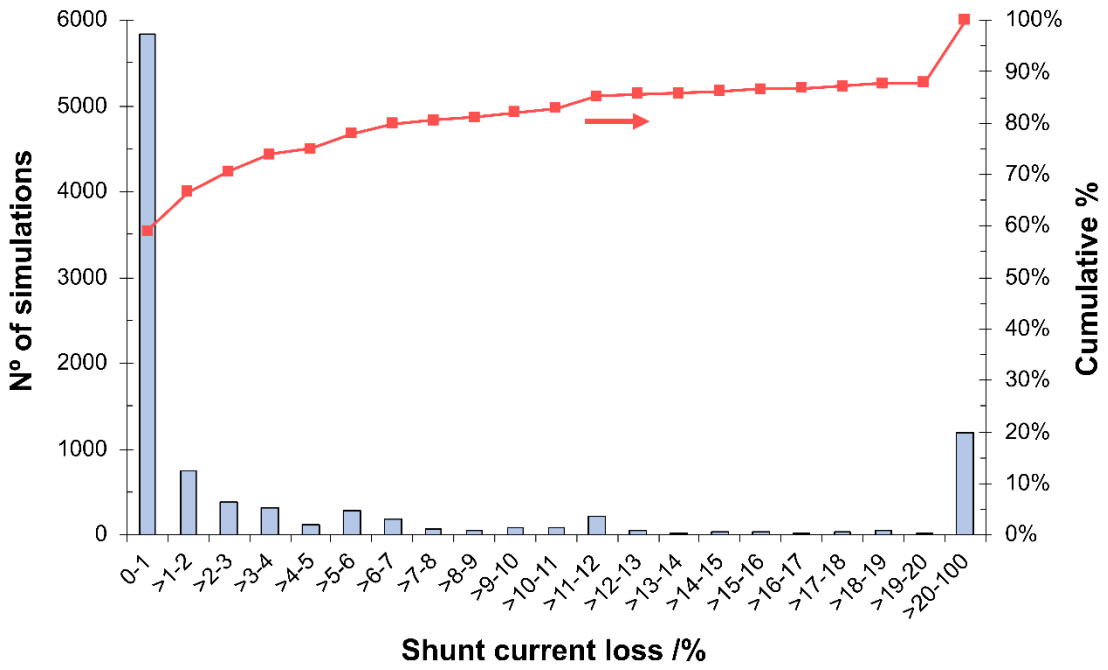

Figure 5.7 – Number of simulations that resulted in shunt current losses (SCL) within a specific range, e.g., above 1 % and less or equal than 2 % (> 1 - 2), and respective cumulative percentage. The simulations were carried out using the equivalent circuit model with different combinations of values of R_m, R_c, I, and N.

Figure 5.7 shows that nearly 60 % of the simulations displayed an SCL of 1 % or lower. Such low SCL could only be obtained when an R_m greater than 327 Ω (Table **Error! Use the Home tab to apply Título 6;ND Appendix Header 1 to the text that you want to appear here.**.8 and Table **Error! Use the Home tab to apply Título 6;ND Appendix Header 1 to the text that you want to appear here.**.9), or when an adequate combination of values of R_m, R_c, I and N was used. A stack with an R_m higher than 327 Ω can greatly simplify the design and manufacturing process of the flow frames. Nonetheless, designing a conventional stack with an R_m greater than 327 Ω may not be feasible; an exceedingly long distance between two adjacent cells or an extremely narrow manifold is required. Thus, different stack designs need to be considered.

To perform a sensitivity analysis, a correlation relating the SCL with R_m, R_c, I, and N must be determined, and its accuracy must be assessed. The following correlation was obtained by providing the results shown in Figure 5.7 to Eureqa software:

$$\mathrm{SCL}(\%) = \frac{1010N^2}{5N^2 + NIR_m + N^2IR_m + 12IR_c - R_c} \tag{5.40}$$

Furthermore, Eq. (5.40) was compared with the dataset provided to the Eureqa software to verify its goodness of fit; a mean absolute error of 2.86 % and a maximum absolute error of 5.72 % were obtained, which demonstrates that Eq. (5.40) has good accuracy for all the 9872 data points used in this work. The highest absolute errors were observed when high values of R_m, low values of R_c or $N = 40$ were used (Table **Error! Use the Home tab to apply Título 6;ND Appendix Header 1 to the text that you want to appear here.**.10 and Table **Error! Use the Home tab to apply Título 6;ND Appendix Header 1 to the text that you want to appear here.**.11). The accuracy of the correlation is further analyzed by comparing Eq. (5.40) with the ECM for different combinations of values of R_m, R_c, R_{cell}, N, and I that can be found in the literature (Table 5.2). The distribution channels and manifold resistances were calculated using Eq. (5.22), Eq. (5.23), and the average resistivity of electrolyte at both half-cells. An SoC of 50 % and a current density of 80 mA cm^{-2} were used for all simulations. The results (Table 5.2) demonstrate that Eq. (5.40) has good accuracy for combinations of values that are not in the dataset of this work, even when the internal resistance is modified; the correlation proposed in this work is easier to use to determine the SCL in an RFB stack than the DPM and ECM models. The sensitivity analysis can be carried out using Eq. (5.40), taking into account that this correlation is only valid within the following ranges: $5 \leq N \leq 40$, $4\ \mathrm{A} \leq I \leq 512\ \mathrm{A}$, $0.08\ \Omega \leq R_c \leq 2621\ \Omega$ and $0.08\ \Omega \leq R_m \leq 2621\ \Omega$.

Table 5.2 – Shunt current loss (SCL) determined using the equivalent circuit model (ECM) and Eq. (5.40) with different combinations of values of manifold resistance, R_m, distribution channels resistance, R_c, internal cell resistance, R_{cell}, active area, A, operating current, I, and number of cells in a stack, N.

SCL /% (ECM)	SCL /% (Eq. (5.40))	R_m /Ω	R_c /Ω	R_{cell} /Ω	A /cm^2	I /A	N	Ref.
4.20	4.08	0.38	90	0.0040	900	72.0	19	[7]
0.61	0.59	1.23	366	0.0036	476	38.1	10	[8]
0.42	0.40	0.28	2764	0.0014	1500	120.0	40	[9]
0.29	0.28	1.07	863	0.0009	3608	288.6	30	[29]
0.44	0.42	1.08	707	0.0013	780	62.4	15	[30]

The sensitivity analysis carried out in this work (Figure 5.8) shows that, on average, the R_m has a much greater impact in the SCL than any other variable; it has the highest sensitivity index (425) and the highest average rate of change $\overline{m}$ (10.8 % Ω^{-1}), followed by R_c (SI = 27.6 and $\overline{m}$ = 0.71 % Ω^{-1}), I (SI = 5.4 and $\overline{m}$ = 0.57 % A^{-1}) and N (SI = 0.23 and $\overline{m}$ = 0.31 % cell^{-1}).

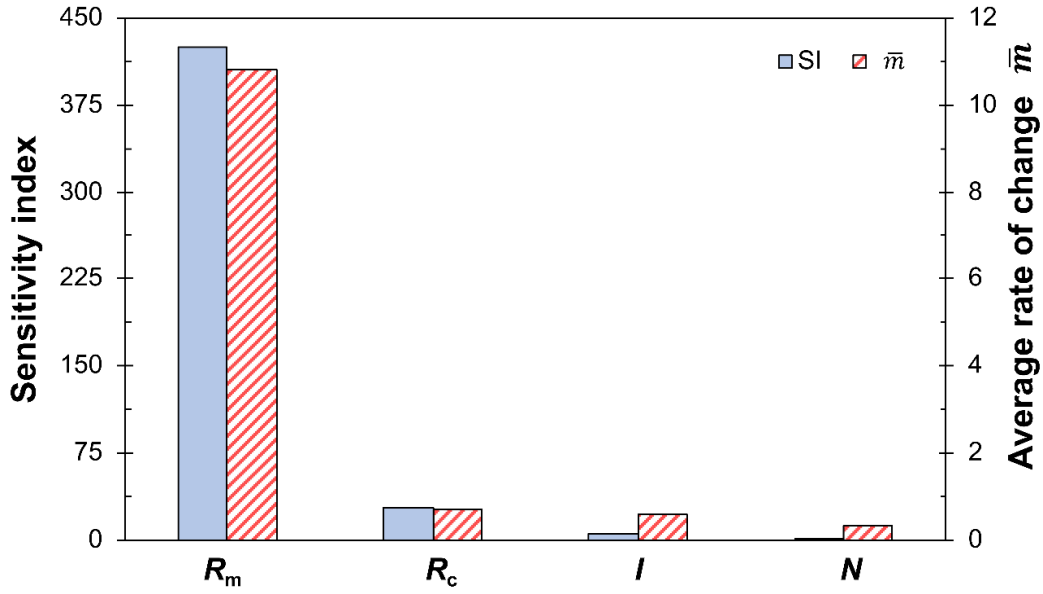

Figure 5.8 – Sensitivity index (SI) and average rate of change $\bar{m}$ ($\partial\overline{\mathrm{SCL}} = \bar{m}\cdot\partial\bar{x}$) of the manifold resistance, R_m, distribution channels resistance, R_c, operating current, I, and number of cells in a stack, N.

These results are in agreement with the results obtained by Yin et al. [13] but not with the work of Xing et al. [8] and Chen et al. [7]. Xing et al. [8] showed that increasing R_c by 50 % provides a greater reduction in the shunt currents than increasing R_m by 50 %. Chen et al. [7] demonstrated that the R_c has a higher impact in the SCL than the R_m by increasing them twofold. However, other authors [13] increased R_c and R_m by a factor of 30 to demonstrate that R_m has a greater impact on the SCL. There is an ongoing discussion regarding the impact of each resistance in the SCL. However, all conclusions are correct; if $m_{Rc}\Delta R_c > m_{Rm}\Delta R_m$ (Eq. (5.32)), where m_i is the local rate of the parameter i, then the change in SCL due to R_c increase is greater than the change in SCL due to R_m increase. The opposite is also true if $m_{Rm}\Delta R_m > m_{Rc}\Delta R_c$. In short, all the previous authors compared the two resistances by using values with very distinctive magnitudes; Xing et al. [8] used an R_c and an R_m of 365.89 Ω and 1.23 Ω, respectively, Chen et al. [7] used R_c = 89.5 Ω and R_m = 0.38 Ω, and Yin et al. [13] used values of R_c and R_m with similar magnitudes. The minimum value of ΔR_c that causes R_c to have a greater impact in the SCL than R_m can be determined using Eq. (5.41).

$$\frac{\partial SCL}{\partial R_c}\Delta R_c > \frac{\partial SCL}{\partial R_m}\Delta R_m \longrightarrow \Delta R_c > -\frac{1010\left(IN + IN^2\right)}{1010 - 12120I}\Delta R_m \qquad (5.41)$$

Eq. (5.41) shows that the minimum value of ΔR_c depends on the stack design and operating conditions. Thus, an in-depth analysis is required to understand the impact of the external resistances in the SCL. This work offers a clearer conclusion since the sensitivity index is independent of the magnitude of the variables. Also, several combinations of values of R_c and R_m with orders of magnitude ranging from 10^{-2} to 10^3 were used. For the same value increment (Δx), R_m is the parameter that affects SCL the most.

The results presented in this work regarding the rate of change are averages and should not be used to estimate the change in SCL caused by a local increment in the value of x. Instead, the first order derivative of Eq. (5.40) with respect to x ($m = \partial \mathrm{SCL}/\partial x$) should be used since it represents a local rate of change, m. Still, there is no circumstance where the local rate of change of R_m is lower than the local rate of change of R_c. Also, it was found that the local rate of change is always negative for R_m, R_c, and I and always positive for N; the SCL always decreases with the increasing R_m, R_c, and I and with the decreasing N. This agrees with the information found in the literature [7, 8, 13]. The SCL is expected to increase with the N since the potential difference between the first and last cells of the stack (the driving force of shunt currents) increases.

The stack design of a VRFB can be improved since $m_{Rm} > m_{Rc}$; Δp can be reduced, and the nominal power delivered by the stack can be increased while maintaining the same SCL. For example, SCL can be reduced by increasing the active area. Nonetheless, the following aspects need to be considered: the electrolyte distribution becomes worse [31], and assembling, handling, and transporting the stack becomes harder with the increasing active area. The latter can be minimized by increasing the ratio between the active area and the flow frame area. Likewise, the pressure drop increases significantly with the increasing electrode height (Eq. (5.33)). Using an active area of 1600 cm^2 in a stack with 40 cells, a wide manifold (R_m = 2.56 Ω) and short flow channels (R_c = 0.08 Ω) is sufficient to achieve an SCL as low as 1.58 % at a current density of 160 mA cm^{-2}; there are no significant improvements in the shunt current losses when developing stacks with an active area above 1600 cm^2.

5.5.4. Novel stack equipped with *M* dumping cells

Given the findings presented above, a novel stack design with lower SCL and pressure drop, Δp, and higher active area than a conventional stack design is proposed in this section: the Δp in a conventional stack can be reduced and the active area can be increased by simply decreasing the length of the distribution channel (Figure 5.3). Though, it is expected the SCL to increase since R_c decreases.

The SCL of a conventional stack with 40 cells using a shorter and a longer distribution channel (SFC and LFC, respectively, Figure 5.3) was determined using Eq. (5.40) and compared. A current density of 80 mA cm^{-2} was assumed for the calculations. The R_m is 4 Ω for both stack designs and the R_c is 3147 Ω for the LFC and 157 Ω for the SFC. Additionally, the Δp was determined using Eq. (5.33)-(5.39) and assuming a flow rate of 4 l min^{-1}. The viscosity of the negative electrolyte and the conductivity of the positive electrolyte were used in the calculation of Δp and SCL, respectively. The electrolyte is assumed to be at 50 % SoC. These conditions are used throughout this section, unless otherwise stated.

As shown in Table 5.3, the Δp was decreased by 45 % when the length of the LFC was reduced, with the consequence of increasing the SCL by 317 %. Also, the active area was increased from 288 cm^2 to 343 cm^2, which corresponds to a nominal power increase of 19.1 % for the same current density; a stack comprising 40 cells with an active area of 288 cm^2, operated at a current density of 160 mA cm^{-2} and displaying an average charge-discharge cycle potential of 1.3 V per cell delivers a nominal power of 2.396 kW. If the active area is increased to 343 cm^2, the stack is now able to deliver a nominal power of 2.854 kW.

Table 5.3 – Pressure drop (Δp) and shunt current loss (SCL) in a conventional stack with 40 cells and long (long frame channel, LFC) and short (short frame channel, SFC) distribution channels at 80 mA cm^{-2}.

Distribution channel	Δp /mbar	SCL /%
LFC	181	1.57
SFC	99	6.55

Since the local rate of change of R_m (m_{Rm}) is always greater than the local rate of change of R_c (m_{Rc}), the best option to reduce the SCL in the stack while using the SFC and maintaining a low Δp, consists in increasing R_m. Dumping cells act as an extension of the manifold and, thus, can be used to reduce the SCL as effectively as the manifold. Therefore, the ECM was used to simulate the SCL in a 40 cell-stack equipped with a dumping cell (Figure 5.4 (c)) after every 20, 10, and 5 cells (Figure 5.9); a total of one, three, and seven dumping cells are used, respectively. The resistance of each dumping cell, R_{dc}, ranged from 50 Ω to 1917 Ω and was incremented by a factor of 1.2 ($x_{i+1} = 1.2\ x_i$). The pressure drop caused by the dumping cells is determined using Eq. (5.34) and assuming that the dumping cell channels have a width and a depth of 15 mm and 10 mm, respectively. The total length of the channel in the dumping cell was determined using Eq. (5.27).

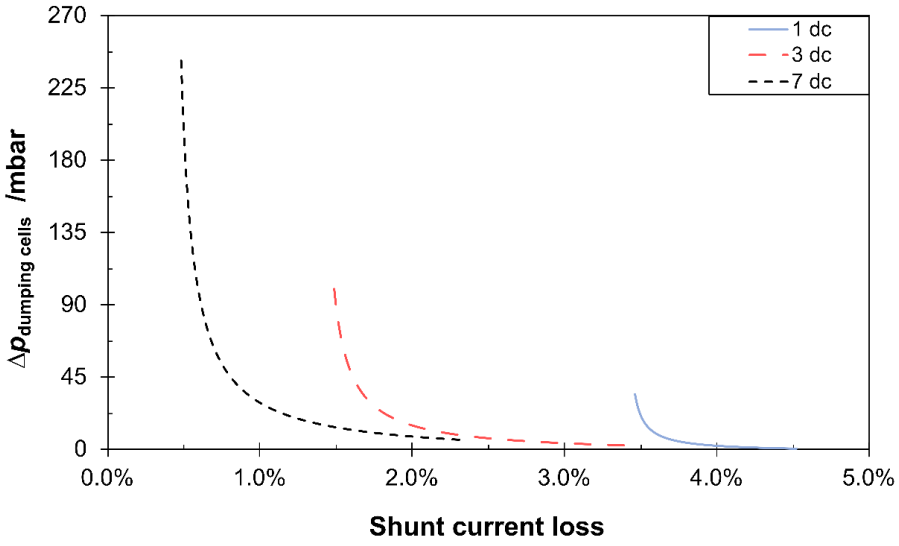

Figure 5.9 – Pressure drop caused by the dumping cells ($\Delta p_{\text{dumping cells}}$) and shunt current loss (SCL) of the 40 cells stack using one, three and seven dumping cells (dc).

Figure 5.9 shows that the SCL can be reduced using dumping cells, even when a low dumping cell resistance to shunt currents (R_{dc}) is considered. In fact, an SCL equal or lower to the SCL of the stack using the LFC can be achieved when three or more dumping cells are used.

A lower Δp is obtained for the same SCL with the increasing number of dumping cells. This trend suggests that the optimal number of dumping cells to minimize SCL and Δp is N-1, which is equivalent to having a conventional stack with a long manifold distance between two adjacent cells, or high R_m. However, the assembly complexity increases as the number of dumping cells increases. Using seven dumping cells appears to be the best trade-off between stack performance and assembly complexity; for the same SCL, seven dumping cells display a pressure drop 35 % lower than three dumping cells. Also, an SCL as low as 0.50 % can be achieved using seven dumping cells. Thus, no further dumping cells are required.

To obtain an SCL as low as 1.57 % (SCL of the conventional stack using LFC) an R_{dc} of, at least, 104 Ω is required when using seven dumping cells (Figure 5.9). Nonetheless, the dumping cell design must be optimized such that the Δp caused by electrolyte flow in the dumping cells is not higher than 82 mbar (Δp_{LFC}-Δp_{SFC}, Table 5.3). Eq. (5.34) was used to calculate the pressure drop in the dumping cell and Eq. (5.27) was used to calculate the R_{dc}. The geometric constraints (constant values) given to optimize the dumping cell design are described above and shown in Figure 5.10.

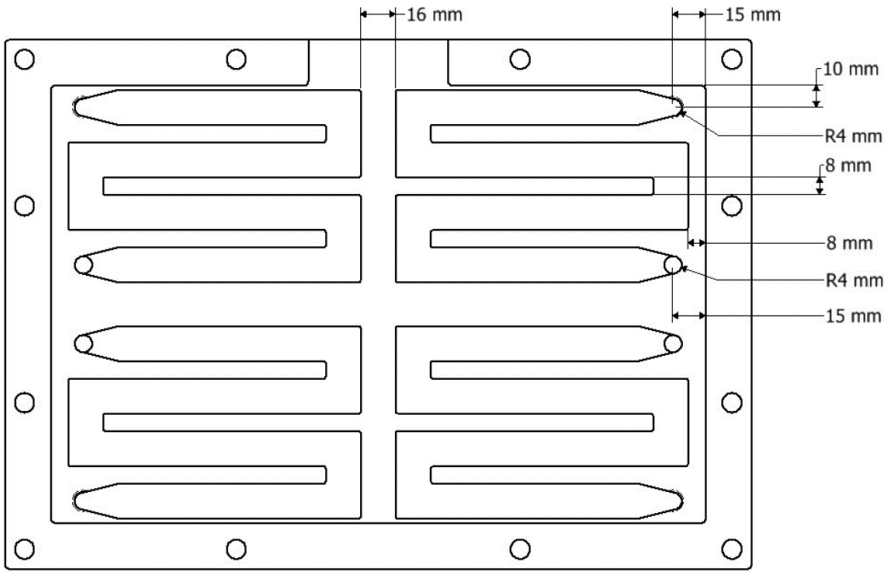

Figure 5.10 – 2D drawing of the optimized dumping cell and geometric constrains used to optimize the dumping cell design.

The Solver add-in (Microsoft Excel) was used to find the optimal values of length, width and depth of the dumping cell channels, in the dumping cell, that minimize Δp (Eq. (5.34)) while $R_{dc} \geq 104\ \Omega$ (Eq. (5.27)). The minimum and maximum depth, width and vertical length of the channels used in the Solver add-in can be found in Table 5.4.

Table 5.4 – Minimum and maximum depth, width, and vertical length of the channels of the dumping cell. Values used in the Solver add-in to optimize the dumping cell flow channel design.

Parameter	Minimum value	Maximum value	Optimized value
Channel depth	1 mm	13 mm	13 mm
Channel width	1 mm	16 mm	16 mm
Channel vertical length	1 mm	96 mm	88 mm

The maximum depth was imposed by the maximum (30 mm) and minimum (4 mm) thickness of the dumping cell. Since both sides of the dumping cell have channels, the maximum depth of the channel is (30 – 4) / 2 = 16 mm. The maximum width of the channel (2 × 8 mm) was set based on the space available from the center of the manifold to the upper border (10 mm, Figure 5.10) and a safety margin (2 mm, Figure 5.10) given on top of the channels to place gaskets to prevent leakages (10 – 2 = 8 mm). A minimum safety margin of 2 mm was also given at the bottom of the channels to place gaskets. The maximum vertical length of the channel was, thus, set to 96 mm (100 – 2 × 2 = 96 mm). The horizontal length of the channel was set to 134 mm, according to the constraints shown in Figure 5.10 (150 – 2 × 8 = 134 mm).

For the dumping cell design presented in this work, the optimal dumping cell channel design consists of a single serpentine channel with a depth, width, and length of 13 mm, 16 mm, and 1012 mm, respectively (Figure 5.2). The total Δp caused by the seven dumping cells is 22.2 mbar and $R_{dc} = 128\ \Omega$. As such, the stack using an SFC and seven dumping cells has a much lower Δp (121 mbar) compared to the stack using an LFC (181 mbar), a 19.1 % higher active area and a lower SCL (1.20 % *vs.* 1.57 %).

The stacks studied in this section have a low active area and the dumping cell was optimized considering a moderate operating current density. Still, the performance was greatly improved. The number of dumping cells required to obtain SCL of 1 % or lower, while minimizing pressure drop, will decrease with the increasing active area or operating current. Thus, using dumping cells to optimize the performance of an RFB stack becomes more viable as the active area of the stack is increased.

The implementation of a dumping cell in a stack requires two gaskets (stack | gasket | dumping cell | gasket | stack) to prevent internal and external leakages, and the dumping cell itself, which can be made of a polymer resistant to sulfuric acid (e.g., polyvinyl chloride or polypropylene) through milling or molding. Thus, it has little impact on the assembly complexity of a stack, and it requires very low maintenance.

5.6. Conclusion

A 2D dynamic phenomenological model (DPM) and an equivalent circuit model (ECM) were successfully used to simulate shunt currents in vanadium redox flow battery stacks. The results obtained using both models were for the first time compared in this work. It was found that the ECM overestimated the shunt currents in the distribution channels by 12.8 % and manifold by 11.7 % when compared to the DPM. The oversimplification of the ECM is demonstrated to be the root of such difference; the ECM overestimates the cell potentials. However, the ECM is considerably faster than the DPM simulating shunt currents. Further improvements, such as including the kinetic and mass transfer resistances, are required in the ECM to minimize the results differences between the two approaches.

This work shows that lower shunt currents are obtained when the internal resistances are decreased; the ohmic resistances are the main contributor for decreasing the shunt currents, followed by mass transfer and kinetic resistances. This was assigned to the decrease of the potential drop across the stack. However, the reduction of the shunt current intensity is only observed when the internal resistance does not directly influence the transport of ions across the manifold and distribution channels; the external (channels and manifold) resistances have a much greater impact on the shunt currents than the internal resistances. Furthermore, the results suggest that more attention towards shunt currents is required when using compact redox flow battery stack designs or highly conductive electrolytes, and in the event of a poor electrolyte distribution.

A correlation relating the shunt current losses (SCL) with the external resistances (manifold, R_m, and distribution channels, R_c), operating current (I), and number of cells (N) was proposed; it agrees well with the ECM for any combination of parameters within the following value ranges: $5 \leq N \leq 40$, $4\ \text{A} \leq I \leq 512\ \text{A}$, $0.08\ \Omega \leq R_c \leq 2621\ \Omega$ and $0.08\ \Omega \leq R_m \leq 2621\ \Omega$. Thus, a method to determine the SCL of an RFB stack with a conventional design that does not require any software is presented; iterating through stack designs becomes faster and easier. The correlation was then used to carry out a sensitivity analysis. The sensitivity analysis was carried out considering more than 20 000 simulations with different stack designs. Thus, this work clarifies contradictory information found in the literature about the impact of the manifolds and channels on the shunt currents. It was found

that R_m has a much greater impact on the SCL than the remaining parameters. Additionally, the SCL always decreases with the increasing R_m, R_c, and I and with the decreasing N. A moderate active area size ($A \leq 1600$ cm^2) is recommended to minimize the SCL, stack design complexity, pressure drop, and handling difficulty, and to avoid carbon material degradation. Using an external hydraulic circuit connected to the manifold, instead of using long distribution channels is also recommended to minimize the SCL and pressure drop.

A novel stack design, equipped with dumping cells, is proposed. This stack displays a high R_m and a low R_c and performs better than a stack with a high R_c and a low R_m (conventional design), as suggested by the parametric study carried out in this work; the novel stack comprises seven dumping cells and displays an SCL 23.6 % and a pressure drop 33 % lower than the stack with conventional design. Additionally, the active area was increased by 19 %, which leads to a nominal power increase by the same amount. The dumping cell design, first presented in this work, can be added to or removed from any conventional stack without additional changes in the stack design. This modularity also offers the advantage of having two different stacks based on the same design with different costs and performance. The nominal power increase may help this technology to hit the market since the price per kW decreases. As such, this work clearly offers critical information regarding the optimization of the stack design.

5.7. References

1. P.R. Prokopius, *Model for calculating electrolytic shunt path losses in large electrochemical energy conversion systems*. 1976, NASA: Washington, D. C.
2. K. Kanari, K. Nozaki, H. Kaneko, and M. Kamimoto. *Numerical analysis on shunt current in flow batteries*. in *Proceedings of the Intersociety Energy Conversion Engineering Conference*. 1990.
3. M. Katz, *Analysis of Electrolyte Shunt Currents in Fuel Cell Power Plants.* Journal of The Electrochemical Society, 1978. **125**(4): p. 515-520.
4. P.P. Pirotskii and N.N. Shevtsov, *Instrument for measuring direct current in electrolyte jets.* Izmeritel'naya Tekhnika, 1961. **12**: p. 43-45.
5. I. Roušar and V. Cezner, *Experimental Determination and Calculation of Parasitic Currents in Bipolar Electrolyzers with Application to Chlorate Electrolyzer.* Journal of The Electrochemical Society, 1974. **121**(5): p. 648.
6. H. Fink and M. Remy, *Shunt currents in vanadium flow batteries: Measurement, modelling and implications for efficiency.* Journal of Power Sources, 2015. **284**: p. 547-553.
7. Y.-S. Chen, S.-Y. Ho, H.-W. Chou, and H.-J. Wei, *Modeling the effect of shunt current on the charge transfer efficiency of an all-vanadium redox flow battery.* Journal of Power Sources, 2018. **390**: p. 168-175.
8. F. Xing, H. Zhang, and X. Ma, *Shunt current loss of the vanadium redox flow battery.* Journal of Power Sources, 2011. **196**(24): p. 10753-10757.
9. A. Tang, J. McCann, J. Bao, and M. Skyllas-Kazacos, *Investigation of the effect of shunt current on battery efficiency and stack temperature in vanadium redox flow battery.* Journal of Power Sources, 2013. **242**: p. 349-356.
10. A. Trovò et al., *Standby thermal model of a vanadium redox flow battery stack with crossover and shunt-current effects.* Applied Energy, 2019. **240**: p. 893-906.
11. Q. Ye, J. Hu, P. Cheng, and Z. Ma, *Design trade-offs among shunt current, pumping loss and compactness in the piping system of a multi-stack vanadium flow battery.* Journal of Power Sources, 2015. **296**: p. 352-364.

12. S. König, M.R. Suriyah, and T. Leibfried, *Model based examination on influence of stack series connection and pipe diameters on efficiency of vanadium redox flow batteries under consideration of shunt currents.* Journal of Power Sources, 2015. **281**: p. 272-284.
13. C. Yin, S. Guo, H. Fang, J. Liu, Y. Li, and H. Tang, *Numerical and experimental studies of stack shunt current for vanadium redox flow battery.* Applied Energy, 2015. **151**: p. 237-248.
14. D.G. Clark, S.H. Joseph, and H.S. Oates, *Electrochemical cell*. 2003: United States.
15. S. Kim et al., *1 kW/1 kWh advanced vanadium redox flow battery utilizing mixed acid electrolytes.* Journal of Power Sources, 2013. **237**: p. 300-309.
16. M. Guarnieri, A. Trovò, A. D'Anzi, and P. Alotto, *Developing vanadium redox flow technology on a 9-kW 26-kWh industrial scale test facility: Design review and early experiments.* Applied Energy, 2018. **230**: p. 1425-1434.
17. L.F. Arenas, F.C. Walsh, and C.P. de León, *3D-Printing of Redox Flow Batteries for Energy Storage: A Rapid Prototype Laboratory Cell.* ECS Journal of Solid State Science and Technology, 2015. **4**(4): p. P3080-P3085.
18. N.M. Delgado, R. Monteiro, M. Abdollahzadeh, P. Ribeirinha, A. Bentien, and A. Mendes, *2D-dynamic phenomenological modelling of vanadium redox flow batteries – Analysis of the mass transport related overpotentials.* Journal of Power Sources, 2020. **480**: p. 229142.
19. M. Schmidt and H. Lipson, *Distilling Free-Form Natural Laws from Experimental Data.* Science, 2009. **324**(5923): p. 81.
20. A. Al-Subhi, *Parameters estimation of photovoltaic cells using simple and efficient mathematical models.* Solar Energy, 2020. **209**: p. 245-257.
21. P. Barmpalexis, K. Kachrimanis, A. Tsakonas, and E. Georgarakis, *Symbolic regression via genetic programming in the optimization of a controlled release pharmaceutical formulation.* Chemometrics and Intelligent Laboratory Systems, 2011. **107**(1): p. 75-82.
22. V. Bellos, I. Nalbantis, and G. Tsakiris, *Friction Modeling of Flood Flow Simulations.* Journal of Hydraulic Engineering, 2018. **144**(12).
23. S. Moaveni, *Engineering Fundamentals: An Introduction to Engineering*. 2016: Cengage Learning.

24. A. Bahadori, *Chapter 1 - Transportation Pipelines*, in *Oil and Gas Pipelines and Piping Systems*, A. Bahadori, Editor. 2017, Gulf Professional Publishing: Boston. p. 1-27.
25. E.A. Kaminski and R.F. Savinell, *A Technique for Calculating Shunt Leakage and Cell Currents in Bipolar Stacks Having Divided or Undivided Cells.* Journal of the Electrochemical Society, 1983. **130**: p. 1103.
26. R. O'Hayre, S.-W. Cha, W. G. Colella, and F. B. Prinz, *Fuel Cell Fundamentals*. third ed. 2016: John Wiley & Sons.
27. Y. Li, J. Bao, M. Skyllas-Kazacos, M.P. Akter, X. Zhang, and J. Fletcher, *Studies on dynamic responses and impedance of the vanadium redox flow battery.* Applied Energy, 2019. **237**: p. 91-102.
28. Y. Song, X. Li, C. Yan, and A. Tang, *Uncovering ionic conductivity impact towards high power vanadium flow battery design and operation.* Journal of Power Sources, 2020. **480**: p. 229141.
29. F.T. Wandschneider, S. Röhm, P. Fischer, K. Pinkwart, J. Tübke, and H. Nirschl, *A multi-stack simulation of shunt currents in vanadium redox flow batteries.* Journal of Power Sources, 2014. **261**: p. 64-74.
30. Y. Zhang, J. Zhao, P. Wang, M. Skyllas-Kazacos, B. Xiong, and R. Badrinarayanan, *A comprehensive equivalent circuit model of all-vanadium redox flow battery for power system analysis.* Journal of Power Sources, 2015. **290**: p. 14-24.
31. M. Perry and R. Darling, *The Influence of Electrode and Channel Configurations on Flow Battery Performance.* Journal of The Electrochemical Society, 2014. **161**: p. A1381-A1387.

Chapter 6

Modelling of a solar redox flow cell

The content of this chapter is adapted from: N.M. Delgado, R. Monteiro and A. Mendes, *The first approach to dynamic modeling of a solar vanadium redox flow cell.* Nano Energy, 2021. **89**: p. 139667

6. Modelling of a solar redox flow cell

Equation Chapter (Next) Section 1

6.1. Abstract

The increasing offer of energy, especially electricity from renewable sources, has been fueling the investment in energy storage technologies. However, most of the energy harvesting technologies produce non-dispatchable electricity. The solar redox flow cell (SRFC) technology stands out by converting sunlight into storable energy. The latter is easily converted into electricity. However, some challenges that need to be addressed before SRFCs become commercially available. Phenomenological models are a powerful tool that can be used to accelerate the development of any technology. This work reports the first multidimensional, dynamic, and phenomenological model of a vanadium SRFC. The mass and momentum conservation equations are incorporated in the model to simulate the electrolyte flow. The charge transport is simulated by implementing the charge conservation, the Nernst-Planck, and drift-diffusion equations. The photoelectrochemical and electrochemical reactions are simulated using the Butler-Volmer equation. The model is validated against experimental data of a vanadium SRFC using a cadmium sulfide semiconductor (*n*-type). The energy band shifting for different bias potentials and the accumulation and depletion of charges at the space charge region are simulated. The photopotential is determined using the minor carrier concentration and it is demonstrated to be equivalent to the potential difference between the *quasi*-Fermi energy levels of the electrons and holes. The impact of recombination mechanisms in the performance of the SRFC is analyzed; the surface recombination competes with surface reactions, affecting the onset potential, while non-surface recombination mechanisms affect the concentration of holes, decreasing the maximum current density.

6.2. Introduction

For the solar redox flow cells (SRFC) to reach the commercialization stage, several key aspects need to be addressed, namely [1]: 1) the energy density is low when compared to other storage solutions since, typically, low electrolyte concentrations are used; and 2) the power density is normally low when compared to other similar technologies, despite the recent developments that report an SRFC with 20.1 % of solar-to-chemical energy conversion efficiency [2].

In such an early stage, the development of dynamic models is essential since it can provide new insights and useful information to accelerate the development of this technology. To the best of the authors' knowledge, dynamic phenomenological models of SRFCs have never been reported. Wei et al. [3] developed a multidimensional steady-state model to analyze the distribution of charges in the photoelectrode of a vanadium SRFC. The authors simulated the positive side and the negative side separately and no model validation was carried out. Moreover, the model included only the charge transport equations at the photoelectrode, which is not sufficient to predict changes in the energy band diagram and the photocurrent. More complex models can be found for photoelectrochemical water splitting; Cendula et al. [4] developed a steady-state 1D model by carrying out an extensive analysis of the photoelectrode energy diagram. Y. Gaudy and S. Haussener [5] introduced a multidimensional electromagnetic wave propagation model to simulate light propagation through the semiconductor and the electrolyte. Iqbal et al. [6-8] focused on the development of a steady-state model capable of simulating surface state phenomena, the photopotential, and the photocurrent at semiconductor | electrolyte interface. These models can only simulate the semiconductor and they were built following a similar approach: the drift-diffusion equation is used to describe the transport of electrons and holes, the Poisson equation is used to describe charge conservation and a pseudo-Schottky contact approximation at the semiconductor | electrolyte interface is considered to simulate the photoelectrochemical reaction. This approximation assumes that the electrolyte acts as a metal. A different approach to simulate the photoelectrochemical reaction consists in using the Butler-Volmer equation, such as in the redox flow batteries (RFB) [9] models; the driving force of the electrochemical reaction, when using a conductor, is given by the difference between the bias

potential and the standard reduction potential (overpotential). When using a semiconductor, intrinsic losses must be considered, and the driving force of the reaction is given by the difference between the *quasi*-Fermi energy level of the minority carrier and the standard reduction potential. H. Zhang, H. Wang, and J. Xuan [10] reported a model for PECs using this approach. However, the activation and ohmic overpotentials were neglected and the reaction was assumed to be promoted only by the photopotential.

In this work, a 2D dynamic model of a vanadium SRFC, using a cadmium sulfide (CdS) semiconductor as the photoelectrode, CdS(s) | V^{3+}, VO^{2+} || V^{3+}, V^{2+} | carbon felt(s), is presented. The model considers the mass, momentum, and charge conservation equations, and the Nernst-Planck and drift-diffusion transport equations. The recombination and generation of holes and electrons in the photoelectrode were also simulated. A comprehensive analysis of the energy band diagram was carried out to model the *quasi*-Fermi energy level of the holes and electrons. The Butler-Volmer and Tafel equations were used to describe the electrochemical and photoelectrochemical reactions, respectively. A set of boundary conditions were implemented to simulate the transport of electrons through the external circuit and the electroneutrality within the SRFC. The model is validated by comparing the simulated *i*-*V* curve with experimental data from the literature [11]. This work aims at exploring the response of the model, especially regarding the photoelectrode, under different bias potentials and studying the impact of the recombination mechanisms on the performance of the SRFC.

6.3. Mathematical model

The SRFC (Figure 6.1) modeled in this work comprises i) a positive half-cell, where a CdS photoelectrode is contacting with the V^{3+}/VO^{2+} electrolyte; ii) a negative half-cell, where a carbon felt electrode is contacting with the V^{2+}/V^{3+} electrolyte; iii) a cation exchange membrane, Nafion® 117, dividing both half-cells. Further information regarding the cell setup may be found elsewhere [11].

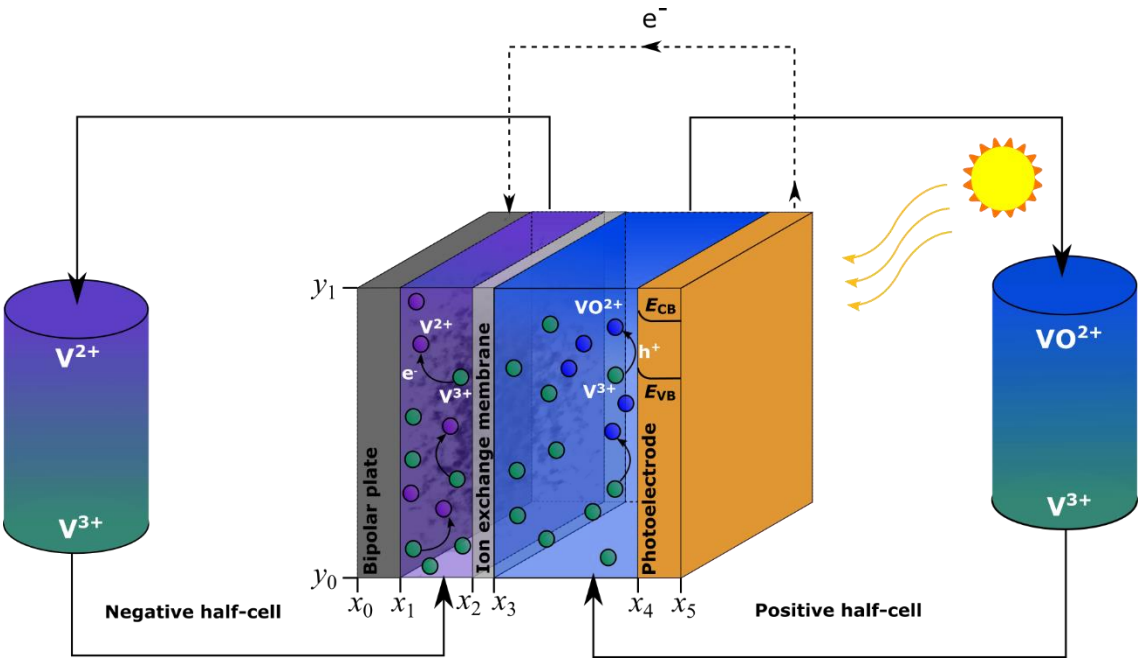

Figure 6.1 – Schematic representation of the all-vanadium solar redox flow cell setup simulated in this work and labeling of boundary conditions.

The photoelectrochemical reaction (Eq. (6.1)) occurs at the surface of the photoelectrode, while the electrochemical reaction (Eq. (6.2)) occurs at the surface of the fibers of the electrode.

$$V^{3+} + H_2O + h^+ \longrightarrow VO^{2+} + 2H^+ \tag{6.1}$$

$$V^{3+} + e^- \rightleftharpoons V^{2+} \tag{6.2}$$

The model was built based on the following main assumptions [12]:

- incompressible fluid;
- isotropic electrode and membrane;
- negligible gravity effect;
- dilute solution approximation (activity coefficients were considered equal to 1);
- negligible membrane crossover;
- negligible hydrogen and oxygen evolution reactions;

- isothermal behavior;
- no precipitation of vanadium;
- non-degenerated photoelectrode.

The energy levels are indicated against the SHE electrode.

6.3.1. Governing Equations

Fluid flow conservation equations

The hydrodynamic flow in the negative electrode was described using Eq. (6.3), which is a balance of linear momentum (Newton's second law) [13]. This equation was solved together with the continuity equation (Eq. (6.4)), which describes the conservation of mass. The total mass of the vanadium electrolyte was assumed constant and, to describe the hydrodynamic flow of the electrolyte, a low Reynolds number – laminar flow – was assumed. The following equations were used in the negative electrode:

$$\frac{\partial(\varepsilon\rho\vec{v})}{\partial t}+\nabla\cdot\left(\varepsilon\rho\vec{v}\vec{v}\right)=-\varepsilon\nabla p+\nabla\cdot\left(\varepsilon\mu\nabla\vec{v}\right)+S_{\text{mom}} \tag{6.3}$$

$$\frac{\partial\varepsilon\rho}{\partial t}+\nabla\cdot\left(\varepsilon\rho\vec{v}\right)=0 \tag{6.4}$$

where ε is the porosity of the electrode, ρ is the density of the electrolyte, $\vec{v}$ is the velocity of the electrolyte, p is the static pressure, μ is the viscosity and S_{mom} is the source term of the momentum equation. The source term of the momentum equation in the electrode region is given by Darcy's law (Eq. (6.5)).

$$S_{\text{mom}}=-\frac{\mu}{K_p}\vec{v} \tag{6.5}$$

The permeability of the electrode (K_{P}) was determined with the Kozeny-Carman equation (Eq. (6.6)).

$$K_{\text{p}}=\frac{d_{\text{f}}^2\varepsilon^3}{16k_{\text{KC}}\left(1-\varepsilon\right)^2} \tag{6.6}$$

where d_f is the fiber diameter of the carbon felt and k_{KC} is the Kozeny-Carman constant, used to describe the morphology of the porous media. On the positive side, no porous media is used ($S_{mom} = 0$ and $\varepsilon = 1$).

Charge transport equations in the electrolyte

The transport of ions in the dilute solution was described by the Nernst-Planck equation, as follows:

$$\frac{\partial \varepsilon c_i}{\partial t} + \nabla \cdot \vec{N}_i = S_i \tag{6.7}$$

where c_i is the molar concentration of ion i and $\vec{N}_i$ is the total flux of ion i. S_i is the source term used to simulate the concentration variations of V^{2+} ($S_{V^{2+}} = -j_-/nF$) and V^{3+} ($S_{V^{3+}} = j_-/nF$) due to the electrochemical reaction that takes place at the negative electrode. In the positive chamber, S_i is set to 0.

The flux of each species, $\vec{N}_i$, was determined considering the additive contribution of three different transport mechanisms: diffusion ($\vec{N}_{diff}$), advection ($\vec{N}_{advec}$) and migration ($\vec{N}_{mig}$) (Eq.(6.8)) [14, 15].

$$\vec{N}_i = \vec{N}_{diff} + \vec{N}_{advec} + \vec{N}_{mig} = -D_i^{eff} \nabla c_i + c_i \vec{v} - \frac{z_i F D_i^{eff}}{RT} c_i \nabla \phi_e \tag{6.8}$$

where D_i^{eff} is the effective diffusivity, ∇c_i is the concentration gradient of ion i, z_i is the valence state, R is the gas constant, F is the Faraday constant (96 485 C mol^{-1}), T is the temperature (assumed to be 298.15 K) and $\nabla \phi_e$ is the electric potential gradient of the liquid phase.

The complete Nernst-Planck equation is:

$$\frac{\partial \varepsilon c_i}{\partial t} + \nabla \cdot (c_i \vec{v}) - \nabla \cdot \left(D_i^{eff} \nabla c_i \right) - \nabla \cdot \left(\frac{z_i F D_i^{eff}}{RT} c_i \nabla \phi_e \right) = S_i \tag{6.9}$$

The effective ion diffusivity (Eq. (6.10)) was calculated using the following equation [16]:

$$D_i^{eff} = \varepsilon^{1.5} D_i \frac{\mu^0}{\mu} \tag{6.10}$$

where μ^0 is the solvent viscosity.

The former equation was solved for V^{2+}, V^{3+}, VO^{2+}, H^+, and HSO_4^- ions. The concentration of SO_4^{2-} was obtained according to the electroneutrality condition (Eq. (6.11)):

$$\sum_i z_i c_i = 0 \tag{6.11}$$

Charge transport equations in the photoelectrode

The transport of electrons and holes in the photoelectrode under bias potential and illumination was simulated using the drift-diffusion equation:

$$\frac{\partial c_i}{\partial t} - \nabla \cdot \left(D_i \nabla c_i \right) - \nabla \cdot \left(\frac{z_i F D_i}{RT} c_i \nabla \phi_{\mathrm{SC}} \right) = G_i - R_{rec,i} \tag{6.12}$$

where $\nabla \phi_{\mathrm{SC}}$ is the electric field in the photoelectrode and G_i is the generation rate of carrier i due to photon absorption given by [17]:

$$G_i = \frac{\eta_{\mathrm{inj}} \alpha(\lambda) I_0 e^{-\alpha(\lambda) x}}{N_a} \tag{6.13}$$

where η_{inj} is the electron injection efficiency, I_0 is the incident photon flux, N_a is the Avogadro number, and x is the distance from the outer surface (x_5) of the photoelectrode into the photoelectrode. The absorption coefficient, $\alpha(\lambda)$, at the wavelength λ, was calculated as follows [18]:

$$\alpha(\lambda) = \frac{A\lambda}{hc_0} \left(\frac{hc_0}{\lambda} - E_{\mathrm{g}} \right)^{1/2} \tag{6.14}$$

where A is the absorption constant, h is the Planck's constant, c_0 is the speed of light in vacuum and E_{g} is the photoelectrode bandgap.

The recombination of electrons and holes is given by the total recombination rate, $R_{rec,i}$, which considers the band-to-band, $R_{rec,\mathrm{BTB}}$, Auger, $R_{rec,\mathrm{Aug}}$, and Shockley-Read-Hall, $R_{rec,\mathrm{SRH}}$, recombination mechanisms [5]:

$$R_{rec,i} = R_{rec,\mathrm{BTB}} + R_{rec,\mathrm{Aug}} + R_{rec,\mathrm{SRH}} \tag{6.15}$$

$$R_{rec,\mathrm{BTB}} = \frac{N_a}{N_{\mathrm{donor}}\tau_{\mathrm{BTB,h}}}\left(c_{\mathrm{n}}c_{\mathrm{p}} - c_{\mathrm{int}}^2\right) \tag{6.16}$$

$$R_{rec,\mathrm{Aug}} = \left(N_a^2 C_{\mathrm{Aug,n}}c_{\mathrm{n}} + N_a^2 C_{\mathrm{Aug,p}}c_{\mathrm{p}}\right)\left(c_{\mathrm{n}}c_{\mathrm{p}} - c_{\mathrm{int}}^2\right) \tag{6.17}$$

$$R_{rec,\mathrm{SRH}} = \frac{\left(c_{\mathrm{e}}c_{\mathrm{h}} - c_{\mathrm{int}}^2\right)}{\tau_{\mathrm{SRH,e}}\left(c_{\mathrm{h}} + c_{\mathrm{int}}\right) + \tau_{\mathrm{SRH,h}}\left(c_{\mathrm{e}} + c_{\mathrm{int}}\right)} \tag{6.18}$$

where N_{donor} is the donor density, $C_{\mathrm{Aug},i}$ is the Auger recombination constant for charge carrier i and τ_i is the lifetime of the charge carrier i, determined with the following equation [18, 19]:

$$\tau_{\mathrm{SRH},i} = \frac{1}{\delta_i \upsilon_{th} N_{\mathrm{trap}}} \tag{6.19}$$

and the intrinsic carrier concentration in the photoelectrode, c_{int}, can be calculated with Eq. (6.20) [19]:

$$c_{\mathrm{int}} = \frac{\sqrt{N_{\mathrm{CB}}N_{\mathrm{VB}}}\,e^{-\frac{FE_{\mathrm{g}}}{2RT}}}{N_a} \tag{6.20}$$

with δ_i as the capture cross-section of charge carrier I and υ_{th} as thermal velocity. N_{trap}, N_{CB}, and N_{VB} are the trap density, electron density in the conduction band (CB), and the hole density in the valence band (VB), respectively.

The concentration of the charge carriers under dark conditions (e.g., when applying a bias potential under no illumination), $c_{i,\mathrm{dark}}$, was determined using the following equation:

$$\frac{\partial c_{i,\mathrm{dark}}}{\partial t} - \nabla\cdot\left(D_i\nabla c_{i,\mathrm{dark}}\right) - \nabla\cdot\left(\frac{z_i F D_i}{RT}c_{i,\mathrm{dark}}\nabla\phi_{\mathrm{SC}}\right) = 0 \tag{6.21}$$

Charge conservation equations

The electric current, expressed as current density ($\vec{i}$), due to transport of ions was determined using the following equation [15]:

$$\vec{i} = F\sum_i z_i\vec{N}_i \tag{6.22}$$

Thus, the charge conservation ($\nabla \cdot \vec{\imath}$) can be simulated by combining Eq. (6.8) with Eq. (6.22) as follows:

$$\nabla \cdot \vec{i} = \nabla \cdot \left(F \sum_i z_i c_i \vec{v} - F \sum_i z_i D_i^{\text{eff}} \nabla c_i - F^2 \sum_i \frac{z_i^2 D_i^{\text{eff}}}{RT} c_i \nabla \phi_{\text{e}} \right) \tag{6.23}$$

and the electrolyte conductivity (σ_{e}) can be estimated with Eq. (6.24).

$$\sigma_{\text{e}} = F^2 \sum_i \frac{z_i^2 D_i^{\text{eff}}}{RT} c_i \tag{6.24}$$

Eq. (6.23) can be rewritten as a function of the electrolyte conductivity as shown in Eq. (6.25). Also, in the event of an electrochemical reaction, charges between the electrolyte and electrode are exchanged. Thus, the volumetric current density (A m^{-3}) in the negative electrode is given by the flux of charges leaving or entering each phase [20]:

$$\nabla \cdot \left(F \sum_i z_i c_i \vec{v} \right) - \nabla \cdot \left(\frac{RT}{F \sum_i z_i} \nabla \sigma_{\text{e}} \right) - \nabla \cdot \left(\sigma_{\text{e}} \nabla \phi_{\text{e}} \right) = + j \tag{6.25}$$

The charge conservation between phases was simulated by assuming the flux of charges entering/leaving the solid phase ($\vec{\imath_{\text{s}}}$) the same as the flux of charges leaving/entering the liquid phase ($\vec{\imath_e}$) (Eq. (6.26)).

$$\nabla \cdot \vec{i}_{\text{s}} = -\nabla \cdot \vec{i}_{\text{e}} = - j \tag{6.26}$$

The charge conservation equation of the solid phase was described using Ohm's law:

$$\nabla \cdot \vec{i}_{\text{s}} = \nabla \cdot \left(\sigma_{\text{s}}^{\text{eff}} \nabla \phi_{\text{s}} \right) \tag{6.27}$$

where ϕ_{s} is the potential in the solid phase and $\sigma_{\text{s}}^{\text{eff}}$ is the effective conductivity of the electrode and bipolar plate.

In the positive chamber, the charge transfer occurs at the surface of the photoelectrode. Thus, it is assumed that j = 0 A m^{-3} (Eq. (6.25)). Instead, a proper boundary condition is applied to simulate the charge conservation, which is described in the section regarding boundary conditions.

The charge conservation ($\nabla \cdot \vec{i}_{\mathrm{e,mem}}$) in the membrane was simulated with Eq. (6.28).

$$\nabla \cdot \vec{i}_{\mathrm{e,mem}} = \nabla \cdot \left(\sigma_{\mathrm{mem}} \nabla \phi_{\mathrm{e,mem}} \right) \tag{6.28}$$

In the bulk of the photoelectrode, the electroneutrality condition is observed. However, near to the interface between the photoelectrode and the electrolyte, electroneutrality may not be observed due to depletion/accumulation of charges. The electrostatic potential at the photoelectrode, ϕ_{SC}, can be determined with the Poisson equation, which considers the distribution of electrons and holes [21]:

$$-\nabla \cdot \left(\nabla \phi_{\mathrm{SC}} \right) = \frac{F}{\varepsilon_{\mathrm{SC}} \varepsilon_0} \left(\frac{N_{\mathrm{donor}}}{N_a} + z_{\mathrm{p}} c_{\mathrm{p}} + z_{\mathrm{n}} c_{\mathrm{n}} \right) \tag{6.29}$$

where $\varepsilon_{\mathrm{SC}}$ and ε_0 are the permittivity of the photoelectrode and vacuum, respectively, and N_{donor} is the donor concentration. The electrostatic potential is assumed constant and equal to the band bending at the bulk of the photoelectrode. To determine the electrostatic potential in the space charge region, the thickness of the space charge layer (SCL), δ_{SCL}, is first estimated using Eq. (6.30) [21].

$$\delta_{\mathrm{SCL}} = \sqrt{\frac{2 \varepsilon_{\mathrm{SC}} \varepsilon_0 \left| \Delta E_{\mathrm{BB,total}} \right|}{F \dfrac{N_{\mathrm{donor}}}{N_a}}} \tag{6.30}$$

Then, Eq. (6.29) is simplified to the following set of equations which were solved in the photoelectrode region:

$$\begin{cases} \phi_{\mathrm{SC}} = \Delta E_{\mathrm{BB,total}} - \dfrac{F \dfrac{N_{\mathrm{donor}}}{N_a} \left(\delta_{\mathrm{SCL}} - x \right)^2}{2 \varepsilon_{\mathrm{SC}} \varepsilon_0} & 0 < x \le \delta_{\mathrm{SCL}} \;\&\; \Delta E_{\mathrm{BB,total}} > 0 \\ \phi_{\mathrm{SC}} = \Delta E_{\mathrm{BB,total}} + \dfrac{F \dfrac{N_{\mathrm{donor}}}{N_a} \left(\delta_{\mathrm{SCL}} - x \right)^2}{2 \varepsilon_{\mathrm{SC}} \varepsilon_0} & 0 < x \le \delta_{\mathrm{SCL}} \;\&\; \Delta E_{\mathrm{BB,total}} \le 0 \\ \phi_{\mathrm{SC}} = \Delta E_{\mathrm{BB,total}} & x > \delta_{\mathrm{SCL}} \end{cases} \tag{6.31}$$

where $x = 0$ is at the photoelectrode | electrolyte interface.

Reaction kinetics

The electrochemical reaction rate (j/nF) at the negative electrode is related to the overpotential by the Butler-Volmer equation [12]:

$$j_{-} = aFc_{\text{red}}^{\alpha_{\text{red}}} c_{\text{ox}}^{\alpha_{\text{ox}}} \left(k_{\text{ox}} \left(\frac{c_{\text{red}}^{\text{s}}}{c_{\text{red}}} \right) e^{\frac{\alpha_{\text{ox}} F\eta^{-}}{RT}} - k_{\text{red}} \left(\frac{c_{\text{ox}}^{\text{s}}}{c_{\text{ox}}} \right) e^{\frac{-\alpha_{\text{red}} F\eta^{-}}{RT}} \right) \tag{6.32}$$

where j is the volumetric current density, a is the surface area of the electrode, c_{red} and c_{ox} are the molar concentrations of the vanadium ion with the lowest and highest oxidation state, respectively; the superscript s refers to the electrode fibers, k is the reaction rate constant, α is the charge transfer coefficient and η^{-} is the overpotential at the negative electrode:

$$\eta^{-} = \phi_{\text{s}}^{-} - \phi_{\text{e}}^{-} - E^{-} \tag{6.33}$$

Similarly, the reaction rate at the surface of the photoelectrode can be related to the overpotential with the Tafel equation:

$$i_{+} = nkFc_{\text{red}}^{\alpha_{\text{red}}} c_{\text{ox}}^{\alpha_{\text{ox}}} \left(\frac{c_{\text{red}}^{\text{s}}}{c_{\text{red}}} \right) e^{\frac{\alpha_{\text{ox}} F\eta^{+}}{RT}} \tag{6.34}$$

where c_i^{s} is the concentration of the charge carrier i at the surface of the photoelectrode. The overpotential at the photoelectrode, η^{+}, is given by the difference between the *quasi*-Fermi energy level of holes, $E_{\text{F,p}}$, the potential in the liquid phase, and the redox potential of the electrolyte at the photoelectrode | electrolyte interface [21]:

$$\eta^{+} = E_{\text{F,p}} - \phi_{\text{e}}^{+} - E^{+} \tag{6.35}$$

where E^i is the cell reaction potential in the absence of current (OCP) in the positive (Eq. (6.36)) and negative (Eq. (6.37)) chambers, estimated from the Nernst equation:

$$E^{+} = E^{0,+} + \frac{RT}{F} \ln \left(\frac{c_{\text{VO}^{2+}} \left(c_{\text{H}^{+}} \right)^2}{c_{\text{V}^{3+}}} \right) \tag{6.36}$$

$$E^{-} = E^{0,-} + \frac{RT}{F} \ln \left(\frac{c_{\text{V}^{3+}}}{c_{\text{V}^{2+}}} \right) \tag{6.37}$$

where $E^{0,i}$ is the standard reduction potential.

Mass transfer

The mass transfer phenomena in the negative electrode can be described as the flux of mass transferred between the electrode fibers and the bulk solution (Eq. (6.38)) [22].

$$N_i^{\mathrm{s}} = k_{m,i}\left(c_i - c_i^{\mathrm{s}}\right) \tag{6.38}$$

where the mass transfer coefficient ($k_{m,i}$) refers to the mass transfer rate of species *i* from the electrode fibers to the bulk electrolyte and *vice-versa*. The mass transfer mechanism is controlled by advection and diffusion mechanisms, while the migration is typically considered negligible [22].

The mass transfer coefficient was computed using a correlation described elsewhere [23]:

$$k_{m,i} = 0.103\left(\frac{\mu}{D_i^{\mathrm{eff}}}\right)^{-0.615}\left(\frac{\rho d_{\mathrm{f}}}{\mu}\right)^{0.409}\vec{v}^{\,0.409} \tag{6.39}$$

The electrochemical reactions occur only at the electrode fibers. Since the charge is conserved, the flux of ions must be in equilibrium with the flux of electrons at the surface of the electrode (Eq. (6.40) and Eq. (6.41)).

$$k_{m,\mathrm{red}}\left(c_{\mathrm{red}} - c_{\mathrm{red}}^{\mathrm{s}}\right) = \frac{j}{aF} \tag{6.40}$$

$$k_{m,\mathrm{ox}}\left(c_{\mathrm{ox}} - c_{\mathrm{ox}}^{\mathrm{s}}\right) = -\frac{j}{aF} \tag{6.41}$$

The expressions used to determine the concentration of vanadium ions at the electrode fibers (c_i^{s}) as a function of the overpotential can be found elsewhere [12].

Quasi-Fermi energy levels at the photoelectrode

To determine the *quasi*-Fermi energy levels at the CdS photoelectrode, a comprehensive analysis of the energy band diagram under different operating conditions is required (Figure 6.2).

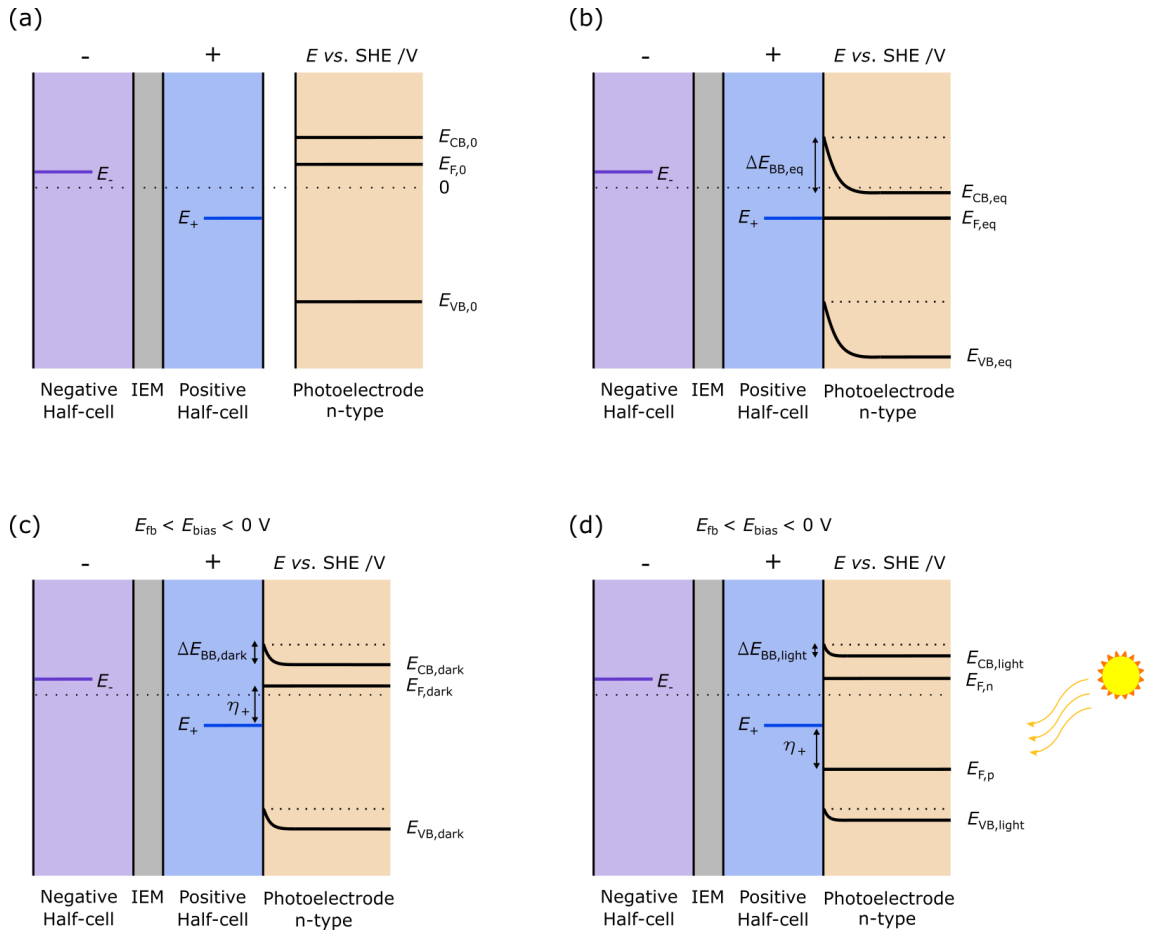

Figure 6.2 – Schematic representation of the energy band diagram of a solar redox flow cell when (a) the photoelectrode (*n*-type) and the electrolyte are not in contact, (b) the photoelectrode and the electrolyte are in contact and in equilibrium, (c) a potential (E_{bias}) is applied to the cell and (d) a potential is applied to the cell and the cell is under solar illumination. Illustration not to scale.

When the photoelectrode is not in contact with the electrolyte, the conduction, $E_{CB,0}$, and valence, $E_{VB,0} = E_{CB,0} + E_g$, bands and the Fermi energy level, $E_{F,0}$ (Eq. (6.42)), are flat (Figure 6.2 (a)) [21].

$$E_{F,0} = E_{CB,0} - \frac{RT}{F} \ln\left(\frac{N_{donor}}{N_{CB}}\right) \tag{6.42}$$

The equilibrium condition is observed when the photoelectrode is in contact with the electrolyte and no potential is applied nor light is reaching the photoelectrode (Figure 6.2

(b)). In equilibrium, the Fermi energy level is equal to the electrolyte redox potential ($E_{F,eq} = E^+$) and the conduction and valence bands suffer a shift equivalent to the difference between the Fermi energy level before the photoelectrode is in contact with the electrolyte and the Fermi energy level under equilibrium conditions, $\Delta E_{BB,eq}$:

$$\Delta E_{BB,eq} = E_{F,eq} - E_{F,0} \tag{6.43}$$

$$E_{CB,eq} = E_{CB,0} + \Delta E_{BB,eq} \tag{6.44}$$

The concentration of electrons under equilibrium conditions, $c_{n,eq}$, is assumed to be equal to the donor concentration, N_{donor}, and the concentration of holes in equilibrium is determined as [19]:

$$c_{p,eq} = \frac{c_{int}^2}{c_{n,eq}} \tag{6.45}$$

When a potential, E_{bias}, is applied to the SRFC and no light is reaching the photoelectrode, the equilibrium condition is no longer observed and the total overpotential of the SRFC can be calculated with the following equation:

$$\eta_{total} = \eta_{total}^{+} + \eta_{total}^{-} = E_{bias} - (E^+ - E^-) \tag{6.46}$$

Under such circumstances, the energy bands are shifted by an amount equivalent to the total overpotential at the photoelectrode, η^{+}_{total} (Eq. (6.47)), when compared to the equilibrium condition (Figure 6.2 (c)):

$$\eta_{total}^{+} = E_{bias} - E^+ + E^- - \eta_{total}^{-} = E_{bias} - E^+ + \phi^- \tag{6.47}$$

where η^{-}_{total} is the total overpotential at the negative electrode, which considers the activation, ohmic, and concentration overpotentials. The band bending and the energy band potentials under dark condition can be calculated as:

$$\Delta E_{BB,dark} = \Delta E_{BB,eq} + \eta_{total}^{+} \tag{6.48}$$

$$E_{F,dark} = E_{F,eq} + \eta_{total}^{+} \tag{6.49}$$

$$E_{CB,dark} = E_{CB,0} + \Delta E_{BB,dark} \tag{6.50}$$

Under illumination, the concentration of free electrons and holes increases when compared to the dark condition. Thus, the shift observed in the energy levels due to the absorption of photons can be estimated by comparing the concentration of electrons under the light condition (Eq. (6.12)) and under the dark condition (Eq. (6.21)) (Figure 6.2 (d)). The band bending and the conduction band potentials of a photoelectrode under illumination and bias potential can be determined as follows:

$$\Delta E_{\mathrm{BB,total}} = \Delta E_{\mathrm{BB,dark}} - \frac{RT}{F}\ln\left(\frac{c_{\mathrm{n}}}{c_{\mathrm{n,dark}}}\right) = E_{\mathrm{F,eq}} - E_{\mathrm{F,0}} + \eta^{+}_{\mathrm{total}} - \frac{RT}{F}\ln\left(\frac{c_{\mathrm{n}}}{c_{\mathrm{n,dark}}}\right) \tag{6.51}$$

$$E_{\mathrm{CB}} = E_{\mathrm{CB,0}} + \Delta E_{\mathrm{BB,total}} \tag{6.52}$$

and the *quasi*-Fermi energy level of electrons, $E_{\mathrm{F,n}}$, can be determined with Eq. (6.53) while the *quasi*-Fermi energy level of holes can be determined using Eq. (6.54):

$$E_{\mathrm{F,n}} = E_{\mathrm{F,dark}} - \frac{RT}{F}\ln\left(\frac{c_{\mathrm{n}}}{c_{\mathrm{n,dark}}}\right) = E_{\mathrm{F,0}} + \Delta E_{\mathrm{BB,total}} \tag{6.53}$$

$$E_{\mathrm{F,p}} = E_{\mathrm{F,dark}} + \frac{RT}{F}\ln\left(\frac{c_{\mathrm{p}}}{c_{\mathrm{p,dark}}}\right) = E_{\mathrm{F,0}} + \Delta E_{\mathrm{BB,total}} + \frac{RT}{F}\ln\left(\frac{c_{\mathrm{p}}}{c_{\mathrm{p,dark}}}\frac{c_{\mathrm{n}}}{c_{\mathrm{n,dark}}}\right) \tag{6.54}$$

Finally, Eq. (6.52) can be rewritten as a function of the electrostatic potential of the photoelectrode as follows:

$$E_{\mathrm{CB}} = E_{\mathrm{CB,0}} + \phi_{\mathrm{SC}} \tag{6.55}$$

Assuming that the Fermi energy level $E_{\mathrm{F,0}}$ is equal to the flat band potential, E_{fb}, Eq. (6.31) becomes similar to the band bending determined using the Mott-Schottky equation:

$$\Delta E_{\mathrm{BB,total}} = E^{+} + \eta^{+}_{\mathrm{total}} - E_{\mathrm{fb}} - \frac{RT}{F}\ln\left(\frac{c_{\mathrm{n}}}{c_{\mathrm{n,dark}}}\right) \tag{6.56}$$

Using Eq. (6.56) in Eq. (6.53) and Eq. (6.54), the *quasi*-Fermi energy levels can be rewritten as:

$$E_{\mathrm{F,n}} = E^{+} + \eta^{+}_{\mathrm{total}} - \frac{RT}{F}\ln\left(\frac{c_{\mathrm{n}}}{c_{\mathrm{n,dark}}}\right) \tag{6.57}$$

$$E_{\mathrm{F,p}} = E^{+} + \eta^{+}_{\mathrm{total}} + \frac{RT}{F}\ln\left(\frac{c_{\mathrm{p}}}{c_{\mathrm{p,dark}}}\right) \tag{6.58}$$

Compared to VRFB models [12], $E^{+} + \eta^{+}_{\mathrm{total}}$ is equivalent to the potential in the solid phase of the positive electrode (conductor), ϕ_{s}^{+}. Thus, the third term on the right-hand side of Eq. (6.57) and Eq. (6.58) represents the potential that arises in a *p*-type and an *n*-type photoelectrode, respectively, due to photogeneration of charges (photopotential), E_{ph}.

6.3.2. Boundary and initial conditions

At the inlet of both chambers ($y = y_0$, $x_1 \leq x \leq x_2$, and $x_3 \leq x \leq x_4$), the electrolyte flow velocity was given as boundary condition (Eq. (6.59)). Additionally, the concentration of each species varied at every timestep (Eq. (6.60)).

$$-\vec{n}\cdot\vec{v} = \frac{Q_{\mathrm{in}}}{A_{\mathrm{in}}} \tag{6.59}$$

$$c_i = c_{\mathrm{in},i}(t) \tag{6.60}$$

where Q_{in} is the inlet volumetric flow rate, A_{in} is the inlet channel area, and $c_{\mathrm{in,i}}(t)$ is the inlet concentration of species *i* at instant *t*.

The inlet concentration $c_{\mathrm{in,i}}(t)$ was determined from a mass balance of the electrolyte tanks (Eq. (6.61)).

$$\frac{\mathrm{d}c_{\mathrm{in},i}(t)}{\mathrm{d}t} = \frac{1}{V_{\mathrm{tank}}}\left(\int \vec{v}_{\mathrm{out}} c_{\mathrm{out},i} dA_{\mathrm{out}} - \int \vec{v}_{\mathrm{in}} c_{\mathrm{in},i} dA_{\mathrm{in}}\right) \tag{6.61}$$

where V_{tank} is the electrolyte volume in each tank and $c_{\mathrm{out},i}$ is the outlet concentration of species *i*.

The absolute pressure at the outlets ($y = y_1$, $x_1 \leq x \leq x_2$, and $x_3 \leq x \leq x_4$) was assumed constant and equal to the atmospheric pressure (p_{atm}, Eq. (6.62)). The no-flux condition was used for the remaining variables:

$$p = p_{\mathrm{atm}} \mid \vec{n}\cdot\left(-D_i^{\mathrm{eff}}\nabla c_i\right) = 0 \mid \vec{n}\cdot\left(-\sigma_{\mathrm{s}}^{\mathrm{eff}}\nabla\phi_{\mathrm{s}}\right) = 0 \mid \vec{n}\cdot\left(-\sigma_{\mathrm{e}}\nabla\phi_{\mathrm{e}}\right) = 0 \tag{6.62}$$

The negative bipolar plate was used as a reference electrode by using the following boundary condition at $y_0 \le y \le y_1$ and $x = x_0$:

$$\phi_s = 0 \tag{6.63}$$

At the photoelectrode | electrolyte interface ($y_0 \le y \le y_1$, $x = x_4$) the following boundary conditions were used to simulate the concentration change of the charged species due to the photoelectrochemical reaction (Eq. (6.1)), and the surface recombination of electrons and holes:

$$\begin{cases} -\vec{n}\cdot\left(-D_{V^{3+}}^{\text{eff}}\nabla c_{V^{3+}}\right) = -\dfrac{i}{nF} \\ -\vec{n}\cdot\left(-D_{VO^{2+}}^{\text{eff}}\nabla c_{VO^{2+}}\right) = +\dfrac{i}{nF} \\ -\vec{n}\cdot\left(-D_{H^{+}}^{\text{eff}}\nabla c_{H^{+}}\right) = +2\dfrac{i}{nF} \\ \vec{n}\cdot\left(-D_{n}\nabla c_{n}\right) = -k_{sr}\left(c_{n} - c_{n,\text{dark}}\right) \\ \vec{n}\cdot\left(-D_{p}\nabla c_{p}\right) = -\dfrac{i}{nF} - k_{sr}\left(c_{p} - c_{p,\text{dark}}\right) \end{cases} \tag{6.64}$$

where k_{sr} is the surface recombination rate. Additionally, the electrostatic potential of the photoelectrode was set to 0 and the following boundary condition was used to simulate the accumulation of positive charges in the electrolyte owing to the photoelectrochemical reaction:

$$\phi_{SC} = 0 \,|\, -\vec{n}\cdot\nabla\cdot\left(\sigma_e\nabla\phi_e\right) = +i \tag{6.65}$$

At the outer surface of the photoelectrode ($y_0 \le y \le y_1$, $x = x_5$) the following boundary conditions were used for the electrostatic potential and electrons transport equation:

$$\phi_{SC} = \Delta E_{BB,\text{total}} \,|\, -\vec{n}\cdot\left(-D_e\nabla c_e\right) = -\frac{i}{nF} \tag{6.66}$$

A single domain approach was adopted for the potential in the liquid phase at the positive chamber, membrane and negative electrode, and for the potential in the solid phase at the negative electrode and negative current collector. For the remaining boundaries ($x = x_1$, $x = x_2$ and $x = x_3$), the no-flux condition was adopted for all variables.

The initial conditions (t = 0 s) used in the present model were:

$$c_i = c_i^0 \mid c_n = c_{n,eq} \mid c_p = c_{p,eq} \mid \phi_s^- = 0 \mid \phi_e^i = (E^+ - E^- + \eta_{total}) \cdot b - E^i \quad (6.67)$$

where b is a constant that assumes values of 0 and 1 at the negative and positive electrodes, respectively. The initial concentration of the species (c_i^0) was defined as a function of SoC (Eq. (6.68)) and total vanadium and sulfuric acid concentration.

$$SoC = \frac{c^-_{V^{2+}}}{c^-_{V^{3+}} + c^-_{V^{2+}}} = \frac{c^+_{VO^{2+}}}{c^+_{V^{3+}} + c^+_{VO^{2+}}} \quad (6.68)$$

The equations used to determine the initial concentrations of the ionic species are summarized in Eq. (6.69).

$$\begin{cases} c^{0,-}_{V^{2+}} = c_V \cdot SoC \\ c^{0,-}_{V^{3+}} = c^{0,+}_{V^{3+}} = c_V (1 - SoC) \\ c^{0,+}_{VO^{2+}} = c_V \cdot SoC \\ c^{0,+}_{H^+} = c_{H_2SO_4} + 2c_V \cdot SoC \end{cases} \quad (6.69)$$

where c_V is the total vanadium concentration in the electrolyte (0.4 M) and c_{H2SO4} is the sulfuric acid concentration in the electrolyte (2 M).

6.3.3. Numerical procedure

The computational domain was divided into five zones with 6000 elements. The governing equations were discretized using a finite volume method and solved using the commercial software package Fluent 19.2. The SIMPLE algorithm, pre-installed within the software package, was used to solve the pressure-velocity coupling for unsteady-state conditions. Species and charge transport equations were implemented using user-defined scalars and solved with the Second Order Upwind discretization method. The remaining equations, including the boundary and initial conditions, were implemented using user-defined functions. The under-relaxation factor was used for the species and charge transport equations to handle the convergence problems. A residual value of 10^{-6} was used as a stop condition for every time step for all governing equations. The value of the parameters used in the simulations can be found in Appendix C.1.

6.4. Results and discussion

6.4.1. Model validation

The proposed model was validated against the experimental polarization (*i*-*V*) curve (Figure 6.3) obtained by Azevedo et al. [11]. The cell is initially discharged (0.05 % SoC). The potential applied to the cell (bias potential) ranged from -1 V to 0 V (assuming the negative electrode as the reference electrode) with a scan rate of 10 mV s^{-1} and the current density was calculated using Eq. (6.34).

Figure 6.3 (a) shows the experimental and simulated *i*-*V* curves; the simulated curve displays an acceptable fitting to the experimental values, with a better agreement at the beginning and at the end of the *i*-*V* curve. The latter are the most relevant zones in an *i*-*V* curve since both are related to characteristics of the photoelectrode: in an *n*-type photoelectrode, the onset potential is the lowest potential at which the photoelectrochemical reaction occurs, leading to a current density increase, and it is related to the Fermi energy level – settled after the band bending potential being established [24], Eq. (6.56). The current density plateau is related to the concentration of holes available for the photoelectrochemical reaction, Eq. (6.35) and Eq. (6.58).

The values used for the fitting parameters are close to those found in the literature, as can be seen in Table 6.1. However, there is no information in the literature regarding the reaction rate constant for the CdS photoelectrode/vanadium electrolyte pair. As expected, this reaction constant is much lower than the corresponding one for the carbon felt electrode [25].

Table 6.1 – Comparison between the values used in the simulation and values found in the literature for the fitting parameters.

Parameter	Fitted value	Literature value	Ref.
Surface recombination rate, k_{sr}	3×10^{3} m s^{-1}	1×10^{5} m s^{-1}	[26]
Absorption constant, A	7.15×10^{6} m^{-1} $eV^{-1/2}$	$3 - 10 \times 10^{6}$ m^{-1} $eV^{-1/2}$	[18, 27]
Conduction band potential, $E_{CB,0}$	-0.763 V	0.72 V	[28]

Figure 6.3 (b) shows that the simulated current density at the photoelectrode (Eq. (6.34)) and at the negative electrode (Eq. (6.32)) are the same. The experimental *i*-*V* curve (Figure

6.3 (a)) was obtained using a two electrodes configuration: the negative side is the counter electrode and the photoelectrode is the working electrode [11]. The same assumption was made for the simulation. Thus, the SRFC will work in closed circuit when a bias potential is applied; the number of electrons leaving the photoelectrode must be the same number of electrons reaching the negative electrode. The current response, which is settled by the reaction, must be the same on both sides; this guarantees charge conservation.

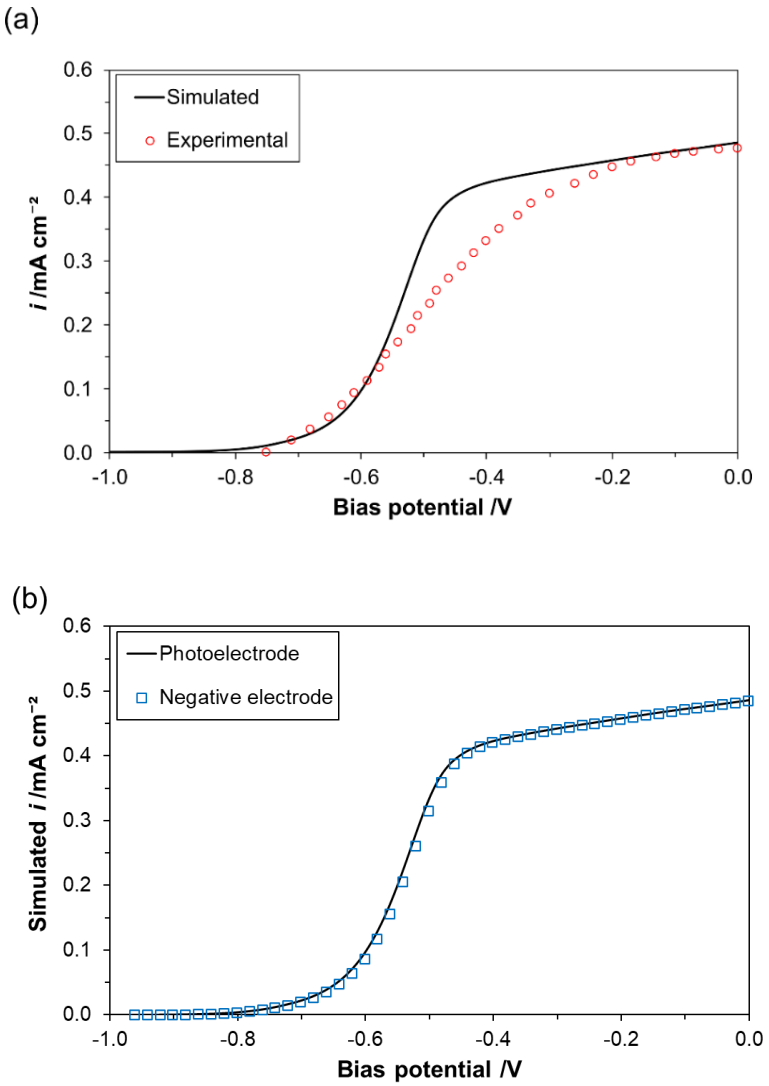

Figure 6.3 – (a) Simulated and experimental current density (*i*) response (*i*-*V* curve) of the photoelectrode in a solar vanadium redox flow cell with 4 cm^2 active area and (b) comparison between the simulated current density response at the photoelectrode and at the negative electrode.

6.4.2. Energy band diagram

To have a deep insight on the model response, especially in which concerns the photoelectrode, the energy band diagram is plotted for three different bias potentials (E_{bias}) and under illumination: when there is an accumulation of electrons at the conduction band ($\Delta E_{BB} < 0$ V, e.g., E_{bias} = -1.00 V, Figure 6.4 (a)) when there is no accumulation/depletion of charges ($\Delta E_{BB} = 0$ V, E_{bias} = -0.73 V, Figure 6.4 (b)) and when there is depletion of electrons ($\Delta E_{BB} > 0$ V, e.g., E_{bias} = -0.50 V, Figure 6.4 (c)). The photopotential, E_{ph}, shown in Figure 6.4, was calculated as $E_{ph} = E_{F,p} - E_{F,n}$. $E_{F,n}$ and $E_{F,p}$ were determined using Eq. (6.57) and Eq. (6.58), respectively.

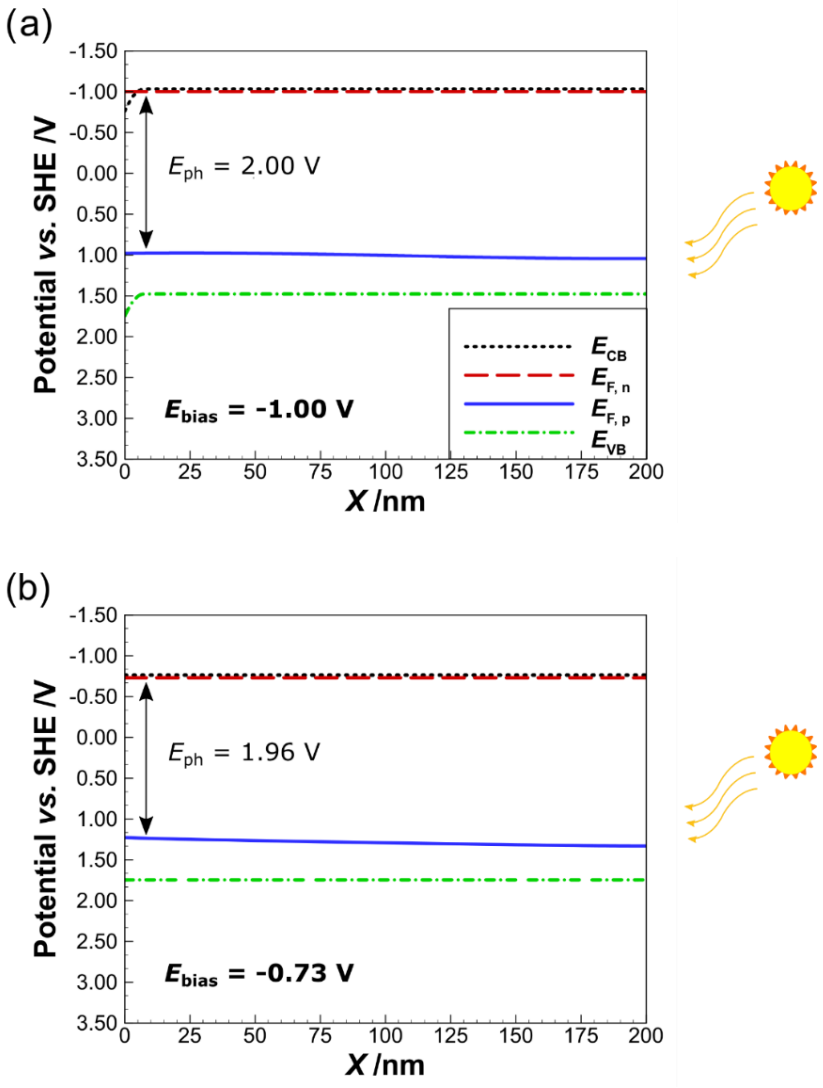

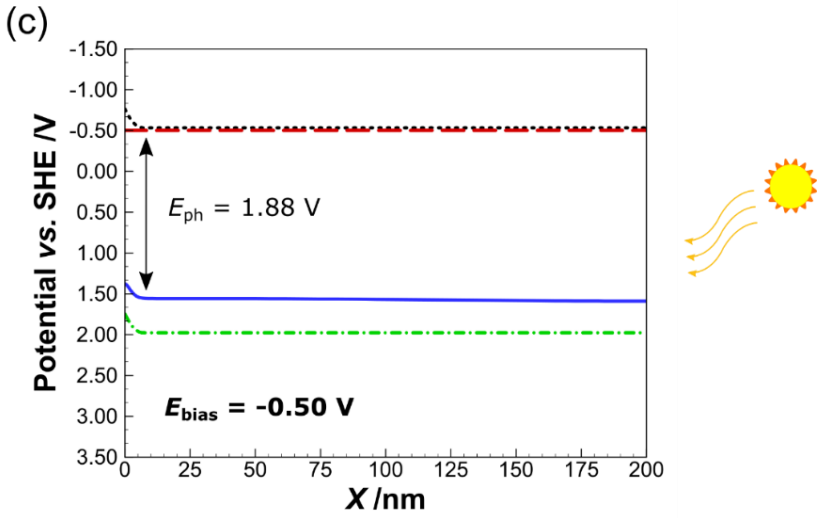

Figure 6.4 – Potential of the conduction band (black dotted line), valence band (green dash-dotted line), *quasi*-Fermi energy level of the electrons (red dashed line), and *quasi*-Fermi energy level of the holes (blue solid line) when there is (a) accumulation of electrons (ΔE_{BB} < 0 V, E_{bias} = -1.00 V), (b) no accumulation/depletion of charges (ΔE_{BB} = 0 V, E_{bias} = -0.73 V) and (c) depletion of electrons (ΔE_{BB} > 0 V, E_{bias} = -0.50 V). X is the distance from the photoelectrode | electrolyte interface (X = 0 nm, x_4, Figure 6.1) to the outer surface of the photoelectrode (X = 200 nm, x_5, Figure 6.1).

Figure 6.4 shows the simulated energy band shift for different bias potentials. The profile of the conduction and valence bands and the *quasi*-Fermi energy level of the electrons follow the trends reported in the literature [25, 29]; the depletion and the accumulation layers are captured when the band bending is positive or negative, respectively, and the *quasi*-Fermi energy level of the electrons remains flat regardless of the bias potential. The *quasi*-Fermi energy level profile of the holes is also shown; since back-illumination was considered, the shape of the *quasi*-Fermi energy level is different from the usual illustrations present in the literature [25, 29].

To further investigate the *quasi*-Fermi energy level profile of the holes, the concentration of holes at the photoelectrode | electrolyte interface, when under bias potential and illumination, and when under dark conditions, is plotted against the bias potential (Figure 6.5).

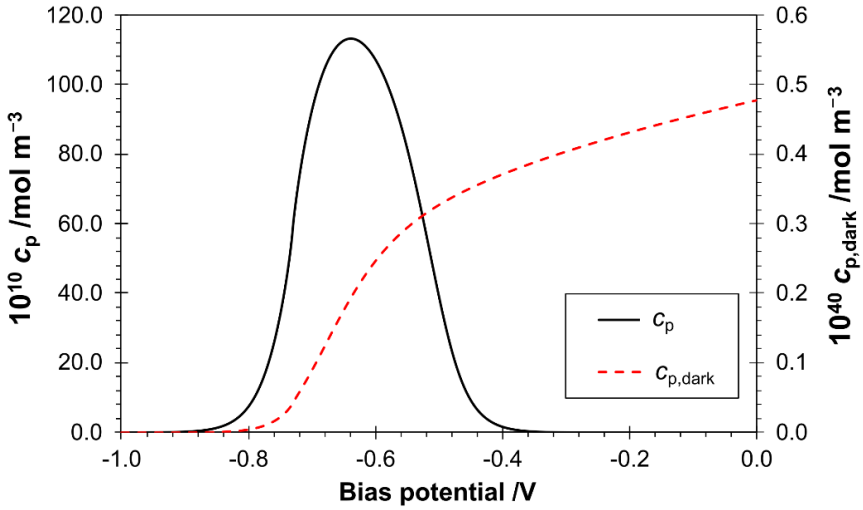

Figure 6.5 – Concentration of holes at the photoelectrode | electrolyte interface under illumination (c_p, black solid line) and dark ($c_{p,dark}$ red dashed line) conditions at different bias potentials.

Figure 6.5 shows that the concentration of holes under illumination increases up to a potential of -0.64 V; surface reaction and recombination are not sufficient to overcome the photogeneration of holes. This trend is reversed when E_{bias} > -0.64 V, when the concentration of holes starts to decrease. Thus, depletion of holes at the photoelectrode | electrolyte interface is expected when E_{bias} > -0.64 V. This is according to Figure 6.4 (c) which shows that, when E_{bias} = -0.50 V, the *quasi*-Fermi energy level of the holes is lowest at the photoelectrode | electrolyte interface.

There is an ongoing discussion regarding whether the photopotential displayed by the photoelectrode should be obtained as the potential difference between both *quasi*-Fermi energy levels [30]. The photopotential is the potential that arises at the photoelectrode due to photogeneration of charges. It can, thus, be determined by subtracting the potential corresponding to the concentration of the minority charge carrier under illumination and the potential corresponding to the concentration under dark - third right-hand side term of Eq. (6.58). A photopotential of 2.00 V, 1.96 V, and 1.88 V was computed when a potential of -1.00 V, -0.73 V, and -0.50 V was applied, which corresponds to the same photopotential determined using the following equation: $E_{ph} = E_{F,p} - E_{F,n}$ (Figure 6.4). The latter equation is

based on the assumption that there is no photogeneration of major carriers: $E_{F,n} = E_{F,dark}$ and, consequently, $c_n = c_{n,dark}$ (*c.f.* Eq. (6.49) and Eq. (6.57)). These results show that the photogeneration of electrons (major carrier) in the CdS photoelectrode does not lead to a significant change in the total concentration of electrons, as indicated by other authors [4].

Ideally, the simulated photopotential should be compared to the experimental photopotential. However, such information was not available at Azevedo et al. [11]. Furthermore, the photopotential, at the photoelectrode | electrolyte interface, does not remain constant for different bias potentials. This behavior is expected since the concentration of charges does not remain constant with the increasing bias potential (Figure 6.5); the rate of consumption of holes, due to photoelectrochemical reaction, becomes greater than the rate of photogeneration of holes, as the bias potential is increased.

6.4.3. The effect of recombination

The recombination of electrons and holes leads to a loss of performance [31]. In this model, four different recombination mechanisms were simulated: surface recombination, radiative band-to-band recombination, Auger recombination, and Shockley-Read-Hall (SRH) recombination. The impact of each recombination mechanism in the performance of the SRFC was assessed by increasing the recombination rate of each recombination mechanism by one order of magnitude (Figure 6.6), compared with the baseline values (Appendix C.1). The recombination rate of the band-to-band and SRH recombination mechanisms can be determined as $k_{BTB,h} = 1/\tau_{BTB,h}$ and $k_{SRH} = 1/\tau_{SRH}$, respectively.

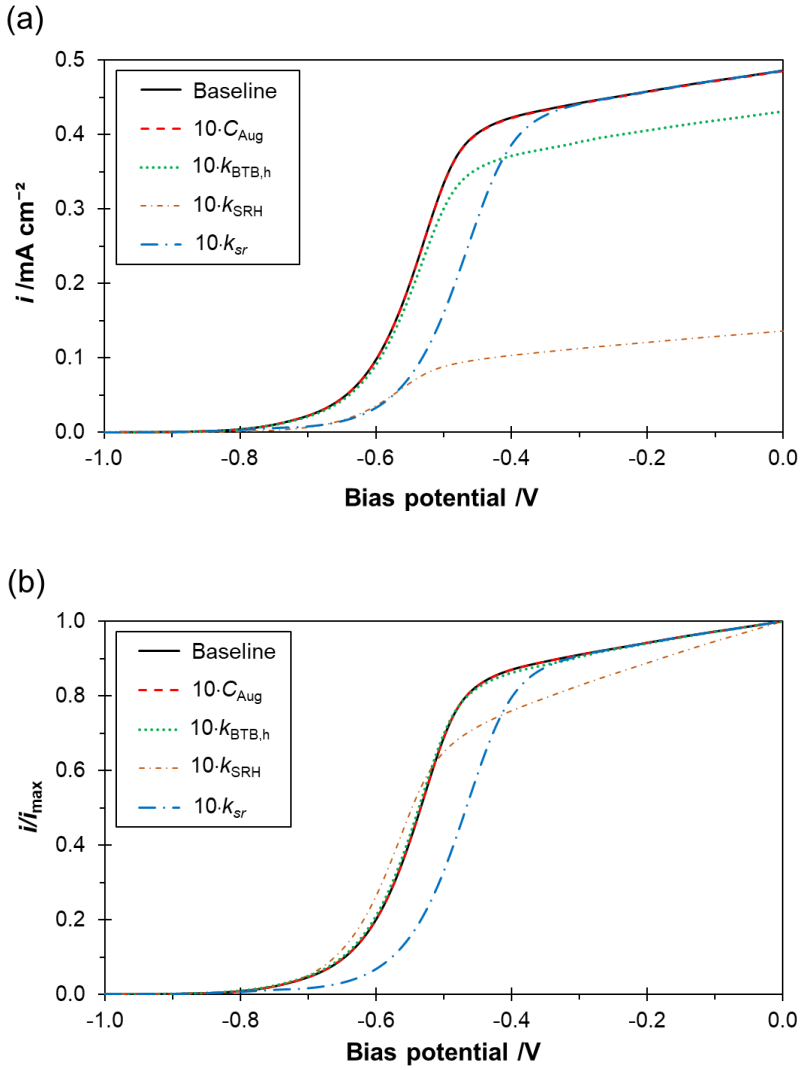

Figure 6.6 – Simulated (a) current density response (*i*-*V* curve) and (b) normalized *i*-*V* curve of the photoelectrode for baseline parameters (black solid line) and for higher band-to-band recombination (green dotted line, 10 × $k_{BTB,h}$), SRH recombination (yellow small dashed line, 10 × k_{SRH}), Auger recombination (red dashed line, 10 × C_{Aug}) and surface recombination (blue long dashed line, 10 × k_{sr}) rates.

As Figure 6.6 shows, increasing the recombination rate of the different recombination mechanisms by a factor of ten does not lead to the same outcome: when the band-to-band and the SRH recombination rates are increased, the maximum current decreases (Figure 6.6 (a)) and the current increases at a higher rate when E_{bias} > -0.45 V (Figure 6.6 (b)). This becomes more evident when the SRH recombination rate is increased. In a pure CdS

photoelectrode, it is expected the band-to-band recombination to be dominant since it is a direct bandgap photoelectrode [25]. Nonetheless, the SRH recombination becomes more significant when the CdS photoelectrode has imperfections [19]. Furthermore, lower current densities are obtained under bias potentials less than -0.35 V when the surface recombination rate is increased. However, no change in the maximum current is observed. This behavior was also observed by Cendula et al. [4], who developed a mathematical model for water splitting. Other authors [32, 33] demonstrated experimentally that surface recombination can modify the onset potential, which supports the model predictions. None of the previous behaviors were observed when increasing the Auger recombination rate since its magnitude is considerably smaller than the remaining recombination rates.

The concentration of holes at the photoelectrode | electrolyte interface, when using the different recombination rates, is illustrated in Figure 6.7. This plot allows further understanding about the impact of recombination in the performance of the SRFC.

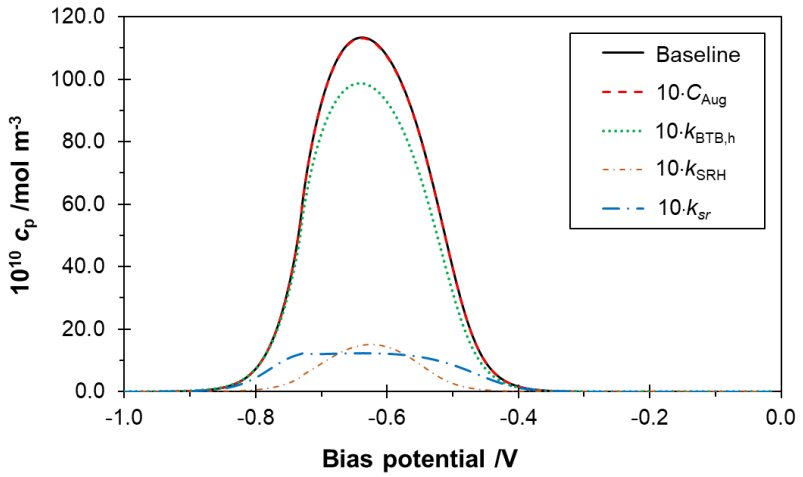

Figure 6.7 – Concentration of holes at the photoelectrode | electrolyte interface (c_p) for baseline parameters (black solid line) and for higher band-to-band recombination (green dotted line, 10 × $k_{BTB,h}$), SRH recombination (yellow small dashed line, 10 × k_{SRH}), Auger recombination (red dashed line, 10 × C_{Aug}) and surface recombination (blue long dashed line, 10 × k_{sr}) rates.

The band-to-band and SRH recombination mechanisms occur in the bulk of the photoelectrode and, as Figure 6.7 shows, these recombination mechanisms affect the

photogeneration of charges; when the recombination rate of such mechanisms increases, the concentration of holes in the photoelectrode decreases. Figure 6.3 (a) and Figure 6.5 show that the maximum current is limited by the concentration of holes. Therefore, the performance loss observed when the band-to-band and the SRH recombination rates increase can be assigned to the holes concentration decrease. This is more noticeable when the SRH recombination rate increases.

The surface recombination has a different effect on the performance of an SRFC when compared to the other recombination mechanisms; the concentration of holes does not suffer a significant change in the bulk of the photoelectrode, but it is greatly reduced at the photoelectrode | electrolyte interface. Thus, it acts as a competing mechanism for the surface reaction. This is observed at - 0.75 V < E_{bias} < -0.50 V (Figure 6.7), where the concentration of holes is greatly decreased but suffers smaller variations compared to the other cases; the surface recombination occurs at a greater extent than the surface reaction and limits the concentration of holes. Ultimately, a higher bias potential is required for the surface reaction to achieve the same extent as in the other cases. For example, when the surface recombination rate increases by one order of magnitude, the concentration of holes starts suffering a significant decrease at E_{bias} > -0.50 V.

6.5. Conclusion

The first 2D dynamic phenomenological model of an SRFC was developed by incorporating the mass, momentum and charge conservation equations, the species and charge transport equations, and the photoelectrochemical and electrochemical reaction equations. The model was used to simulate an *i-V* curve which was then compared to the experimental data [11]. Despite the clear challenge of simulating a photoelectrode due to scarce information, the simulation was successfully validated; the simulated data fitted well to the experimental data in the most relevant zones.

Energy bands were simulated using different bias potentials and the response of the model agrees with the information found in the literature for the conduction and valence bands and for the *quasi*-Fermi energy level of the electrons. The accumulation of electrons was observed in the space charge region when the bias potential was lower than the flat band potential, while the electrons depletion was observed when the bias potential was higher than

the flat band potential. In addition, the *quasi*-Fermi energy level of the electrons remains flat regardless of the bias potential. The holes' *quasi*-Fermi energy level profile obtained in this work is different from schematic diagrams found in the literature since back illumination was considered. Regardless, the depletion of holes due to surface reaction and surface recombination is accurately observed in the space charge region.

The model was also used to study the impact of the recombination mechanisms in the performance of an SRFC. It was found that the maximum current density decreases with the band-to-band and SRH recombination rates increase; both recombination mechanisms lower the concentration of holes in the bulk of the photoelectrode. On the other hand, surface recombination acts as a competing mechanism with the photoelectrochemical reaction. Thus, higher bias potentials are required for the photoelectrochemical reaction to overcome the surface recombination, and the onset potential is shifted towards higher values. Ultimately, it can be concluded that the model has a good response to variations in the bias potential and surface recombination rates.

6.6. References

1. L. Cao, M. Skyllas-Kazacos, and D.-W. Wang, *Solar Redox Flow Batteries: Mechanism, Design, and Measurement.* Advanced Sustainable Systems, 2018. **2**(8-9): p. 1800031.
2. W. Li et al., *High-performance solar flow battery powered by a perovskite/silicon tandem solar cell.* Nature Materials, 2020. **19**(12): p. 1326-1331.
3. Z. Wei, Y. Shen, D. Liu, and F. Liu, *An All-vanadium Continuous-flow Photoelectrochemical Cell for Extending State-of-charge in Solar Energy Storage.* Scientific Reports, 2017. **7**(1): p. 629.
4. P. Cendula et al., *Calculation of the Energy Band Diagram of a Photoelectrochemical Water Splitting Cell.* The Journal of Physical Chemistry C, 2014. **118**(51): p. 29599-29607.
5. Y.K. Gaudy and S. Haussener, *Utilizing modeling, experiments, and statistics for the analysis of water-splitting photoelectrodes.* Journal of Materials Chemistry A, 2016. **4**(8): p. 3100-3114.
6. A. Iqbal and K. Bevan, *The impact of boundary conditions on calculated photovoltages and photocurrents at photocatalytic interfaces.* MRS Communications, 2018: p. 1-8.
7. A. Iqbal and K.H. Bevan, *Simultaneously Solving the Photovoltage and Photocurrent at Semiconductor–Liquid Interfaces.* The Journal of Physical Chemistry C, 2018. **122**(1): p. 30-43.
8. A. Iqbal, M.S. Hossain, and K.H. Bevan, *The role of relative rate constants in determining surface state phenomena at semiconductor–liquid interfaces.* Physical Chemistry Chemical Physics, 2016. **18**(42): p. 29466-29477.
9. N.M. Delgado, R. Monteiro, M. Abdollahzadeh, P. Ribeirinha, A. Bentien, and A. Mendes, *2D-dynamic phenomenological modelling of vanadium redox flow batteries – Analysis of the mass transport related overpotentials.* Journal of Power Sources, 2020. **480**: p. 229142.
10. H. Zhang, H. Wang, and J. Xuan, *Rational design of photoelectrochemical cells towards bias-free water splitting: Thermodynamic and kinetic insights.* Journal of Power Sources, 2020. **462**: p. 228113.
11. J. Azevedo et al., *Unbiased solar energy storage: Photoelectrochemical redox flow battery.* Nano Energy, 2016. **22**.

12. D. You, H. Zhang, and J. Chen, *A simple model for the vanadium redox battery.* Electrochimica Acta, 2009. **54**(27): p. 6827-6836.
13. G. Galdi, *An Introduction to the Mathematical Theory of the Navier-Stokes Equations*. Vol. I. 2011, New York: Springer.
14. R. O'Hayre, S.-W. Cha, W. G. Colella, and F. B. Prinz, *Fuel Cell Fundamentals*. third ed. 2016: John Wiley & Sons.
15. R.F. Probstein, *Physicochemical Hydrodynamics*. second ed. 2005: Wiley-Interscience.
16. X.L. Zhou, T.S. Zhao, L. An, Y.K. Zeng, and X.H. Yan, *A vanadium redox flow battery model incorporating the effect of ion concentrations on ion mobility.* Applied Energy, 2015. **158**: p. 157-166.
17. L. Andrade, T. Lopes, H.A. Ribeiro, and A. Mendes, *Transient phenomenological modeling of photoelectrochemical cells for water splitting – Application to undoped hematite electrodes.* International Journal of Hydrogen Energy, 2011. **36**(1): p. 175-188.
18. A. Benmir and M.S. Aida, *Simulation of a thin film solar cell based on copper zinc tin sulfo-selenide Cu2ZnSn(S,Se)4.* Superlattices and Microstructures, 2016. **91**: p. 70-77.
19. P. Würfel and U. Würfel, *Physics of Solar Cells: From Basic Principles to Advanced Concepts*. third ed. 2016: Wiley.
20. Y. Ashraf Gandomi, D. S. Aaron, T. A. Zawodzinski, and M.M. Mench, *In Situ Potential Distribution Measurement and Validated Model for All-Vanadium Redox Flow Battery.* Journal of The Electrochemical Society, 2016. **163**: p. 5188-5201.
21. S. Giménez and J. Bisquert, *Photoelectrochemical solar fuel production: From basic principles to advanced devices*. first ed. 2016: Springer. 1-559.
22. E.L. Cussler, *Diffusion: Mass Transfer in Fluid Systems*. third ed. 2009, Cambridge: Cambridge University Press.
23. M.D.R. Kok et al., *Mass transfer in fibrous media with varying anisotropy for flow battery electrodes: Direct numerical simulations with 3D X-ray computed tomography.* Chemical Engineering Science, 2019. **196**: p. 104-115.
24. M.T. Mayer, *Photovoltage at semiconductor–electrolyte junctions.* Current Opinion in Electrochemistry, 2017. **2**(1): p. 104-110.
25. R. Van de Krol and M. Grätzel, *Photoelectrochemical Hydrogen Production* 2012.

26. U. Saha and M.K. Alam, *A heterojunction bipolar transistor architecture-based solar cell using CBTSSe/CdS/ACZTSe materials.* Solar Energy, 2019. **184**: p. 664-671.
27. M. Haghighi, M. Minbashi, N. Taghavinia, D.-H. Kim, S.M. Mahdavi, and A.A. Kordbacheh, *A modeling study on utilizing SnS2 as the buffer layer of CZT(S, Se) solar cells.* Solar Energy, 2018. **167**: p. 165-171.
28. S. Chen and L.-W. Wang, *Thermodynamic Oxidation and Reduction Potentials of Photocatalytic Semiconductors in Aqueous Solution.* Chemistry of Materials, 2012. **24**(18): p. 3659-3666.
29. Z. Mi, L. Wang, and C. Jagadish, *Semiconductors for Photocatalysis*. first ed. 2017: Elsevier Science.
30. Z. Chen et al., *Photoelectrochemical Water Splitting: Standards, Experimental Methods, and Protocols*. first ed. 2013: Springer.
31. H. Lan, Y. Xia, K. Feng, A. Wei, Z. Kang, and J. Zhong, *Co-doped carbon layer to lower the onset potential of hematite for solar water oxidation.* Applied Catalysis B: Environmental, 2019. **258**: p. 117962.
32. Y. Zhu et al., *Insight into the influence of high temperature annealing on the onset potential of Ti-doped hematite photoanodes for solar water splitting.* Chinese Chemical Letters, 2018. **29**(6): p. 791-794.
33. P. Dias, L. Andrade, and A. Mendes, *Hematite-based photoelectrode for solar water splitting with very high photovoltage.* Nano Energy, 2017. **38**: p. 218-231.

Chapter 7

Conclusions and future work

7. Conclusions and future work

Equation Chapter (Next) Section 1

7.1. Final remarks

The main objective of this work was to study and propose improvements to the design of vanadium redox flow batteries (VRFB). These improvements should increase the performance and lifetime of VRFBs and, therefore, increase the market penetration of VRFBs. A 2D dynamic phenomenological model (Chapters 4 and 5), an electrical equivalent circuit model, and an empirical model (Chapter 5) were used to study the mechanisms of performance losses and provide insights for design optimization. Experiments were also conducted to validate the 2D dynamic phenomenological model (Chapter 4) and to compare the performance of two different cell designs (Chapter 3). The most relevant conclusions of this work are:

- Concentration polarization is a performance loss mechanism that is related to the electrolyte regeneration rate at the electrode. This mechanism decreases the energy efficiency and the lifetime of a VRFB. The results from Chapter 3 demonstrated that when low flow rates are used – when the electrolyte regeneration rate is low – the electrolyte flow velocity should be increased to minimize the concentration polarization and increase the energy efficiency. However, when high flow rates are used (high electrolyte regeneration rate), the performance of the battery is mostly affected by the electrolyte flow distribution since the electrolyte regeneration rate is high. Distribution channels are typically engraved in the flow frames (used to provide structural support to the cells) of the VRFB stack to feed uniformly the electrode with electrolyte but they should also be used to promote a higher electrolyte flow velocity; the system energy efficiency is maximized when the battery is operated at lower flow rates since the pump energy consumption is lower. Ideally, the distribution channels should be wide, to create an accumulation zone before and after the electrode and improve the electrolyte distribution, and

thin, to promote a higher flow velocity. The flow velocity can also be increased by using narrower electrodes since the cross-sectional area is lower.

- Multi-dimensional DPMs are a tool that can be used to research performance loss mechanisms at a cell and stack scale. For example, they can simulate the performance of a VRFB and provide relevant information about spatial distribution of energy losses related to concentration polarization (concentration overpotential). Thus, a 2D dynamic phenomenological model for VRFBs was successfully developed and validated against experimental data (Chapter 4). From the simulations, it was found that the concentration overpotential can be reduced by up to 3.9 % by positioning the distribution channels closer to the membrane. The ionic transport between the ion exchange membrane and the electrolyte is much slower than the transfer of electrons between the bipolar plate and the electrode. Thus, the concentration overpotential is greater near the membrane and the energy efficiency of the battery can be improved by increasing the electrolyte flow velocity at this zone. The 2D dynamic phenomenological model was also used to study the concentration overpotential during charge-discharge cycling. For optimizing the performance and lifetime of VRFBs, it is recommended to reduce the potential range when performing charge-discharge cycles at high current densities. The concentration overpotential scales exponentially with the state of charge and with the state of discharge, and the rate of change of such overpotential increases for higher current densities. Thus, the maximum state of charge and state of discharge should be lowered to avoid sudden local over charge at the electrodes. Based on these results, it was recommended to operate the VRFB between 20 % and 80 % state of charge.

- Shunt currents are a phenomenon that decreases the energy efficiency and the storage capacity of VRFBs. A poor design of distribution channels and stack design originates higher shunt currents. The 2D dynamic phenomenological model was used to simulate shunt currents in a six cells-stack (Chapter 5) and the simulations demonstrated that the shunt currents are slightly dependent of internal components, such as electrodes, membrane, and bipolar plates, but highly dependent on the electrolyte properties and on the geometric dimensions of the

distribution channels and manifold (used to feed each cell with electrolyte). The impact of the geometric dimensions of the channels and manifold, operating current, and number of cells in a stack in the shunt currents was thoroughly studied. More than 20 000 simulations were carried out using electrical equivalent circuit models to develop an empirical model and perform a sensitivity analysis. Compared to the dynamic phenomenological model, the simulations using the electrical equivalent circuit models are considerably faster. The sensitivity analysis showed that the best strategy to reduce shunt currents consists in using long and narrow manifolds. Using long, narrow, and thin distribution channels, increasing the active area, or reducing the number of cells in a stack also reduce the shunt currents. For example, for a 40 cells-stack, using an active area size of 1600 cm^2 per cell is sufficient to obtain shunt current losses as low as 1.58 % for a current density of 160 mA cm^{-2}, regardless the geometric dimensions of the manifold and distribution channels. However, the size of the active area should not be larger than 1600 cm^2 to minimize the stack design complexity, pressure drop, and handling difficulty.

- Based on the results of Chapter 5, a novel stack design comprising a dumping cell after every 5 cells-stack was proposed. The dumping cell consists in a cell with no electrochemical activity which acts as a manifold extension, significantly reducing the shunt currents. Conventional stacks use long distribution channels to reduce shunt currents instead of long manifolds. However, the novel stack design does not require long distribution channels since the dumping cell reduces the shunt currents. Thus, for the same flow frame size, the new stack has a higher active area than for the conventional stack and consequently, a higher nominal power (19 %). The new stack design also displays a pressure drop 33 % lower than the conventional stack design.

Finally, the first 2D dynamic phenomenological model for solar vanadium redox flow cells (SRFC) reported in the literature is successfully developed and validated with literature values. Equations to simulate the transport and generation of electrons and holes, recombination mechanisms, the photoelectrochemical reaction and variations in the energy

band level of the photoelectrode were implemented in the SRFC model. The results demonstrate that the model can correctly simulate the energy band shifting for different bias potentials. Depletion and accumulation of charges at the electrolyte | photoelectrode interface are also correctly captured by the model. Furthermore, the model was used to study the different recombination mechanisms. It was found that the performance of SRFCs (e.g., maximum current density) is mostly affected by the recombination mechanisms that occur in the bulk of the electrode, while the ability to charge the electrolyte to a high state of charge unbiased is affected by the surface recombination mechanism.

7.2. Future work

There are several suggestions for future work that can improve the competitiveness of VRFBs:

- There is an ongoing discussion in the literature about which flow field is the most suitable for VRFBs. Most studies are performed at a lab scale and using different materials or operating conditions. It is critical to carry out extensive research comparing different flow field-electrode configurations at relevant scales. For example, mathematical models (e.g., continuum, reduced-order, or lumped parameter models combined with equivalent circuit models) can be used to perform a sensitivity analysis to geometric properties of the flow field and electrode, active area size and operating conditions to find the flow field-configuration that maximizes the system energy efficiency and minimizes production costs. For the sensitivity analysis, a similar approach as used in Chapter 5 can be adopted, or a design optimization software (e.g., Ansys DesignXplorer) can be used.
- The introduction of the dumping cell in a VRFB stack is a demonstration that the overall performance and lifetime of the battery can be improved by optimizing the stack design. More importantly, it is the demonstration that a commercial VRFB does not need long electrolyte distribution channels. The next steps towards increasing the competitiveness of VRFBs should include cheaper alternatives to the dumping cell.

- Research of VRFBs using artificial intelligence is scarce. However, it is a great tool that can be used for developing new materials. Furthermore, it can be used as a tool for controlling and monitoring the state of charge and health of the battery, and for optimizing the operating conditions (e.g., flow rate) in real-time. The artificial intelligence algorithm could be trained using experimental data or by combining experimental and simulation data (e.g., using a lamped parameter model) to predict the previous parameters. This approach has the potential to reduce the cost of the overall system since it can, for example, reduce the number of electronic devices and sensors.

Regarding solar redox flow cells, the first approach towards phenomenological modelling of solar redox flow cells and batteries is provided in this thesis. The model should be enhanced by, for example, implementing partial differential equations to simulate the *quasi*-Fermi energy levels. A more sophisticated model (e.g., multi-dimensional model) to simulate light absorption in the photoelectrode should also be implemented.

Appendixes

Appendix A. Supplementary information for Chapter 4

Equation Chapter 1 Section 2

A.1. Figures

Figure **Error! Use the Home tab to apply Título 6;ND Appendix Header 1 to the text that you want to appear here.**.1 – Graphite plate of a VRFB with 16 cm^2 active area used in the experimental test and with milled distribution channels before and after the reactional area.

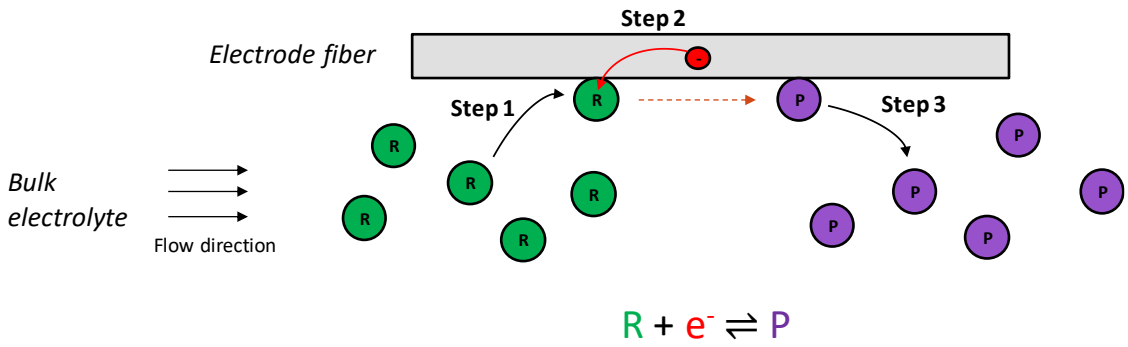

Figure **Error! Use the Home tab to apply Título 6;ND Appendix Header 1 to the text that you want to appear here.**.2 – Schematic representation of the mass transfer mechanism between the electrode fibers and bulk electrolyte.

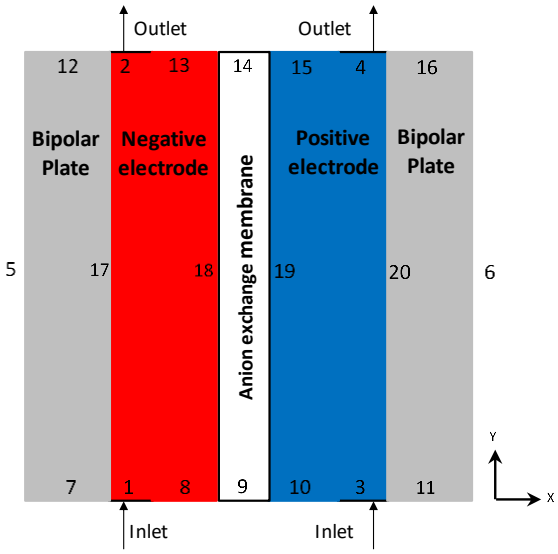

Figure **Error! Use the Home tab to apply Título 6;ND Appendix Header 1 to the text that you want to appear here.**.3 – 2D schematic representation of the computational domain with labelled boundaries from 1 to 20.

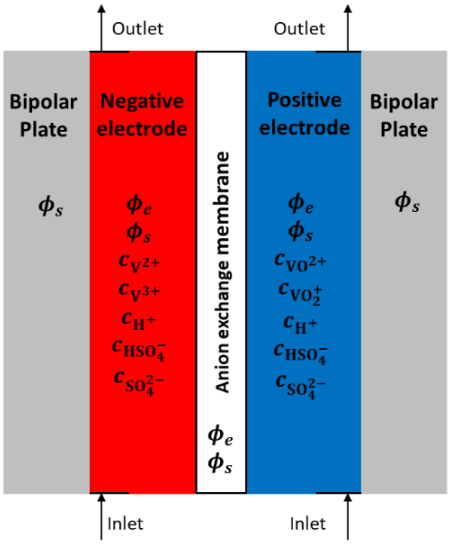

Figure **Error! Use the Home tab to apply Título 6;ND Appendix Header 1 to the text that you want to appear here.**.4 – Schematic representation of the computational domain and variables solved in each domain.

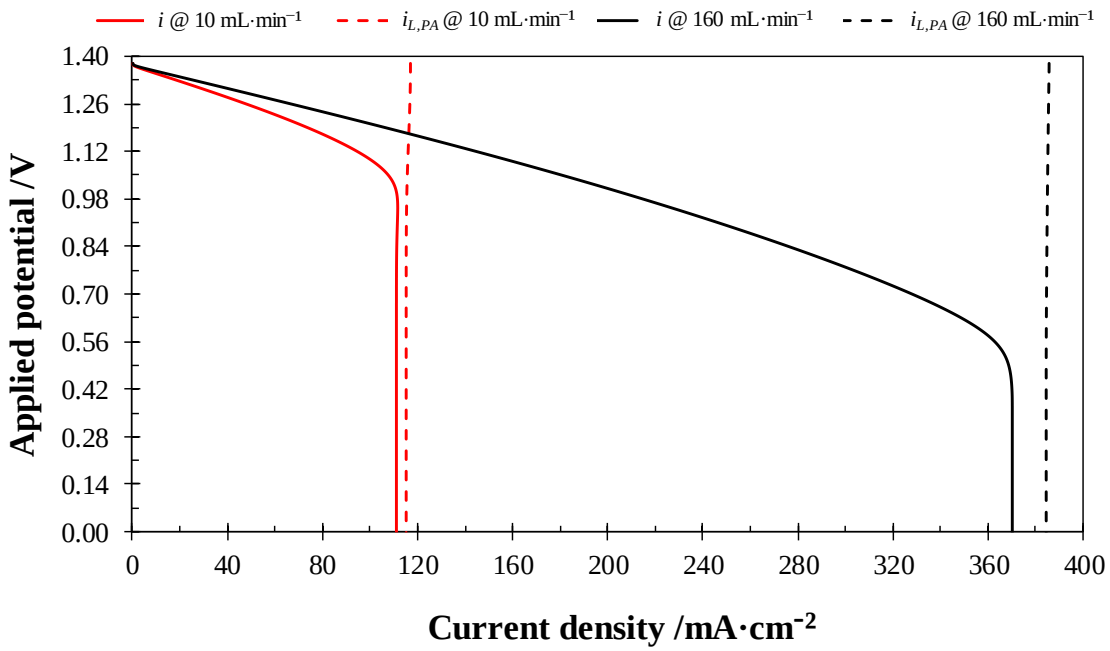

Figure **Error! Use the Home tab to apply Título 6;ND Appendix Header 1 to the text that you want to appear here.**.5 – Simulated polarization curve (the current density is based on the projected area – solid line) and limiting current based on the polarization curve (dashed line, Eq. (4.43)) for feed flow rates of 10 ml min^{-1} and 160 ml min^{-1} and at a constant SoC of 50 %.

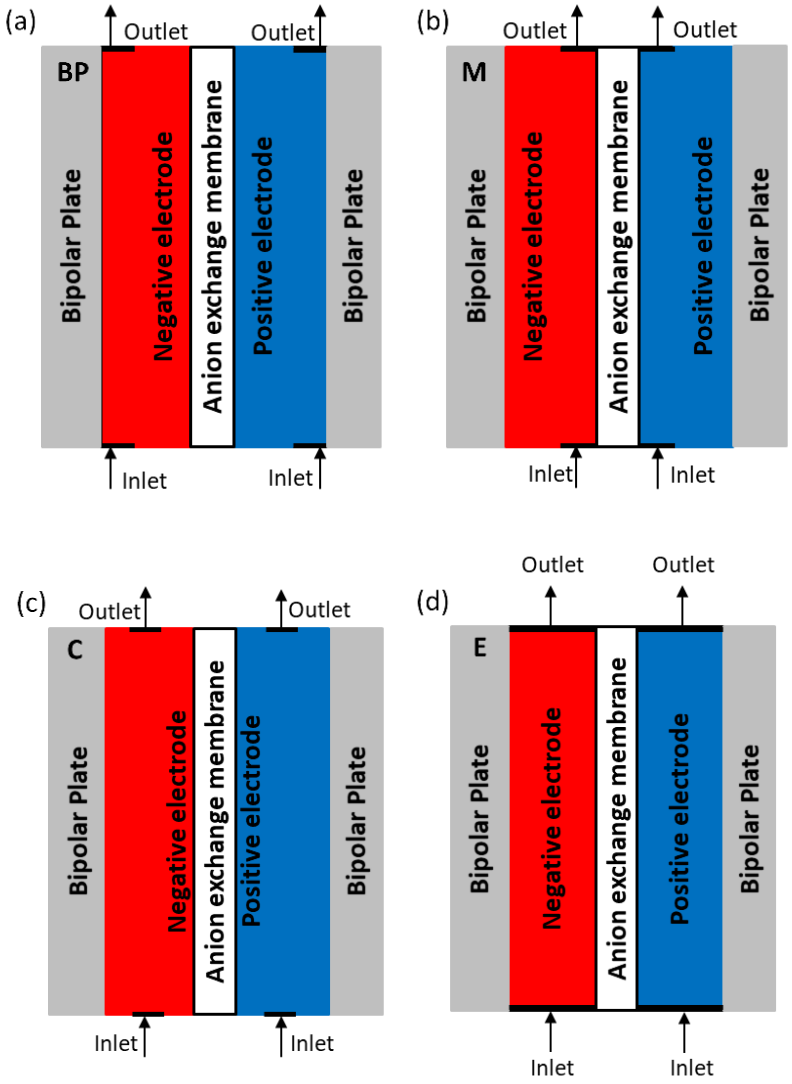

Figure **Error! Use the Home tab to apply Título 6;ND Appendix Header 1 to the text that you want to appear here.**.6 – Schematic representation of (a) cell BP, with inlet/outlet channel close to the bipolar plate, (b) cell M, with inlet/outlet channel close to the membrane, (c) cell C, with inlet/outlet channel at the center of the electrode and (d) cell E with inlet/outlet channel with the same length as the thickness of the electrode.

A.2. Parameters for simulation

Table **Error! Use the Home tab to apply Título 6;ND Appendix Header 1 to the text that you want to appear here.**.1 – Parameters used as electrolyte properties.

Parameter	Value	Ref.
Viscosity of the positive electrolyte, μ_+	3.467-0.635·SoC mPa s	[1]
Viscosity of the negative electrolyte, μ_-	4.229-0.999·SoC mPa s	[1]
Conductivity of the positive electrolyte, $\sigma_{e,+}$	30.8+14.6·SoC S m^{-1}	[2]
Conductivity of the negative electrolyte, $\sigma_{e,-}$	19.6+10.7·SoC S m^{-1}	[2]
Density, ρ	1350 kg m^{-3}	Supplier
Total vanadium concentration, c_V	1600 mol m^{-3}	Supplier
Sulfuric acid concentration, $c_{H_2SO_4}$	2000 mol m^{-3}	Supplier
Volume (each tank), V_{tank}	80 ml	Measured
Volumetric flow rate, Q_{in}	160 ml min^{-1}	Measured
V^{2+} diffusion coefficient, $D_{V^{2+}}$	2.400×10^{-10} m^2 s^{-1}	[3]
V^{3+} diffusion coefficient, $D_{V^{3+}}$	2.400×10^{-10} m^2 s^{-1}	
VO^{2+} diffusion coefficient, $D_{VO^{2+}}$	3.900×10^{-10} m^2 s^{-1}	
VO_2^+ diffusion coefficient, $D_{VO_2^+}$	3.900×10^{-10} m^2 s^{-1}	
H^+ diffusion coefficient, D_{H^+}	9.312×10^{-9} m^2 s^{-1}	
HSO_4^- diffusion coefficient, $D_{HSO_4^-}$	1.330×10^{-9} m^2 s^{-1}	[4]
SO_4^{2-} diffusion coefficient, $D_{SO_4^{2-}}$	1.065×10^{-9} m^2 s^{-1}	

Table **Error! Use the Home tab to apply Título 6;ND Appendix Header 1 to the text that you want to appear here.**.2 – Parameters used as electrode, bipolar plate and membrane properties.

Parameter	Value	Ref.
Length of electrode, l	0.04 m	Measured
Width of electrode, W	0.04 m	Measured
Thickness of electrode, d_e	0.00345 m	Measured
Thickness of inlet/outlet channel, $d_{in/out}$	0.001 m	Measured
Thickness of membrane, d_m	50×10^{-6} m	Supplier
Porosity of electrode, ε	0.90	[5]
Specific surface area, a	4×10^{5} m^2 m^{-3}	[5]
Conductivity of the electrode, σ_s	338 S m^{-1}	[6]
Conductivity of the bipolar plate, σ_s	1000 S m^{-1}	[3]
Conductivity of the membrane, σ_m	1.2 S m^{-1}	Supplier
Fiber diameter, d_f	17.6×10^{-6} m	[3]
Kozeny-Carman constant, k_{ck}	4.28	[3]

Table **Error! Use the Home tab to apply Título 6;ND Appendix Header 1 to the text that you want to appear here.**.3 – Electro-kinetic parameters used in the simulation.

Parameter	Positive electrode (+)	Negative electrode (-)	Ref.
Reaction rate constant, k_i	1.3×10^{-6} m s^{-1}	2.2×10^{-7} m s^{-1}	[7]
Charge transfer coefficient, α	0.50		[3]
Standard equilibrium potential, E^0_i	1.004 V	-0.255 V	

A.3. Determination of initial ion concentrations

Table **Error! Use the Home tab to apply Título 6;ND Appendix Header 1 to the text that you want to appear here.**.4 – Equations used to determine the initial concentration of ion species at a specific SoC.

Variable	Charge separation	Charge phase
$c^0_{\mathbf{V^{2+},-}}$	$c^{pre}_{V^{2+},-} = 0$	$c^0_{V^{2+},-} = c_V \mathrm{SoC}$
$c^0_{\mathbf{V^{3+},-}}$	$c^{pre}_{V^{3+},-} = c_V$	$c^0_{V^{3+},-} = c_V \left(1-\mathrm{SoC}\right)$
$c^0_{\mathbf{VO^{2+},+}}$	$c^{pre}_{VO^{2+},+} = c_V$	$c^0_{VO^{2+},+} = c_V \left(1-\mathrm{SoC}\right)$
$c^0_{\mathbf{VO_2^{+},+}}$	$c^{pre}_{VO_2^{+},+} = 0$	$c^0_{VO_2^{+},+} = c_V \mathrm{SoC}$
$c^0_{\mathbf{H^{+},+}}$	$c^{pre}_{H^{+},+} = c_{H_2SO_4} + 2c_V f_{V^{3+}/VO^{2+}} - \frac{c_V}{3} f_{V^{3+}/VO^{2+}}$	$c^0_{H^{+},+} = c^{pre}_{H^{+},+} + 2c_V \mathrm{SoC} - \frac{c_V}{3}\mathrm{SoC}$
$c^0_{\mathbf{H^{+},-}}$	$c^{pre}_{H^{+},-} = c_{H_2SO_4} - 2c_V\left(1- f_{V^{3+}/VO^{2+}}\right) + \frac{c_V}{3}\left(1- f_{V^{3+}/VO^{2+}}\right)$	$c^0_{H^{+},-} = c^{pre}_{H^{+},-} + \frac{c_V}{3}\mathrm{SoC}$
$c^0_{\mathbf{HSO_4^{-},+}}$	$c^{pre}_{HSO_4^{-},+} = c_{H_2SO_4} + \frac{c_V}{3} f_{V^{3+}/VO^{2+}}$	$c^0_{HSO_4^{-},+} = c^{pre}_{HSO_4^{-},+} + \frac{c_V}{3}\mathrm{SoC}$
$c^0_{\mathbf{HSO_4^{-},-}}$	$c^{pre}_{HSO_4^{-},-} = c_{H_2SO_4} - \frac{c_V}{3}\left(1- f_{V^{3+}/VO^{2+}}\right)$	$c^0_{HSO_4^{-},-} = c^{pre}_{HSO_4^{-},-} - \frac{c_V}{3}\mathrm{SoC}$

where c_V is the initial total vanadium concentration, $c_{H_2SO_4}$ is the initial concentration of sulfuric acid, $c_i^{0,+}$ and $c_i^{0,-}$ are the initial concentration of the ion species *i* in the positive and negative electrodes, respectively, $f_{V^{3+}/VO^{2+}}$ is the ratio of V^{3+} and VO^{2+} ions in the electrolyte before charge separation step and the superscript *pre* refers to the ion concentration after the charge separation step. The concentration of SO_4^{2-} ions was determined considering the electroneutrality condition.

A.4. Determination of the concentration overpotential

Figure **Error! Use the Home tab to apply Título 6;ND Appendix Header 1 to the text that you want to appear here.**.7 shows the concentration overpotential during a charge-discharge cycle determined with Eq. (A.1) for two different conditions:

a) The current density (i) based on the surface area (j/a) and the mass transfer coefficient is the same as in this work ($k_{m,1}$) – alternatively, the current density can be determined as $I/(a \cdot V_{\text{electrode}})$;

b) The current density based on the projected area (i = 800 A·m^{-2}) and the mass transfer coefficient ($k_{m,2}$) is three orders of magnitude higher than $k_{m,1}$ [8] – above 85 % SoC (122 min) and 85 % state of discharge (238 min) this set of conditions is not valid, even though the mass transfer coefficient is higher since the theoretical limiting current density i_L is lower than the current density based on the projected area; in practice, the cell would not be able to charge/discharge further.

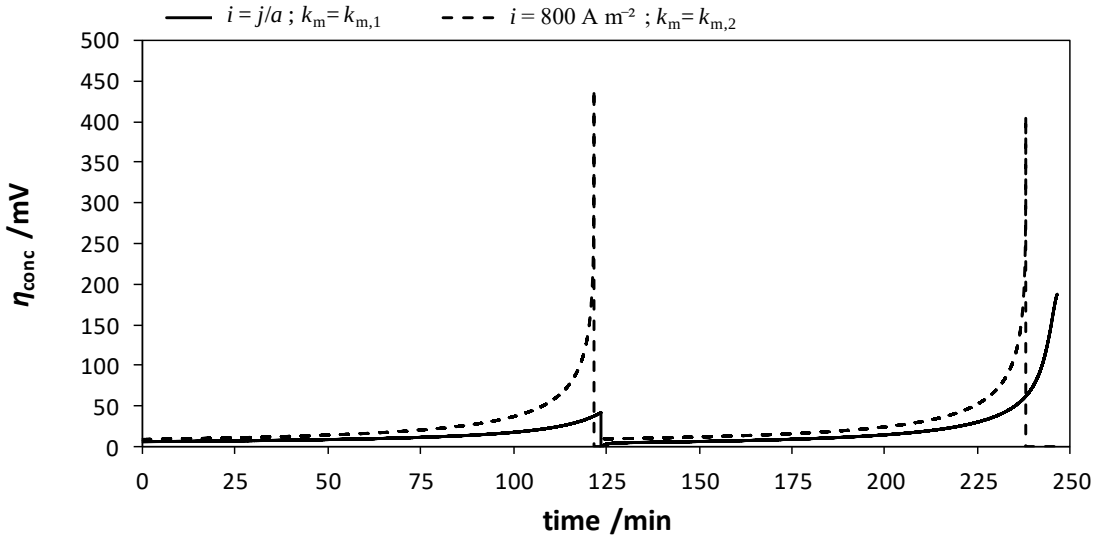

Figure **Error! Use the Home tab to apply Título 6;ND Appendix Header 1 to the text that you want to appear here.**.7 – Concentration overpotential during charge-discharge cycling at 80 mA cm^{-2} and 160 ml min^{-1} considering the current density based on the surface area and a lower mass transfer coefficient (solid line) and the current density based on the projected area and a higher mass transfer coefficient (dashed line).

$$\eta_{\text{conc}} = \frac{RT}{F}\ln\left(\frac{i_L^-}{i_L^- - i}\right) + \frac{RT}{F}\ln\left(\frac{i_L^+}{i_L^+ - i}\right) \tag{A.1}$$

$$k_{m,1} = 5.35\times10^{-3}\left(\frac{\mu}{D_i^{\text{eff}}}\right)^{-0.615}\left(\frac{\rho d_{\text{f}}}{\mu}\right)^{0.409}\vec{v}^{\,0.409} \tag{A.2}$$

$$k_{m,2} = 1.6\times10^{-4}\vec{v}^{\,0.40} \tag{A.3}$$

The limiting current density was determined with the following equation, which is based on the surface area of the electrode:

$$i_L = nFk_m c_R \tag{A.4}$$

A.5. References

1. F.T. Wandschneider et al., *Model of a vanadium redox flow battery with an anion exchange membrane and a Larminie-correction.* Journal of Power Sources, 2014. **272**: p. 436-447.
2. F.T. Wandschneider, S. Röhm, P. Fischer, K. Pinkwart, J. Tübke, and H. Nirschl, *A multi-stack simulation of shunt currents in vanadium redox flow batteries.* Journal of Power Sources, 2014. **261**: p. 64-74.
3. D. You, H. Zhang, and J. Chen, *A simple model for the vanadium redox battery.* Electrochimica Acta, 2009. **54**(27): p. 6827-6836.
4. X. Yang, Q. Ye, P. Cheng, and T.S. Zhao, *Effects of the electric field on ion crossover in vanadium redox flow batteries.* Applied Energy, 2015. **145**: p. 306-319.
5. R. Jervis et al., *In situ compression and X-ray computed tomography of flow battery electrodes.* Journal of Energy Chemistry, 2018. **27**(5): p. 1353-1361.
6. J.T. Davies and J.J. Tummino, *High-Performance Vanadium Redox Flow Batteries with Graphite Felt Electrodes.* C — Journal of Carbon Research, 2018. **4**(1).
7. M. Becker and T. Turek, *Combination of impedance spectroscopy and potential probe sensing to characterize vanadium redox-flow batteries.* Journal of Power Sources, 2020. **446**: p. 227349.
8. Q. Zheng, F. Xing, X. Li, G. Ning, and H. Zhang, *Flow field design and optimization based on the mass transport polarization regulation in a flow-through type vanadium flow battery.* Journal of Power Sources, 2016. **324**: p. 402-411.

Appendix B. Supplementary information for Chapter 5

Equation Chapter (Next) Section 1

B.1. Parameters used in the simulations

Table **Error! Use the Home tab to apply Título 6;ND Appendix Header 1 to the text that you want to appear here.**.1 – Parameters used as electrode, bipolar plate and membrane properties.

Parameter	Value	Ref.
Length of the electrode, *l*	0.04 m	Measured
Width of the electrode, *W*	0.04 m	Measured
Thickness of the electrode, d_{elec}	0.00345 m	Measured
Thickness of membrane, d_{mem}	50×10^{-6} m	Supplier
Thickness of bipolar plate, d_{BP}	1.0×10^{-3} m	Assumed
Thickness of the current collector, d_{cc}	3.0×10^{-3} m	Measured
Porosity of electrode, ε	0.90	[1]
Electrode surface area, *a*	4×10^{5} m^2 m^{-3}	[1]
Conductivity of the electrode, σ_s	338 S m^{-1}	[2]
Conductivity of the bipolar plate/current collector, $\sigma_{BP/cc}$	1000 S m^{-1}	[3]
Conductivity of the membrane, σ_m	1.2 S m^{-1}	Supplier
Fiber diameter, d_f	17.6×10^{-6} m	[3]
Kozeny-Carman constant, k_{ck}	4.28	[3]

Table **Error! Use the Home tab to apply Título 6;ND Appendix Header 1 to the text that you want to appear here.**.2 – Dimensions of the channels and manifold of the six cells-stack.

Parameter	Value
Length of the manifold, l_m	0.00695 m
Length of the channel, l_c	0.02 m
Thickness of the manifold, d_m	0.001 m
Thickness of the inlet/outlet channel, d_c	0.001 m
Area of the manifold, A_m	4.0×10^{-5} m^2
Area of the inlet/outlet channel, A_c	4.0×10^{-5} m^2

Table **Error! Use the Home tab to apply Título 6;ND Appendix Header 1 to the text that you want to appear here.**.3 – Parameters used as electrolyte properties.

Parameter	Value	Ref.
Viscosity of the positive electrolyte, μ_+	3.467-0.635·SoC mPa s	[4]
Viscosity of the negative electrolyte, μ_-	4.229-0.999·SoC mPa s	[4]
Conductivity of the positive electrolyte, $\sigma_{e,+}$	30.8+14.6·SoC S m^{-1}	[5]
Conductivity of the negative electrolyte, $\sigma_{e,-}$	19.6+10.7·SoC S m^{-1}	[5]
Density, ρ	1350 kg m^{-3}	Supplier
Total vanadium concentration, c_V	1600 mol m^{-3}	Supplier
Sulfuric acid concentration, $c_{H_2SO_4}$	2000 mol m^{-3}	Supplier
Volume (each tank), V_{tank}	480 ml	Assumed
Volumetric flow rate, Q_{in}	160 ml min^{-1}	Measured
V^{2+} diffusion coefficient, $D_{V^{2+}}$	2.400×10^{-10} m^2 s^{-1}	[3]
V^{3+} diffusion coefficient, $D_{V^{3+}}$	2.400×10^{-10} m^2 s^{-1}	
VO^{2+} diffusion coefficient, $D_{VO^{2+}}$	3.900×10^{-10} m^2 s^{-1}	
VO_2^+ diffusion coefficient, $D_{VO_2^+}$	3.900×10^{-10} m^2 s^{-1}	
H^+ diffusion coefficient, D_{H^+}	9.312×10^{-9} m^2 s^{-1}	
HSO_4^- diffusion coefficient, $D_{HSO_4^-}$	1.330×10^{-9} m^2 s^{-1}	[6]

SO_4^{2-} diffusion coefficient, $D_{SO_4^{2-}}$	1.065×10^{-9} m^2 s^{-1}

Table **Error! Use the Home tab to apply Título 6;ND Appendix Header 1 to the text that you want to appear here.**.4 – Electro-kinetic and mass transfer parameters used in the simulation.

Parameter	Positive electrode (+)	Negative electrode (-)	Ref.
Reaction rate constant, k_i	1.3×10^{-6} m s^{-1}	2.2×10^{-7} m s^{-1}	[7]
Charge transfer coefficient, α	0.50		[3]
Standard equilibrium potential, E^0_i	1.004 V	-0.255 V	[3]
Mass transfer coefficient, k_m	$5.35\times10^{-3}\left(\frac{\mu}{D_i^{\text{eff}}}\right)^{-0.615}\left(\frac{\rho d_f}{\mu}\right)^{0.409}\vec{v}^{\,0.409}$		[8]

B.2. Model comparison data

Table **Error! Use the Home tab to apply Título 6;ND Appendix Header 1 to the text that you want to appear here.**.5 – Shunt current in each channel and each manifold and potential of each cell of the positive side of the VRFB six cells-stack obtained using the dynamic phenomenological model (DPM) and the equivalent circuit model (ECM). The relative difference between models is calculated using the DPM as reference. The shunt currents were simulated at 50 % state of charge, for the charging step, and with a current density of 80 mA cm^{-2}.

	DPM			ECM			Relative difference		
	Shunt current /A		Potential /V	Shunt current /A		Potential /V	Shunt current /A		Potential /V
Cell nº	Manifold	Channel		Manifold	Channel		Manifold	Channel	
1	0.117	-0.117	1.45	0.131	-0.131	1.52	11.5%	11.6%	5.3%
2	0.173	-0.056	2.87	0.194	-0.063	3.02	12.0%	13.2%	5.2%
3	0.190	-0.017	4.29	0.213	-0.019	4.51	12.1%	13.7%	5.3%
4	0.174	0.016	5.70	0.194	0.019	6.01	11.8%	14.6%	5.5%
5	0.118	0.056	7.12	0.131	0.063	7.53	11.1%	13.0%	5.8%
6		0.118	8.56		0.131	9.10		11.0%	6.3%

B.3. Mesh quality analysis

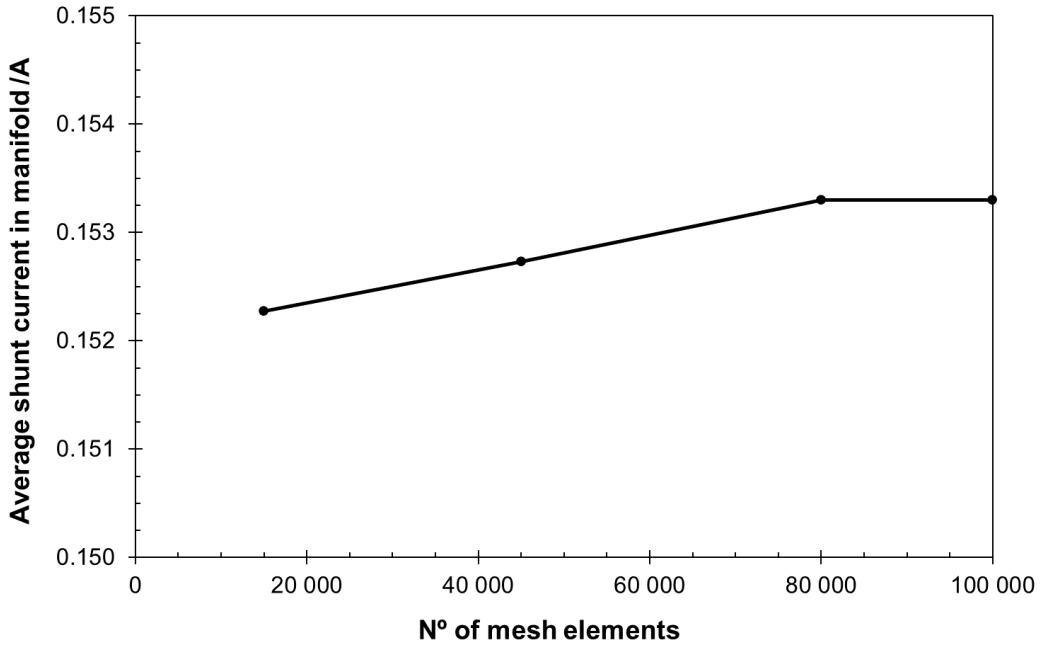

Figure **Error! Use the Home tab to apply Título 6;ND Appendix Header 1 to the text that you want to appear here.**.1 – Average shunt current in the positive manifold of the six cells-stack using a mesh with 15 000, 45 000, 80 000 and 100 000 elements.

B.4. Effect of the internal resistances in the shunt currents

Table **Error! Use the Home tab to apply Título 6;ND Appendix Header 1 to the text that you want to appear here.**.6 – Shunt current in each channel of positive side of the VRFB with six cells obtained for the simulation using the baseline parameters and for the simulations using tenfold higher reaction rate constant, k, mass transfer coefficient, k_m, electrode surface area, a and electrode, σ_s, and membrane, σ_{mem}, conductivities, using fivefold higher electrolyte conductivity, σ_e, tenfold lower flow rate, Q, and a lower electrode thickness (δ_{elec} = 2.0 mm).

	Shunt current in channel nº /A					
Simulation	**1**	**2**	**3**	**4**	**5**	**6**
Baseline (BL)	0.1159	0.0556	0.0166	-0.0163	-0.0558	-0.1173
10·k	0.1158	0.0556	0.0166	-0.0162	-0.0557	-0.1172
10·k_m	0.1151	0.0551	0.0164	-0.0162	-0.0553	-0.1163
10·a	0.1150	0.0551	0.0164	-0.0162	-0.0552	-0.1162
10·σ_{mem}	0.1131	0.0543	0.0161	-0.0161	-0.0546	-0.1141
10·σ_s	0.1142	0.0550	0.0166	-0.0158	-0.0550	-0.1162
5·σ_e	0.5070	0.2455	0.0779	-0.0652	-0.2424	-0.5275
Q/10	0.1173	0.0562	0.0167	-0.0165	-0.0564	-0.1187
↓δ_{elec}	0.1356	0.0706	0.0219	-0.0223	-0.0731	-0.1428

Table **Error! Use the Home tab to apply Título 6;ND Appendix Header 1 to the text that you want to appear here.**.7 – Shunt current in each manifold of positive side of the VRFB with six cells obtained for the simulation using the baseline parameters and for the simulations using tenfold higher reaction rate constant, k, mass transfer coefficient, k_m, electrode surface area, a and electrode, σ_s, and membrane, σ_{mem}, conductivities, using fivefold higher electrolyte conductivity, σ_e, tenfold lower flow rate, Q, and a lower electrode thickness (δ_{elec} = 2.0 mm).

	Shunt current in manifold nº /A					
Simulation	**1**	**2**	**3**	**4**	**5**	**Average**
Baseline (BL)	0.1161	0.1719	0.1887	0.1727	0.1171	0.1533
10·k	0.1160	0.1718	0.1887	0.1726	0.1171	0.1532
10·k_m	0.1153	0.1706	0.1872	0.1712	0.1161	0.1521
10·a	0.1152	0.1704	0.1870	0.1711	0.1160	0.1519
10·σ_{mem}	0.1133	0.1678	0.1842	0.1683	0.1139	0.1495
10·σ_s	0.1144	0.1696	0.1864	0.1708	0.1160	0.1515
5·σ_e	0.5078	0.7541	0.8329	0.7685	0.5268	0.6780
Q/10	0.1175	0.1740	0.1909	0.1747	0.1185	0.1551
↓δ_{elec}	0.1376	0.2099	0.2335	0.2128	0.1414	0.1871

B.5. Effect of R_m, R_c, I and N in the shunt currents

Table **Error! Use the Home tab to apply Título 6;ND Appendix Header 1 to the text that you want to appear here.**.8 – Total number of simulations that resulted in shunt current losses (SCL) lower or equal to 1 % and greater than 1 % for each value of manifold resistance, R_m, and channel resistance, R_c.

R_m			R_c		
Nº of simulations		**Value/Ω**	**Nº of simulations**		**Value /Ω**
SCL ≤ 1%	**SCL > 1%**		**SCL ≤ 1%**	**SCL > 1%**	
134	368	0.08	300	285	0.08
134	398	0.16	300	288	0.16
134	430	0.32	300	291	0.32
135	464	0.64	300	295	0.64
144	491	1.28	301	298	1.28
191	449	2.56	303	302	2.56
243	397	5.12	309	300	5.12
300	340	10.24	316	300	10.24
362	278	20.48	329	293	20.48
428	212	40.96	344	284	40.96
497	143	81.92	367	268	81.92
569	71	163.84	397	242	163.84
640	0	327.68	434	206	327.68
640	0	655.36	475	165	655.36
640	0	1310.72	509	131	1310.72
640	0	2621.44	547	93	2621.44

Table **Error! Use the Home tab to apply Título 6;ND Appendix Header 1 to the text that you want to appear here.**.9 – Total number of simulations that resulted in shunt current losses (SCL) lower or equal to 1% and greater than 1% for each value of electric current, *I*, and number of cells in the stack, *N*.

I			***N***		
Nº of simulations		**Value/A**	**Nº of simulations**		**Value /-**
SCL ≤ 1%	**SCL > 1%**		**SCL ≤ 1%**	**SCL > 1%**	
374	733	4	1384	628	5
473	696	8	1240	752	10
579	640	16	1115	856	20
687	570	32	1061	891	30
794	486	64	1031	914	40
891	389	128			
978	302	256			
1055	225	512			

Table **Error! Use the Home tab to apply Título 6;ND Appendix Header 1 to the text that you want to appear here.**.10 – Mean absolute error between the shunt current losses (SCL) determined using the Simulink model and the correlation (Eq. (41)) for each value of manifold resistance, R_m, and channel resistance, R_c.

R_m		R_c	
Value /Ω	**SCL mean absolute error /%**	**Value /Ω**	**SCL mean absolute error /%**
0.08	2.70	0.08	3.86
0.16	2.45	0.16	3.73
0.32	2.28	0.32	3.58
0.64	2.19	0.64	3.42
1.28	2.19	1.28	3.24
2.56	2.28	2.56	3.07
5.12	2.41	5.12	2.91
10.24	2.55	10.24	2.74
20.48	2.73	20.48	2.58
40.96	2.91	40.96	2.45
81.92	3.06	81.92	2.37
163.84	3.19	163.84	2.34

327.68	3.33	327.68	2.34
655.36	3.51	655.36	2.37
1310.72	3.74	1310.72	2.44
2621.44	3.97	2621.44	2.54

Table **Error! Use the Home tab to apply Título 6;ND Appendix Header 1 to the text that you want to appear here.**.11 – Mean absolute error between the shunt current losses (SCL) determined using the Simulink model and the correlation (Eq. (41)) for each value of electric current, *I*, and number of cells in the stack, *N*.

I		***N***	
Value /A	**SCL mean absolute error /%**	**Value /-**	**SCL mean absolute error /%**
4	2.66	5	0.94
8	2.72	10	2.77
16	2.80	20	3.35
32	2.85	30	3.58
64	2.90	40	3.69
128	2.94		
256	2.97		
512	2.98		

B.6. References

1. R. Jervis et al., *In situ compression and X-ray computed tomography of flow battery electrodes.* Journal of Energy Chemistry, 2018. **27**(5): p. 1353-1361.
2. J.T. Davies and J.J. Tummino, *High-Performance Vanadium Redox Flow Batteries with Graphite Felt Electrodes.* C — Journal of Carbon Research, 2018. **4**(1).
3. D. You, H. Zhang, and J. Chen, *A simple model for the vanadium redox battery.* Electrochimica Acta, 2009. **54**(27): p. 6827-6836.
4. F.T. Wandschneider et al., *Model of a vanadium redox flow battery with an anion exchange membrane and a Larminie-correction.* Journal of Power Sources, 2014. **272**: p. 436-447.
5. F.T. Wandschneider, S. Röhm, P. Fischer, K. Pinkwart, J. Tübke, and H. Nirschl, *A multi-stack simulation of shunt currents in vanadium redox flow batteries.* Journal of Power Sources, 2014. **261**: p. 64-74.
6. X. Yang, Q. Ye, P. Cheng, and T.S. Zhao, *Effects of the electric field on ion crossover in vanadium redox flow batteries.* Applied Energy, 2015. **145**: p. 306-319.
7. M. Becker and T. Turek, *Combination of impedance spectroscopy and potential probe sensing to characterize vanadium redox-flow batteries.* Journal of Power Sources, 2020. **446**: p. 227349.
8. N.M. Delgado, R. Monteiro, M. Abdollahzadeh, P. Ribeirinha, A. Bentien, and A. Mendes, *2D-dynamic phenomenological modelling of vanadium redox flow batteries – Analysis of the mass transport related overpotentials.* Journal of Power Sources, 2020. **480**: p. 229142.

Appendix C. Supplementary information for Chapter 6

Equation Chapter (Next) Section 1

C.1. Simulation parameters

The parameters used in the simulation can be found in Table **Error! Use the Home tab to apply Título 6;ND Appendix Header 1 to the text that you want to appear here.**.1-Table **Error! Use the Home tab to apply Título 6;ND Appendix Header 1 to the text that you want to appear here.**.4. Due to the lack of experimental data, the viscosity and density of the electrolyte were assumed to be the same as an aqueous solution of 2 M of sulfuric acid. This is a reasonable assumption since the concentration of vanadium is low, 0.4 M. Other parameters, such as the Auger recombination coefficient, were obtained from the literature. The surface recombination rate, the absorption constant, the conduction band potential, and the reaction rate constant at the positive side were used as fitting parameters.

Table **Error! Use the Home tab to apply Título 6;ND Appendix Header 1 to the text that you want to appear here.**.1 – Properties of the negative electrode, bipolar plate, positive design chamber, photoelectrode, and membrane.

Parameter	Value	Ref.
Length of the electrode, L	20×10^{-3} m	[1]
Width of the electrode, W	20×10^{-3} m	[1]
Thickness of the electrode, δ_{elec}	6.0×10^{-3} m	[1]
Width of the positive chamber (x_4 -x_3), δ_{pos}	10×10^{-3} m	[1]
Thickness of the photoelectrode, δ_{SC}	200×10^{-9} m	[1]
Thickness of the membrane, δ_m	183×10^{-6} m	Supplier
Porosity of the electrode, ε	0.95	Supplier
Specific surface area, a	6.4×10^{4} m^{-2} m^{-3}	Supplier
Conductivity of the electrode, σ_s	83.3 S m^{-1}	Supplier
Conductivity of the bipolar plate, σ_s	1000 S m^{-1}	[2]

Conductivity of the membrane, σ_m	10 S m^{-1}	Supplier
Carbon-based felt fiber diameter, d_f	17.6×10^{-6} m	[2]
Kozeny-Carman constant, k_{ck}	4.28	[2]
Photoelectrode permittivity, ε_{SC}	9	[3]

Table **Error! Use the Home tab to apply Título 6;ND Appendix Header 1 to the text that you want to appear here.**.2 – Characteristics of the electrolytes.

Parameter	Value	Ref.
Viscosity of the electrolyte, μ	1.5 mPa s	Assumed
Viscosity of the solvent, μ^0	1.0 mPa s	[4]
Electrolyte density, ρ	1300 kg m^{-3}	Assumed
Volume (each tank), V_{tank}	80 ml	[1]
Volumetric flow rate, Q_{in}	20 ml min^{-1}	
V^{2+} diffusion coefficient, $D_{V^{2+}}$	2.400×10^{-10} m^2 s^{-1}	[2]
V^{3+} diffusion coefficient, $D_{V^{3+}}$	2.400×10^{-10} m^2 s^{-1}	
VO^{2+} diffusion coefficient, $D_{VO^{2+}}$	3.900×10^{-10} m^2 s^{-1}	
VO_2^+ diffusion coefficient, $D_{VO_2^+}$	3.900×10^{-10} m^2 s^{-1}	
H^+ diffusion coefficient, D_{H^+}	9.312×10^{-9} m^2 s^{-1}	
HSO_4^- diffusion coefficient, $D_{HSO_4^-}$	1.330×10^{-9} m^2 s^{-1}	[5]
SO_4^{2-} diffusion coefficient, $D_{SO_4^{2-}}$	1.065×10^{-9} m^2 s^{-1}	

Table **Error! Use the Home tab to apply Título 6;ND Appendix Header 1 to the text that you want to appear here.**.3 – Electro-kinetic parameters used in the simulation.

Parameter	Positive side (+)	Ref.	Negative side (-)	Ref.
Reaction rate constant, k_i	3.0×10^{-15} m s^{-1}	Fitted	2.2×10^{-7} m s^{-1}	[6]
Charge transfer coefficient, α	0.50	Assumed	0.50	[2]
Standard equilibrium potential, E^0_i	0.337 V	[7]	-0.255 V	[2]

Table **Error! Use the Home tab to apply Título 6;ND Appendix Header 1 to the text that you want to appear here.**.4 – Parameters used to simulate electrons and holes dynamic behavior in the photoelectrode.

Parameter	Value	Ref.
Injection efficiency, η_{inj}	0.95	Assumed
Wavelength, λ	300 nm	[1]
Incident photon flux, I_0 @ 1.5 AM	1.51×10^{21} m^{-2} s^{-1}	-
Absorption constant, A	7.15×10^{6} m^{-1} $eV^{-1/2}$	Fitted
Electron diffusion coefficient, D_n	25.7×10^{-5} m^2 s^{-1}	[8]
Hole diffusion coefficient, D_p	6.42×10^{-5} m^2 s^{-1}	[8]
Donor concentration, N_{donor}	5.0×10^{24} m^{-3}	[9]
Electron density in the conduction band, N_{CB}	18×10^{24} m^{-3}	[3]
Hole density in valence band, N_{VB}	2.2×10^{24} m^{-3}	[3]
Trap density, N_{trap}	0.1×10^{24} m^{-3}	[10]
Conduction band potential, $E_{CB,0}$	-0.763 V	Fitted
Bandgap potential, E_g	2.51 V	[11]
Holes band-to-band lifetime, $\tau_{BTB,p}$	1×10^{-9} s	[9]
Auger recombination constant - electrons, $C_{Aug,n}$	28×10^{-44} m^6 s^{-1}	[12]
Auger recombination constant - holes, $C_{Aug,p}$	9.9×10^{-44} m^6 s^{-1}	[12]
Thermal velocity, υ_{th}	1×10^{5} m s^{-1}	[8]
Electrons capture cross section, δ_n	1×10^{-21} m^2	[13]
Holes capture cross section, δ_p	1×10^{-17} m^2	[3]
Surface recombination rate, k_{sr}	3×10^{3} m s^{-1}	Fitted

C.2. References

1. J. Azevedo et al., *Unbiased solar energy storage: Photoelectrochemical redox flow battery.* Nano Energy, 2016. **22**.
2. D. You, H. Zhang, and J. Chen, *A simple model for the vanadium redox battery.* Electrochimica Acta, 2009. **54**(27): p. 6827-6836.
3. M. Courel, J.A. Andrade-Arvizu, and O. Vigil-Galán, *Loss mechanisms influence on Cu2ZnSnS4/CdS-based thin film solar cell performance.* Solid-State Electronics, 2015. **111**: p. 243-250.
4. X.L. Zhou, T.S. Zhao, L. An, Y.K. Zeng, and X.H. Yan, *A vanadium redox flow battery model incorporating the effect of ion concentrations on ion mobility.* Applied Energy, 2015. **158**: p. 157-166.
5. X. Yang, Q. Ye, P. Cheng, and T.S. Zhao, *Effects of the electric field on ion crossover in vanadium redox flow batteries.* Applied Energy, 2015. **145**: p. 306-319.
6. M. Becker and T. Turek, *Combination of impedance spectroscopy and potential probe sensing to characterize vanadium redox-flow batteries.* Journal of Power Sources, 2020. **446**: p. 227349.
7. W.M. Haynes, *CRC Handbook of Chemistry and Physics*. 2016: CRC Press.
8. A. Kuddus, M.F. Rahman, S. Ahmmed, J. Hossain, and A.B.M. Ismail, *Role of facile synthesized V2O5 as hole transport layer for CdS/CdTe heterojunction solar cell: Validation of simulation using experimental data.* Superlattices and Microstructures, 2019. **132**: p. 106168.
9. S. Hinckley, J.F. McCann, and D. Haneman, *A flux analysis of multiple junction solar cells: The general equations, with computations for an n-CdS/n-GaAs photoanode.* Solar Cells, 1986. **17**(2): p. 317-342.
10. A. Benmir and M.S. Aida, *Simulation of a thin film solar cell based on copper zinc tin sulfo-selenide Cu2ZnSn(S,Se)4.* Superlattices and Microstructures, 2016. **91**: p. 70-77.
11. S. Chen and L.-W. Wang, *Thermodynamic Oxidation and Reduction Potentials of Photocatalytic Semiconductors in Aqueous Solution.* Chemistry of Materials, 2012. **24**(18): p. 3659-3666.
12. L. Chen, S. Wu, D. Ma, A. Shang, and X. Li, *Optoelectronic modeling of the Si/α-Fe2O3 heterojunction photoanode.* Nano Energy, 2018. **43**: p. 177-183.

13. W. Chen, X. Huang, Q. Cheng, C. Chen, D. Yun, and F. Zhang, *Simulation analysis of heterojunction ZnO/CdS/Cu(In,Ga)Se2 thin-film solar cells using wxAMPS.* Optik, 2016. **127**(1): p. 182-187.